H2 Technology Consulting, LLC
kgross@h2techconsulting.com
tel: (510) 468-7515

Recommended Best Practices for Characterizing Engineering Properties of Hydrogen Storage Materials

Mechanical Properties of Hydrogen Storage Materials

Karl J. Gross, H2 Technology Consulting LLC

We gratefully acknowledge assistance and financial support from the U.S. Department of Energy Office of Energy Efficiency and Renewable Energy Hydrogen Storage Program.

National Renewable Energy Laboratory Contract No. 147388
Contract Technical Monitor: Dr. Philip Parilla

Table of Contents

List of Figures

List of Tables

Recommended Reading

This document is not meant to be a thorough review of the leading work in this field, but rather an overview and series of instructive examples of important issues concerning the measurement of the chemical, physical, and engineering properties of hydrogen storage materials. The following resources are a good place to find more detailed information on the key topics.

1 Hydrogen Storage

The book "Solid-state hydrogen storage: materials and chemistry", edited by Walker.[1]

The book "Hydrogen Storage Materials (Materials Science Forum)" edited by Barnes.[2]

The review article "Hydrogen-storage materials for mobile applications" by Schlapbach and Züttel.[3]

European Commission Joint Research Centre Institute for Energy (JRC) Scientific and Technical Reports by D. P. Broom, "Hydrogen Sorption Measurements on Potential Storage Materials".[4]

The book "Hydrogen Storage Technology Materials and Applications" edited by Lennie Klebanoff (CRC Press, Boca Raton, FL, USA, 2013).

2 Hydrides

The book "Hydrides" by Wiberg and Amberger.[5]

3 Metal Hydrides

The book "Metal Hydrides" edited by Muller, Blackledge, and Libowitz.[6]

The book "Transition Metal Hydrides" edited by Dedieu.[7]

The review article "A panoramic overview of hydrogen storage alloys from a gas reaction point of view" by Sandrock.[8,9]

4 Off-board Regenerable Hydrogen Storage Materials

The article "Ammonia–borane: the hydrogen source par excellence?" by Frances H. Stephens, Vincent Pons and R. Tom Baker.[10]

The chapter "Aluminum Hydride" by Ragaiy Zidan in the book, "Handbook of hydrogen storage: New Materials for Future Energy Storage".[11]

5 Physisorption Storage

The review article "Hydrogen adsorption and storage on porous materials" by K.M. Thomas.[12]

6 Thermodynamics

The review article “Materials for hydrogen storage: current research trends and perspectives” by A.W.C. van den Berg and C.O. Arean.[13]

The article “Heat of Adsorption for Hydrogen in Microporous High-Surface-Area Materials” by B. Schmitz, U. Muller, N. Trukhan, M. Schubert, G. Ferey, and M. Hirscher.[14]

“Perry's Chemical Engineers' Handbook” by R. H. Perry and D. W. Green.[15]

B. N. Roy (2002). Fundamentals of Classical and Statistical Thermodynamics. John Wiley & Sons. ISBN 0-470-84313-6.[16]

F. Reif (1965). “Chapter 5 – Simple applications of macroscopic thermodynamics”. Fundamentals of Statistical and Mechanical Physics. McGraw-Hill. ISBN 0070518009.[17]

7 Engineering Mechanical Properties

The chapter “Hydrogen Storage in Metals” by R. Wiswall in the book “Hydrogen in Metals II”.[18]

The chapter “Metal-Hydride Technology: A Critical Review” by P. Dantzer in the book “Hydrogen in Metals III”.[19]

The chapter “Applications” by G. Sandrock, S. Suda, and L. Schlapbach in the book “Hydrogen in Intermetallic Compounds II”.[20]

The book chapters 9, 10 and 11 in “Engineering Properties of Hydrogen Storage Materials”.[21]

The book, “New Quantitative Approach to Powder Technology” by Y. Wanibe and T. Itoh.[22]

The book, “Bulk Solids Handling”, by D. McGlinchey.[23]

Section 7: Measurements of Engineering Mechanical Properties of Hydrogen Storage Materials

Knowledge of the mechanical properties behavior of materials is critical in the engineering design of materials-based scaled-up hydrogen storage systems. Mechanical properties such as porosity, packing density, lattice volume expansion, decrepitation, compaction and grain interlocking, segregation of component phases, mechanical forces, mechanical durability of structured materials all have a large impact on the performance, efficiency, durability and cost of the storage system. Engineered systems will rely heavily on the ability not only to modify the material and system's mechanical properties, but also on our ability to measure these properties accurately and in a manner that is highly representative of how the materials will behave in a full-scale system and, in this case, over repetitive use (cycling).

Some important considerations are: 1) the relative impact of mechanical properties of hydrogen storage materials on total system performance, 2) how mechanical properties data can be used to aid in the engineering design of a storage system, and 3) what types of mechanical properties data are currently available, useful, or not available but needed.

This section of the Best Practices document provides a review of measurement techniques currently being used for measuring mechanical properties of hydrogen storage materials. As this has not been done extensively in the hydrogen storage field, this section also includes an evaluation of common mechanical property measurement methods used in other applied materials fields that may be appropriate for hydrogen storage materials. The main focus of this section is to clarify problem areas in these measurements and to establish common methods and best practices. The following key aspects (and difficulties) of mechanical property measurements are covered herein:

Topics covered:

- Appropriate methods for measuring mechanical properties of different hydrogen storage materials (reversible hydrides, off-board regenerable, and physisorption hydrogen storage materials). These will include both solids and liquids over a wide range of operating temperatures (77 K to 500 K).
- An evaluation of the accuracy or issues related to the accuracy of different measurement techniques when applied to hydrogen storage materials.
- The ability to make measurements under hydrogen at typical application pressures.
- Methods and the importance of performing measurements at specific materials hydrogen storage concentrations.

- The ability to perform simple and accurate measurements on materials that require controlled environments (airless setup or inert gas glove box operations).
- The validity of translating measurements on small samples to full systems scale performance.
- The impact on the measurement technique of materials being in loose powder, compressed powder, bulk compact forms or a liquid.
- The ability to generate useful data for modified materials including the use of additives, designed materials morphology, or incorporated mechanical enhancement components and structures.
- The impact on mechanical property changes due to cycling or, in the case of off-board regenerable materials, decomposition.

Mechanical Properties of Hydrogen Storage Materials

1 Background and Theory

The following is a brief introduction to the general concepts of the mechanical properties of materials. For a detailed review of capacity, kinetics, thermodynamics and cycle-life properties of hydrogen storage materials, please refer to Section 1-5 of Thermodynamics of the Best Practices document "Recommended Best Practices for the Characterization of Storage Properties of Hydrogen Storage Materials".[24]

This document can be downloaded from:

***http://www1.eere.energy.gov/hydrogenandfuelcells/pdfs/best_practices_hydrogen_storage.pdf*.**

1.1 Definitions

The density of particles, powders, and compacts is an important property that often has a significant impact on the performance of hydrogen storage. With proper procedures (see density measurement section 2.1) the mass of a sample can be determined with sufficient accuracy using a laboratory analytical balance. However, in determining various different types of density, it is often the ability to make accurate volume measurements of the same material that is the most difficult. This is particularly true for powder and porous materials, where clear definitions of density are critical.[25] In many cases the terminology can be confusing or overlapping. For this reason, the definitions of commonly utilized terms that are important for hydrogen storage materials development are presented below.

Because many volume and, thus, density measurements are dependent on the measurement method and conditions, as well as sample history or preparation, it is critical that published data be presented with a clear description of:

1) what type of data (e.g. bulk or poured density, tapped density, compressed pellet density) is being presented,

2) what equipment was used to measure it,

3) how the measurements were performed,

4) what under what conditions the measurements were made, and

5) how the sample was prepared or handled prior to measurement.

1.1.1 Material Level Definitions

Powder: A powder is a dry, bulk solid composed of a large number of very fine particles that may flow freely when shaken or tilted. Powders are a special sub-class of granular materials, although the terms powder and granular are sometimes used to distinguish separate classes of material. In particular, powders refer to those granular materials that have the finer grain sizes, and that therefore have a greater tendency to form clumps when flowing. Granulars refers to the coarser granular materials that do not tend to form clumps except when wet.

Porous material: A material containing pores (voids). The skeletal portion of the material is often called the "matrix" or "frame". The pores are typically filled with a fluid (liquid or gas).

Pores: Voids that connect to the surface of a particle are referred to as open pores. Interior voids inaccessible from the surface are called closed or blind pores.

Interparticle Void Volume (V_{void}): Is the space between particles that does not include pores or external void volumes at the surface of a powder sample.

For example, for a powder sample this is defined as:

Equation 1 $$V_{void}(\text{powder}) = 1/\rho_{bulk} - 1/\rho_{sk}$$

External Void Volume ($V_{void\ ext}$): For lack of a standard definition, is referred to as the void volume between a uniform surface and that of a closely fitting envelope surrounding an object. If a perfect plane were to be laid on one of the surfaces of a solid object, there would be many voids sandwiched between the two surfaces. External void volume does not include pores that penetrate the interior of the object. While vague, but this volume can provide an indication of surface roughness.

For example, the void volume for a pressed powder pellets is:

Equation 2 $$V_{void}(\text{pellet}) = 1/\rho_{env} - 1/\rho_{sk}$$

Crystal Density (or Theoretical Density) (ρ_{sc})**:** The crystal density of a substance is the average mass per unit volume of a pure crystalline substance, exclusive of all voids and defects that are not a fundamental part of the atomic or molecular packing arrangement. The crystal density is an intrinsic property of the substance, and hence should be independent of the method of determination. The crystal density can be determined either by calculation (theoretical density) or by measurement of a pure crystalline (mono-crystal) sample.

X-ray Crystal Density (ρ_{XC})**:** The X-ray crystal density is the Crystal Density specifically determined using crystallographic data (size and composition of the unit cell) of a perfect crystal and the molecular mass of the substance.

True Density (ρ_T)**:** True density is the density of the solid portion of a material that excludes the volume of any open and closed spaces or pores. The true density of a single or even multi-component material may approach the theoretical density (crystal density) of the material. The degree to which the measured true density matches the theoretical density can be indicative of the purity and degree of crystallinity of the material.

Apparent Particle (or Skeletal) Density (ρ_{sk})**:** The apparent particle density is similar to the true density except the volume of closed pores, bubbles, or spaces, within a particle are also included. Gas pycnometry measures the volume of the material accessible to the probe gas. For materials with inaccessible, non-solid spaces, gas pycnometry provides the apparent volume and, thus, apparent density of the material. If the true density of a material is known, the closed pore volume can be determined from the difference between the apparent volume and true volume.

Particle Density: Particle density addresses both the crystal density and the intra-particulate porosity (sealed and/or open pores). Particle density depends on the method of measurement that is used to measure the particle's volume. Particle density can be determined using one of the two following methods.

> **Pycnometric density** is determined by measuring the volume of gas displaced by a powder sample using a gas displacement pycnometer. The measured volume of gas includes the volume occupied by open pores but excludes the volume occupied by sealed pores or pores inaccessible to the gas. Pycnometry typically uses helium as the test gas due to its small molecular size and high diffusivity. Thus, most open pores are accessible to the gas. The pycnometric density of a finely milled powder is generally not very different from the crystal density.
>
> **Mercury porosimeter density** (also called granular density) uses mercury as the measurement fluid. This method also excludes contributions from sealed pores. However, it includes the volume of open pores larger than a certain size limit. This pore size limit or minimal access diameter depends on the mercury intrusion pressure applied during the measurement. Mercury typically does not penetrate the finest pores accessible to helium. One advantage of this method is that granular density distributions can be obtained by measuring mercury porosimetry densities at different intrusion pressures.

Apparent Powder Density (ρ_A)**:** The apparent powder density is similar to the bulk density except that it does not include the voids within the pieces, and the voids among the pieces of the powder sample.

Envelope Density (ρ_E)**:** Envelope density is determined from the volume of the solid material, open pores, and closed pores. System density is given by a single, consolidated quantity of material with no interparticle voids between packed particles. The envelope volume is an imaginary, closely conforming skin that envelops the material and may include the volume of small surface irregularities. When skeletal and true densities are both known, the total pore volume, percent porosity, and solid fraction of the sample can be calculated.

Bulk Density (ρ_B)**:** The bulk density of a material such as powders includes the volume of the solid material, open and closed pores, and interparticle voids. Bulk density is not an intrinsic property of a material. It can change depending on how the material is handled. For example, a powder poured into a cylinder will have a particular bulk density. If the cylinder is disturbed, the powder particles may settle, resulting in a higher bulk density. The total volume of interparticle voids may change with packing, leading to the concept of Tap Density.

Packing Density (ρ_B)**:** The packing density of a material is essentially the bulk density of a material after condensing or packing by some means, such as: compression, vibration, tapping, etc.

Tap Density (ρ_{TAP}, ρ_0, ρ_f)**:** Tap Density is given by the mass of a sample and the measurement of the volume of a mass of the sample after tapping the container. Tap density is specific method of measuring packing densities. "Tapping" causes the particles to move and align into a closer packing formation. At the limit of complete compression of the material (such as compression at high forces in a die), the void volume and compressed density can be determined as a function of the applied pressure. (ρ_0 is the initial poured or untapped density and ρ_f is the final or tapped stated density)

Packing Fraction (φ): is the ratio of the bulk or tap density to the skeletal density of a powder material.

Equation 3 $$\varphi = \rho_B/\rho_{sk}$$

where ρ_B is the bulk density and ρ_{sk} is the skeletal density.

Excess adsorption (n_{ex}): is a term associated with physisorption hydrogen storage materials. It is the extra hydrogen present due to adsorption of hydrogen to the surface of the adsorbent. It represents excess hydrogen per unit sample over what would be present if the density of gas were the same all the way to the surface as it is in the bulk. The value can be positive, negative or zero. Excess adsorption is the material hydrogen storage capacity value that is directly determined using volumetric and gravimetric methods, and is often presented either in units of moles of H_2 per kilogram of adsorbent (mole/kg) or as a percentage of the combined H_2 and

sorbent mass (wt. %).

Absolute adsorption (n_a): is a term associated with physisorption hydrogen storage materials. It is the total amount of hydrogen present in the space where the attractive potential from the surface is effective (adsorbed phase). It includes all of the gas in the adsorption boundary layer including the bulk phase gas and the surface excess gas. Because the boundary layer is a hypothetical construct, the absolute adsorption capacity cannot be measured experimentally. It can be a useful conceptual quantity but relies on uncertain assumptions regarding the arbitrary placement of the dividing line and surface shape between adsorbed and bulk gas. It is related to excess adsorption by

Equation 4 $$n_a = n_{ex} + V_a\rho_g,$$

where V_a is the adsorbate volume and ρ_g is the bulk hydrogen gas density.

Total storage (or Total Material Storage) (n_T): for physisorption hydrogen storage materials is the total amount of hydrogen (both adsorbed and gaseous) present within the volumes of material. This includes all hydrogen absorbed in the bulk, all gas adsorbed to the surface of a material, and gas present within the pores and cracks of individual particles or between particles in the envelope volume of the material. Thus, total adsorption often includes compressed gas, which is not present in the adsorption boundary layer. It provides a measure of the effectiveness of an adsorbent in increasing the storage capacity of a fixed volume when filled with the adsorbent. The total hydrogen storage amount for sorbent mass $m_{sorbent}$ is equal to

Equation 5 $$N_t = m_{sorbent}(n_{ex} + V_v\rho_g),$$

where the void volume has been defined for powders (Equation 1) and pellets (Equation 2). When presented as a fraction of total adsorbent volume (assuming a monolith), it has the form

Equation 6 $$n_{t,vol} = \rho_{env} n_{ex} + \left(1 - \frac{\rho_{env}}{\rho_{sk}}\right)\rho_g,$$

where ρ_{env} should be replaced with ρ_{bulk} for a powder sample. This total volumetric storage quantity can be considered as a material property (as opposed to a system property). Although, it does depend on material post-processing such as mechanical compaction and composite formation.

Total storage (or Total Material Storage) (n_T): for reversible hydride hydrogen storage materials is the releasable hydrogen stored within the hydride but also includes the pressurized gas stored in the void volume.

Many of these terms are often co-mingled in the literature, causing some confusion. One reason for this may be the differing perspectives of the study of powders of solid materials versus porous materials. As an example, the term “bulk density” is variously used for both apparent density and packing density. The bulk density and apparent density would only be the same if there were no interparticle spaces, or essentially for a single particle sample (with or without closed pores). As another example, the density obtained from filling a container with the sample material and vibrating it to obtain near optimum packing is also called “bulk density”.[26] However, due to compaction, this is what is technically referred to, and referred to here, as the packing density. Similarly, the true density may be equivalent to the X-ray crystal density for pure crystalline materials. This may be the case for porous crystalline as well as well as powder materials. In the case of pure crystalline defect-free open-framework materials having no closed pores, the apparent density, skeletal density, true density, and crystal density will all be the same. The tables and figures below are presented to provide additional clarification for these terms.

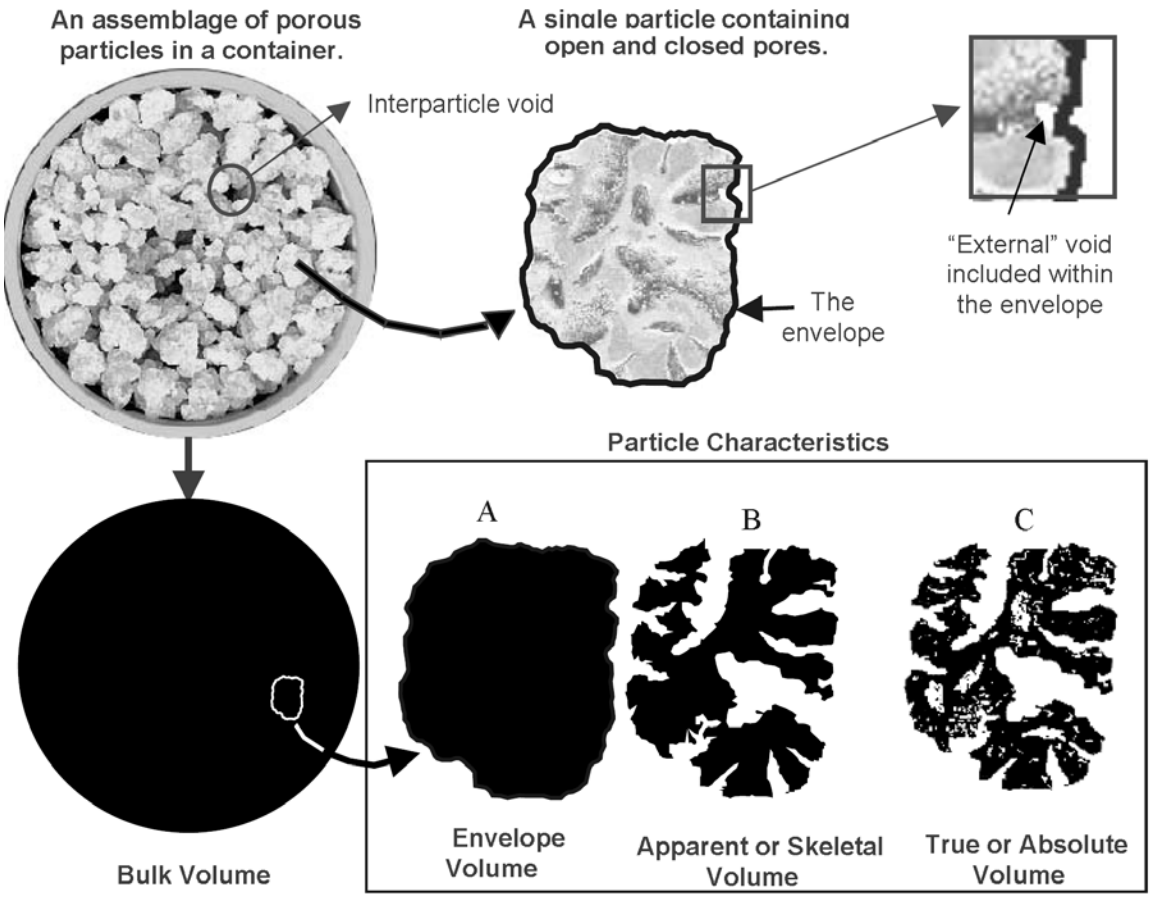

Figure 1. Illustration of various volume types. At the top left is a container of individual particles illustrating the characteristics of bulk volume in which interparticle and "external" voids are included. At the top right is a single porous particle from the bulk. The particle cross-section is shown surrounded by an enveloping band. In the illustrations at the bottom, black areas shown are analogous to volume. The three illustrations at the right represent the particle. Illustration A is the volume within the envelope, B is the same volume minus the "external" volume and volume of open pores, and C is the volume within the envelope minus both open and closed pores.[27]

Volume Definitions	Volumes Included in Definition				
	Solid Material Volume	Open Pore Volume	Closed Pore Volume	Inter-particle Void Vol.	External Void volume
Absolute powder volume: (also called Absolute volume): The volume of the solid matter after exclusion of all the spaces (pores and voids) (BSI).	X				
Apparent particle volume: The total volume of the particle, excluding open pores, but including closed pores (BSI).	X		X		
Apparent powder volume: The total volume of solid matter, open pores and closed pores and interstices (BSI).	X	X	X	X	
Bulk volume: The volumes of the solids in each piece, the voids within the pieces, and the voids among the pieces of the particular collection (implied by ASTM D3766).	X	X	X	X	X
Envelope volume: The external volume of a particle, powder, or monolith such as would be obtained by tightly shrinking a film to contain it (BSI). The sum of the volumes of the solid in each piece and the voids within each piece, that is, within close-fitting imaginary envelopes completely surrounding each piece (Implied by ASTM D3766; see Table 2).	X X	X X	X X	X	X X
Geometric volume: The volumes of a material calculated from measurements of its physical dimensions.	X	X	X	X	X
Skeletal volume: The sum of the volumes of the solid material and closed (or blind) pores within the pieces (Implied by ASTM D3766).	X		X		
True volume: Volume excluding open and closed pores (implied by BSI).	X				
Void: Space between particles in a bed (BSI).				X	

Table 1. Definitions of various types of volumes. BSI = British Standards Institute, ASTM = American Society for Testing and Materials.[27]

Depending upon the measurement method, various types of volumes as defined in Table 1 can be determined. Obtaining two or more volume values by different methods allows extraction of porosity information by the application of simultaneous equations.

Bulk Volume:

Equation 7 $$V_B = V_S + V_{OP} + V_{CP} + V_I + V_{EXT}$$

Apparent Particle Volume:

Equation 8 $$V_{APart} = V_S + V_{CP}$$

Apparent Powder Volume:

Equation 9 $$V_{APow} = V_S + V_{OP} + V_{CP} + V_I$$

Envelope Volume (BSI):

Equation 10 $$V_E = V_S + V_{OP} + V_{CP} + V_I + V_{EXT}$$

Envelope Volume (ASTM):

Equation 11 $$V_E = V_S + V_{OP} + V_{CP} + V_{EXT}$$

Skeletal Volume:

Equation 12 $$V_{SK} = V_S + V_{CP}$$

True Volume:

Equation 13 $$V_T = V_S$$

In the above equations, V_S is the volume of the solid material, V_{OP} the volume of open pores, V_{CP} the volume of closed pores, V_I the volume of interparticle voids, and V_{Ext} the external void volume.

Density Definitions	Volumes Included in Definition				
	Solid Material Volume	Open Pore Volume	Closed Pore Volume	Inter-particle Void Vol.	External Void volume
Absolute powder density: The mass of powder per unit of absolute volume (BSI).	X				
Apparent particle density: The mass of a particle divided by its apparent (particle) volume (BSI).	X		X		
Apparent powder density: The mass of a powder divided by its apparent volume (BSI).	X	X	X	X	
Bulk density: (also called Bulk powder density): The apparent powder density under defined conditions (BSI). The mass of the particles divided by the volume they occupy that includes the space between the particles (ASTM D5004). The ratio of the mass of a collection of discrete pieces of solid material to the sum of the volumes of: the solids in each piece, the voids within the pieces, and the voids among the pieces of the particular collection (ASTM D3766).	X X	X X	X X	X X	
Effective particle density: The mass of a particle divided by its volume including open and closed pores (BSI).	X	X	X		
Envelope density: The ratio of the mass of a particle to the sum of the volumes of: the solid in each piece and the voids within each piece, that is, within close-fitting imaginary envelopes completely surrounding each piece (ASTM D3766). The ratio of the mass of a particle to the envelope volume of the particle (implied by BSI).	X X	X X	X X	X	X X
Skeletal density: The ratio of the mass of discrete pieces of solid material to the sum of the volumes of: the solid material in the pieces and closed (or blind) pores within the pieces (ASTM D3766).	X		X		
Tap density (also called Tap powder density): The *apparent powder density* obtained under stated conditions of tapping (BSI).	X	X	X	X	
Theoretical density: The ratio of the mass of a collection of discrete pieces of solid material to the sum of the volumes of said pieces, the solid material having an ideal regular arrangement at the atomic level (ASTM).	X				
True density (also called True particle density): The mass of a particle divided by its volume, excluding open pores and closed pores (BSI).	X				

Table 2. Definitions of various types of densities that follow from the volume definitions of Table 1. BSI = British Standards Institute, ASTM = American Society for Testing and Materials.[27]

1.1.2 System Level Definitions

System Volume (V_{SYS}): This is the volume of the container or vessel that holds the complete storage material, whether it is a single mass, powder, pellets or other forms. With respect to hydrogen storage materials development a system level volume should include the volume of the tank itself and the ancillary components of the storage system. According to the US DOE's "Technical System Targets: Onboard Hydrogen Storage for Light-Duty Fuel Cell Vehicles"[28], the system volume used in determining system level hydrogen storage properties is "the volume of the complete storage system, including all stored hydrogen, media, reactants (e.g., water for hydrolysis-based systems), and system components".

System Density (ρ_{SYS}): The system density is valuable in evaluating materials (and systems) at an application level. The system density consists of the mass of the complete storage system divided by the volume of the vessel. In determining system level storage capacities, "Generally the 'full' mass (including hydrogen) is used; for systems that gain weight, the highest mass during discharge is used. All capacities are net useable capacity able to be delivered to the power plant. Capacities must be met at end of service life."[28]

Total System Storage (n_{SYS}): is all hydrogen in the tank, including hydrogen absorbed in the bulk, all gas adsorbed to the surface of a material, and gas present within the pores and cracks of individual particles or between particles in the bulk volume of the material. It is important for determining the actual hydrogen delivery from a storage tank. However, it requires specific knowledge of the complete hydrogen storage system, including weight and volume and thus is rarely reported.

However, at a materials development level the exact nature of the mass and volume of the complete storage tank and components may not be known or even roughly defined. For this reason, publication or presentation of system's level performance based on mass, volume or densities should be very clear about what actual masses and volumes are included (or excluded) in the determination of values.

With respect to mass, for example, variations on such application oriented terms may include only the mass of the active storage material divided by the system volume, or mass of active material and inactive performance augmentation materials divided by the system volume. Examples of performance augmentation materials are additives that enhance thermal conductivity, structural integrity, resistance to impurities, etc.

With respect to system volume, an example of further refinement on this definition can be found in the US DOE document "Targets for Onboard Hydrogen Storage Systems for Light-Duty Vehicles"[29] where the "system volume" is defined as the exact or water volume given by the

minimum volume required by the storage vessel and the onboard hydrogen storage system. This includes every component required to safely accept hydrogen from the delivery infrastructure, store it onboard, and release conditioned hydrogen to the power plant. Note, in that document, the volumetric “Ultimate Full Fleet” capacity targets were estimated where “a correction factor of 15 percent above the average required volumetric capacity was used. The 15 percent volume adjustment is motivated by two factors. First, as the volumes quoted in Table 3 (of the referenced document) refer to exact or water volumes, they represent the minimum volume required by the storage vessel. The effective/box volume available onboard the vehicle is typically less. Within the spacing available, designers must allow for system serviceability, impact requirements, etc. The correction factor to estimate the packaging inefficiency may vary significantly based on the type of system and internal design requirements of each OEM. For example single versus multiple tank configurations will have different correction factors; plumbing routes for fill lines also impact volume. In practice, the realistic "engineering volume" consumed by a hydrogen storage system will always exceed its water volume. Second, three of the four vehicles in the NREL dataset are crossover or small-SUV-type. Packaging of hydrogen storage in these larger vehicles will generally be easier than in smaller ones. Taking these two factors into account, a target value slightly higher than the NREL average was adopted.”

These are but a couple of examples of the variations in how “System” level mass and volumes are presented. Again, at a development level the exact nature of the mass and volume of the complete storage system may not be known or well defined.

These different volumes as we have defined them here and the related densities are represented schematically in Figure 2.

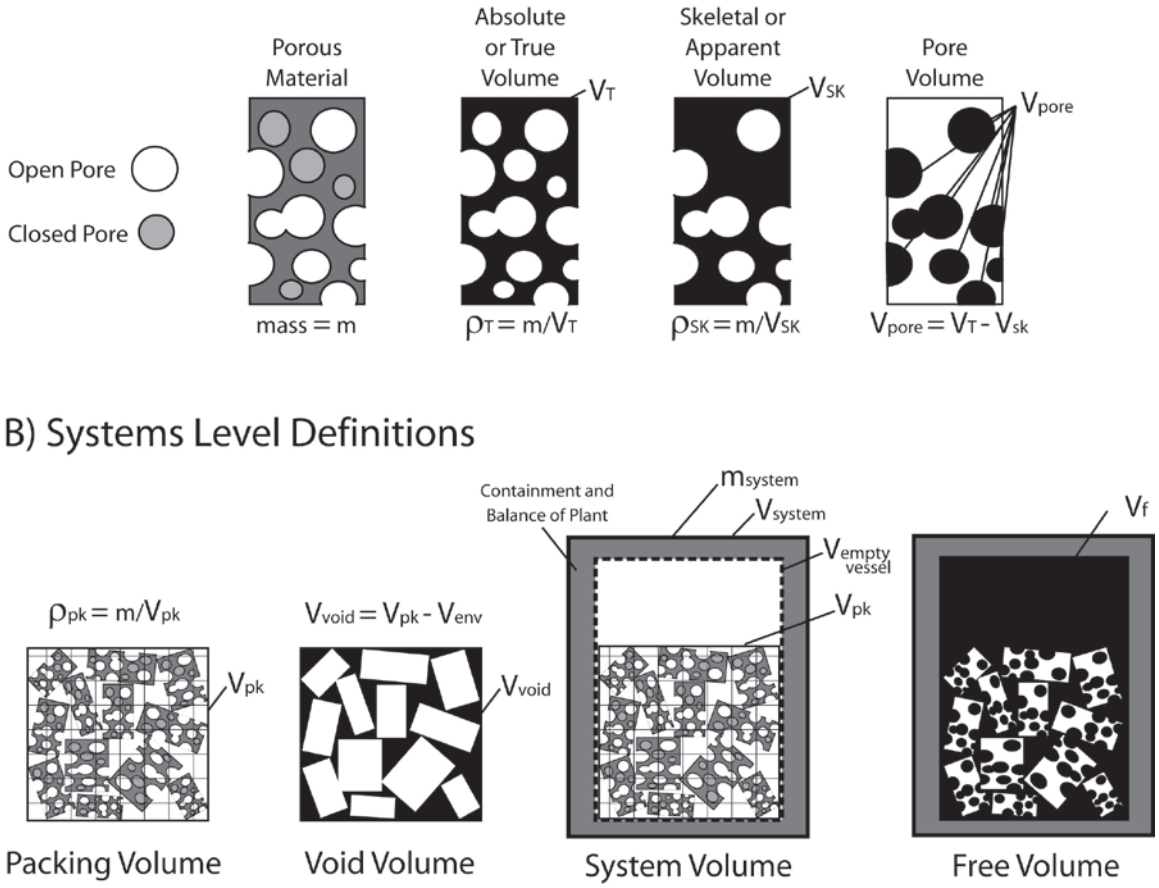

Figure 2. Volume and Density Definitions: Illustration of volume and density definitions relevant to hydrogen storage capacities at a materials and systems level.

1.2 Introduction

In general, hydrogen storage materials can be classified into 4 different classes of materials: (1) conventional metal hydrides (also referred to as classic metal hydrides or intermetallic hydrides), (2) complex hydrides, (3) sorbents, and (4) chemical hydrides. The relevant features of these four materials classes can be found in the preface Subsection 5 of "Recommended Best Practices for the Characterization of Storage Properties of Hydrogen Storage Materials"[24] and the excellent review by Yang et al.[30] An overview of the hydrogen storage properties of these 4 classes of materials is shown in their figure below.

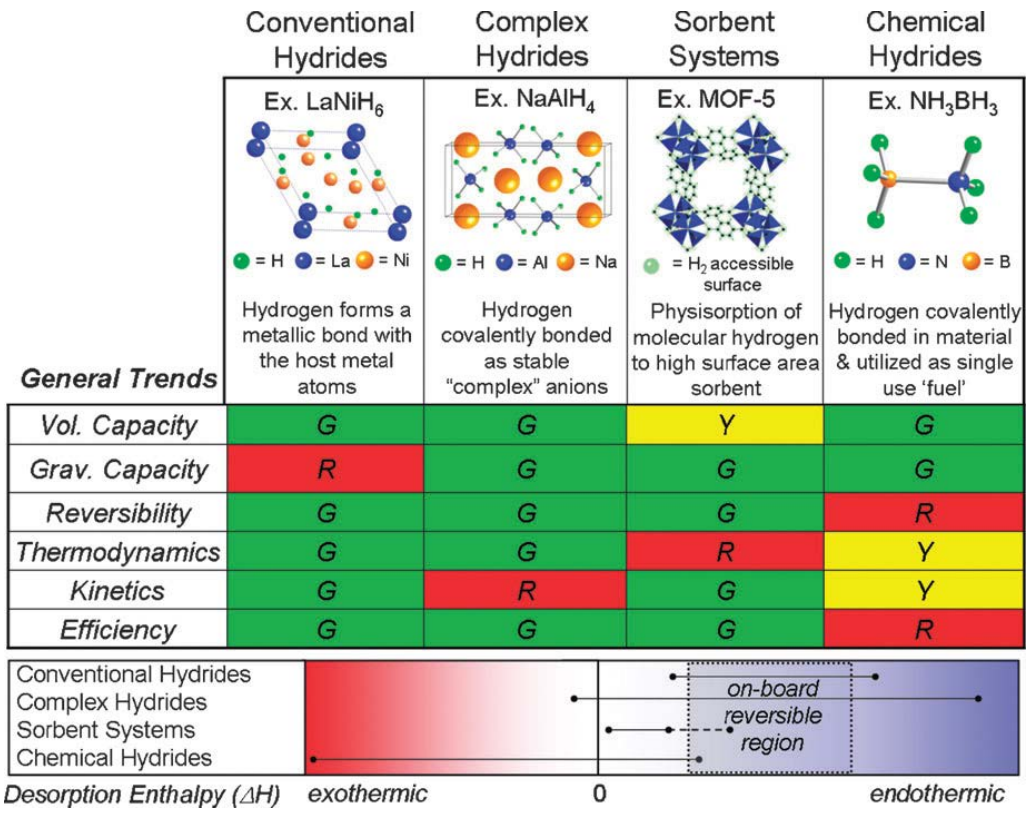

Figure 3. Overview of the properties of the major hydrogen storage materials classes. Trends for technical challenges for each class are delineated by color code: Red indicates significant challenges remain towards achieving DOE targets; Green signifies satisfactory performance; Yellow indicates some improvement is required. Trends and reaction enthalpies are meant to be generally descriptive for the entire class; exceptions are possible for individual materials.[30]

Each class of hydrogen storage materials will have mechanical property issues that need to be addressed to improve overall storage performance. Many of these mechanical properties issues are the same for all classes, such as the need to improve volumetric capacity by reducing void volume (generally through compaction). However, each class (and certain materials within a class) may have specific mechanical property issues.

For example, intermetallic hydride forming alloys typically undergo large lattice expansion on hydriding followed by decrepitation into fine metal powders on hydrogen cycling. This effect can cause increased bulk density, large mechanical expansion forces, and decreased thermal conductivity, all of which impact the storage performance of these materials.

Complex hydrides may also undergo significant lattice expansions on hydride formation, however some of the expansion force and thermal conductivity issues may be mitigated by the fact that hydrogen uptake and release occur through chemical decomposition and

recombination. This, by its nature, involves the physical mobility of reactants which can accommodate stress and provide for reduced void formation relieving some expansion force and thermal conductivity issues. At the same time, this mobility creates the opportunity for phase-segregation with cycling, which can lead to a form of mechanical/chemical degradation in performance.

Sorbents or physisorption materials are generally not impacted by volume changes on hydrogen uptake. Nevertheless, generally low packing densities can lead to poor volumetric hydrogen storage capacities, which again may be improved by compaction. However, unlike most hydrides, compaction of physisorption materials may eventually lead to reduced surface areas, producing a loss in the intrinsic storage capacity of these materials.

Chemical hydrides vary widely in their hydrogen storage process and characteristics. Thus, mechanical properties issues vary on a case-by-case basis. These may be as similar as the need for powder compaction, to as unique as the ability to form a liquid slurry of the reactants or products or the mechanical properties of the material with respect to transport into a reactor by flow methods or physical means.

This document focuses on the most common mechanical properties issues associated with the majority of materials within these four classes. A large portion of the materials that are being developed for hydrogen storage applications are (by synthesis or as a result of hydriding) in the form of powders. The following sections cover important aspects of the mechanical properties of hydrogen storage materials including, to a large extent, powders. There appears to be a vital need to develop a better understanding of powder structures themselves as well as their physical properties and the impact on hydrogen storage performance. Sections 1.5 to 1.16 cover new advances that are being made in modeling physical properties of powder compacts of hydrogen storage materials. Currently there is limited experimental data on topics such as the packing densities, thermal conductivity, and gas transport in hydrogen storage materials, and the relationship between these properties and powder particle structures.

Hopefully, this Best Practices section will provide some insight into:

1. the work that is being pursued in these topics,
2. the experimental methods that are being used to generate data to support system design and validate modeling efforts,
3. issues associated with making such measurements, and
4. the types of mechanical properties studies that are needed to advance our uderstanding of how to further improve the performance of hydrogen storage materials.

1.3 Volume Changes of Hydrogen Storage Materials

It is well known that many hydrogen storage materials (hydrides and to some extent physisorption materials) undergo significant volume and density changes on the uptake or release of hydrogen. For example, the hydride $CeMn_{1.5}Al_{0.5}H_x$ undergoes an extraordinary lattice volume expansion of over 35% on hydriding.[31] A portion of the in-situ neutron diffraction measurements during deuteration are shown in Figure 4. The coexistence of the α and β phases up to the completion of the α - β phase transformation is apparent. A dramatic lattice expansion is observed after the completion of the α - β phase transformation. This change was attributed to further absorption of deuterium into the β phase with increasing pressure to form a solid solution deuteride (β' phase). While the effects of deuterium absorption appear dramatic, all three phases (α, β and β') continue to maintain the same $P6_3/mmc$ crystal symmetry of the host-metal structure.

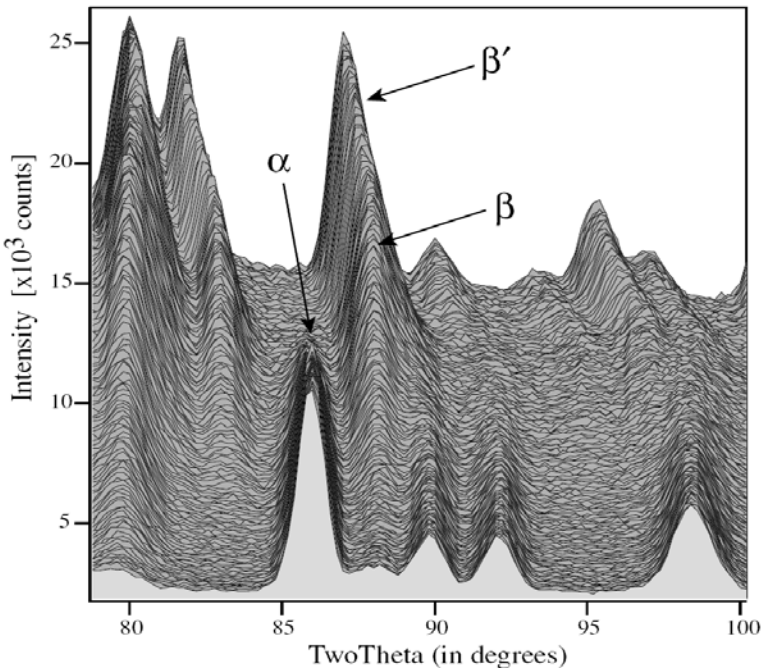

Figure 4. A portion of the real-time neutron diffraction measurements of $CeMn_{1.5}Al_{0.5}D_X$ as the deuterium concentration is varied from 0 to 170 ncm^3 D_2/g-sample (instrument D1B, λ = 2.521Å). The α phase solid solution disappears and the β phase deuteride grows with increasing deuterium content. At a concentration of x = 3 HD/f.u. (f.u. = formula unit; $CeMn_{1.5}Al_{0.5}D_3$) the β' phase solid solution deuteride appears and grows as observed by a large lattice expansion.[31]

From these measurements relative content of the α and β phases have been calculated from the diffraction patterns and are plotted versus the total deuterium content of the sample in Figure 5a. Similarly the lattice parameters for the α, β and β′ phases have been extracted from these patterns and are presented in Figure 5b. A discrete lattice expansion can be observed in the transition from the α to the β phase. A continuous lattice expansion takes place within each of the three phases as the deuterium content is increased. This is more clearly illustrated by plotting the percent change in lattice parameters (Figure 5c). The expansion is small and isotropic for the α phase, small and anisotropic for the β deuteride, and large and anisotropic for the β′ solid solution. Overall, the volume expansion on the formation of the deuteride (and similarly for the hydride) is very large.

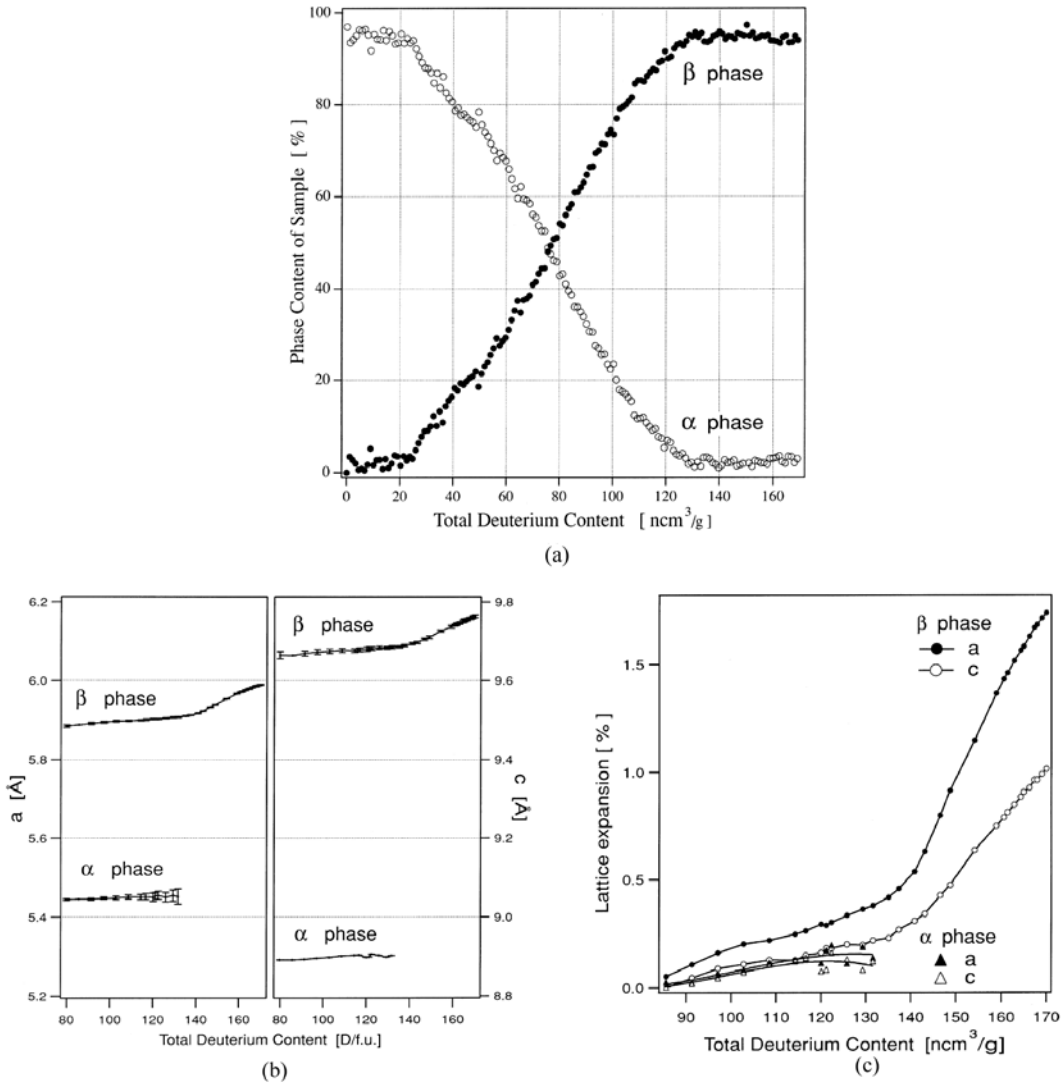

Figure 5. a) α phase solid solution and β phase deuteride content of the sample, b) Lattice parameters *a* and *c* for the α phase solid solution and the β phase deuteride, and c) the percent change in the lattice parameters as a function of the sample total

deuterium content. The α phase expands isotropically, whereas the β (and β') phases have a greater relative expansion in the *a* direction.[31]

The volume expansion between the coexisting α- and the β-phase in metal hydrides corresponds in many cases to 10–20% of the metal lattice. Therefore, at the phase boundary a large amount of stress is built up and often leads to a decrepitation of brittle host metals such as intermetallic compounds. The final hydride is a powder with a typical particle size of 10–100 μm. Such lattice volume expansions are not uncommon for metal hydride hydrogen storage materials and, as such, must not only be determined, but must also be included as an important factor in the engineering design of the storage system.

1.4 Decrepitation of Hydrogen Storage Materials

The process of hydrogenation and dehydrogenation of a metal lattice usually causes lattice expansion and contraction with approximately 2 to 5 $Å^3$ per H atom.[32] In general, the strain caused by the difference in lattice dimensions at the metal-to-hydride interface causes defects leading to crack formation. Through this process, the hydriding of most intermetallic alloys and compounds ultimately causes fragmentation that result in the formation of irregular faceted particles.[33] This process is referred to as *decrepitation.*

Decrepitation takes place with each hydrogen absorption/desorption cycle. After repeated cycling, large particles disintegration into smaller and smaller particles.[34] This systematic reduction in the average particle size has been observed as the number of hydriding cycles increases.[35,36] The dependence of particle size distribution on the number of hydriding cycles was investigated by Hahne and Kallweit.[37] They observed a five-fold reduction in average particle size after 30 cycles. The degree of decrepitation depends on the number of cycles and the plastic behavior of the alloy or metal. Hydrides can reach a state of decrepitation at which particles become mechanically stabilized, and the size distribution does not change with further cycling.[37] In the case of $LaNi_5$, the particle slowly disintegrates to some minimum dimensions after which there is very little reduction in particle size. This may be due micro-plasticity exhibited in intermetallics, which are generally very brittle. Many of the elemental hydrides have metallic character and plastic deformation occurs during hydriding that accommodates the strain thus inhibiting significant decrepitation.

The starting materials to make hydrides are often coarse metal particles, each on the order of several mm in size. Each particle generally consists of a host of single crystal domains, or grains. Grain boundaries within the particle are typically on the scale of micrometers. Once molecular hydrogen comes in contact with the particle surface, dissociation occurs through a catalytic reaction and generates atomic hydrogen (H) interstitials which transport relatively fast through

the grain boundaries (at low temperatures) and diffuse more slowly through the volume of the grain. At a given potential (or pressure and temperature) hydride formation will occur between the interstitial atomic hydrogen and metal lattice.[38] For metal-hydrides this fragmentation process exposes fresh chemically active surfaces and is essential to achieving fast hydriding kinetics.[39]

On the negative side, the fragmented nature of metal hydride particles inhibits heat transfer and thus the dissipation of heat from hydride formation.[40] Heat transfer can be improved by the addition of expanded graphite[41,42,43] and metal[44,45,46] additives. Unfortunately, these chemically inactive materials reduce overall hydrogen storage density and permeability. The densification of decrepitated hydrides can improve hydrogen storage density and permeability, but the dependence of the effective thermal conductivity on the packed structure of hydride powders has only had a limited amount of investigation.

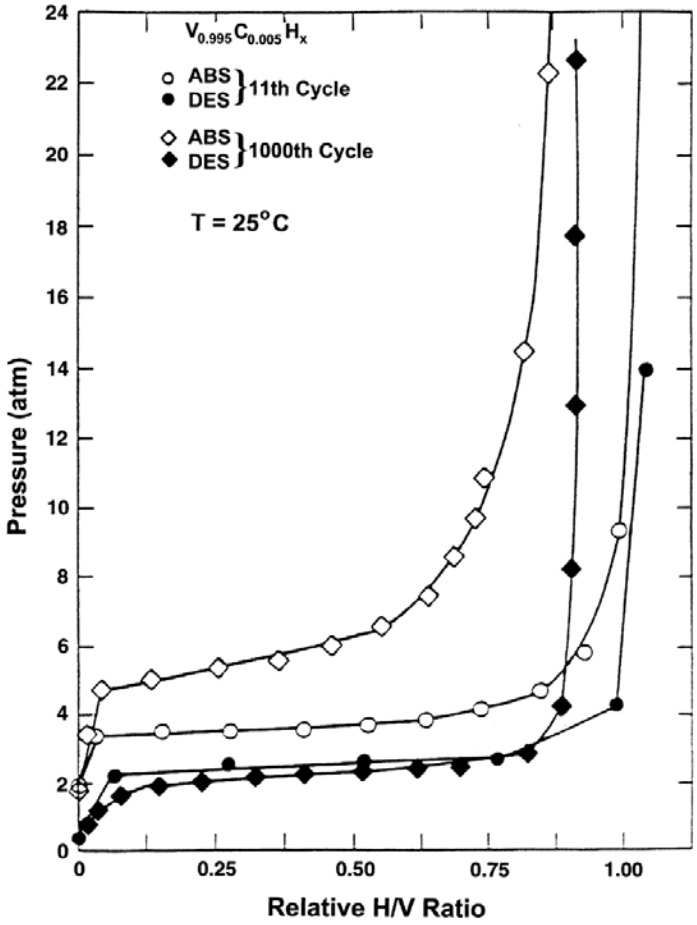

Figure 6. Reversible portions of the pressure–composition isotherms obtained at 298 K on thermal cycled $V_{0.995}C_{0.005}H_X$.[47]

A good example of this is the hydrides of vanadium and some vanadium alloys. [47,48] Although the VH, V–C–H, and V–Zr–C–H systems cannot experience the intrinsic chemical disproportionation reactions that occur in $LaNi_5H_X$ [49] and other ternary hydrides, minor changes were observed in the isotherms for vanadium hydride and some vanadium-alloy hydrides after several hundred absorption–desorption cycles across the β–γ plateau region. Room temperature isotherms of $V_{0.995}C_{0.005}H_X$ taken after 11 and 1000 thermal cycles are shown above in Figure 6.

The morphology of decrepitated powers can affect packing, which in turn can lead to internal gas impedance and container deformation. The morphology of the powders also affects heat transfer. Most hydride powders have poor heat transfer coefficients and require engineering for thermal enhancement (e.g., Al foam, internal fins, etc.). This is made worse by decrepitation leading to the loss of thermal contact with the heat transfer media. The end result is that the decrepitation that occurs with each hydriding cycle may have an important and unpredictable effect on the Cycle-Life properties of a hydrogen storage material.

The decrepitation process is something that should be taken into account in making Cycle-Life measurements. In general, decrepitation is one of several processes that take place in the first few to tens of cycles and is wrapped up in what is commonly called the *Activation* process. In Cycle-Life measurements, the material will likely show increased capacity in the first activation cycles before reaching a more steady-state cycling behavior (usually a slow loss in capacity). It was pointed out in prior chapters that it is important to make sure the sample is fully activated before ascribing long-term hydrogen storage properties to a material. This is equally true for Cycle-Life measurements and is best achieved by recording complete uptake and release data in the first 20 or so cycles.

An example is given below of hydrogen-induced decrepitation of a typical intermetallic alloy during hydride formation. Arun and Ramaprablu performed an X-ray diffraction study on hydrogenated $Zr_{0.2}Tb_{0.8}Co_3$ that revealed that the alloy does not decompose upon hydrogenation. They then performed particle size measurements on $Zr_{0.2}Tb_{0.8}Co_3$ and ZrMnFe alloys before and after hydrogenation. Those measurements demonstrated that the decrepitation in $Zr_{0.2}Tb_{0.8}Co_3$ is far less than that in the much harder material ZrMnFe.[50] Particle size distributions for both alloys and their hydrides are shown in Figures 7 and 8. These were measured using and optical microscope and SEM images. The $Zr_{0.2}Tb_{0.8}Co_3$ alloy was subjected to 35 hydrogen absorption/desorption cycles, while the ZrMnFe alloy was only cycled 8 times. While the method is simple, the results show a much more prominent decrease in particle size for the ZrMnFe alloy due to hydrogen induced decrepitation.

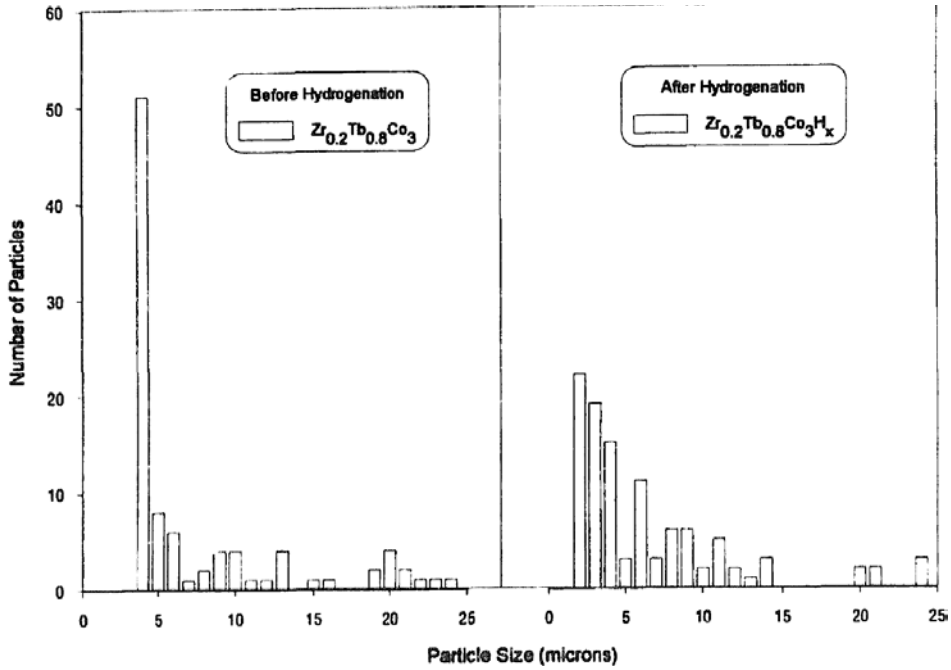

Figure 7. Particle size distributions in $Zr_{0.2}Tb_{0.8}Co_3$ and $Zr_{0.2}Tb_{0.8}Co_3H_x$.[50]

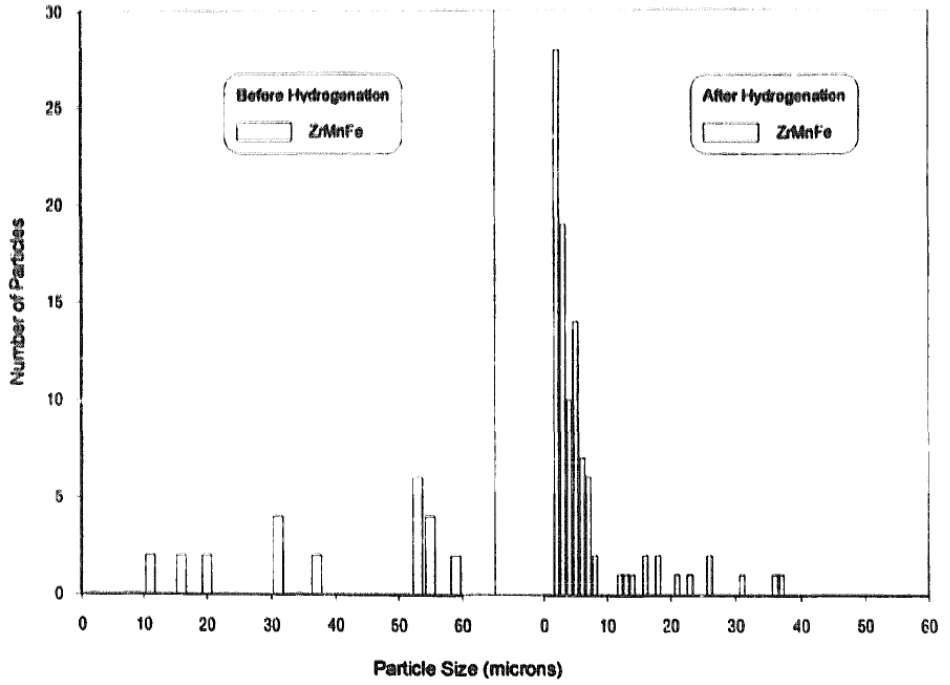

Figure 8. Particle size distributions in ZrMnFe and $ZrMnFeH_x$.[50]

1.5 Mechanical Changes and Durability of Hydrogen Storage Materials

Changes in the mechanical-physical properties of hydrogen storage materials with use (such as hydrogen uptake and release cycling) may not only result in degradation of the material's storage properties, but can also cause serious systems engineering level challenges. For example, hydrogen absorption in metal hydrides typically causes lattice volume expansion (section 1.3), which leads to varying degrees of decrepitation (section 1.4). These two effects combined with cycling and vibration in normal hydrogen storage applications can cause densification and interlocking of microscopic particles, which, by subsequent expansion during hydriding, can impart enormous forces on a containment vessel.

An example of the detrimental effect such material volume expansion can have on a hydrogen storage vessel is shown in Figure 9.

Figure 9. Hydride hydrogen storage vessel deformation caused by material expansion on hydride formation.[51]

Expansion induced stress depends on:

- The compressibility of the media as it changes chemical form during hydrogen uptake,
- The composition of the media, which at equilibrium, depends on the temperature and gas pressure,
- The history of cycling and/or the loading/discharge rates of the media, and
- The propensity of the media to "lock-up" during expansion. That is, the inability of the media to flow freely so that it occupies the full available volume during expansion.

A schematic rendition of the process of how hydride-induced expansion forces can impact a storage system is illustrated in Figure 10 below.

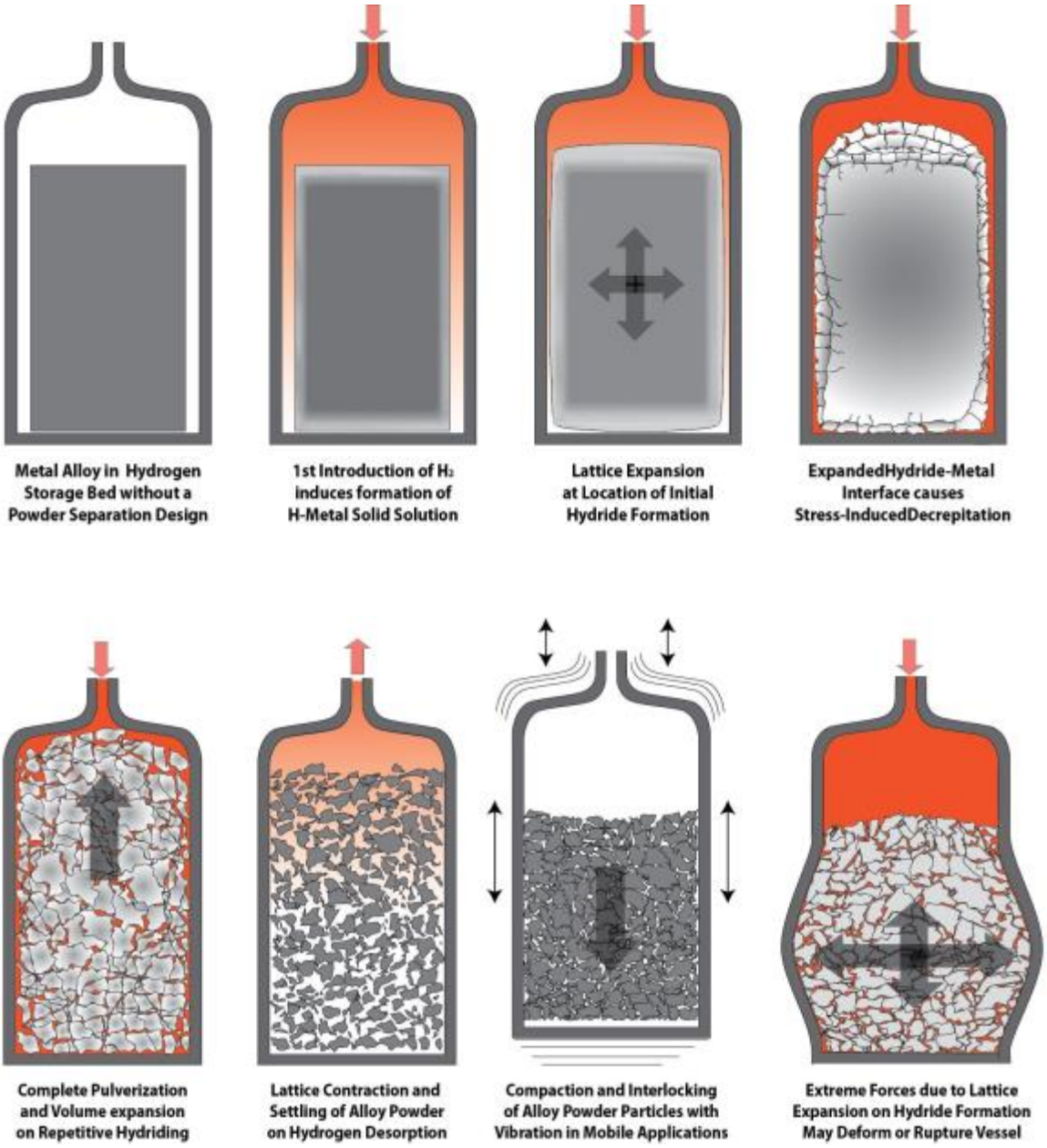

Figure 10. Schematic illustration of material volume expansion upon hydriding and the detrimental effect it can have on a storage system without explicit materials safety engineering design.

Clearly, knowledge (and accurate data) on a material's hydrogen storage mechanical properties is vital in the design of intrinsically safe, durable, and optimally performing materials-based hydrogen storage systems. Some of the mechanical properties to be evaluated are: Lattice (or other) volume changes on hydrogen uptake, propensity for decrepitation and/or degradation on cycling, and the physical interactions of powders and compacts with extensive use.

1.6 Particle Size of Powders and Compacts

The influence of particle size on performance

Particle size influences many properties of hydrogen storage materials. Besides the effects particle size may have on reaction kinetics, heat transfer, adsorption capacity, etc., the size and shape of powders influences scaled-up engineering properties such as compaction, heat transfer, and permeation. The ability to measure particle size is critical for analyzing storage materials after processing (such as by mechanical milling, etc.) as well as to optimize the material's compaction and hydrogen storage properties. In addition, determining the particle size of powders to be mixed with additives can be important to achieve an even distribution of the additive because similar and narrower distributions are less prone to segregation.

Particle Diameter

It is important to note that is the symbols used for diameter vary. The traditional notation followed in the United States uses the character "d" followed by a subscript to define the manner in which the diameter has been computed. ISO standards refer to diameter using the character "x" with the same subscripts.

Caution should be taken when using term "particle diameter" as a quantitative measure of the particle size. The term "diameter" implies particles having spherical shapes. In most cases, however, powders are more irregular in shape and thus, the term "diameter" may be interpreted in different ways.

The analyses of the shape factor (or divergence from a spherical shape) often produce different results depending on the type of particle size measurement method used. Different methods rely on the different physical principles, which may be affected differently by particle shape factors. As an example, using sieving to quantify particle sizes will tend to emphasize the second smallest particle dimension because of the way particles must orient themselves to pass through the mesh opening. A sedimentometer, which measures the rate of fall of particles through a viscous medium, will cause flatter plate-like particles to orient to maximize drag while sedimenting. For such irregular particles, this can skew the reported particle size to smaller values. On the other hand, a light scattering instrument will average the various dimensions as the particles flow randomly through the light beam, producing a distribution of sizes from the smallest to the largest dimensions.

A schematic representation of a sphere versus an example of a true particle shape and the "shape factor" is presented in Figure 11.

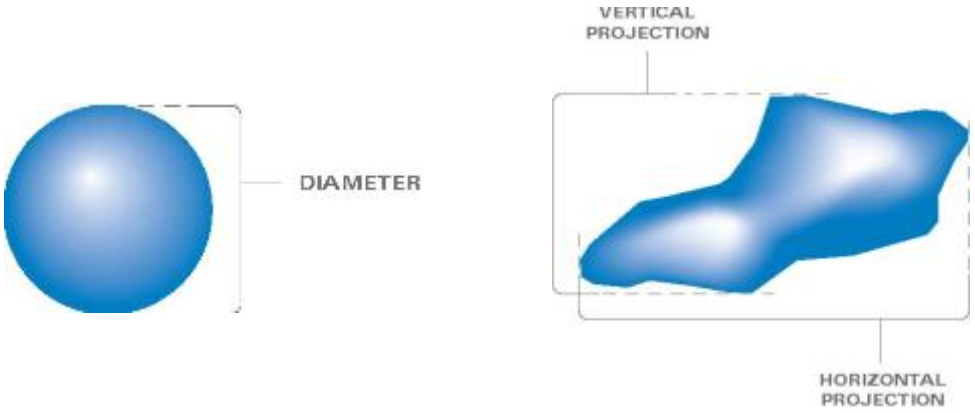

Figure 11. SHAPE FACTOR Many techniques make the general assumption that every particle is a sphere and report the value of some equivalent diameter. However, microscopy or automated image analysis are the only techniques that can describe particles with multiple values related to the shape of particles with larger aspect ratios.[52]

Microscopy or automated image analysis are the only techniques that are able to describe particle size using multiple values. For example the non-spherical particle shown in Figure 11 could be described using an image analysis system to provide: the longest and shortest diameters, perimeter, projected area, or again by equivalent spherical diameter. In such analysis, it is common to report a particle size distribution in terms of the equivalent spherical diameter on the x-axis and percent on the y-axis. In general, the x-axis value is typically displayed as length rather than equivalent spherical diameter only for elongated or fibrous particle materials.

Various expressions for particle diameter have been put forth by Allen,[53] Svarovsky,[54] and other authors such as the equivalent sphere diameters, equivalent circle diameters, and statistical diameters. An important issue put forth by Allen is that determination of a particle size should be conducted by a technique such that the obtained results represent a property of the powder that is critical for the powder application. For example, powders used in chemical reactions should be characterized by their surface area.

Equivalent Sphere-based Particle Diameters

The equivalent sphere description refers to the diameters of regular, homogeneous spheres that would have the same property as the particle being measured. The term d_v (or x_v) refers to volume diameter and is defined as the diameter of a regular, homogeneous sphere that has the same volume as the particle being measured. Equivalent spherical diameters represent three-dimensional properties of the real particle, and thus are most reliable when used for practical applications that are influenced by volume-based properties (density, surface area, etc.)

Drag diameter (d_d): Diameter of a sphere that has the same resistance to motion in the same fluid (having same viscosity), moving at the same velocity as the particle
Free-falling diameter (d_f): Diameter of a sphere having the same density and the same free-falling speed as the particle in the same fluid
Surface diameter (d_s): Diameter of a sphere having the same surface area as the particle
Surface volume diameter (d_{sv}): Diameter of a sphere having the same surface to volume ratio as the particle
Stokes' diameter (d_{st}): Diameter of a free falling sphere (i.e., particle having attained the Stokes velocity) in the laminar flow region
Sieve diameter (d_A): Diameter of a sphere equivalent to the size of the minimum square aperture through which the particle will pass
Volume diameter (d_v): Diameter of a sphere having the same volume as the particle

Table 3. Definitions of Volume-Based Diameters.[55]

Equivalent Circle-based Particle Diameters

When the method of measuring particle size is based on the projected profile of a particle, evaluation of the particle's diameter is based on equivalent two-dimensional circles (see Table 4). For this reason, equivalent circles analysis is used mostly for optical or electron microscopy-based techniques. While these expressions are very useful for observing and reporting the sizes of spherical particles, the results of irregular particles can be erroneous if adequate precautions are not taken. The orientation of an irregular particle at rest can significantly influence the calculated diameter, and the more irregular a particle, the greater the possibility of surface details being obscured. An obvious solution is to sample a large number of random particles in order to minimize variations. However, the number of particles that need to be sampled depends on the sample and can vary from as few as a few hundred to many thousands of particles. The development of software for image analysis has aided in speeding up and automating the process of size analysis. At the same time, it is important that the strengths and limitations of any image analysis software are well understood. Clearly, an initial test is to conduct measurement and analysis using certified size standards.

Projected area diameter (d_a): Diameter of a circle having the same area as the projected area of the particle at rest in a stable position
Projected area diameter (d_P): Diameter of a circle having the same area as the projected area of the particle at rest in a random orientation
Perimeter diameter (d_C): Diameter of a circle having the same perimeter as the projected area of the particle, irrespective of the particle orientation

Table 4. Size Definitions Based on Equivalent Circle Diameter.[55]

A serious limitation of the spherical and circular definition is the inability to describe the shape of the particle. Materials may contain particles with large aspect ratios. Projected image methods may not be able to discern the true size of particles depending on orientation, and the shape of the particles may be of significant importance in the performance of the material (such as anisotropic thermal conductivity).

Equivalent Statistical-based Particle Diameters

Statistical diameters are probably the most useful to define the shape of a particle and the most useful for particles with a large aspect ratio. This analysis involves the calculation of a linear dimension measured with respect to a defined direction. The use of these expressions is common while using microscopy-based measurement techniques. Advanced software that automates image analysis greatly improves the reliability and ease of such investigations. Examples of common statistical-based particle diameters are presented in Table 5.

Feret's diameter (d_F): Mean value of the distance between pairs of parallel tangents to the projected outline of the particle
Martin's diameter (d_M): The mean chord length of the projected outline of the particle
Unrolled diameter (d_R): The mean chord length through the center of gravity of the particle
Maximum chord diameter (d_{CH}): The maximum length of a line limited by the particle contour
Shear diameter (d_{SH}): Particle width obtained with an image-shearing device

Table 5. Size Definitions Based on Statistical Diameters.[55]

Particle Size Analysis

While it may seem convenient to describe a sample by its "average" particle diameter, a single number does not describe the distribution of particle sizes in a sample and may be very misleading with respect to the properties of the material. The best practice is to report both a central point of the distribution along with one or more values to describe the width of distribution.

Particle sizes can be expressed in terms of mean, median and modal diameters, which are determined from the diameter distribution of the measured sample (using one of the definitions of diameter described above).

Mean Diameter: The arithmetic Mean Diameter is the sum of the diameters of all the individual particles in the distribution divided by the total number of particles in the distribution. The geometric mean is the n^{th} root of the products of the diameters of n particles in the system. The mean diameter of a powder can be its length, surface, volume, or moment mean diameter.

The ASTM E799[56] generalized form of the equations for different Mean Diameter values is:

Equation 14

$$\overline{D}_{pq}^{(p-q)} = \frac{\sum D_i^p}{\sum D_i^q}$$

Where:

D = the diameter

$\overline{D}$ = the average diameter

$(p-q)$ $p > q$ = the algebraic power of D_{pq}

D_i = the diameter of the i^{th} particle

$\sum$ = the summation of D_{ip} or D_{iq}, representing all particles in the sample

Some of the more common representative diameters are:

D_{10} = arithmetic or number mean

D_{32} = volume/surface mean (also called the Sauter mean)

D_{43} = the mean diameter over volume (also called the DeBroukere mean)

Median Diameter: The Median Diameter is the size at which half of all the particles in the distribution are coarser than the Median Diameter, and the other half are finer.

Modal Diameter: The Modal Diameter is the most frequently occurring size value of the particles measured and is, thus, the peak of the frequency distribution. It appears as the diameter of the highest peak in the distribution.

For symmetric distributions such as the one shown in Figure 12 all three representative diameters are equivalent: mean = median = mode.

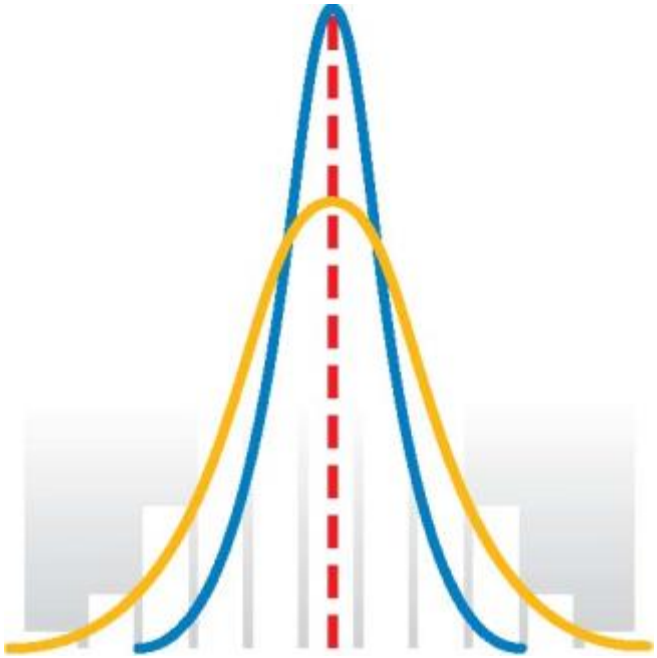

Figure 12. Symmetric Distribution where Mean = Median = Mode.[52]

For a non-symmetric distribution the mean, median and mode will be three different values as shown below in Figure 13.

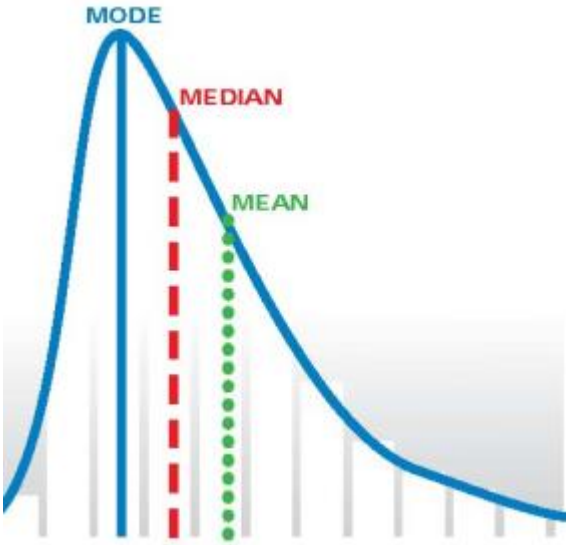

Figure 13. A non-symmetric distribution. Mean, median, and modal diameters will be three different values.[52]

It is important to note that the mean value can be the same for significantly different shapes of distribution and size range over which the distribution is spread. At a minimum, the use of more than one definition (e.g., stating both the mean and modal diameters) may provide some information about the non-symmetrical nature of the distribution. For example, Figure 14 shows a measurement of the differential volume as a function of the particle size and indicates the occurrence of the different size measures (mode, mean and median diameters) for the same distribution.

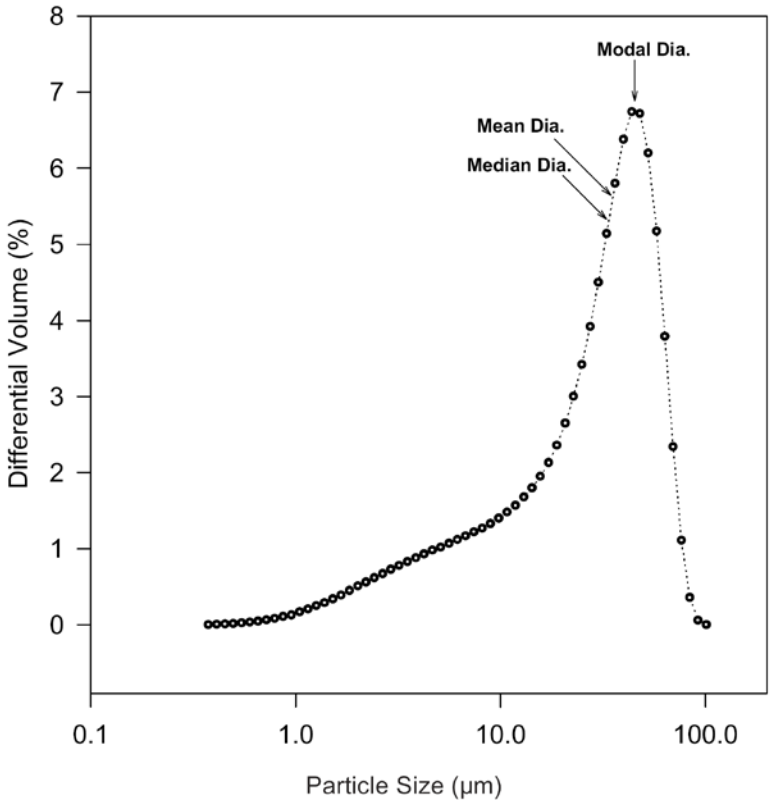

Figure 14. An example of the particle size distribution of a powder obtained by laser light scattering.[55]

In addition to a central diameter value (whether it be mean, media, or modal) other terms are needed to describe the width of the distribution of particle sizes. The most commonly used statistical values in the field of particle analysis are standard deviation and variance. An example of standard deviation is shown in Figure 15 where 68.27% of the total population lies within +/- 1 standard deviation, and 95.45% lies within +/- 2 standard deviation of the mean.

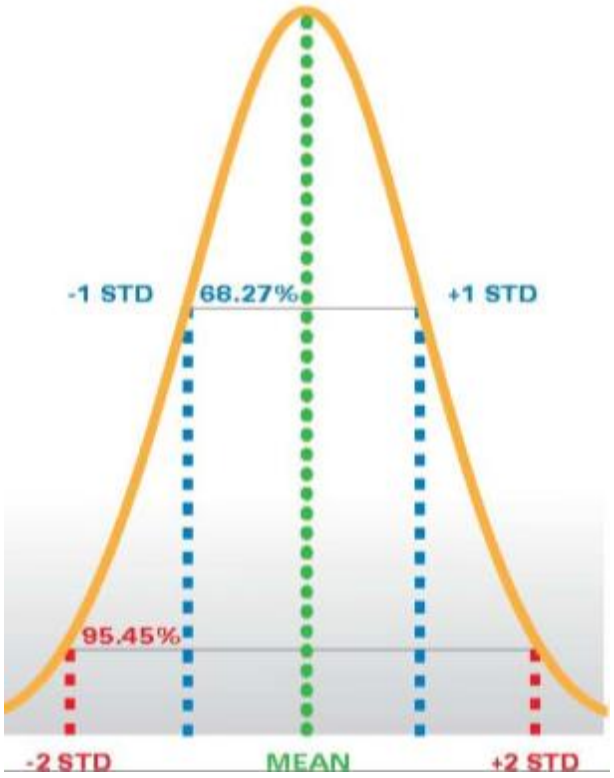

Figure 15. Example of a normal distribution where the mean value is flanked by 1 and 2 standard deviation points.[52]

Although still occasionally cited, the use of standard deviation has declined since the hardware and software advanced beyond assuming normal or Rosin-Rammler distributions. Once "model independent" algorithms were introduced, many particle scientists began using different calculations to describe distribution width. A common value used for laser diffraction results is the span, in which the volume diameters over the range of 10-90% of the particles are divided by the Median Diameter (Equation 15 and Figure 16).

Equation 15 $$\text{Span} = (D_{V0.9} - D_{V0.1}) / D_{V0.5}$$

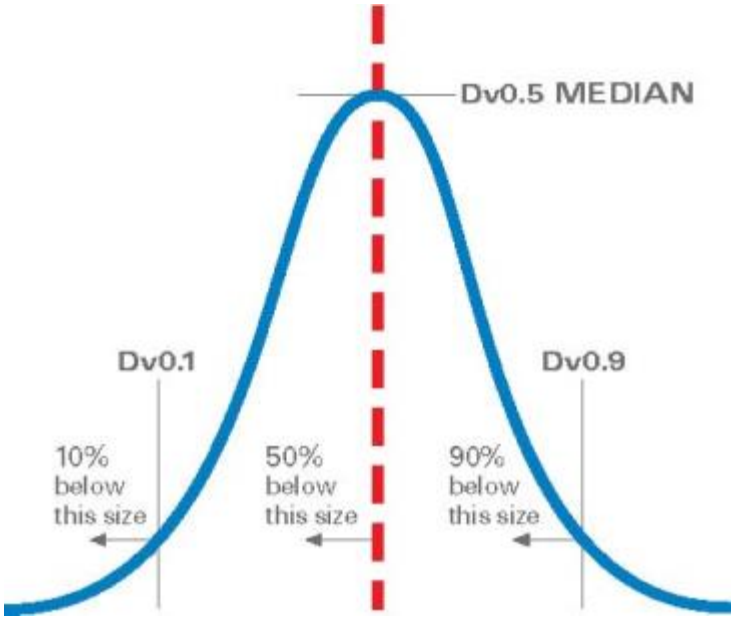

Figure 16. THREE X-AXIS VALUES D10, D50 and D90.[52]

One term to describe the distribution width is to normalize the standard deviation by dividing by the mean. This is known as the Coefficient of Variation (COV) or the relative standard deviation (RSD). The ISO13320 standard for laser diffraction particle size analysis measurements encourages the measurement of any sample at least 3 times, calculating the mean, standard deviation, and COV (standard deviation/mean), and the standard sets pass/fail criteria based on the COV values.[57]

Particle Size Analysis: Number vs. Volume distributions

There are a number of ways to evaluate the particle size distribution of a material. The choice may depend on the physical properties of interest. For example, is it the number of particles, surface area, or mass of the particles that is of most interest (e.g. catalysis vs. bulk H_2 storage)? In a number distribution, each particle is counted by some analytical technique and assigned a size (diameter), which has equal weighting. As an example, consider the nine particles shown in Figure 17. Three particles are 1 µm, three are 2 µm, and three are 3 µm in size (diameter).

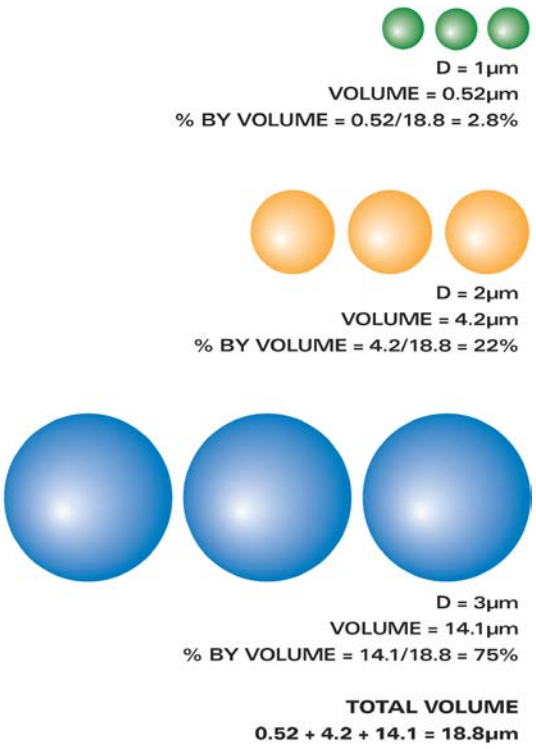

Figure 17. Illustration of particles 1, 2 and 3 µm in size. Calculations show percent by volume for each size range.[52]

The distribution results for these particles are shown in Figure 18. On a number basis (a), each particle size accounts for one third of the total. On a volume basis (b), the results demonstrate that 75% of the total volume comes from the 3 µm particles, and less than 3% comes from the 1 µm particles.

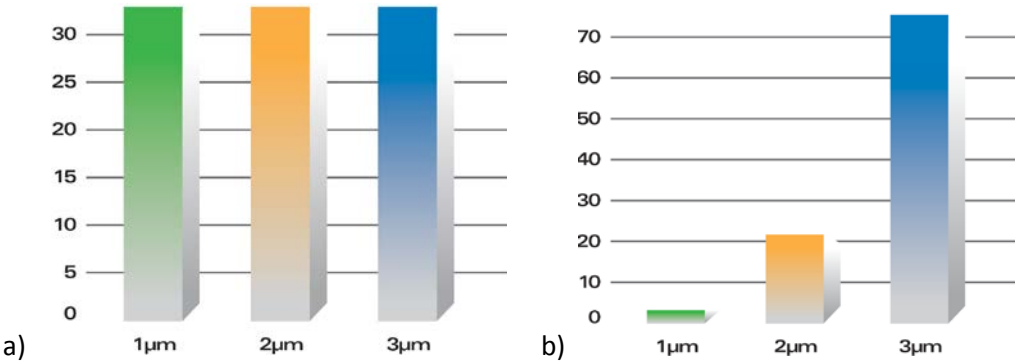

Figure 18. Percentage composition of sample a) on a number basis and b) on a volume basis.[52]

When presented as a volume basis it becomes clear that the majority of the total particle mass or volume comes from the 3 µm particles. Nothing changes between the left and right graph except for the basis of the distribution calculation.

The type of particle size distribution measured varies depending on the experimental technique being employed. Microscopes or image analyzers collect results as a number distribution. Laser diffraction methods collect results as a volume distribution. It is often possible using data analysis software to convert the results from a number basis to a volume basis or vice versa. Care should be taken when converting results from one basis to another. Transform image analysis results from a number to volume basis is common. However, converting a volume result from laser diffraction to a number basis can lead to errors and is only suggested when comparing to results generated by microscopy. Figure 19 below shows an example in which a laser diffraction result is transformed from a volume to both a number and a surface area-based distribution. Notice the large change in median from 11.58 µm to 0.30 µm when converted from volume to number. The error associated with these conversions may have an impact on how the results are interpreted for hydrogen storage materials. For example, ideal physisorption materials will have a large surface area to volume ratio (surface area providing adsorption sites and volume creating unwanted weight). As seen in Figure 18 and Figure 19 the majority of the volume (hence mass) of a powder may be in a few large particles, whereas the majority of the surface area is attributed to the large number of smaller particles. Thus, for high gravimetric physisorption capacities, a narrow distribution of particles with high surface areas would be desirable. However, the conversion from volume distribution to surface area distribution is highly dependent on the shape of the particles. In this case, one would want to have reliable data for a materials surface area distribution.

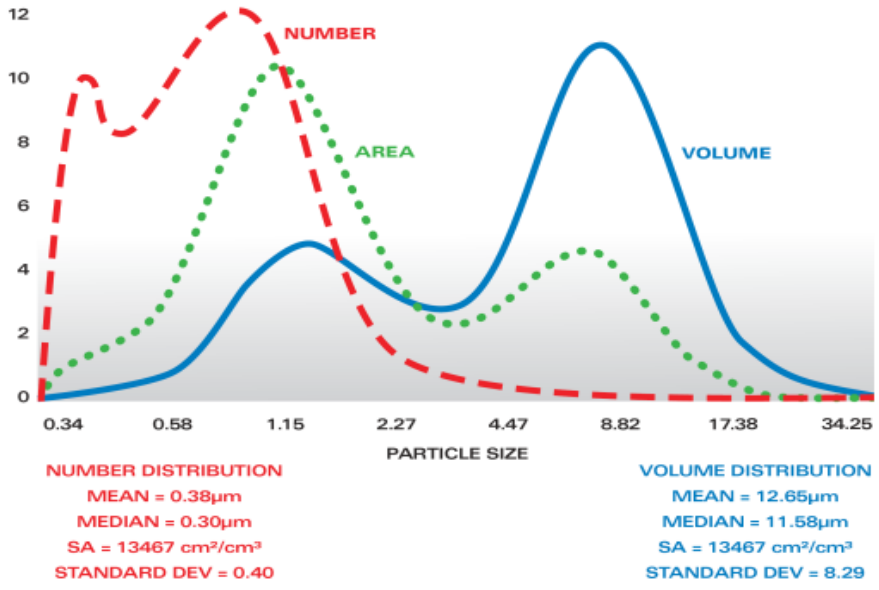

Figure 19. Volume distributions converted to area and number distributions.[52]

1.7 Porosity of Powders and Compacts

It is useful to have a good knowledge of the range of pore sizes in a porous solid. The pore sizes in a porous solid must be of a suitable size to admit, hold, and discharge individual gas molecules. If the pores are too small, the gas molecules cannot enter. If they are too large, most of the molecules of gas in the pore behave as a gas under pressure with rapid movement and molecular collisions. They are not packed as tightly and are bound to the surface in the adsorbent structure.[58,59]

The individual pores may vary greatly both in size and in shape within a given solid and between materials. The conventional classification for pore size has been defined by the International Union of Pure and Applied Chemistry (IUPAC) and is summarized below. The classification is arbitrary and was developed on the basis of the adsorption of nitrogen at 77 K on a wide range of porous solids.[60] The basis of the classification is that each of the size ranges corresponds to characteristic adsorption effects.

CLASSIFICATION OF PORES ACCORDING TO THEIR WIDTH[59]

PORE TYPE	WIDTH
Micropores	Less than ~ 20 Å (~2 nm)
Mesopores	Between ~ 20 (~2 nm) and ~ 500 Å (~50 nm)
Macropores	More than ~ 500 Å (~50 nm)

Porous materials may contain pores made up of highly regular structures or consists of cracks, crevices, and tortuous passageways. For all of these materials three distinctly different types of density measurements are possible, one that includes and one that excludes these pores. And a third definition that defines sample volume in terms of the volume of a container into which a known quantity of material (powder or pieces) can be filled or packed. This last density includes not only the pore spaces within the material but also the spaces among the particles or pieces. The following is a summary of these three different density definitions:

1. Absolute or True density, excludes both the intraparticle spaces and the interparticle spaces (closed pores).
2. Skeletal of Apparent density: includes the intraparticle but excludes interparticle spaces (closed pores).
3. Bulk density or Packing density: includes both intra- and interparticle spaces.

These terms are defined in detail in section 1.1

For reporting hydrogen storage capacity measurements, it is important to make clear the distinction between the *true density* and *skeletal density*, which may be different for highly microporous materials. The skeletal or apparent density includes both the volume occupied by the solid material of the adsorbent and the closed (or inaccessible) pore volume:

Equation 16

$$\rho_{SK} = \frac{m}{V_{SK}} = \frac{m}{V_T + V_{pore}}$$

where m is the mass of the adsorbent V_{SK} is the skeletal volume and V_{pore} is the pore volume. The skeletal or apparent density can be determined from the slope of the helium buoyancy correction.[61] For a pure crystalline sample with no closed pores, the skeletal density is the same as the crystallographic density.

These three different definitions of density use quite different equipment to be measured. Helium can fill all open spaces including that of the pores of sizes as small as 0.3 nm. Therefore, the resulting density from using helium is the skeletal or apparent density, which is being ever more frequently referred to simply as the "helium density".

Note however, that the assumptions listed above, ***in particular that helium does not adsorb to the material during helium density measurements***, are not always valid for many high-surface area materials.[62] While it is typical to use helium measurements on hydrogen storage materials samples to determine an "apparent volume" there may be some concern that the sample itself will adsorb significant amounts of the inert gas causing large errors in the "apparent" void volume of the sample cell. This becomes an important concern for high-surface area materials being measured at low (cryogenic) temperatures where inert gas uptake may be large. In such cases, the void volume of the sample cell, with the sample in it, is usually determined from helium expansion measurements at room temperature and low pressures. Under these conditions the effect of helium adsorption is generally considered to be small enough to have little impact on the volume calibration. However, this may not necessarily be the case.[63,64]

The relationship between materials and system volumes can be expressed as follows (and were shown schematically in Figure 2):

Equation 17

$$\textbf{Free Volume: } V_f \approx V_{He}$$

Equation 18

$$V_f = V_{empty\ vessel} - V_{pk} + V_{void} + V_{pore}$$

Equation 19

$$V_f = V_{empty\ vessel} - V_{skeletal}$$

Because knowledge of the skeletal density of the material is crucial to the accuracy of both gravimetric and volumetric measurements, great care should be taken in the determination of the skeletal density of samples being measured.

1.8 Particle Shape and Modeling

Hydrogen-induced fracture can result in faceted particles having irregular shape (e.g. Figure 20) in contrast to faceted particles produced from growth of single crystals. This behavior has been observed for a wide variety of intermetallic metal hydrides for which particle size distributions have been measured (e.g., in Reference 37). Only recently has efforts to predict the size distribution and shapes of irregular hydride particles theoretically been pursued. Smith and Fisher have developed a multiphysics modeling approach for heat conduction in metal hydride powders. The simulations include particle shape distribution, size distribution, granular packing structure, and effective thermal conductivity which is reported to produce quantitative experimental agreement with metal hydride powders of various compositions.[65,66,67,68] More specifically, the simulations cover modeling of particle shape and size distribution, quasi-static packing through the energy-based simulation of granular jamming, and heat transfer through direct solution of the heat diffusion equation. In addition, a structure-transport theory inspired by recent experiments on fine powder was developed to relate non-cohesive jammed system properties to experimental packings with solid density below that of the non-cohesive jammed system. The following is an overview of the modeling, correlation with experimental measurements, and conclusions of that work.

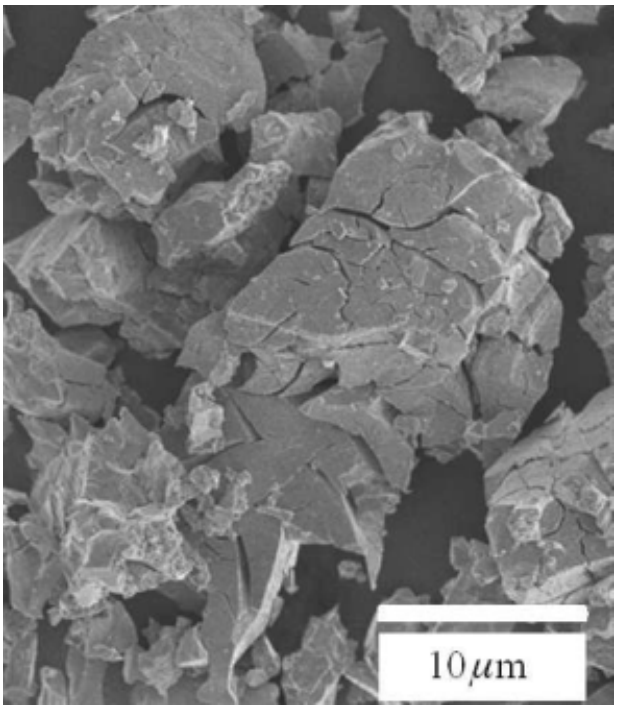

Figure 20. $Ti_{1.1}CrMn$ particles with crack fissures produced from cyclic hydriding and dehydriding. The particles produced after further cycling have irregular faceted shapes.[65]

In this cited work, Smith et al. reported that particle shape and size distributions resulting from fracture cannot be replicated by a simple single-particle unit cell model, such as those of Asakuma and co-workers[69,70] and Zehner, Bauer, and Schliinder.[71] Reduced conduction through the gas phase as a result of boundary scattering and interfacial impedance mismatches of thermal energy carriers depend on the confining pore geometry of the packed powder. The gas-phase boundary scattering mechanism has often been interpreted as the Smoluchkowski effect in the packed bed literature.[71] Metal hydride particles inherently exhibit small contact areas in the packed state resulting in reduced solid-state heat transfer. Thermal conduction in the solid phase may also depend strongly on whether all or some of the particle is in the hydrided or desorbed state. Currently, the extent to which each of these mechanisms limits heat transfer in metal hydride powders, and other types of porous media in general, is not well understood or quantified.

Smith et al. used an idealized statistical geometric model to simulate the particle size and shape distribution of decrepitated metal hydride powders.[65] The major underlying assumptions of their model were the following: (1) infinitely extending planar surfaces are formed from instances of fracture and (2) planes of fracture have isotropic statistical orientation and position throughout the material. Both assumptions are well justified for polycrystalline metals, such as $Ti_{1.1}CrMn$. This model is described as a 3D Poisson plane field, which is closely related to the 2D Poisson

line field that has been studied previously.[72] Simulation of this geometric field of planes is accomplished through sequential sectioning of a unit cube centered at the origin with randomly oriented and positioned planes. Their model was implemented numerically, and can be interactively accessed through nanohub.org.[73] The resulting ensemble of particles formed by the intersection of 200 planes in the Poisson field is presented in Figure 21. Qualitatively, the field reflects many of the features of decrepitated metal hydride particles, including faceted particle shapes and a volume of individual particles spanning nearly six orders of magnitude.

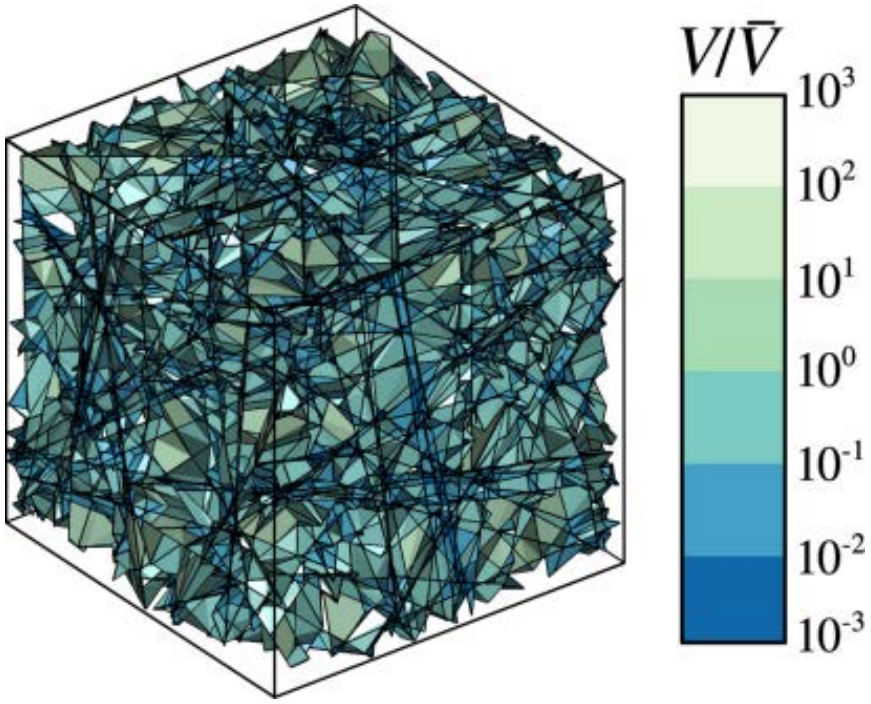

Figure 21. Particles generated by intersections of planes in the 3D Poisson field. Particles are colored according to their volume *V* relative to the volume-weighted average particle volume *V* for the ensemble. Particles intersecting the domain boundary (black edges) are excluded to neglect edge effects.[65]

To validate the model, Smith et al. had particle size distribution measurements performed on the high-pressure metal hydride alloy, $Ti_{1.1}CrMn$, using laser diffraction.[74] The author's cumulative size distribution of aqueous sonicated $Ti_{1.1}CrMn$ in addition to those of several other metal hydrides from the literature is displayed in Figure 22.

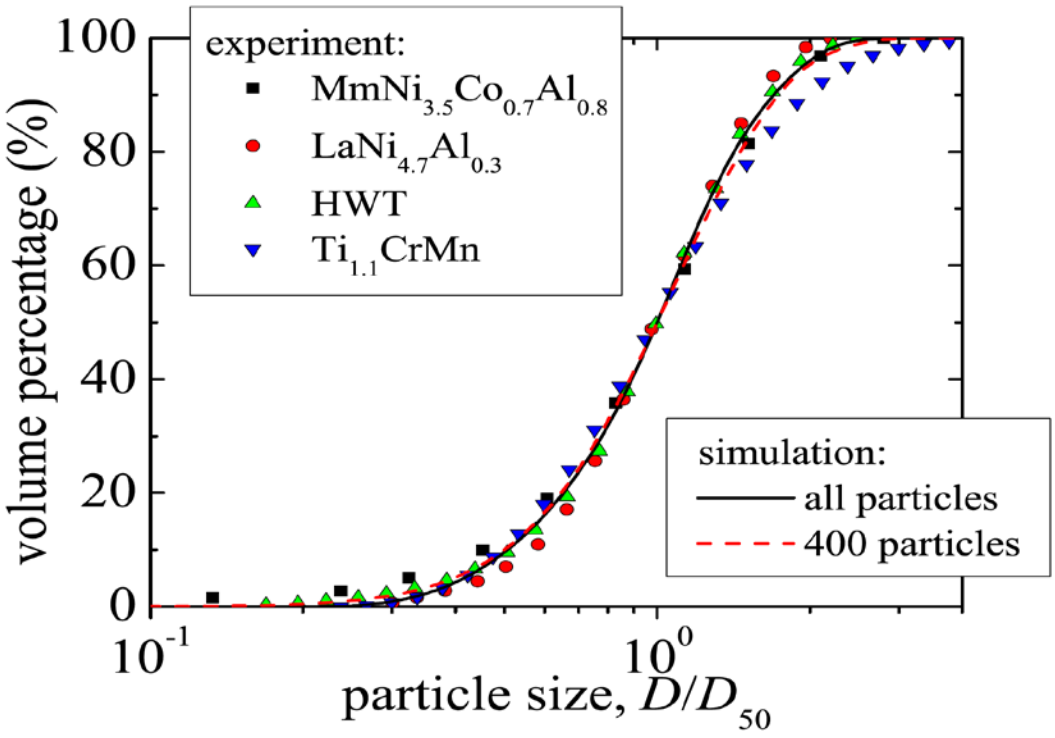

Figure 22. Modeled and experimental cumulative size distributions for cycled metal hydride powders.[75] Volume effective sphere diameter D is plotted for theoretical size distributions. D is normalized by its median value D_{50}. Kernel density estimates of the simulated distributions are shown.[65]

The different metal hydrides showed similar particle size distribution despite being different AB_2 and AB_5 alloys. The largest difference was for the largest particles, and was suggested to be due to the presence of agglomerates and differing degrees of cycling. It was noted however, that there was not a strong correlation between how many cycles each sample underwent and the mean particle size, which is consistent with the degree of decrepitation being highly dependent on the alloy composition and mechanical properties. The Poisson plane field modeling effort found that the computed particle size distribution was in the middle of the spread of experimental size distributions, indicating a good match between modeling and experimental results.[65]

1.9 Packing Theory and Simulation

To improve the volumetric capacity of hydrogen storage powder materials, it will be necessary to increase powder packing densities of these materials at a materials and system level. The optimal packing density (best capacity and kinetic hydrogen storage performance) will be very different from one material to another. This optimized powder packing depends not only on the

materials static properties (particle size, size distributions, shape, porosity, and mechanical characteristics), but also on the behavior of the materials with repetitive hydrogen uptake and release cycles (such as lattice expansion, decrepitation, segregation, etc. for reversible materials). Packing theory, simulation and testing may play an important role in the development of real-world systems using powder-based hydrogen storage materials. The following is a brief introduction to packing theory and simulations relevant to hydrogen storage.

The efficiency of packing a powder can be presented by the powder's particle or solid **Volume Fraction**. This is the powder's apparent particle volume divided by the bulk volume. Packing fraction is the volume taken by a number of particles in a given space of volume after some form of packing. It represents the percentage of volume in a packed powder taken up by the powder's solid matter and inaccessible pores. Together with the mass, the packing fraction defines the packing density.

Random close packing (RCP) is an empirical parameter used to describe the maximum volume fraction of powder particles obtained when they are packed randomly. Because of the difference in shapes and sizes of powder particles, RCP does not have a precise geometric definition but rather is defined statistically and measured empirically. The measurement of RCP consists of filling a container randomly with the test powder, and then shaking or tapping the container until the powder will not compact any further. The volume fraction at this point is the RCP. It has been shown that the volume fraction increases with the number of taps until the RCP is reached, and that the volume fraction increases as the tapping amplitude decreases. Thus RCP is the packing fraction given by the combination of the limit as the tapping amplitude goes to zero, and the limit as the number of taps goes to infinity.

The particle volume fraction at RCP depends on the shape of the particles being packed. If the powder consists of particles of different sizes, then the volume fraction depends non-trivially on the size-distribution and can be arbitrarily close to 1.0. For powders composted of particles of essentially one size the value for RCP depends on the particle shape. For spheres this number has been measured to be 0.64 or 64%.[76] Analytical predictions have shown that the volume fraction in RCP cannot exceed a density limit of 63.4% for spheres of one diameter.[77] This is significantly smaller than the maximum theoretical filling fraction of 0.74048 that results from hexagonal close packing. This difference demonstrates that the "randomness" of RCP is vital not only to the definition, but also to the actual nature of packed powders.

Based on the cumulative particle size distribution in the previous section (Figure 22), Smith and Fisher studied athermal (i.e., low particle kinetic energy) jamming of frictionless metal hydride-like particles.[65] The structure of systems of tetrahedra prepared by such methods have shown agreement with experimental results. [66,78]

The mechanics model used by Smith and Fisher permitted computation of energy, forces, and moments for contact between two arbitrarily shaped dissimilar particles. The generality of the model is especially important for metal hydrides because of the random shape of particles in the

Poisson plane field. To simulate jamming, these metal hydride particles were arranged in a dilute setting with random particle position and orientation in a periodic cubic supercell. Detailed expressions for forces and moments and the numerical methods employed for structural optimization are described in Reference 66.

The jammed microstructure obtained through their simulation is depicted in Figure 23. The simulations revealed that small particles are well distributed and contact other small particles. Conversely, large particles may be isolated from other large particles and at most will only contact two other large particles.

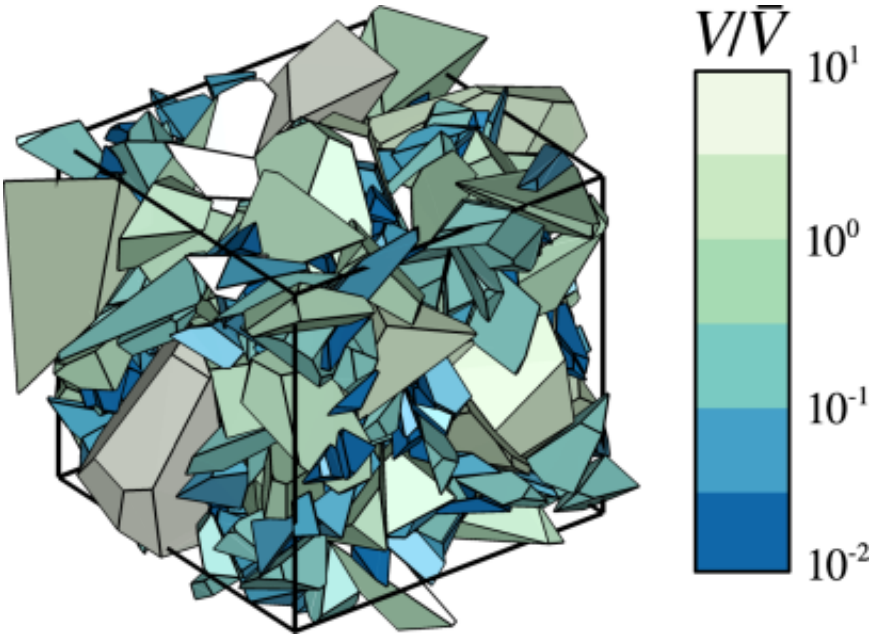

Figure 23. Jammed packing of 400 particles randomly sampled from the Poisson plane field at a density of (φ) = 0.633. Particle color indicates volume *V* relative to the volume-weighted average particle volume *V*. The cube-shaped periodic supercell is indicated by black edges.[65]

1.10 Compaction of Hydride Storage Materials

Complex metal hydrides like the Ti-doped sodium alanate SAH (Sodium Aluminum Hydride) and mixtures of LAMH (Lithium Hydride and Magnesium Amide) offer a high gravimetric hydrogen storage capacity (e.g. SAH: 3.2 wt. % H2; 1:1 LAMH: 8.2 wt. %) but have relatively low "crystal" or "X-ray" densities, which affects their volumetric capacity.

In a recent analysis of automotive hydrogen storage requirements at a materials level, Pasini et al. mapped out "crystal" densities and the associated "crystal" volumetric hydrogen storage capacities of many hydrides as a function of the materials gravimetric capacity (Figure 24).[79]

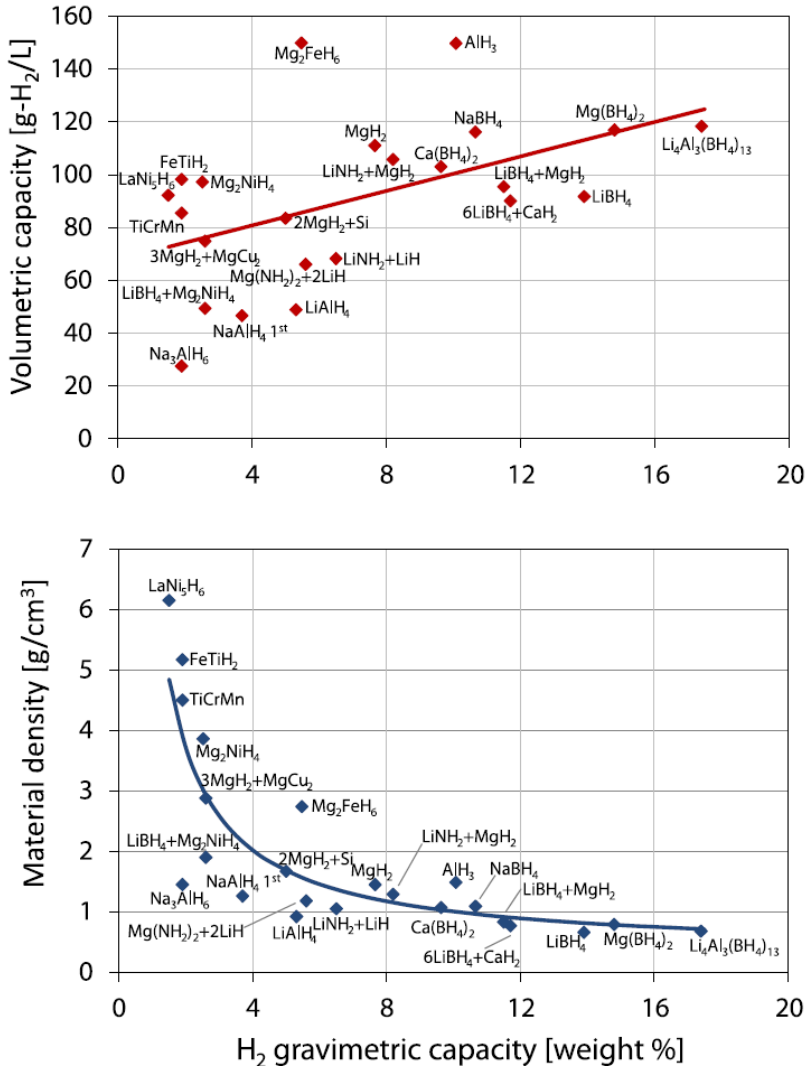

Figure 24. Volumetric capacity (top) and density (bottom) as a function of the pure material gravimetric capacity. The solid bottom curve corresponds to the linear fit of the top graph.[79]

The material's "crystal" density is only the first of three different volumes that control the volumetric storage capacity of a materials-based hydrogen storage system. The second is the "packing" density (or void space in the bulk material), and the third is the system volume which includes empty space in the storage tank and the volume of the tank and all ancillary components of the storage system. While the "crystal" density is a function of the material, the

"packing" density and system volume are properties that have the potential to be improved through materials engineering design and system engineering design.

Improving volumetric capacity through materials engineering has focused in large part on increasing "packing" densities through powder compaction. Examples of improvements in the packing density of hydrogen storage materials have generally focused on uniaxial compression of confined powder samples (typically in cylindrical tube presses). However, there are many different methods for densification and measuring the packing density of powders, and often several different control parameters in each process that will ultimately affect the compacted product. Some different methods of powder compaction include:

1. Pressing: powder is compressed in a die which may be composed a wide variety of components, motions and forces.

2. Tapped Densification: is obtained by mechanically tapping a graduated measuring cylinder or vessel containing a powder sample. After observing the initial powder volume or mass, the measuring cylinder or vessel is mechanically tapped, and volume or mass readings are taken until little further volume or mass change is observed. The mechanical tapping is achieved by raising the cylinder or vessel and allowing it to drop, under its own mass, a specified distance. Devices that rotate the cylinder or vessel during tapping may be preferred to minimize any possible separation of the mass during tapping down.

3. Vibrational Densification: is the densification of bulk solids by vibration, known as vibratory compaction. This involves supplying energy to a bed of particles at a selected frequency and amplitude for a period of time.

4. Centrifugal Casting: powder is spun in a mold and packed by centrifugal force. A uniform density is obtained as a result of centrifugal force acting on each particle of the powder.

5. Powder Deaerator: material is aspirated and held on a filter drum by vacuum. It is simultaneously pressed between the filter and pressure drums. The combination of vacuum and pressure causes a deaerating and densification of the powders. At the end of the densification process, the product is stripped off the filter drum by a kniff edge.

6. Slip Casting: a slurry consisting of the powder and a liquid is poured in to porous mold. The free liquid in the slurry is absorbed by the mold causing a solid layer of powder material on the surface of mold. The mold may be vibrated to increase the density of powder. The components are dried and possibly sintered to provide strength.

7. Extruding: both hot and cold extrusion processes are used for compacting powders. In cold extrusion the powder is mixed with binder and the mixture is often compressed into billet before being extruded. The binder may be removed from the material, in

particular, before or during possible sintering. In hot extrusion the powder is compacted into billet and is then heated to the extruding temperature (typically in non-oxidizing atmosphere) and pressed through an extrusion die.

8. Rolling: the powder is fed in between two rollers, which compress and interlock the powder particles to form a sheet of sufficient strength. It may then be sintered, or re-rolled and heat treated.

9. Iso-static Molding: is used to obtain materials with uniform density and strength in all directions. In this method, the powder is placed in an elastic (deformable) mold which is compressed with gas at high pressure.

Each of these methods will produce different results depending not only on the control parameters of the process (such as vibration frequency, amplitude, duration, applied pressure, temperature, etc.) but also on many properties of the powder materials themselves (such as resilience, friction, particle shape and size, material density, additives, original handling of the samples, etc.).

For this reason, it is very important that published or presented results describe in detail not only the method of compaction employed, but the known properties of the material (such as particle size distribution) and all of the parameters of the compaction process.

The following are two examples of studies on the ability to improve performance in hydrogen storage materials through powder compaction.

Example 1:

One example of mechanical and performance properties testing on compacted hydrogen storage materials is the work on complex hydrides and amides done by United Technologies Research Center under contract to the DOE.[80] A selection of their results is presented below.

The LAMH material was much more difficult to compact than sodium alanates and required the addition of expanded natural graphite (ENG) binder in order to obtain samples with a sufficient strength.[80] Kinetic measurements from Ti-doped sodium alanates powder and pellets were analyzed in order to obtain values of the model parameters in the kinetic expressions that are used in the detailed COMSOL Multiphysics™ model.[81,82] This model was developed to gain a better understanding about the impact on H_2 absorption rates of thermal gradients that occur during refueling. From the modeling, small diameter aluminum tubing with aluminum fins was projected to provide sufficient heat transfer in order to reach 90% of the materials H_2 storage gravimetric capacity in about 10.5 minutes. Figure 25 clearly shows the benefit of compaction on the volumetric capacity of the sodium alanates bed.

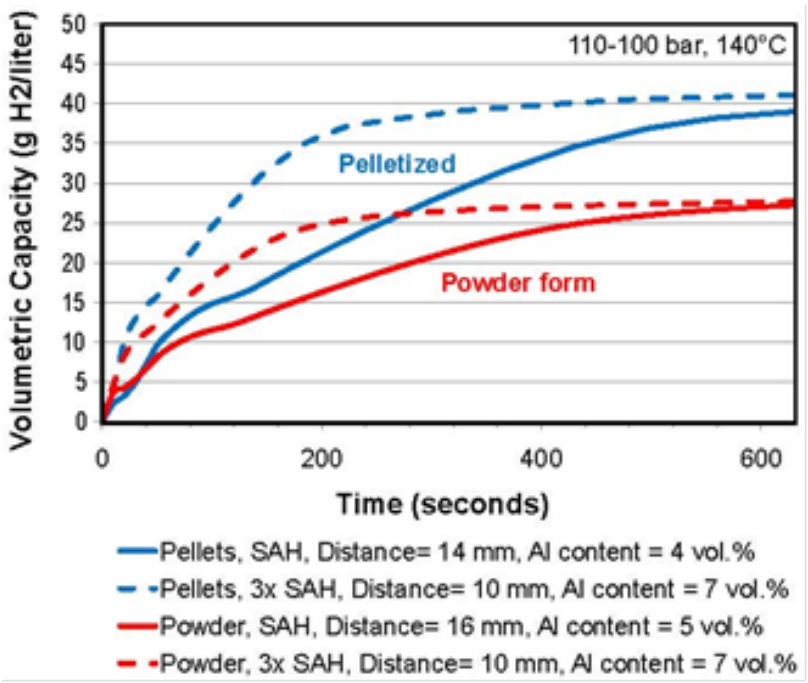

Figure 25. Volumetric capacity of the sodium alanates bed including the aluminum fin and tube heat exchanger, optimized for a 10.5 minute refueling time with sodium alanates in powder or compacted form.[80]

In addition to compaction studies, UTRC investigated the benefit of adding aluminum powder or ENG to improve the heat transfer properties of these materials. The results showed that the effective thermal conductivity of the sodium alanate/aluminum mixtures follows the series model for thermal conductivity. This makes aluminum powder fairly ineffective in improving the thermal conductivity of sodium alanates as a large aluminum volume fraction would be required.[83] It was found that it is better to use aluminum fins in a fin and tube heat exchanger. With this configuration an effective thermal conductivity of 4 W $m^{-1} K^{-1}$ can be achieved with only 4 volume percent of aluminum and using compacted sodium alanates pellets.

The results of testing expanded natural graphite demonstrated that the effective thermal conductivity of sodium alanates mixed with ENG followed a parallel model for thermal conductivity.[83] This produced high values of the thermal conductivity at a relatively low volume fraction of ENG. Best results were obtained when using ENG “worms”. This additive introduces anisotropic thermal conductivity upon uniaxial compaction. The highest value of the thermal conductivity was determined to be perpendicular to the pressing direction and in the direction of the heat exchanger tube. A COMSOL model was developed and used to extract information about the thermal conductivity anisotropy from the thermal conductivity measurements. Ultimately, through the combined experimental measurements and modeling, it was determined that heat exchanger tubes no longer require fins when using compacted sodium alanates pellets with about 5 wt. % ENG “worms” to improve the thermal conductivity.

Thermal conductivity measurements showed that LAMH required a larger weight fraction of ENG "worms" (e.g. 15 wt. %) than sodium alanates (e.g. 5 wt. %) in order to obtain high thermal conductivity values in the direction of the heat exchanger tube that would allow a rapid refueling process when it would be possible to substantially improve the slow H_2 absorption kinetics and reversibility of the current LAMH material.

Ultimately, the experimental and modeling information was employed in a collaborative effort to predict hydrogen storage capacities at a system level.[80] The results of the gravimetric and volumetric capacity of these two hydride hydrogen storage systems are shown in Figure 26.

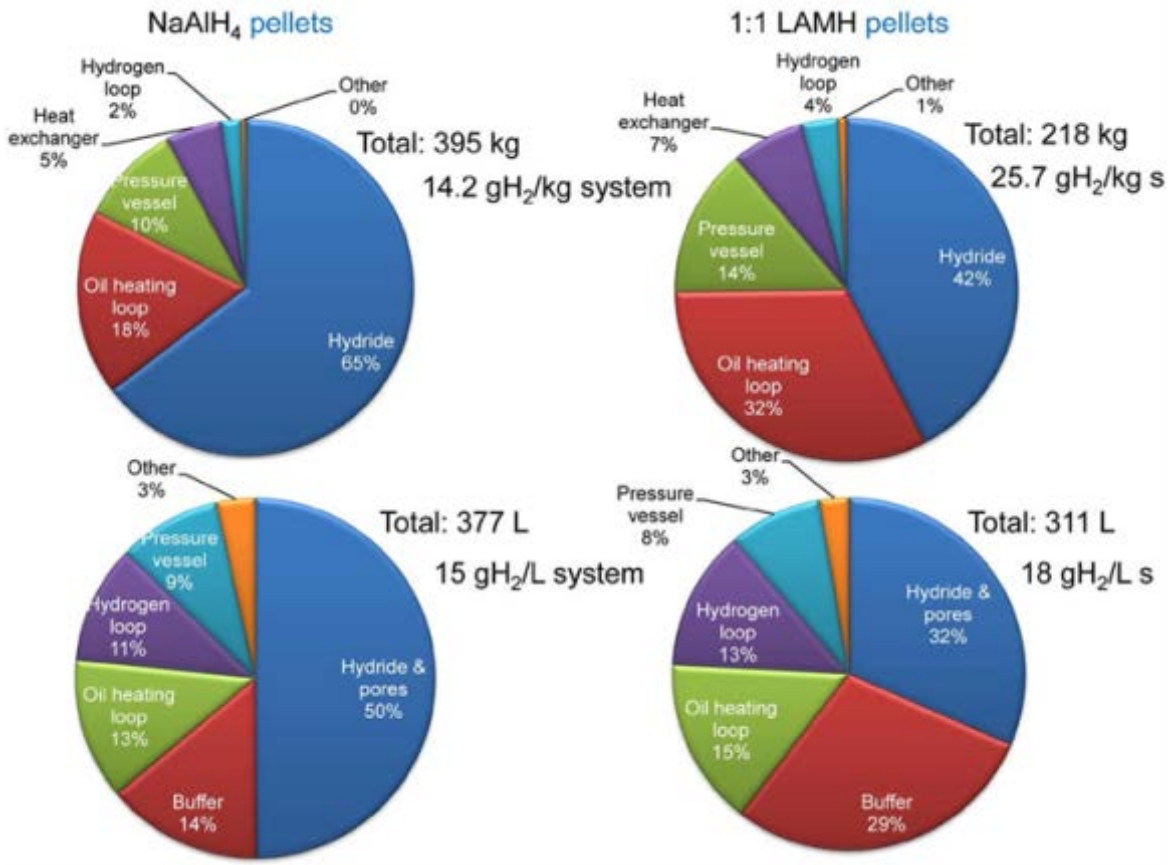

Figure 26. Effect of BOP Components on the Gravimetric and Volumetric Capacity of H_2 Storage Systems using sodium alanates or LAMH.[80]

The conclusion of that effort was that while the compacted forms of the materials show dramatic improvements over loose powders, the gravimetric and volumetric capacities of both hydride systems were below the U.S. DOE 2010 targets. Thus, reducing the BOP weight and volume is critical when developing on-board reversible metal hydride H_2 storage systems.

Example 2:

Another example of simulation modeling and the need for mechanical properties data is the work by Lozano et al. which examined a tubular tank configuration for hydrogen storage based on sodium alanates.[84, 85] In this work the influence on performance of adding thermal conductivity enhancers and compacting the materials were measured and included in system storage bed simulations.

Estimates of the effective thermal conductivity of Ti-doped sodium alanates powders with and without expanded graphite flakes (EG) was measured using a 15 mm diameter cell equipped with five type-K thermocouples (Figure 27). The cell was designed to enable measurements up to temperatures of 400 °C and pressures up to 200 bar. The temperature measurements throughout the hydride bed with this cell made it possible to analyze the heat flow during the reactions and to estimate the effective thermal conductivity of the bed.

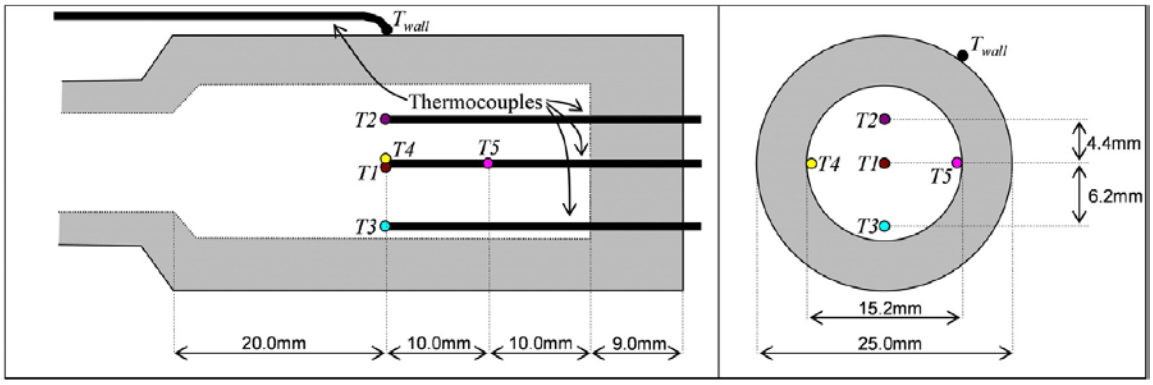

Figure 27. Thermocouple positions in the 15 mm diameter cell for heat flow analysis during absorptions and desorptions.[85]

The positions of the thermocouples in the measurement cell seen in Figure 27 were chosen in order to estimate the effective thermal conductivity of the material bed. The thermocouple positions were arranged in such a way that a parabolic radial temperature profile could be measured with uniform and sufficient temperature variation between thermocouple positions T1, through T2, to T3. Hydrogen content was measured on the 3rd hydrogen desorption (5 bar) using a Sieverts apparatus. The initial temperature was 125 °C. An example measurement is shown in Figure 28.

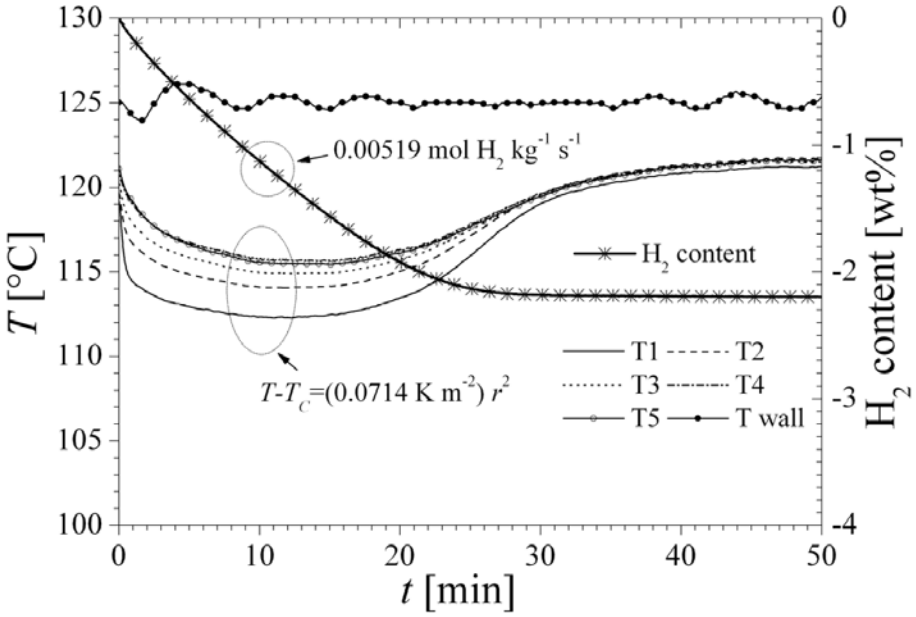

Figure 28. Desorption of $NaAlH_4$ at 5 bar and 125 °C. Initial temperature was 125 °C. The temperature profile was fit and the desorption rate was calculated in order to estimate the effective thermal conductivity of the hydride bed.[85]

An example of the measurements and fit to a temperature profile is given in Figure 29.

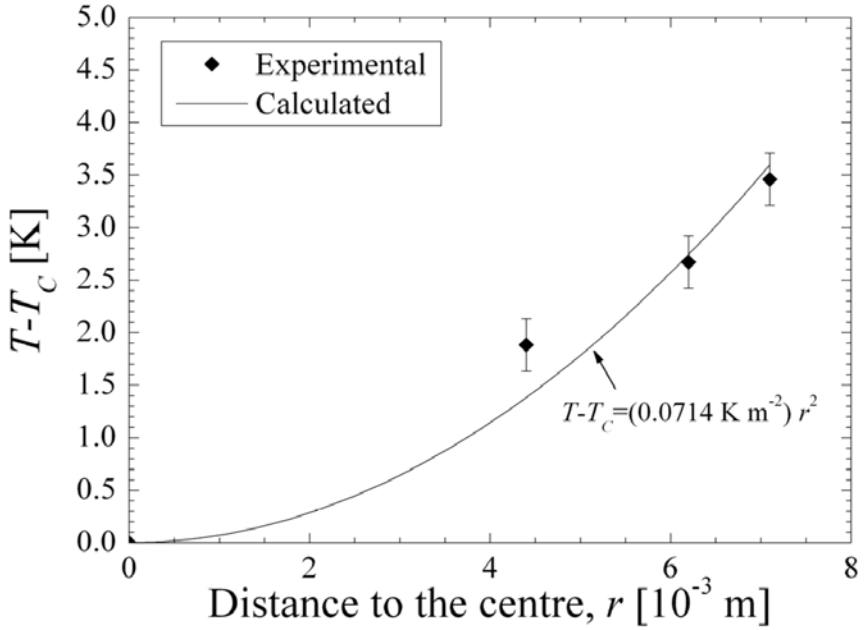

Figure 29. An example of the temperature of the hydride bed with respect to the distance from the center of the cell. The fitting was used to estimate the effective thermal conductivity of the hydride bed.[85]

The estimated thermal conductivities are summarized in Figure 30 for material without and with a small amount of carbon addition as a milling lubricant. The addition of carbon during milling leads to a roughly 50% higher thermal conductivity, amounting to around 0.8 W m^{-1} K^{-1}. The values obtained for the material without carbon are in good agreement with values reported in the literature[86] providing some validation of the measurements and analysis.

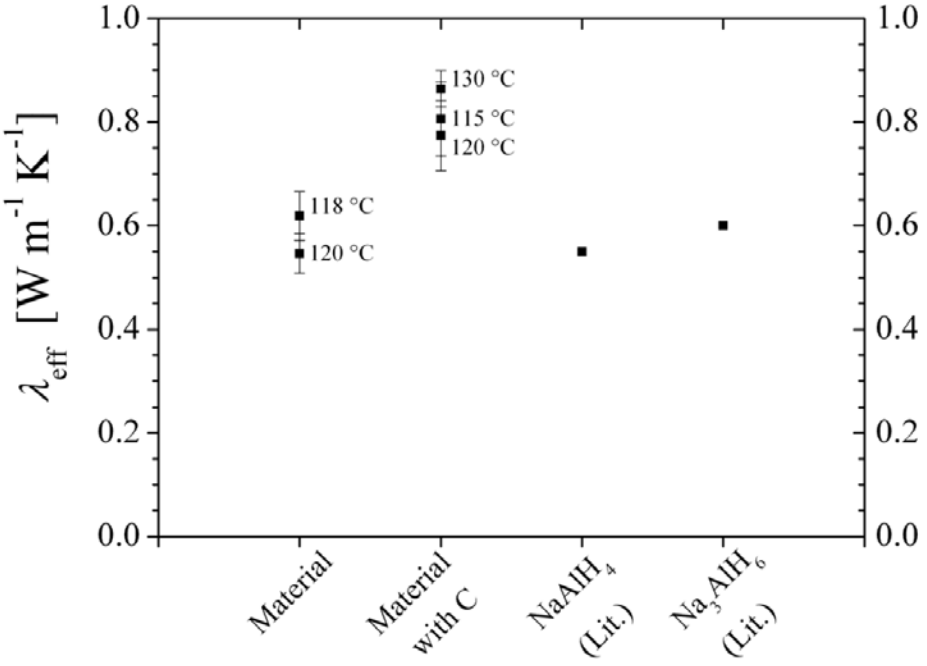

Figure 30. Estimated effective thermal conductivity of hydride bed for $NaAlH_4$ with and without carbon addition during desorption at 5 bar H_2 in comparison with literature values near room temperature from Reference 86. The temperatures reported are the mean temperatures of the hydride bed.[85]

Next, sodium alanate material was mixed with 0, 5, 18 and 50 wt. % flakes of EG by ball milling. The different ratios displayed very different absorption behavior and temperature profiles. It was observed that the highest peak of the temperature profile measured during absorption was lower for higher EG concentrations. The temperature increase was nearly 100 °C for the mixture without EG, whereas the mixture with 50 wt. % EG had a temperature increase of < 1 °C.

The estimated thermal conductivities of the mixtures with EG flakes are presented in Figure 31. The mixture with 5 wt. % EG has an estimated thermal conductivity between 1.3 and 1.8 W m^{-1} K^{-1}, which almost doubles compared to the material without EG. Higher EG content in the hydride bed leads to higher values of the effective heat conductivity.

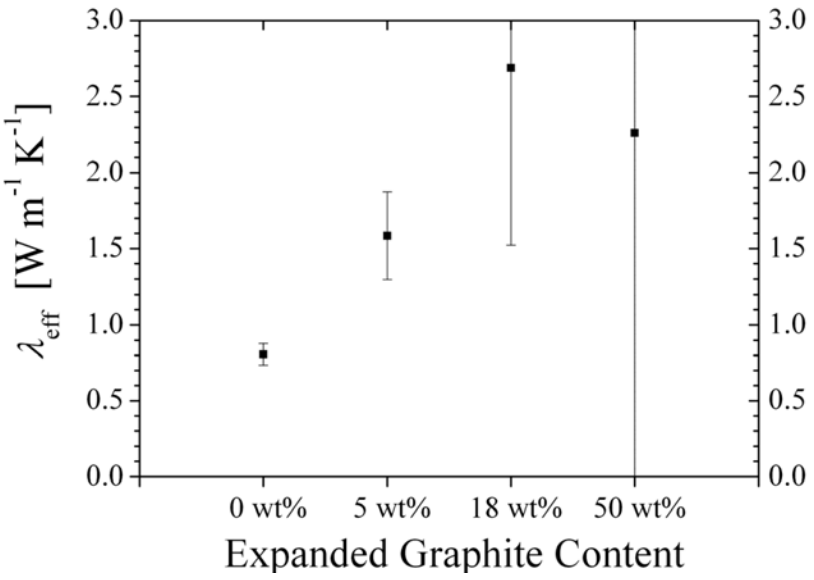

Figure 31. Estimated effective thermal conductivity of hydride bed of sodium alanate material mixed with different contents of EG. Measured under desorption at 5 bar.[85]

Note that according to the error calculations done by Lozano, the estimation method is only appropriate for low values of thermal conductivity as represented by the error bars in the figure.[85] At high values of the thermal conductivity (> 2 W m^{-1} K^{-1}), the temperature profile used for the estimations becomes quite narrow. This, combined with the error of the temperature measurement, leads to high uncertainties. However, both the narrow temperature profile and the much lower thermal excursions indicate that the effective thermal conductivity clearly increases with higher EG content.

One of the major advantages of metal hydrides over compressed hydrogen for storage, even at high pressures, is their idealized greater volumetric hydrogen density of hydrides based upon the host material density. However, activated hydrides are almost always powders and the effective volumetric hydrogen density is reduced due to the void volume present inside the bed. This is especially true of loose powders versus compacted powders. For example, loose sodium alanate material of this example investigation had a porosity of more than 60%. Thus, less than half of the volume of the hydride bed is actually occupied by the hydrogen absorbing material.

In addition to storage bed optimization through the addition of thermal conductivity enhancers, Lozano et al. also investigated improvements in volumetric hydrogen storage capacity using powder compaction.[85] Compacts of hydrides have several advantages over loose powder in a hydride bed. Besides the greater volumetric hydrogen density, compacts are much easier to handle, and their effective thermal conductivity should increase since the particles are closer to each other, facilitating heat conduction through the solid phase. A potential negative is that the lower porosity of a compact may result in higher resistance to hydrogen permeation. In their

work, Lozano et al. produced sodium alanate compacts by compressing desorbed alanate (with 5 wt. % carbon from the milling process) in cylindrical molds of 4 and 8 mm diameter using a hydraulic axial press. All preparation was carried out inside a glove box with purified argon atmosphere.

The packing density (represented as apparent density in the publication) of the compacts were determined geometrically using the compact mass and measured cylindrical volume. The apparent densities of compacts as a function of applied compaction pressure are shown in Figure 32.

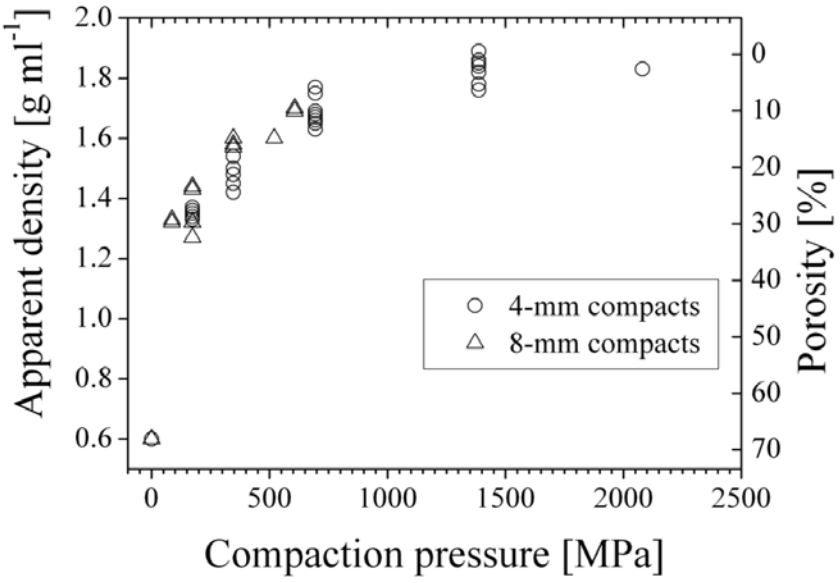

Figure 32. Apparent density and porosity of 4-mm and 8-mm compacts of sodium alanate material in the desorbed state.[85]

The hydrogen sorption kinetics of compacts produced under different pressures was measured using a Sieverts' apparatus.[87] Absorption and desorption behavior of compacts are presented in Figure 33 and Figure 34 respectively. Measurements were made for both low 1.3 g cm^{-3} compaction pressure of 200 MPa (a in both figures) and high 1.65 g cm^{-3}, 700 MPa (b in both figures) density samples. Samples included three of each of the 4 mm and 8 mm compacts together in the same sample cell. The hydrogen absorption and desorption measurements of the low density compacts proceeds faster during the first two or three cycles compared with the high density material.

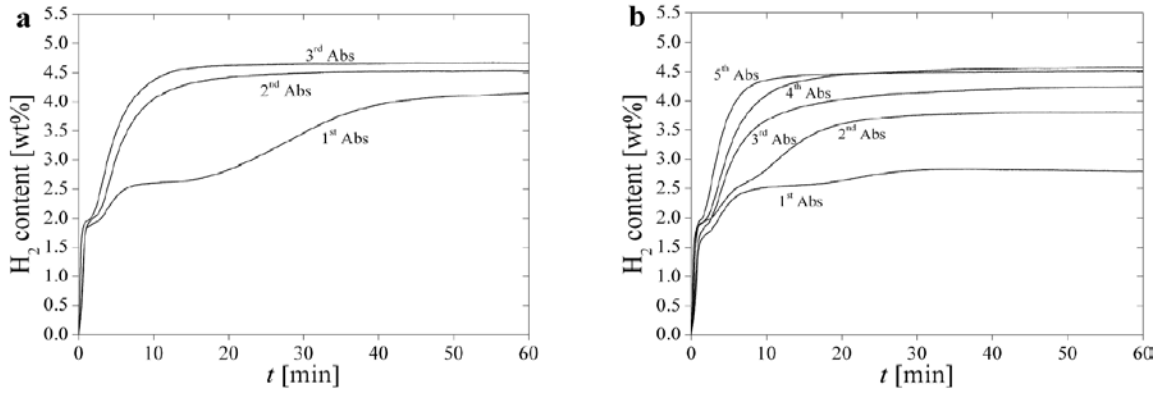

Figure 33. Hydrogen absorption by sodium alanate compacts at 100 bar and 125 °C. (a) Compacts of initial low density (1.3 g cm^{-3}). (b) Compacts of initial high density (1.6 g cm^{-3}).[85]

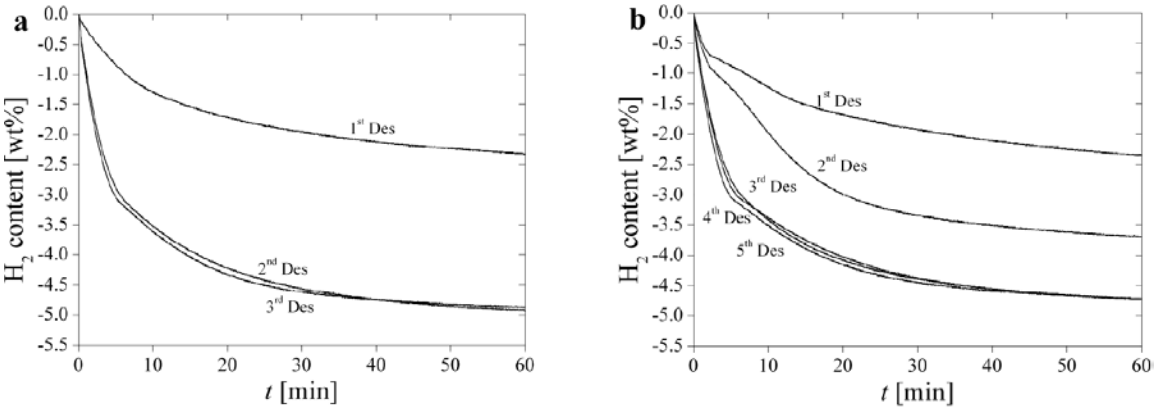

Figure 34. Hydrogen desorption from sodium alanate compacts at 0 bar and 160 °C. (a) Compacts of initial low density (1.3 g cm^{-3}). (b) Compacts of initial high density (1.6 g cm^{-3}).[85]

Through this compaction study, it was shown that after consolidation under different pressures, the apparent density of the sodium alanate material compacts can be increased from 0.6 g cm^{-3} to over 1.8 g cm^{-3}, tripling the effective volumetric hydrogen storage capacity of the desorbed material. Compaction with pressures from 0 MPa up to 700 MPa steadily increased the apparent density of the materials, but at pressures greater than 1400 MPa the increase in density tapers off, asymptotically approaching the theoretical density of the desorbed material (1.88 g cm^{-3}). Cycling the compacts increased the sorption kinetics and hydrogen capacity. Lozano et al. explained this through changes of the internal packing arrangement and expansion of the compacts, as well as through an increase of the interface area. The low porosity of the compacts may reduce permeability for hydrogen flow, causing lower hydrogen uptake in the first cycles. During these cycles, volume expansion of the hydride creates pathways for hydrogen by expanding and fracturing the compacts. This results in higher hydrogen uptake and faster kinetics. This effect occurs in earlier cycles in the low density compacts due to higher initial

porosities. Measurements showed that the apparent density after cycling approached the same value (1 to 1.1 g cm^{-3}) for both low and high density compacts.

From this study, Lozano et al. concluded compaction of the powder provides advantages in increased storage capacity and safety.[85] Higher hydrogen uptake by the compacts was obtained compared to unconsolidated powder. This may be due to lower particle segregation leading to more intimate interactions for the solid-solid reaction in the compacts. Compacts also proved to be safer to handle in contact with air and water compared to the unconsolidated power.[85]

1.11 Vibrational Densification of Powder Particles

The "Bulk Density" is a property of powders that has important meaning for hydrogen storage materials. It is defined as the mass of the particles of the material divided by the total volume they occupy. The total volume includes particle volume, interparticle void volume, and internal pore volume. The bulk density affects the total volumetric storage capacity of the system.

It is important to note that the bulk density is not an intrinsic property of a material; it can change depending on how the material is handled. For example, a powder poured into a cylinder will have a particular bulk density; if the cylinder is disturbed (such as through road vibration), the powder particles will shift and usually settle closer together, resulting in a higher bulk density. For this reason, the bulk density of powders is usually reported both as "freely settled" (or "poured" density) and "tapped" density (where the tapped density refers to the bulk density of the powder after a specified compaction process, usually involving vibration of the container).

A potential issue particularly associated hydride powders is that when fine particles are densified by vibration they tend to interlock. Upon expansion the friction and shear forces between particles prevent free-flow motion and translate expansion forces to the surrounds. The degree to which to forces are imposed on a surrounding containment vessel depends on the degree to which the powder is compacted and interlocked. The upper limit of a fully compacted material would impose forces approaching that of an expanding single monolith. Thus, the characterization of powder densification as a result of vibration may be particularly important for many hydrogen storage applications.

Such studies have not been performed extensively on hydrogen storage materials. However, this is an important industrial issue in the production, transport and packaging of granular materials. In particular, there has been extensive work on the identification of the factors that affect bulk density, including how the material has been handled throughout its processing history. A common phenomenon is the increase in bulk density that takes place when a container of granular materials is shaken, tapped or vibrated. A good reference that presents highlights of

the history of this topic, ranging from very fundamental investigations on the development of packing algorithms and microstructural analysis to more practical experimental and numerical studies is a paper by Zhang and Rosato.[88] In the same paper, the authors report on their findings from experiments and discrete element simulations on the relaxation behavior of assemblies of uniform spheres that are vertically oscillated. Physical measurements of the bulk solids fraction, qualitatively reproduced in the simulations, reveal noticeable trends in the data dependent on the vibration amplitude and frequency. Based on extended simulations, a 'phase' chart depicting the percentage improvement in bulk density in terms of amplitude and frequency was then obtained. They conclude that the behavior revealed in this chart may be characteristic of density relaxation in bulk solids.

The Zhang and Rosato experimental apparatus was comprised of an acrylic cylinder containment vessel of diameter D formed from stacked rings that were mounted onto a shaker.[88] An accelerometer attached to the piston provided feedback control through which precise adjustments to the frequency and amplitude could be made. Figure 35 shows a schematic of the experimental system used in that study.

The experimental procedure involved first measuring the initial (before vibrations are applied to the piston) bulk solids fraction. Particles (acrylic spheres, d = 3.175 mm) were slowly poured into the cylinder and then the top layer was removed by sliding the top ring across. This was done to ensure that the cylinder was filled with a level surface to a height of 30d. The poured bulk solids fraction v_0 (where v(n) is the solid fraction at n taps and n = 0 indicates the starting apparent density) could then be computed from the volume of the cylinder and weight of its contents. For the aspect ratio D/d = 20 used in the experiments, they obtained an average value v_0 = 0.604 that is typically associated with a loose random packing.[89] This was followed by vibration experiments carried out by filling the cylinder with mono-disperse acrylic spheres (d = 3.175 mm) to an undisturbed bed depth $H \approx 95.3$ mm. The filled cylinder was rigidly mounted onto the shaker head, which was sinusoidally oscillated over a range of amplitudes $0.04 \leq a/d \leq 0.24$ (where a is the amplitude), and frequencies (ω) between 25 and 100Hz (corresponding to relative accelerations $\Gamma \equiv a\ \omega^2/g$ between 0.94 and 11.54). For each selected frequency and amplitude, the shaker was run for ten minutes, with each experiment repeated several times to confirm the results. In order to reduce the buildup of static charge, the inside tube wall and particles were treated with a household antistatic agent. In measuring the bulk solids fraction v_1 after the vibrations were stopped, a level particle surface was formed using the same procedure as described in the pouring experiments. From those measurements, they found improvements in the solids fraction, $((v_1 - v_0) \times 100/v_1)$ versus acceleration Γ for increasing values of amplitude a/d.

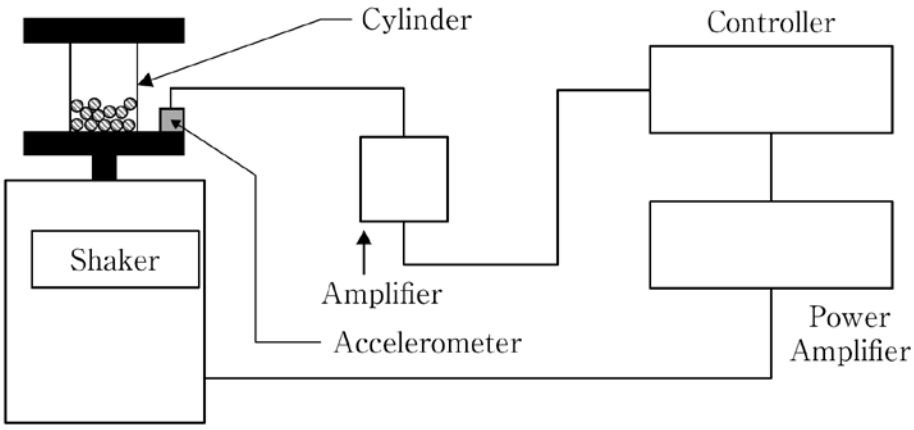

Figure 35. Schematic of particle vibration experimental apparatus.[88]

The study revealed four trends in the behavior of v versus Γ that depend on the level of the displacement amplitude. Figure 36 shows that for a/d = 0.04, the solids fraction increases with Γ, but the improvement is only about 3.3% at Γ = 5.1. Observations of the vibrated bed indicated that there was little or no bulk motion with the exception of some activity of the particles at the top surface for Γ > 2. We conjecture that at these excitation levels the bulk density increases through slow, cooperative particle rearrangements throughout the assembly, analogous to the "push filling" mechanism suggested by An et al.[90]

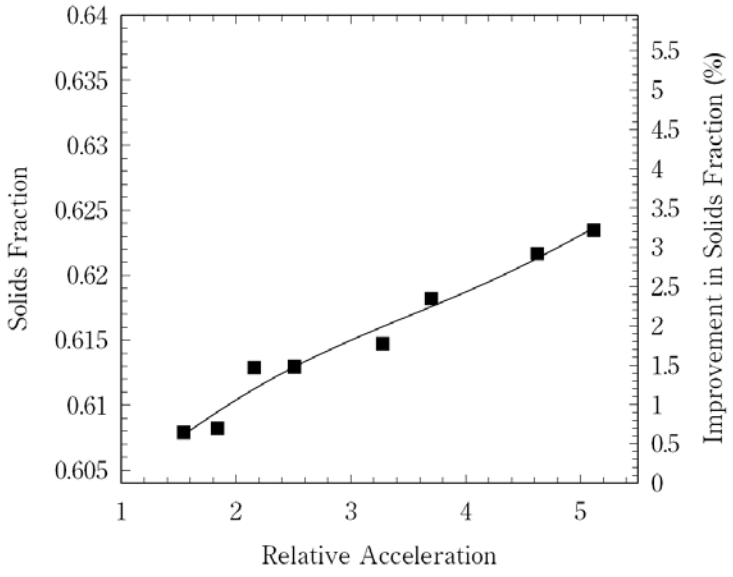

Figure 36. Solids fraction versus relative acceleration at a/d = 0.04. The solid line is a best-fit curve to show the trend.[88]

Figure 37a shows that when a/d is between 0.06 and 0.10 a maximum exists in the bulk solids fraction ($v_m \approx 0.636$, corresponding to an improvement > 5%) when Γ is between 5 and 7, followed by a slight expansion of the bed (or a reduction in ν) with a further increase of Γ. Near the peaks (at $\Gamma = \Gamma_c$), particles near the cylinder walls were seen to remain in contact with each other and to travel downwards in a collective manner, a phenomenon indicative of convective motion that has been reported in other studies. Further observations made near the walls and on the surface at Γ_c revealed a random close packing of spheres (v = 0.6366) arrangement of the particles as illustrated in Figure 37b. The authors concluded that the influence of the cylinder walls in the presence of the slow convection was responsible for the creation of these structures, which in turn contribute to the overall increase in bulk solids fraction. They noted that Nowak et al. also pointed out that the walls of the cylindrical container used in their experiments may have influenced the compaction process.[91]

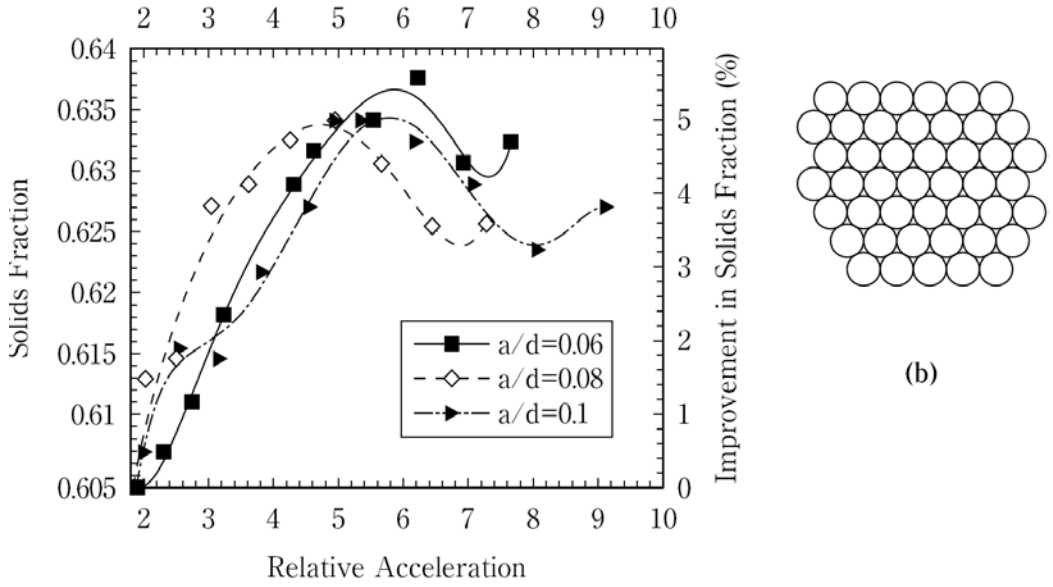

Figure 37. (a) Solids fraction versus relative acceleration at a/d = 0.06, 0.08 and 0.10; the lines are best fit curves to show the trends in the data. (b) Illustration of particle arrangement near the cylinder wall at Γ_c.[88]

This example study also found distinct oscillations in the solids fraction versus Γ when a/d = 0.16 (Figure 38). At this amplitude level, convection could still be observed as particles adjacent to the walls moved downward.

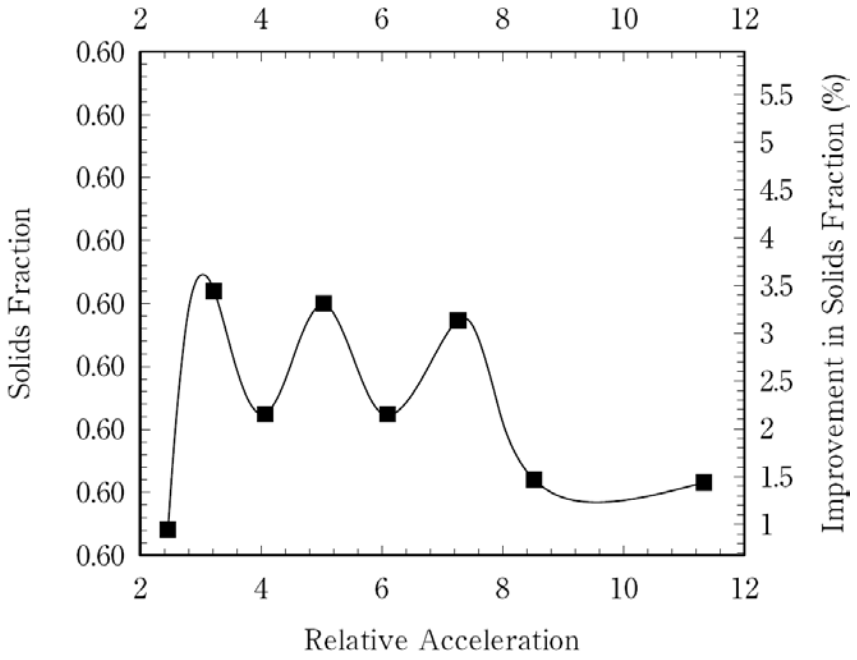

Figure 38. Solids fraction versus relative acceleration at *a*/*d* = 0.16. The solid line is a best-fit curve to show the trend.[88]

At the highest amplitude level used (*a*/*d* = 0.24), the solids fraction versus Γ remained almost constant and little improvement in density was attained. At these conditions, a marked expansion of the bed depth occurred and the system resembled a dense, energetic "gas" of particles.

The authors then performed discrete element simulations of the experimental measurements employing the soft "partially latching spring model" developed by Walton et al. for elastic-plastic collisions.[92] Although there were quantitative differences between the simulated and experimental results, the simulations did generate all of the important critical phenomena and were in reasonable qualitative agreement with the experiments. Following that validation phase, a series of case studies was carried out spanning vibration amplitudes and frequencies $0.02 < a/d < 0.48$ and $10 \text{ Hz} < \Gamma < 90 \text{ Hz}$. Figure 39 presents their results in the form of a chart of the improvement in bulk solids fraction as a function of amplitude and frequency. A region of optimal improvement in packing densities by nearly a factor of 50 is clearly visible (lightest color in the amplitude-frequency space) which was in agreement with the experimental results. At the poorest levels of improvement, the vibrated system was found to be in a relatively high energetic state, which settled to a static configuration with little or no increase in bulk density.[88]

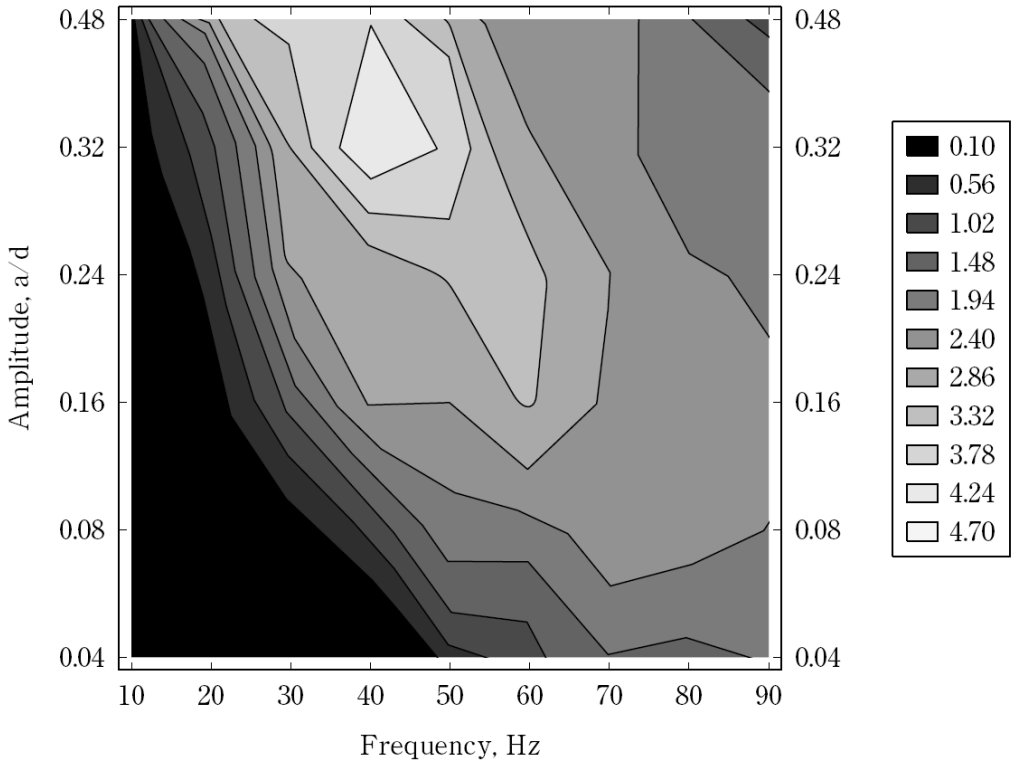

Figure 39. Chart showing improvement (increase) in solids fraction as a function of vibration amplitude and frequency for an 8000 particle system in which *L/d* = 25.[88]

This example describes some of the methodologies that could be employed in the study of 1) the deliberate vibrational compaction (for improved volumetric capacity and heat transfer) of powdered hydrogen storage materials, or 2) the unintended compaction of hydrogen storage materials due to vibration when used in mobile applications.

The study presented above was for ideal spherical particles. The behavior of highly irregular, fractured particles (e.g., activated hydrides) may be considerably different. Besides the improvement in volumetric densities obtained by densification of powders, another important consideration, particularly for hydrides, is the potential for large bulk lattice volume expansion forces in compacted powders. The interlocking of particles that may lead to expansion force on hydrogen absorption in hydrides will be a function not only of such vibrational densification but also on particle shapes and surface morphology. In this respect, densification measurements and microscopy will play an important role in the investigation of the mechanical properties of actual hydrogen storage powder materials.

1.12 Heat Transfer

In proceeding with the engineering design of a hydrogen storage system, it may be very important to accurately model effective thermal conductivity taking into account the packing structures of powder materials. For example, a packed hydride powder may be considered a granular material with a jamming point that represents the state at which a granular material develops rigidity and mechanical stability.[93] The jamming threshold density φ_j is the density at which this transition occurs.

When the length scale through which heat is transported is smaller than the diffusive length scale (the mean free path between scattering events) the transport regime is referred to as ballistic. Multiscale features present in granular materials can result in ballistic and diffusive behavior throughout a heterogeneous medium. The reduction of heat flow through the gas phase occurs as a result of interfacial interactions of thermal energy carriers with the confining pore geometry of a granular medium. Smith and Fisher simulated heat transfer in a metal hydride powder bed taking this transition of thermal carriers into account. Details of the theory behind the heat transfer modeling can be found in reference 65.

The mean effective conductivity of the jammed system at a density just below the jamming point was computed for a range of solid-gas conductivity ratios as displayed in Figure 40. The ratios approach an asymptote for high solid conductivities. The authors concluded that the solid phase does not form a high-conductivity path through which heat preferentially flows.[65] The structure of the granular medium induced by the jamming of these highly irregular, faceted particles is responsible for this behavior. Heat is forced to flow through the gas phase in order to reach highly conductive solid islands. Such poor solid continuity is consistent with observations in the literature of very low effective conductivity of evacuated metal hydride powder.[37] Under vacuum, no gas is present in the pores of the powder, and therefore only radiative transfer through vacuum between solid particles and conduction through the solid phase contact network is available to transfer heat.

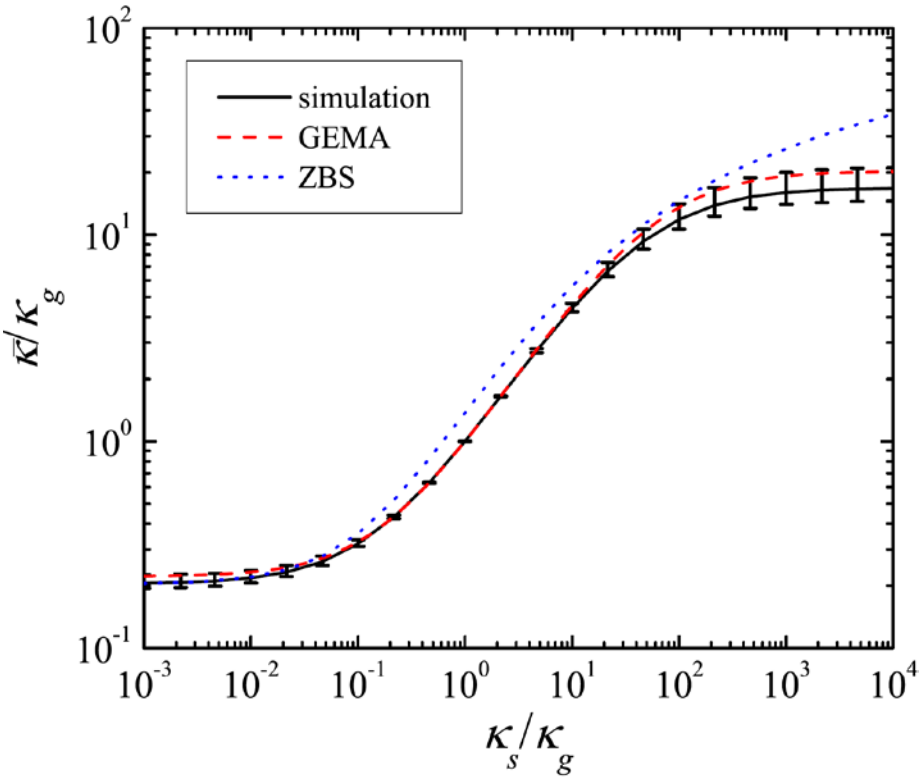

Figure 40. Mean effective conductivity as a function of solid-fluid conductivity ratio κ_S/κ_g for the jammed system at ϕ = 0.633. Error bars represent bounds of the principal values of the effective conductivity tensor κ. Theoretical data presented are based on the granular effective medium approximation (GEMA)[94,95] and the Zehner-Bauer-Schliinder (ZBS) model.[65,71]

Figure 41 presents the calculated temperature field for the jammed system at a density just below the jamming point. Solid phase islands can be observed that are nearly isothermal because of the lack of connectivity of these islands.

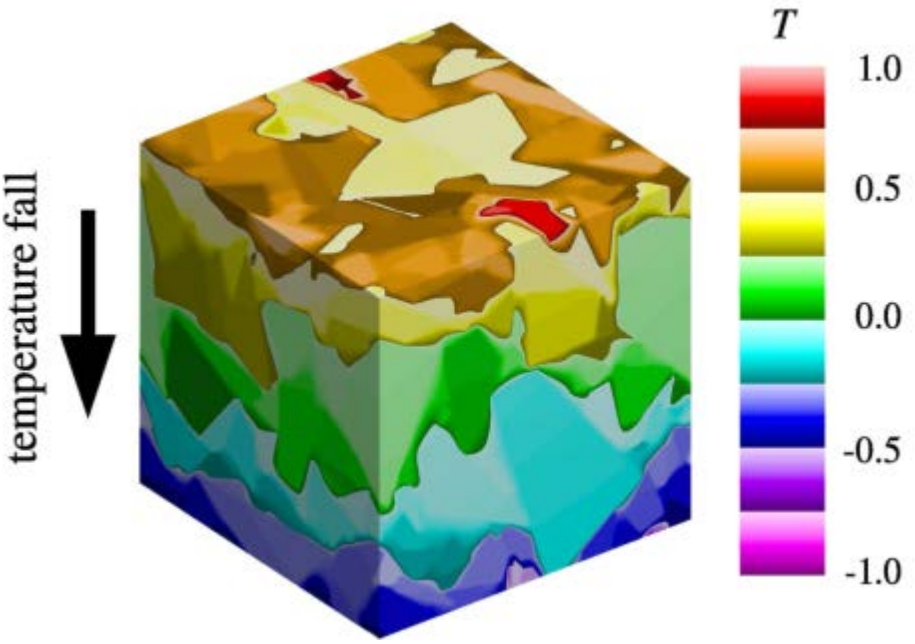

Figure 41. Temperature field of the jammed system with κ_s/κ_g = 103 at φ = 0.633. The field is induced by a unitary periodic temperature fall applied to the primary simulation supercell along the indicated direction.[65]

The compositional makeup of a typical metal hydride hydrogen storage system consists of: 1) Transition metals, such as Ni and Ti with thermal conductivities that span nearly an order of magnitude from 21.9 to 90.7 W $m^{-1} K^{-1}$ at room temperature,[96] 2) Pressed solid pellets of H_2 storage alloys (e.g., $LaNi_{4.7}Al_{0.3}$ and HWT) with thermal conductivities on the order of 10 W $m^{-1} K^{-1}$,[37] and 3) H_2 gas with a thermal conductivity of 0.183 W $m^{-1} K^{-1}$ at 300 K.[96] The general result is that the ratio κ_s/κ_g for a metal hydride powder system is likely > 100. Given such a high conductivity ratio, it is unlikely that enhancement of the intrinsic conductivity of metal hydride particles will yield significant enhancement of the effective thermal conductivity of the system given the non-percolating solid-phase granular topology in the powder produced by the above simulations.[65]

Using this model, the dependence of the effective thermal conductivity of the hydride storage system $\bar{\kappa}$ on the Knudsen number K_n for hydrogen was then determined by expressing κ_g as a function of K_n.[65] The Knudsen number K_n is a dimensionless number defined as the ratio of the molecular mean free path length of a hydrogen molecule to a representative physical length scale. Figure 42 shows that moderately to highly conducting solids ($\kappa_S \approx 20$ W $m^{-1} K^{-1}$) yield very similar effective thermal conductivities. Because the Knudsen number K_n scales inversely with gas pressure, the modeling results reflect the high-pressure limit of effective thermal conductivity in which the Smoluchowski effect is diminished.

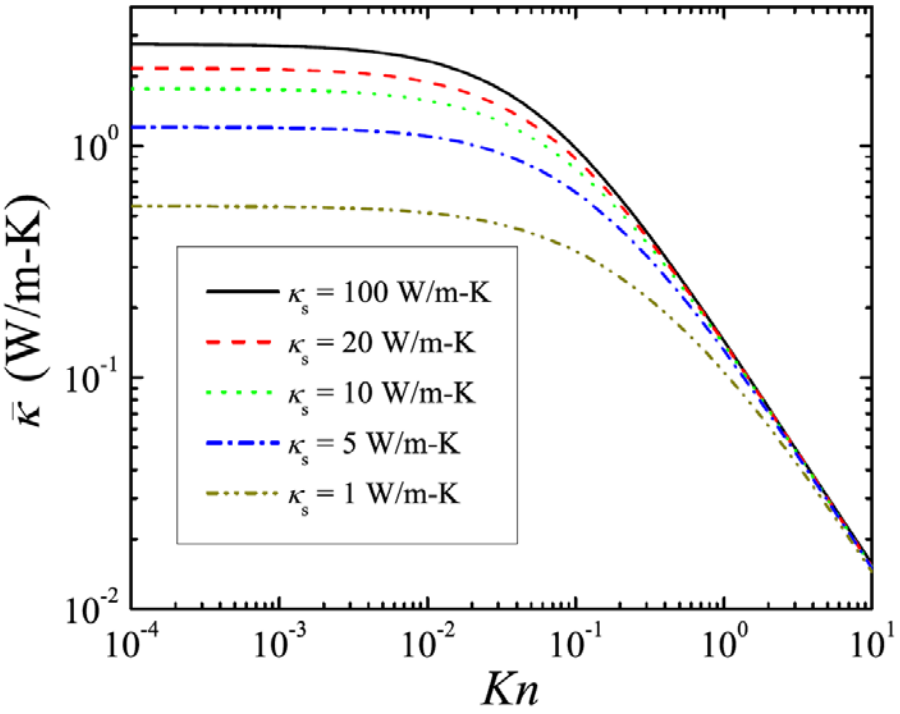

Figure 42. Mean effective conductivity $\bar{\kappa}$ for the jammed system at φ = 0.633 as a function of Knudsen number K_n for solid conductivities κ_S and H_2 gas at 290 K.[65]

1.13 Generalized Powder Structure / Thermal Transport Modeling

In the work of Smith and Fisher presented above, the simulated jammed density of particles from the Poisson plane field (φ = 0.665 ± 0.015) is much higher than from experimental typical measurements of packed metal hydride powders. They explain that attractive surface interactions between micron sized metal hydride particles reduce the actual powder densities well below the jamming density, and that such interactions are known to decrease packing density dramatically,[97] but that the non-cohesive jamming point remains a reference state after such systems have undergone compaction.[98,99] In cohesive packings, agglomerates form as jammed domains with cohesion[98] embedded in void space.[99] These agglomerates form a fractal-like structure with high dimensionality of 2.53.[99]

Based on the hypothesis that hydride powders form this type of structures, Smith and Fisher then created a model based on a low-density packing of metal hydride powder with a granular backbone having local density and structure close to that of the non-cohesive system.[65] In this case the cohesive granular medium is modeled as bi-porous; pores reminiscent of the non-cohesive jammed state are formed with larger pores present due to the steric hindrance of cohesive clusters. The granular effective medium approximation (GEMA) was employed to model the effective thermal conductivity of cohesive metal hydride powder (Figure 43).

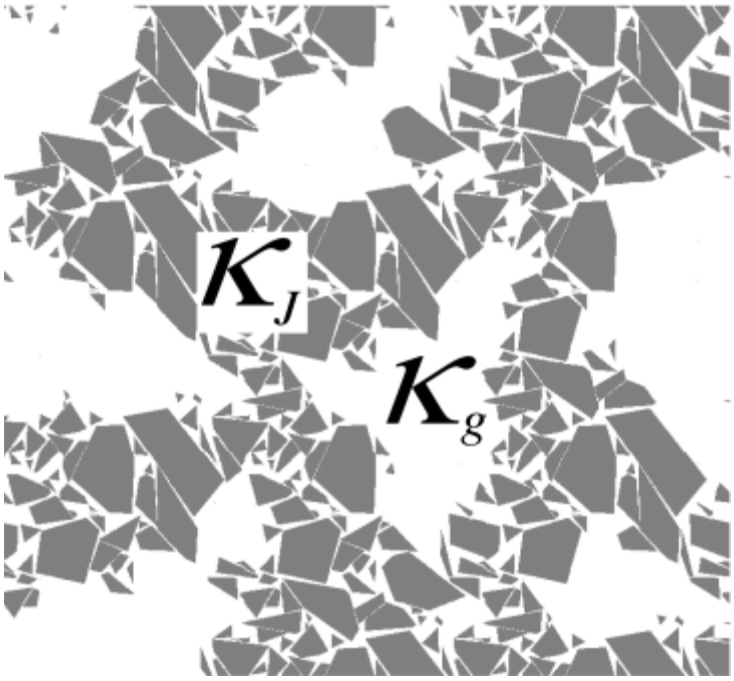

Figure 43. Illustration of a hypothetical cohesive microstructure of metal hydride powder. Inspired by References 98 and 99, the microstructure is bi-porous with aggregate jammed regions having micropores with conductivity κ_j and void regions forming macropores with gas phase conductivity κ_g.[65]

The validity of the hypothesis of Smith and Fisher was supported by experimental effective thermal conductivity data at high gas pressure (small K_n) of various hydride powders as shown in Figure 44.[65] Measured κ_S values for solid pellets of $LaNi_{4.7}Al_{0.3}$ and HWT are approximately 10 W m^{-1} K^{-1}.[37] This corresponds well with the modeled curve of the effective thermal conductivity of the bi-porous structured material with a solid-phase conductivity of 10 W m^{-1} K^{-1}.[65] From their model results (Figure 44), it appears that at high pressure, thermal conductivity depends weakly on solid conductivity compared to density. This again supports the proposition that little enhancement of metal hydride powder thermal conductivity can be achieved by increasing the intrinsic thermal conductivity of solid metal particles. Instead, strategies should be employed to modify the packing structure of the particles. A logical next step would be to apply the models to composite compacts such as hydrides and low thermal conductivity physisorption materials with thermally conductive additives such as ENG.

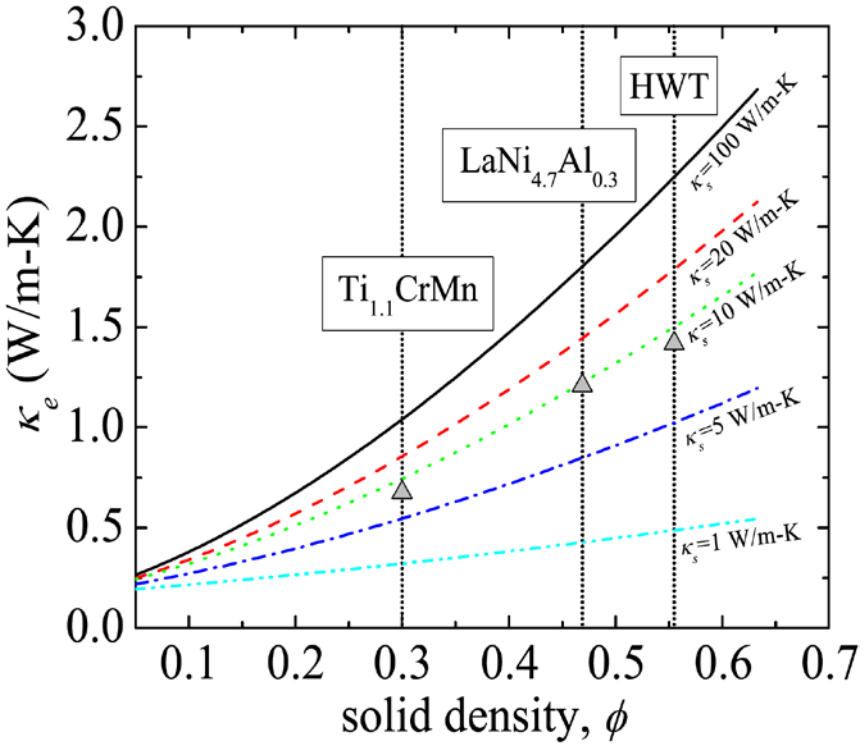

Figure 44. Theoretical prediction of effective thermal conductivity for a bi-porous cohesive metal hydride powder in H_2 gas at high pressure (i.e., $K_n \rightarrow 0$). Triangles represent data for packed metal hydride powder in high pressure H_2 gas near 290 K ($Ti_{1.1}CrMn$ at 230 bar (K_n ~0.001)[39], $LaNi_{4.7}Al_{0.3}$ at 20 bar (K_n ~0.008) and HWT at 40 bar (Kn ~0.004)[37]).[65]

The results above were based on the high pressure limit of gas-phase conductivity in which the Smoluchowski effect is inoperative. Taking into account the above effects of reduced density, Smith and Fisher then modeled the powder structure under varying hydrogen gas pressures.[65] The results are compared in Figure 45 to experimental data for the high pressure metal hydride $Ti_{1.1}CrMn$.[39] Their calculated results are displayed for two densities to reflect the effect of volumetric expansion of particles during hydriding. At low pressure (high K_n) the experimental data follow the theoretical results with a solid conductivity of 2 W $m^{-1} K^{-1}$; at high pressure the experimental data follow the theoretical results for solid conductivity of 10 W $m^{-1} K^{-1}$.

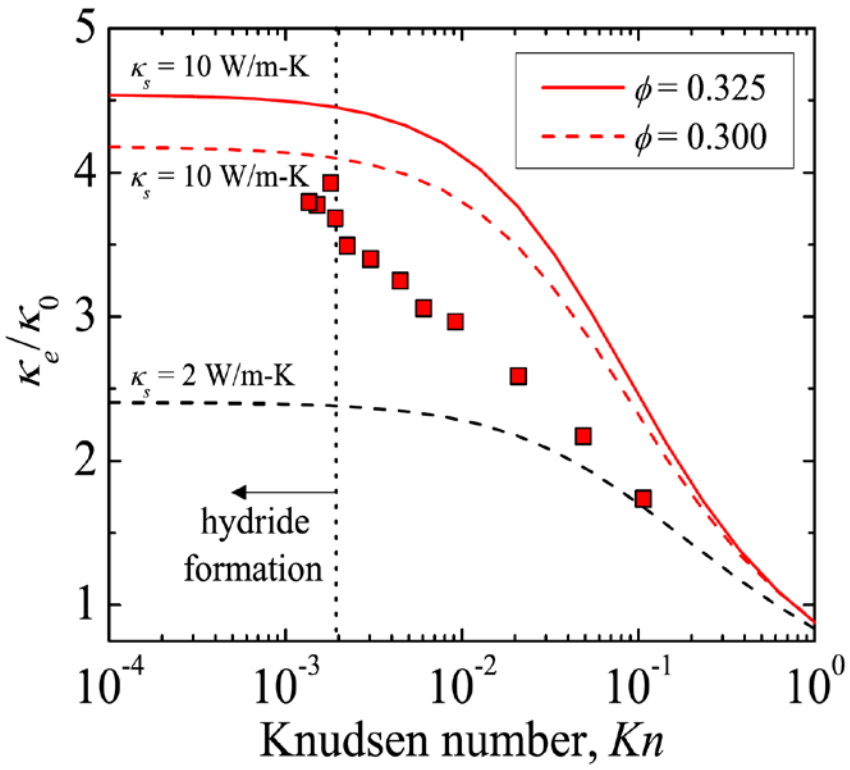

Figure 45. Normalized effective conductivity κ_e/κ_o as a function of Knudsen number K_n of the present theory. The dashed curves represent values for the density of ϕ = 0.3 for cycled and packed $Ti_{1.1}CrMn$ in Reference 39, while the solid curve represents values at higher density (ϕ = 0.325) as a result of volumetric expansion upon hydriding (see Table 2). Curves for ϕ = 0.3 are shown for various values as a reference. Solid squares represent the experimental data of Reference 39 for cycled $Ti_{1.1}CrMn$, where Knudsen number K_n was estimated with a characteristic pore size equal to the median particle diameter determined in the present work, D_{50} 3.6 μm.[65]

From Figure 45 it appears that the "solid" phase has a conductivity that depends strongly on H_2 gas pressure. At first this might appear to relate to hydride formation within the solid, but the authors point out that this is unlikely because the divergence between experimental and modeling results are below the pressure at which the hydride forms. Instead, the authors suggest that at intermediate pressures, cracks within the particles themselves reduce the "effective solid" conductivity.

1.14 Bulk Changes of Hydrogen Storage Materials

In addition to structural, physical, and morphological changes at the particle level with hydrogen uptake and release cycling, hydrogen storage materials are known to exhibit significant bulk changes. These include expansion, migration, and channeling, all of which will affect the mechanical properties of the bulk material and consequently the engineering systems design.

An example of this was seen in the scaled up alanate hydrogen storage system developed by Sandia National Laboratory in partnership with General Motors.[100] In that work, scaled-up beds of alanates were tested for performance characteristics such as fill time and capacity. Sandia developed experimentally based models for heat transfer, mass transfer, and chemical kinetics to facilitate the design and analysis of the scaled-up test system. However, permeability was not explicitly measured during the design process of the storage system. Model validation testing of the full-scale system then showed that transport bottlenecks existed due to hydrogen flow limitations in the porous solid. Following this, the permeability properties of the alanate compacts were measured at various pressures and temperatures. With this data, an accurate model was produced that was appropriate for the range of flow regimes present within a hydrogen storage system for automotive applications.

With the advanced models and scaled-up test bed, the coupled heat transfer, mass transfer, and chemical kinetics models were validated through two methods: 1) a filling measurement that resulted in the time resolved quantity of hydrogen absorbed, and 2) a direct pressure drop measurement across the bed.[100] Figure 46 shows the filling measurement for the sodium alanate hexahydride absorption process. The measurement showed that hydrogen uptake was faster than the rate predicted using only bulk permeability. To resolve the total measured effective permeability through the bed a channeling model needed to be included. A channeling model with the best fit to the actual transport within the system was found to consist of channeling in 2% of the cross-sectional flow area.

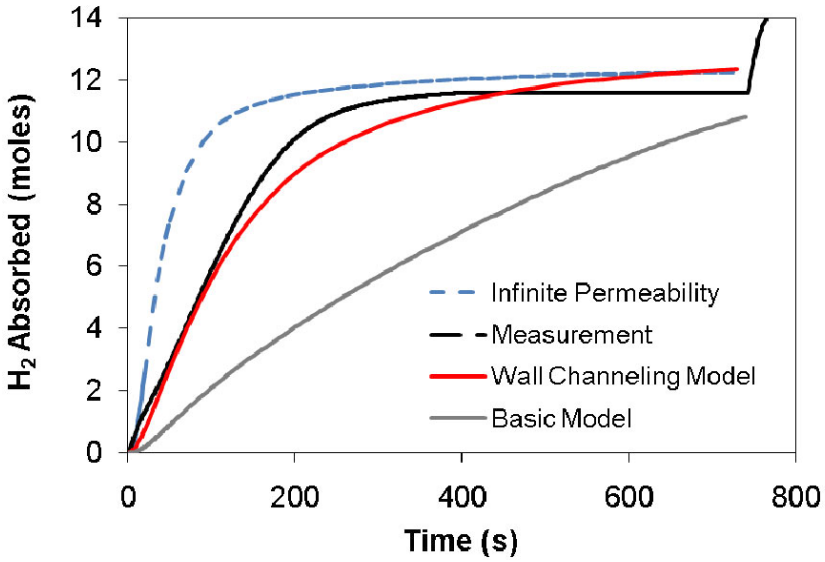

Figure 46. Verification measurements of the coupled models using the large-scale bed. Results indicate that the characteristic permeability of the bed is larger than the bulk permeability of the sodium alanate composite.[100]

However, as can be seen in Figure 46, application of the wall-channeling model under predicts the absorption rate initially before over predicting the absorption at later times. The authors hypothesized that the initial low predicted flow rate was due to the model under predicted permeability and that the over predicted capacity indicates inaccuracies with the kinetics model that was used.

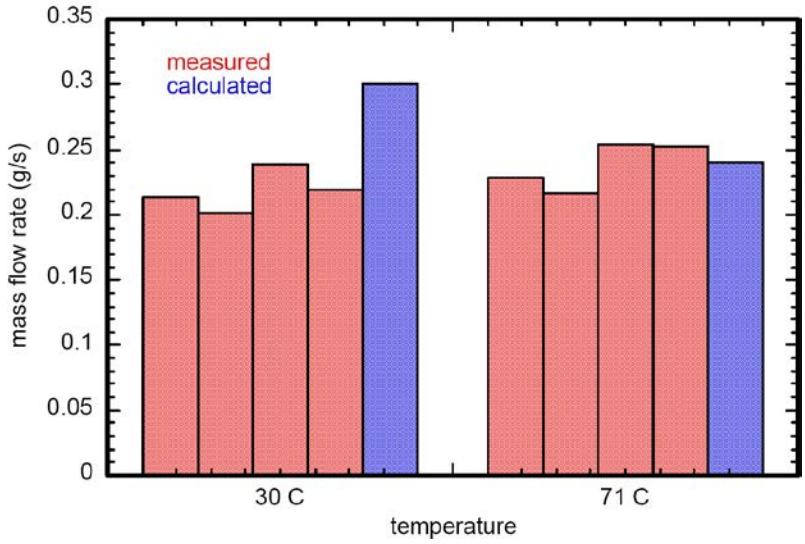

Figure 47. The comparison of measured and calculated mass flow rates for 4 individual tubes is inconsistent.[100]

To evaluate the bed permeability, four hydride tube vessels were modified to allow hydrogen to flow into the tube on one end and out the other, where a fixed pressure drop was applied to each tube and the flow rate measured. The results show the model over predicts the hydrogen flow rate for a tube temperature of 30 °C, although the agreement is better for a tube temperature of 71 °C. In contrast to Figure 46, the comparison shown in Figure 47 suggests that the model used over predicted the permeability.[100]

The test bed was then disassembled to investigate the origin of the apparent contradictions in the permeability model shown in Figure 46 and Figure 47.[100] The sodium alanate composite was removed and a flow channel of ~ 0.127 mm was observed. This indicated that the alanate material had pulled away from the wall and formed a small free flow channel. Additional flow channels were observed in the form of both discontinuous fissures and continuous worm holes (see Figure 48). These observations showed that the wall channel that was used in the model was too large. Furthermore, the observed fissures and worm holes provide radial pathways into the material. It was concluded that including these factors in the model would improve the fit to the measured absorption rate.

Figure 48. The presence of continuous "wormholes" was observed (left) in addition to discontinuous fissures (right).[100]

This example demonstrates the need to evaluate and include bulk mobility and changes in hydrogen storage materials as a part of future systems design.

1.15 Apparent Density Changes with Cycling

In addition to the examples in the previous section, the studies of Lozano et al. also provide a good example of an investigation into what happens to compacts of reversible hydrogen storage

materials when they are cycled.[85] After each of the absorption/desorption kinetics measurements (shown in Figure 33 and Figure 34) the sample cell was opened to inspect the compacts and measure their apparent density. The measured apparent densities of the initially low and high density 4 mm and 8 mm compacts are presented in Figure 49. The values shown are the averages of the three compacts of same diameter and compression.

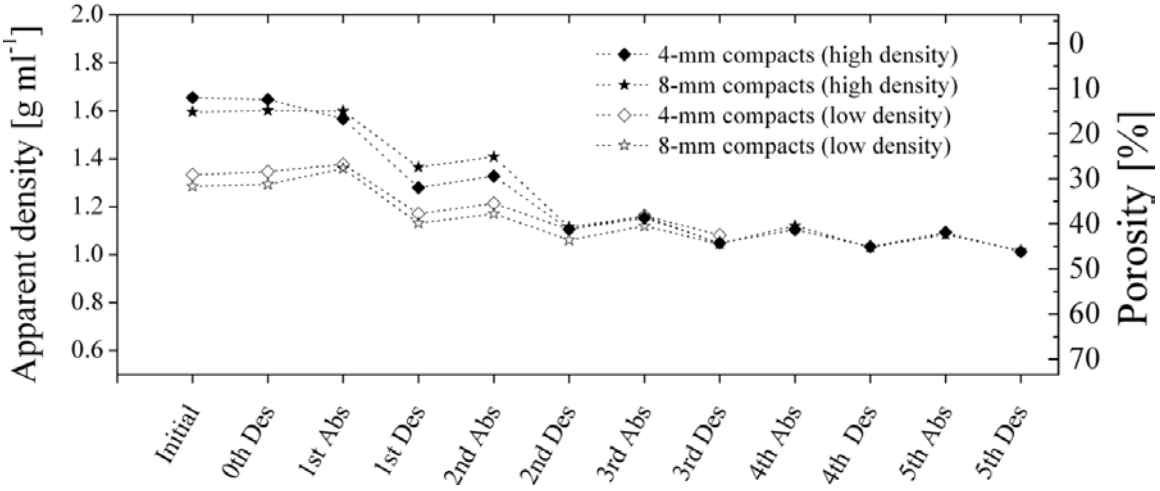

Figure 49. Apparent densities of compacts after hydrogen absorptions and desorption cycles for compacts of initial low (1.3 g cm^{-3}) and high (1.6 g cm^{-3}) density.[85]

From these measurements, they found that the apparent density of the compacts decreases for both low and high density compacts. After several cycles, the apparent density of both low and high density compacts approach the same value of about 1.1 g cm^{-3}, which corresponds to a porosity of approximately 45%. Inspection of compacts showed that after cycling the surface is no longer smooth or shiny and fissures appeared on the surface of the initially high density compacts.

A very interesting observation was that the compacts expanded more during hydrogen desorption than absorption. This is shown more clearly in Figure 50. The expansion during absorptions is consistently less than for desorptions and even exhibits slight shrinking in some cycles.

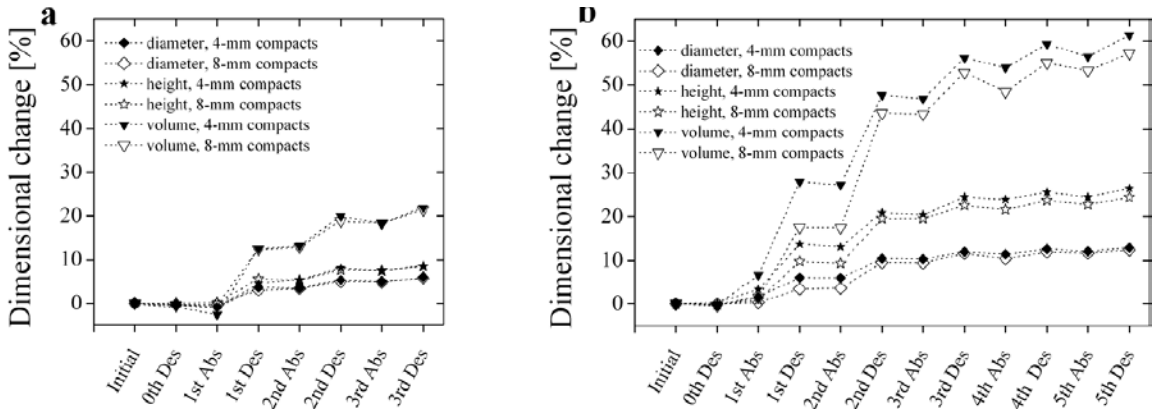

Figure 50. Dimensional change of diameter, height and volume of the compacts after each absorption and desorption. a) Initial low (1.3 g cm^{-3}) and b) high (1.6 g cm^{-3}) density.[85]

The formation and decomposition of alanates involves long-range transport of metal species. This unusual expansion behavior in the compacts may be due to this restructuring of particles because of this transport of species and the release of hydrogen gas to form bubbles or fissures.

The expansion of the compacts is an important mechanical property that must be considered when designing a storage system. Not only is there a potential loss in volumetric capacity in allowing for this expansion, but other property (such as thermal conductivity) improvements of the compacts may degrade with cycling due to bulk expansion. Such issues point out the need for more advanced (and perhaps more complex) materials engineering design.

Note: the unusual behaviors in these measurements mentioned above show interesting similarities with other measurements made by Dedrick et al.[200] This is discussed in detail at the end of section 2.5 where a potential explanation for the behavior is presented.

1.16 Durability of Compacted Hydride Storage Materials

An example of first steps in developing materials engineered compacts is the work by UTRC to develop and test the durability of such advanced compacts. Because hydrogen storage systems are expected to experience 1,500 cycles over their lifetime, UTRC performed a series of tests to study the effect of H_2 absorption and desorption cycles on the strength of sodium alanate pellets.[80,101] Sodium alanate pellets were reinforced with aluminum mesh to improve the strength of the pellets. However, while the strength increases over unreinforced pellets, the strength of both types of pellets rapidly degrades upon cycling due to a substantial expansion of the pellets (Figure 51).

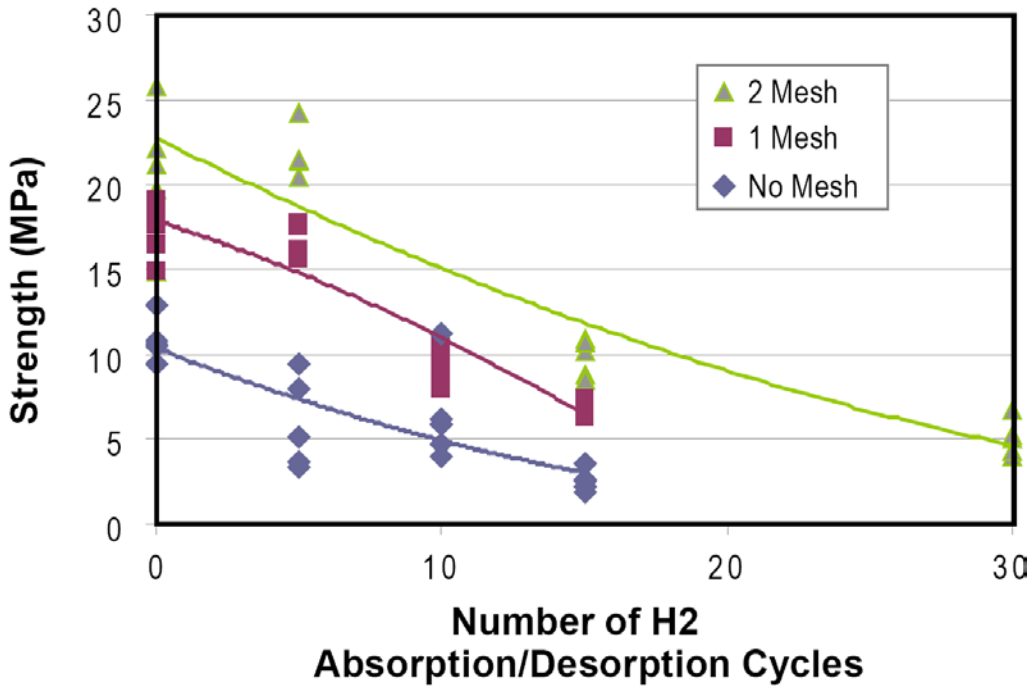

Figure 51. Effect of H_2 absorption and desorption cycles on the biaxial flexure strength of sodium alanate pellets with and without internal mesh reinforcement.[80]

1.17 Particulates and Impurities from Hydride Storage Materials

The three categories of H_2 storage systems (on-board reversible hydrides, on-board reversible physisorption materials, and off-board regenerable hydrides) have issues related to H_2 quality that need to be addressed.[102] In most cases, the hydrogen storage materials are powders or powder compacts. These materials will inevitably entrain particulates into the hydrogen supplied to the energy conversion device. This is clearly not desirable and so means will need to be investigated and developed to either prevent particulate separation from the bulk storage material or to prevent particulates from leaving the hydrogen storage system. Particulate filters have been recommended in order to contain the cryo-adsorbent and on-board reversible metal hydride materials within the pressure vessel while meeting the SAE J2719 APR2008 H_2 purity guideline (particulate size: < 10 µm; particulate concentration: < 1 µg L^{-1}).[80] The standard test method ASTM D7650 standard has been identified for assessing the presence of particulates in hydrogen released by the storage systems.[80]

In addition to solid particulates, gas, vapor, or liquid impurities originating from the hydrogen storage materials may also be detrimental to the downstream equipment. An example of testing solutions for these problems was the effort by UTRC to characterize chemical and physical adsorbents for removing NH_3 from hydrogen that is released by the chemical hydride ammonia

borane (AB) and the metal hydride LAMH.[80] They found that most of the sorbents had a NH_3 dynamic sorption capacity of about 2 wt. %. They also found that there were trade-offs in capacity, regenerability, and cost of the various sorbents they tested. This is an area of research and in particular measurements that need further development and attention.

1.18 Segregation and Incomplete Reactions of Hydrogen Storage Materials

Wrapped up in mechanical and engineering properties in general are the issues of decomposition and segregation of the components of hydride-based storage materials. Some of these issues are thermodynamic in nature, but may be able to be controlled or overcome by good system design that prevents thermal spikes due to poor heat conduction. Intimately tied to thermal transport is the mechanical design and durability of the engineered hydrogen storage materials.

It is well known that if a ternary or intermetallic hydride of the form AB_zH_x is composed of elements in which one of the elements forms a very stable binary hydride AH_x, the intermetallic hydride is usually metastable and will tend to disproportionate into AH_x and additional B-enriched compounds or hydrides.[103,104,105,106,107] The disproportionation reaction requires the diffusion of metal atoms, so its impact is usually small around room temperature. When the ternary hydrides are cycled to elevated temperatures for desorption of gas, however, disproportionation can cause losses in reversible storage capacity and degrade the PCT curves.[106,107] This problem is particularly severe for hydrides of the $LaNi_5$ alloys. As shown in Figure 52, the partial substitution of some of the Ni by Sn greatly reduces the rate of degradation from disproportionation.[106]

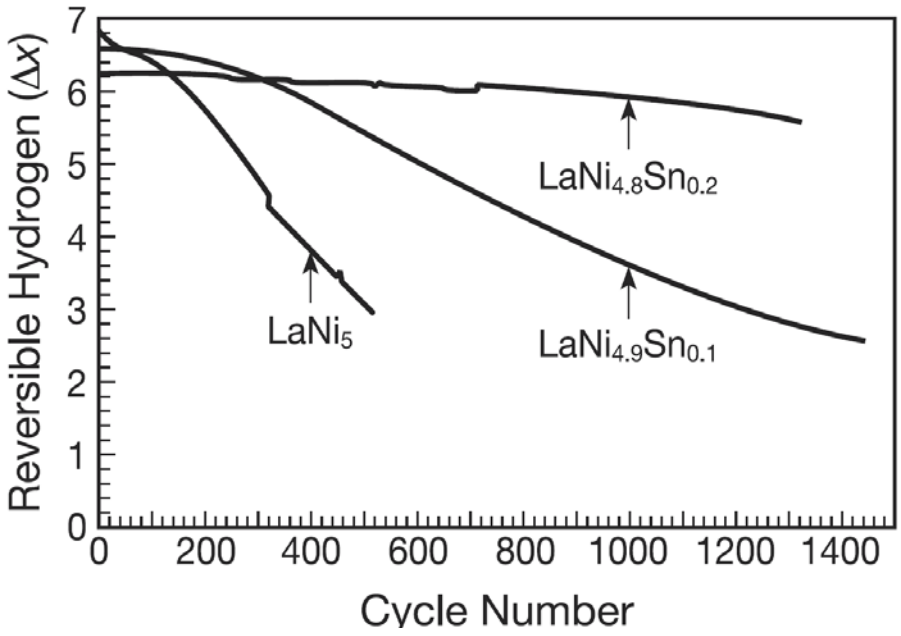

Figure 52. Effect of Sn substitution on the reversible hydrogen storage capacity of $LaNi_{5-X}Sn_X$ hydrides after cycling between 295 K and 510 K.[106]

Similar improvements have been found for Al, Ge, and Si substitution. Furthermore, degradation from disproportionation can usually be reversed by vacuum annealing at 600 K, since disproportionation does not involve the formation of irreversible phases such as oxides or carbides, which are common during contamination reactions.[104] There have also been a few studies on the behavior of the ABH_x and AB_2H_x systems during temperature cycling. Wanner et al.[107,108] have reported that $Ti_{0.98}Zr_{0.02}V_{0.43}Fe_{0.09}Mn_{1.5}H_{1.95}$ had only a 6% loss in capacity after 100 cycles between 318 K and 393 K, while Lee and Lee[109] found a 22% capacity loss from $Zr_{0.9}Ti_{0.1}Cr_{0.9}Fe1.1H_{3.2}$ after just 1200 cycles between 298 K and 593 K. Enhanced diffusion rates of the host metal atoms at increasing temperature will promote phase segregation and the disproportionation reaction.

Segregation of component phases impacts the performance of hydrogen storage materials based on decomposition-reformation reactions. One way to address this issue is the introduction of additives that improve performance. In one example, the effect of Li_3N additive on the Li-Mg-N-H system was examined with respect to the reversible dehydrogenation performance.[110] A screening study with varying Li_3N additions (5, 10, 20, and 30 mol %) demonstrated that all additions are effective for improving the hydrogen desorption capacity (Figure 53).

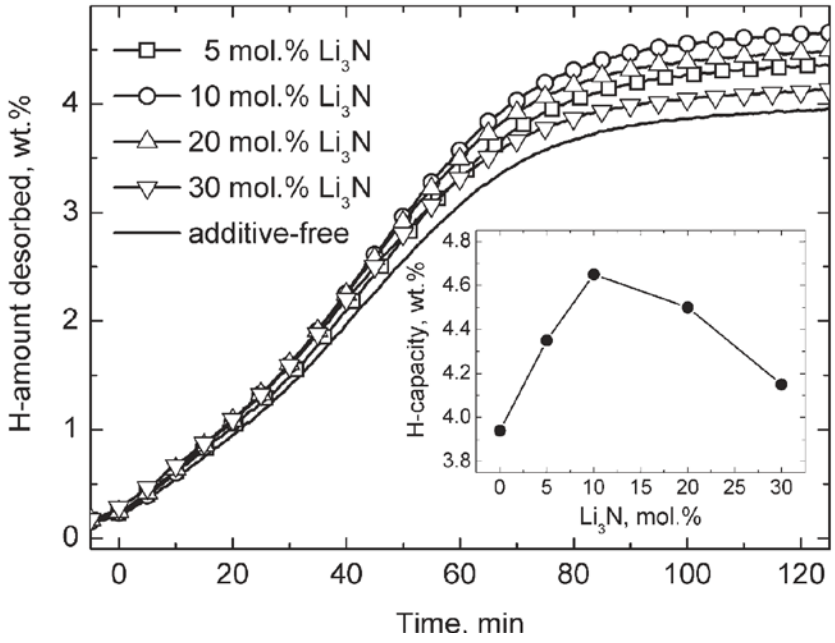

Figure 53. Effect of Li_3N additive on the hydrogen desorption performance of the Li-Mg-N-H sample at 0.1 MPa and 200 C in the 2nd cycle. The inset highlights the evolution of hydrogen capacity as a function of the Li_3N addition, with the deviation of 0.05 wt. % in capacity values.[110]

The incorporation of 10 mol % Li_3N was shown to increase the practical capacity of this system from 3.9 wt. % to approximately 4.7 wt. % hydrogen at 200 C, which drives the dehydrogenation reaction toward completion. Importantly, the capacity enhancement remained stable up to the 10 de-/rehydrogenation cycles that were tested (Figure 54).

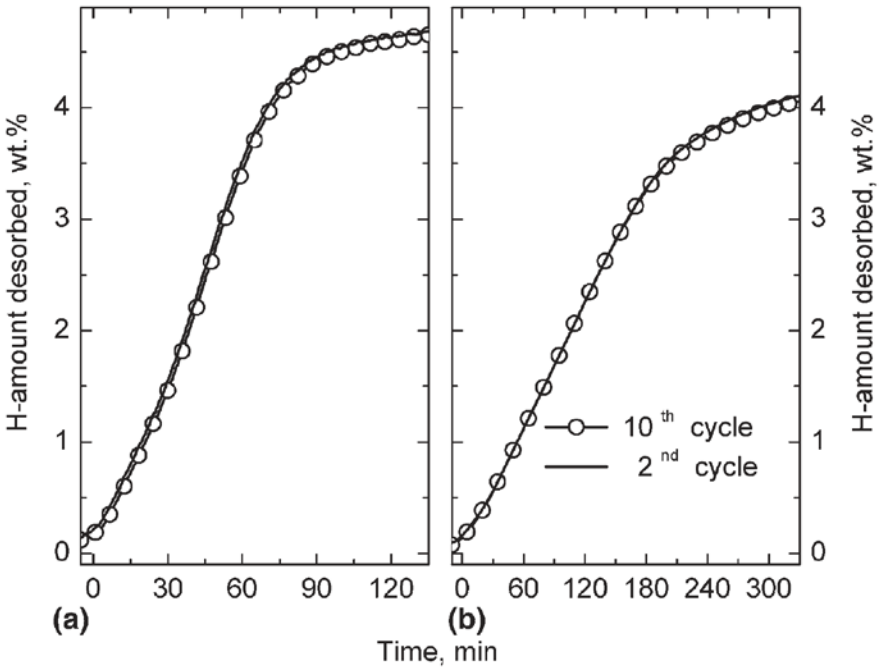

Figure 54. Hydrogen desorption performance of the 10 mol % Li_3N added Li-Mg-N-H sample under 0.1 MPa at desired temperatures in the 2nd and 10th cycles: (a) 200 °C and (b) 180 °C. Rehydrogenation was performed at 200 °C under 5 MPa hydrogen pressure.[110]

In that investigation, systematic X-ray diffraction was used to understand the reason for these improvements. XRD patterns showed that for the Li_3N-added samples, no diffraction peaks from Li_3N were present. However, characteristic diffraction peaks from $LiNH_2$ and LiH phases appeared. This indicated that Li_3N additive transforms into $LiNH_2$ and LiH phases and which remain during hydrogen cycling. The study's combined structure/property investigations suggested that $LiNH_2$ "seeding" is responsible for the capacity enhancement, which reduces the kinetic barrier associated with the nucleation of the intermediate $LiNH_2$. It was also concluded that the excess presence of LiH is effective for mitigating the ammonia release, which is another potential cause of capacity degradation with cycling in the amide materials.

1.19 Reversible Hydride Storage Systems

An example of simulation modeling and the need for mechanical properties data on reversible hydrogen storage systems is the work by Lozano et al. which examined a tubular tank configuration for hydrogen storage based on sodium alanates (Figure 55).[85]

A simulation model was used to optimize total system weight of the storage system. Their optimization criterion was: total mass of hydrogen has to be charged in a given time rather than prescribing percentages of the total hydrogen storage capacity. The effects of material compaction, addition of expanded graphite, and different tubular tank diameters were evaluated. For their model system, it was found that compaction of the material was the most influential factor for optimizing the storage system.

The system configuration they investigated was a shell and tube design, in which heat transfer fluid was flowing around the tubular tank for cooling/heating purposes and gaseous hydrogen dispersed to the hydride via a central filter tube.

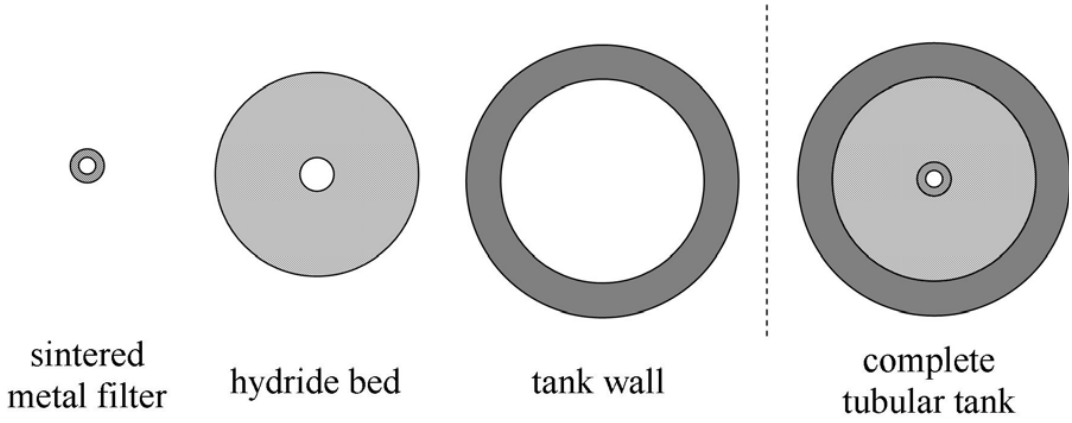

Figure 55. Cross-section of a tubular tank filled with sodium alanate material.[84]

Two material modifications were considered to improve the performance of the system. These were 1) compaction of the active material and 2) addition of expanded graphite (EG) to the active material for thermal conduction enhancement. Loose powder was compared with compacted material. The compacted material had the advantage of higher volumetric hydrogen density and higher thermal conductivity. However, it was found that the permeability decreases and the volumetric heat release on hydrogenation increases.

The absorption behavior of tubular tanks of different internal diameters was simulated for loose powder, compacts and compacts with addition of EG.[84] The conditions applied to the system simulations were:

1. Time to charge = 4.5 kg H_2 in 10 min

2. Total hydrogen capacity of the storage system = 5 kg H_2

3. Tank wall material is stainless-steel 1.4571

4. Pressure for absorption and tank wall thickness calculation is 100 bar

5. Temperature for absorption and tank wall thickness calculation is 250 °C

The total optimized system weight was calculated and plotted as a function of the tank internal diameter, Figure 56. For loose powder, the minimum total system weight was 640 kg for a tubular tank with an internal diameter of 35 mm. In the case of compacts, with and without EG addition, the minimum system weight was between 350 and 400 kg respectively.

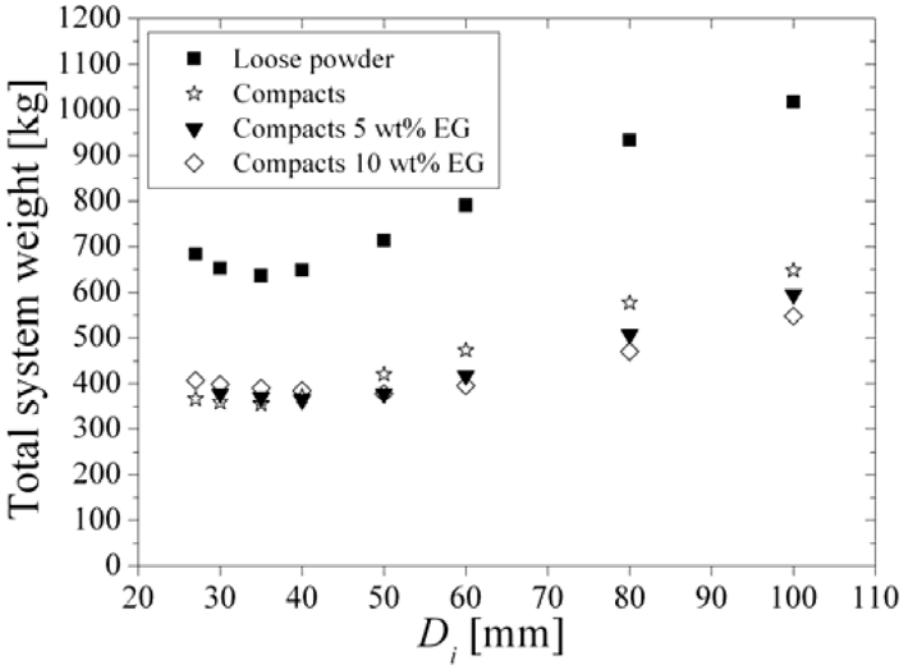

Figure 56. Calculated system weight of a tubular storage tank filled with sodium alanate material as a function of the internal diameter. The temperature of the heat transfer fluid and the initial temperature of the system was 110 °C. The heat transfer coefficient of the heat transfer fluid side was 500 W m^{-2} K^{-1}.[84]

Lozano et al. found that there were two contrary effects that explain the optimal diameters for the minimum total system weight as shown in Figure 56. First, as the internal tank diameter was increased, the ratio of mass of hydride bed to mass of tank wall increases, improving performance. Figure 57 shows the calculated ratio of the mass of hydride to the tank mass for loose and compacted materials as a function of the internal tank diameter. The ratio increases for internal diameters from 10 mm to 40 mm. For larger diameters the ratio tends asymptotically to a constant value. The opposing effect is that when the internal diameter was increased, the resistance to heat transfer and hydrogen transport also increases, lowering the performance of the system.

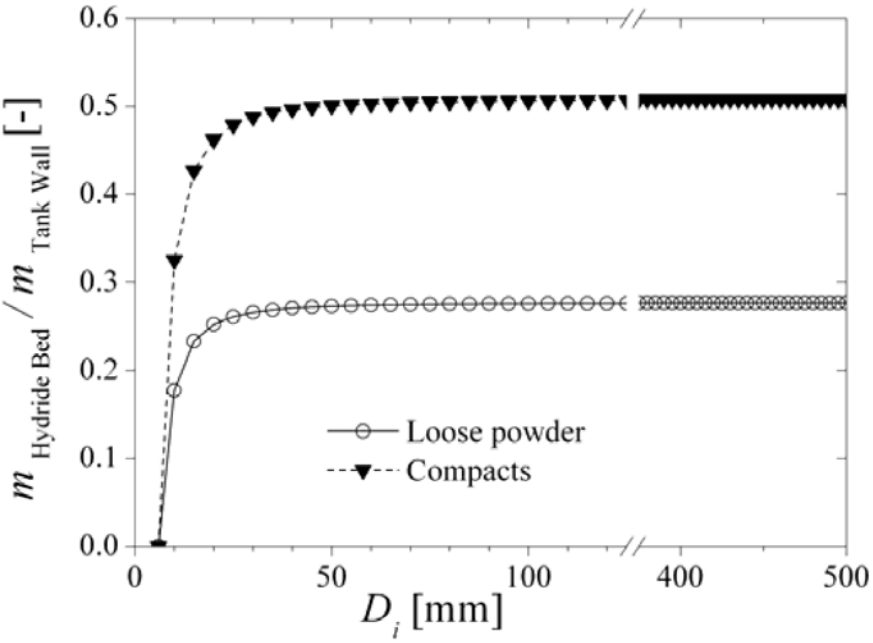

Figure 57. Ratio of mass of hydride bed to mass of tank wall as function of the internal diameter of the tubular tank. The ratio for compacts refers to materials with and without addition of EG.[84]

The simulations showed that proportional mass of the hydride to tank is significantly higher for compacted material than for loose material (Figure 57). Using the optimum tube diameters, the compaction of sodium alanate material was calculated to produce a total reduction of almost 45% of the weight of a tubular storage tank compared to loose powder.

It was expected that the enhanced thermal conductivity through the additional EG would lead to optimal diameters with less total system weight, since the heat transfer should be improved. However, these simulations showed that the additional EG in the compacted material did not achieve lower optimal system weights (Figure 56). Only at diameters > 40 mm was it observed that the weight of the system was the lower for compacted material with 5 or 10 wt. % EG. The author's explanation was that the addition of EG increases the inactive weight of the system. In addition, while enhanced heat transfer should allow larger vessel diameters, after a certain point increasing the diameter has little effect on the mass ratio of the hydride to the tank (Figure 57), at least not enough to compensate for the additional weight of the EG.

1.20 Physisorption Materials

Many physisorption hydrogen storage materials such as MOF-5 have intrinsically low thermal conductivities. This can limit the performance of adsorption-based hydrogen storage systems. One possibility to improve the thermal properties of these materials is to add thermal conductivity enhancers. However, these additives likely contribute very little to the adsorption capacity themselves and, thus, may reduce the overall mass and volume hydrogen storage capacity. This combined with the low bulk density of most physisorption materials points to the interest in investigating ways to increase the material density. An example of such work is the study by Purewal et al. that examined the hydrogen storage properties of a series of high density MOF-5 composites containing 0–10 wt. % expanded natural graphite (ENG), which served as a thermal conduction enhancer.[111]

The measurement of hydrogen capacity in physisorption materials provides the excess adsorption capacity as the direct output. However, it is the total storage capacity that is most relevant at an applications level. The total capacity includes both the excess hydrogen near the adsorbent surface plus the bulk hydrogen gas residing throughout the entire void volume (intracrystalline pores, intercrystalline voids, interstitial or interparticle spaces).

MOF-5 is commonly synthesized as a powder (crystallite size less than 1 μm) with low bulk density (0.13−0.2 g cm^{-3}). It is advantageous, therefore, to prepare pellets or extrudates from the powder to reduce the size or presence of pores, voids, and especially interparticle spaces, where the amount of higher density adsorbed hydrogen will be small.[112,113,114] Compacted pellets are more attractive than loose powders for on-board hydrogen storage applications due to the potentially larger volumetric storage density and the improved ease of handling. In a previous study Purewal et al. found that compaction of MOF-5 into pellets produced modest decreases in the gravimetric hydrogen storage capacity, offset by much larger increases in the volumetric capacity.[115] It has been shown that compaction decreases micropore volume due to amorphization of the MOF-5 crystal structure.[116] However, it was possible to reduce this effect by controlling the pellet density. Similar results for the compaction of MOF-177[117,118] and activated carbons[119] have also been reported.

In their paper Purewal et al. pointed out that presentation of the sorption results require clear definitions of different Adsorbent Density and Hydrogen Storage Capacity terms.[111] These are presented in detail in section 1.1. Using these definitions, Purewal et al. determined various material density and hydrogen storage capacity values for the MOF-5 samples they prepared and studied with the following results:

Skeletal density (ρ_{sk}): using helium pycnometer, a value of ρ_{sk} = 2.03 g cm^{-3} was determined.

Single-crystal density (ρ_{sc}): The theoretical MOF-5 crystallographic density is 0.605 g cm^{-3}.

Envelope density (ρ_{env}): The envelope density was used only for pellets, not for powder MOF-5 (for which the ρ bulk density is used instead). Envelope density was calculated from the physical dimensions of a single pellet.

Bulk density (ρ_{bulk}): The bulk density of powder MOF-5 depends on factors such as particle size, electrostatic interactions between particles, and the method of density measurement varying between 0.13 and 0.2 g cm^{-3}. In this case, the powdered MOF-5 bulk density was measured after the powder had settled following tapping or vibration. It was measured to be ρ_{bulk} = 0.13 g cm^{-3} using a calibrated volume and approximately 10 s of tapping.

The bulk density was used for powder MOF-5 and the envelope density was used to describe compacted MOF-5/ENG monoliths to provide a realistic estimate of the density of an actual sorbent bed.[111] The specific void volume for pellets was:

Equation 20 $$v_v(\text{pellet}) = 1/\rho_{env} - 1/\rho_{sk}$$

while for the MOF-5 powder it was defined as:

Equation 21 $$v_v(\text{powder}) = 1/\rho_{bulk} - 1/\rho_{sk}$$

The bulk system density of MOF-5/ENG pellets was based on the volume of a rigid storage tank occupied by a random packing of cylindrically shaped pellets. The packing ratio of mono-size solid spheres after settling is typically close to 60%, although the packing ratio for cylindrical pellets could be improved by stacking them in close-packed arrays.[120]

With respect to material hydrogen storage capacity, the absolute adsorption (n_a) is related to the excess adsorption (n_{ex}) by

Equation 22 $$n_a = n_{ex} + v_a\rho_g,$$

where v_a is the adsorbate volume and ρ_g is the bulk hydrogen gas density. In this current example it was assumed that v_a is constant with respect to adsorption amount and temperature and that $\rho_a = n_a/v_a$ equals an average adsorbate density. The magnitude of v_a should be close to the
MOF-5 intracrystalline open pore volume, $v_{pore} = 1/\rho_{sc} - 1/\rho_{sk}$ = 1.2 g cm^{-3}).

The Total Material Storage is given by

Equation 23 $$N_t = m_{sorbent}(n_{ex} + v_v\rho_g),$$

where $m_{sorbent}$ is the sorbent mass and the void volume has been defined for powders (Equation 21) and pellets (Equation 20). When presented as a fraction of total adsorbent volume (assuming a monolith), it has the form

Equation 24

$$n_{t,vol} = \rho_{env} n_{ex} + \left(1 - \frac{\rho_{env}}{\rho_{sk}}\right)\rho_g,$$

where ρ_{env} should be replaced with ρ_{bulk} for powder MOF-5. This total volumetric storage quantity is considered as a material property (as opposed to a system property). Although, it does depend on material post-processing such as mechanical compaction and composite formation.

The addition of 10 wt. % ENG to MOF-5 and compaction to 0.5 g cm^{-3} was found to increase the thermal conductivity relative to neat MOF-5 of the same density by a factor of 5.[121]

Purewal et al. performed detailed measurements of the hydrogen storage capacities of MOF-5/ENG compressed composites between 77 and 295 K.[111] The effect of varying ENG content and pellet density on the excess and total hydrogen storage properties of the MOF-5 composites was investigated systematically.

In this example, hydrogen adsorption was measured on a volumetric Sieverts-type instrument. The samples were outgassed for 3 hours at room temperature and 3 hours at 403 K under continuous vacuum prior to hydrogen measurement. The void volume of the sample holder was determined by helium expansion for each sample. To improve accuracy, a calibration test for each MOF-5/ENG sample was done using an equivalent displacement volume of nonporous Al_2O_3 powder and identical measurement settings. The maximum instrument error was about 0.3 mmol of hydrogen, compared to the 10 mmol of H_2 that was typically adsorbed by each sample.

The adsorption kinetics were rapid for the MOF-5 composites at all temperatures, even for the high density pellets (equilibrium was reached within 3 min).[111] Isotherms were measured for temperatures between 77 and 295 K with temperature stabilities within 1 K.

First, hydrogen adsorption isotherms at 77 K were measured for a complete set of ENG/MOF-5 composites (0– 10% ENG) for several densities. The measured samples were

- powder MOF-5 (ρ_{bulk}: 0.13 g cm^{-3})
- 0% ENG (ρ_{env}: 0.31, 0.41, 0.52, 0.60, 0.79 g cm^{-3})
- 1% ENG (ρ_{env}: 0.49 g cm^{-3})
- 5% ENG (ρ_{env}: 0.32, 0.47, 0.65 g cm^{-3})
- 10% ENG (ρ_{env}: 0.32, 0.48, 0.72 g cm^{-3})

The 77 K isotherms for all medium density (i.e., 0.5 g cm^{-3}) composites are shown in Figure 58. The plotted isotherms include both adsorption and desorption curves. Excess adsorption for the medium density composites are compared with powder MOF-5 in the top panel. In the lower panel, the total volumetric storage (calculated using Equation 24) is compared with the density of cryo-compressed H_2 at 77 K. Total hydrogen storage and at 100 bar, along with total usable stored hydrogen delivered at 5 bar, is also illustrated for the 0% ENG data at 77 K in the lower panel.

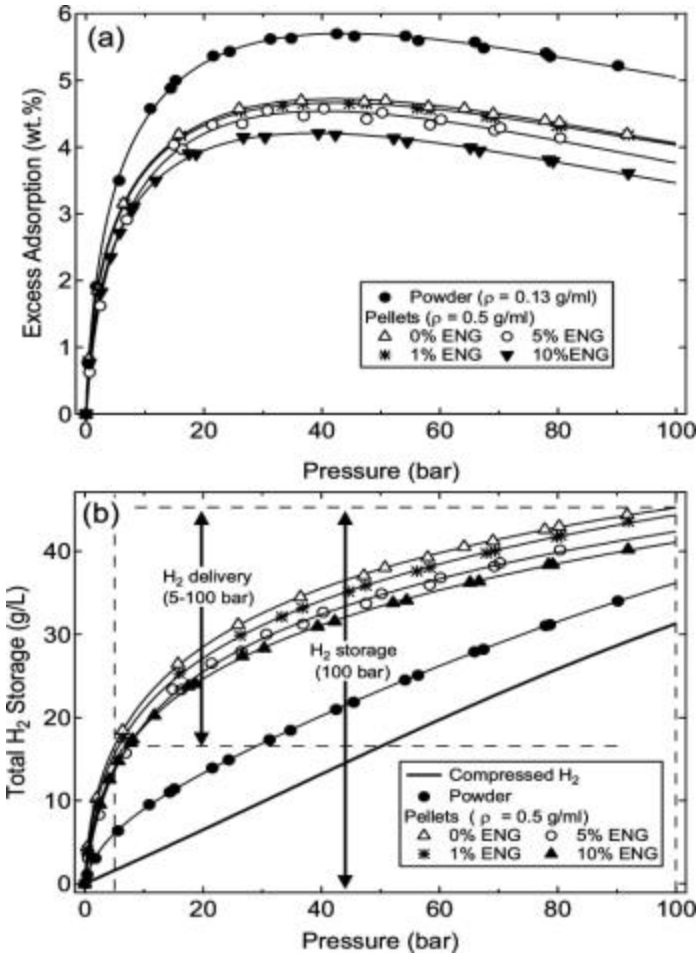

Figure 58. Hydrogen adsorption isotherms measured at 77 K for medium density (ρ_{env} ≈ 0.5) composite pellets. Powder MOF-5 data is included for comparison. (a) Excess adsorption isotherms, where the excess amounts are presented as a percentage of the combined hydrogen and sample mass. (b) Total volumetric hydrogen storage; cryo-compressed hydrogen is included for comparison. Hydrogen storage at 100 bar and delivery at 5 bar is illustrated for the 0% ENG data series.[111]

The volumetric total storage increases with sample density for the MOF-5 composites. Results of their 77 K measurements on the complete series of samples showed that for 0.5 g cm^{-3} density 0% ENG pellets, there is a 41% improvement compared to cryo-compressed hydrogen and a 23% improvement compared to powder MOF-5.[111] The addition of ENG produces only a small decrease for volumetric storage relative to neat MOF-5 media of equal density. For the composites with density 0.5 g cm^{-3}, the penalty for the addition of 10% ENG is a 6% decrease in total volumetric storage. For 0.7 g cm^{-3} composites, the "weight penalty" for 10% ENG addition is only a 3% decrease in storage.

Purewal and colleagues did an in-depth analysis to compare the fit of three different sorption models (Unilan, Tóth, Dubinin−Astakhov) with their data.[111] They found that the Unilan model was the most successful in matching the data, requiring only five temperature invariant parameters to accurately fit the data across a wide temperature range. The Unilan model (i.e., uniform energy distribution and Langmuir local isotherm) is an attractive empirical model for describing hydrogen adsorption in MOF-5. It uses the (monolayer) Langmuir equation to describe the local isotherms. This model treats energetic heterogeneity by assuming a uniform distribution of adsorption enthalpies between E_{max} and E_{min} and zero elsewhere.[122,123,124,125,126]

Following this they performed a series of hydrogen uptake measurements on the samples at several temperatures between 77 K and room temperature. The results of those measurements are shown in Figure 59. Hydrogen storage at 100 bar for selected MOF-5/ENG composites is plotted versus temperature (77−295 K) using the Unilan model.[111]

In panel (a) the relative contributions to total hydrogen storage at 100 bar made by excess adsorption, absolute adsorption, and free H_2 in the volume $v_g = v_v - v_a$ are presented. The sum of the absolute adsorption and free hydrogen equals the total storage. Panel (b) gives the same comparison for the 0% ENG pellets of density 0.52 g cm^{-3}. It can be seen that for a loosely packed powder, the majority of stored hydrogen is bulk hydrogen gas outside of the adsorbate volume. In contrast, for the compacted MOF-5 absolute adsorption makes up a much larger percentage of the total hydrogen storage with only a small fraction of the stored hydrogen consisting of free gas.

Figure 59c presents the volumetric absolute adsorption (n_a) at 100 bar for MOF-5/ENG composites plotted as a function of temperature. It can be seen that compacting powder MOF-5 to a density of 0.52 g cm^{-3} increases the absolute adsorption by a factor of approximately 3.

Figure 59d presents total volumetric hydrogen storage at 100 bar versus temperature. Values are also shown for single crystal and loose powder MOF-5. The single crystal data were derived from the powder data by using a density of ρ_{sc} = 0.605 g cm^{-3} versus the powder density of

ρ_{bulk} = 0.13 g cm^{-3}. The single crystal MOF-5 values represent an upper limit for volumetric hydrogen storage of compacted MOF-5. The 0% ENG sample at 0.52 g cm^{-3} gave the highest volumetric storage results.

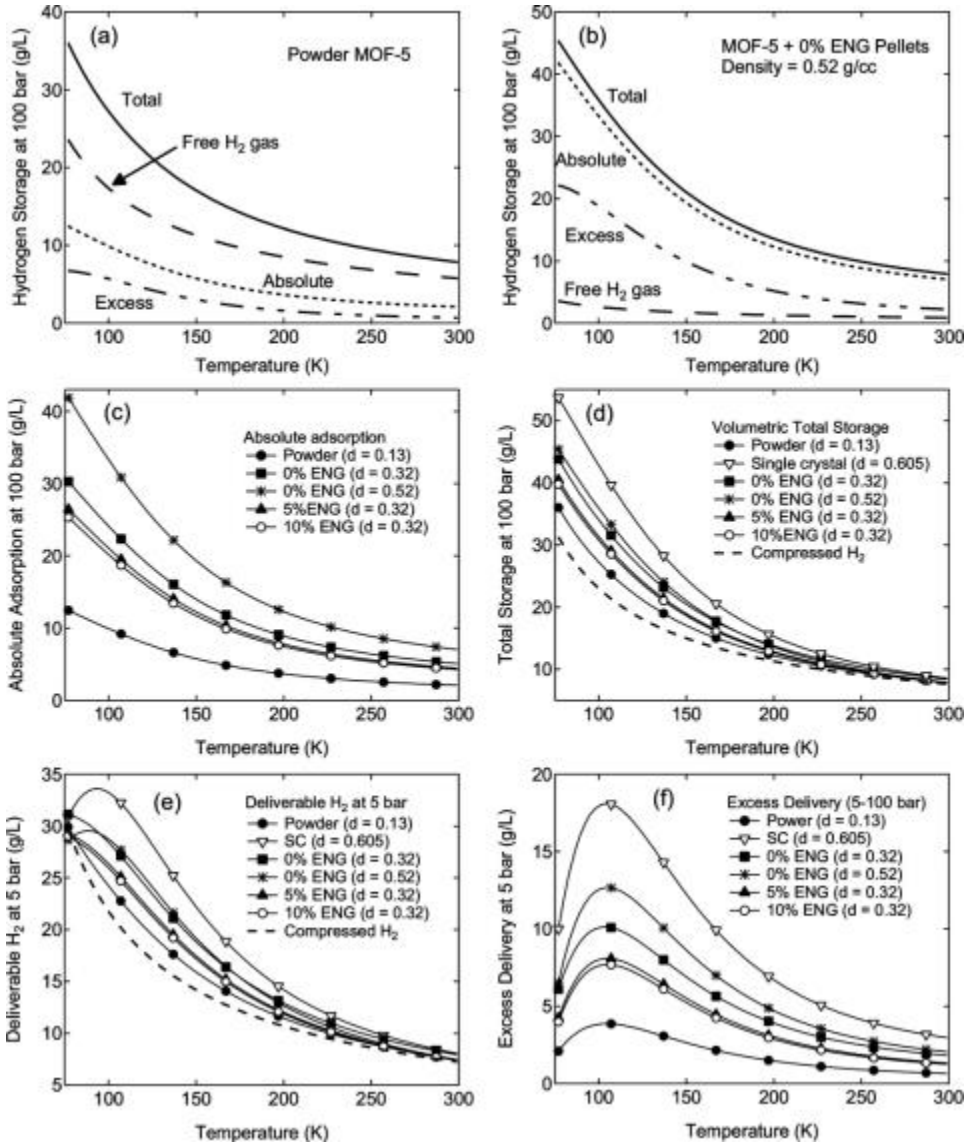

Figure 59. Total hydrogen storage at 100 bar versus temperature for selected MOF-5/ENG composites, using Unilan model parameters from Table 2b. (a) Hydrogen storage in powder MOF-5 at 100 bar; compares the relative contributions to total hydrogen storage made by excess adsorption, absolute adsorption, and bulk H_2. (b) Hydrogen storage at 100 bar in neat MOF-5 pellets with density 0.52 g cm^{-3}. (c) Absolute hydrogen adsorption at 100 bar, on a volumetric basis, for MOF-5/ENG composites. (d) Total hydrogen storage at 100 bar plotted versus temperature. (e) Total hydrogen delivery between 100 and 5 bar. (f) Excess hydrogen delivery, defined here as the difference in excess adsorption, between 100 and 5 bar.[111]

Figure 59e presents the total hydrogen delivery (isothermal) between 100 and 5 bar plotted as a function of temperature. Based on these measurements and analysis, cryo-compressed demonstrated more deliverable hydrogen at 77 K than most MOF-5/ENG composites (with the exception of 0% ENG 0.5 g cm^{-3} pellets and single-crystal MOF-5). However, above 77 K the MOF-5/ENG composites exceeded the deliverable hydrogen capacity of cryo-compressed hydrogen. The largest improvement occurred for the 0.52 g cm^{-3} pellets with 0% ENG at a temperature of approximately 122 K. The isothermal delivery being 24.7 g L^{-1} or about 23% and 41% greater than the respective values for powder MOF-5 and compressed H_2.

Based on the combined impact of ENG addition and pellet density on thermal conductivity and hydrogen storage capacity of MOF-5 media, Purewal et al. found that optimal properties were obtained for ENG additions of 5−10 wt. % and pellet densities near 0.5 g cm^{-3}. This clearly demonstrates the potential advantage that can be achieved through the use of additives and by the mechanical compression of physisorption hydrogen storage materials.

1.21 Off-board Hydride Storage Materials

The physical form and mechanical properties of off-board regenerable hydrogen storage materials is extremely important to the functioning of viable systems. In particular these properties are crucial in the mobility, transport, and transfer of these materials because the materials themselves are not stationary, but must be transferred in and out of the storage system.

There are many concepts that could be used to transport chemical hydrides like AB (Ammonia Borane) in their solid form on board a vehicle. In one example, a flexible screw feeder concept was selected for an experimental evaluation (Figure 60).[80]

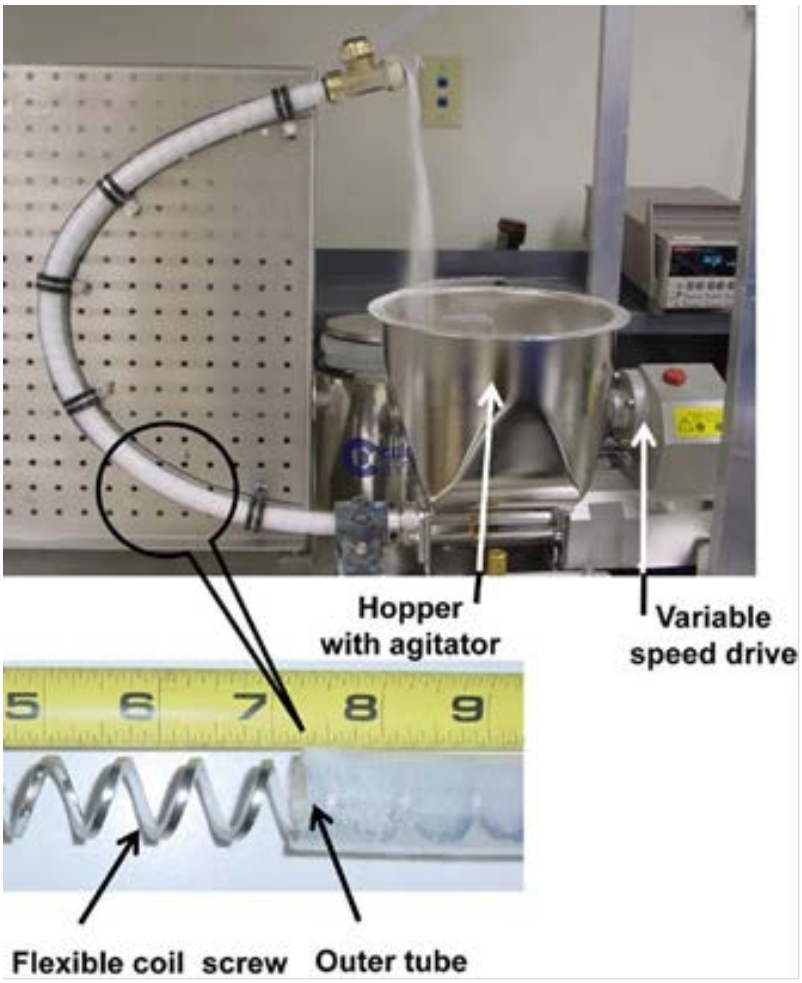

Figure 60. Solid Transport of a Surrogate Material with a Flexible Screw along a Complex Path.[80]

The test system for this study was built using standard off-the-shelf components. An extruder for plastics was outfitted for hydrogen generation, by insulation, insertion of multiple thermocouples, and placed in a plastic case under an inert atmosphere to prevent any hydrogen generated from reacting with oxygen in the atmosphere. Tests involved moving a simulated AB material through a complex path with several bends using a flexible screw mechanism. Measurements were performed to quantify solid transport rate as a function of the flexible screw pitch, rotational speed and bend angle. Hydrogen was successfully generated from the reactor with AB/MC as the chemical hydride simulant. However, the auger reactor consistently clogged. This solid transport method was rejected as a viable technology after practical problems were experienced with transporting AB powder through a heated zone by means of an auger.[80] This is another area of research and measurement of the mechanical properties of hydrogen storage materials that needs further development and attention.

The following ASTM Standards should be considered for doing measurements on the flow properties of off-board hydrogen storage powder materials:

ASTM D6128

This method covers the apparatus and procedures for measuring the cohesive strength of bulk solids during both continuous flow and after storage at rest. In addition, measurements of internal friction, bulk density, and wall friction on various wall surfaces are included.

ASTM D6773

This test method covers the apparatus and procedures for measuring the unconfined yield strength of bulk solids during both continuous flow and after storage at rest. In addition, measurements of internal friction, bulk density, and wall friction on various wall surfaces are included.

2 Mechanical Properties Measurement Methods

2.1 Density Measurements

Generally speaking, to measure density one must measure the mass and volume of a sample. Often, particularly for fine powders or highly porous materials, it is the accurate measurement of sample volume that is the most difficult. Volume measurement methods for skeletal, bulk, and tap density determinations are presented in detail in subsections 2.1.2 – 2.1.4 below.

With respect to the volume measurement, it is critical that one specify exactly what volume is being measured to provide the desired density (i.e. skeletal density, bulk or poured density, tapped density, compressed pellet density, etc.). Detailed definitions of the different types of volumes and densities are presented in section 1.1. This is particularly true for powder and porous materials, where clear definitions of density are critical.[25] In many cases the terminology can be confusing or overlapping. For this reason, the definitions of commonly utilized terms that are important for hydrogen storage materials development are presented below.

Because many volume and, thus, density measurements are dependent on the measurement method and conditions, as well as sample history or preparation, it is critical that published data be presented with a clear description of:

1) what type of data (e.g., bulk or poured density, tapped density, compressed pellet density) is being presented,

2) what equipment was used to measure it,

3) how the measurements were performed,

4) what under what conditions the measurements were made, and

5) how the sample was prepared or handled prior to measurement.

2.1.1 Mass Measurements

Mass is most often determined using standard high-accuracy analytical balances. Given the adsorptive and/or reactive nature of most hydrogen storage materials, it can be important that the material mass be measured in an inert or vacuum environment. This is easily done using a balance in an inert gas glove box or making measurements with a balance in a controlled atmosphere chamber such as a magnetic suspension balance or gravimetric instrument. For

hydrogen storage materials measurements it is critical (especially for physisorption materials) that the sample's mass be weighed in its pure form after all impurities and adsorbents are thoroughly removed via an appropriate bake-out procedure. This typically involves heating the sample under a moderate to high vacuum. The temperature used will depend on the stability of the material and types of impurities. The duration of a bake-out also depends on the material properties (pore size, surface area, etc.) and the type of impurities. Ideally, one would like to be able to monitor the outgassing of the sample with equipment such as a mass spectrometer. To avoid further adsorption of impurities certain materials should be weighed under an inert gas.

If sample buoyancy is a significant issue, the sample mass should be weighed under vacuum. For a simplistic example, a 1 g (not counting adsorption) sample of high surface area carbon with an idealized skeletal density of 2.62 g cm^{-3} will have a buoyancy effect of 0.7 mg when weighed in a 1 atm argon atmosphere (or 0.07 % difference between the mass weighed under argon or vacuum). This is on the order of the accuracy of many laboratory balances. Note that the gas displacement volume of the sample was considered in this simple example to be the skeletal volume of the sample, however, adsorption of the surrounding gas (argon) increases the effective volume of the sample increasing the buoyancy effect. In the case of high-surface-area materials, this increase in effective volume (and buoyancy) can be considerable.[127] Thus, this example error is at best a minimum value.

Remembering that hydrogen capacities are often expressed as ratios or percentages, this effect on measuring the mass of the sample may have little effect on the outcome. For example, if the same 1 gram sample adsorbs 10 mg H_2 per sample, then a change in the measurement of the initial sample's mass due to buoyancy would be: 0.01 / (1 - 0.0007 + 0.01) = 0.9908 wt. % H_2 [sample mass measured in argon] versus 0.01 / (1 + 0.01) = 0.9901 wt. % H_2 [sample mass measured in vacuum]. This buoyancy error will remain the same (percentage) as the sample size decreases, for example, if one is attempting measurements on very small samples (e.g. 100 mg). Note however, that this is referring to the measurements of the initial mass of the sample, not the buoyancy effect present when measuring hydrogen uptake with a balance in a hydrogen atmosphere, which can be a much larger effect. For instance, the same sample in 200 bar H_2 would have a buoyancy effect of an equivalent mass change of approximately 7 mg, which is on the order of the 1 wt. % H_2 assumed hydrogen capacity mentioned before and thus must be taken into account as a correction in the calculation of hydrogen uptake.

It is clear that the accuracy of a density measurement is subject to the accuracy of the sample mass measurement. Given that sample masses are often much less than 1 g and that hydrogen uptake is often less than 1 wt. %, it is important that the balance being used for density measurements have a precision and accuracy that is at least one order of magnitude and preferably two or three orders of magnitude better than this.

2.1.2 Skeletal Volume and Density by Gas Pycnometry

A key factor in making accurate density measurements is the accuracy and precision with which the sample's skeletal volume is measured. A gas pycnometer is also known as a constant volume gas pycnometer. A gas pycnometer operates by detecting a pressure change resulting from displacement of gas by a solid object. In its most simple form a gas pycnometer instrument consists of two chambers; one with a removable gas-tight lid to hold the sample and a second chamber (reservoir or reference) of a known (calibrated) volume. There will be a valve to admit input gas to the reference chamber, and a dosing valve to equalize the pressure between the two volumes. There may be only one pressure sensor on the reference volume or two independent pressure sensors, one on the reference volume and one on the sample holder volume. A simple form of the apparatus is shown in Figure 61. In practice the sample may occupy either chamber; that is, gas pycnometers can be constructed such that the sample chamber is pressurized first, or such that the reference chamber is filled with the higher pressure, or both cases. An analysis of various designs and parameters was done by Tamari.[128]

The typical two-step operation of a gas pycnometer is shown in Figure 61. An object of unknown volume V_S is sealed in the sample changer of known volume V_{SH}. In the first step (a) a pressure differential is created between the two volumes. This is often done by first evacuating (or providing a low pressure to) the sample holder volume, closing the dosing valve and then filling the reference volume with a higher pressure. The pressures are then measured in each volume and recorded after the gas has reached thermal equilibrium. In the second step (b) the valve between the two volumes is opened and after an appropriate period of time the gas will be in thermal and pressure equilibrium between the two volumes.

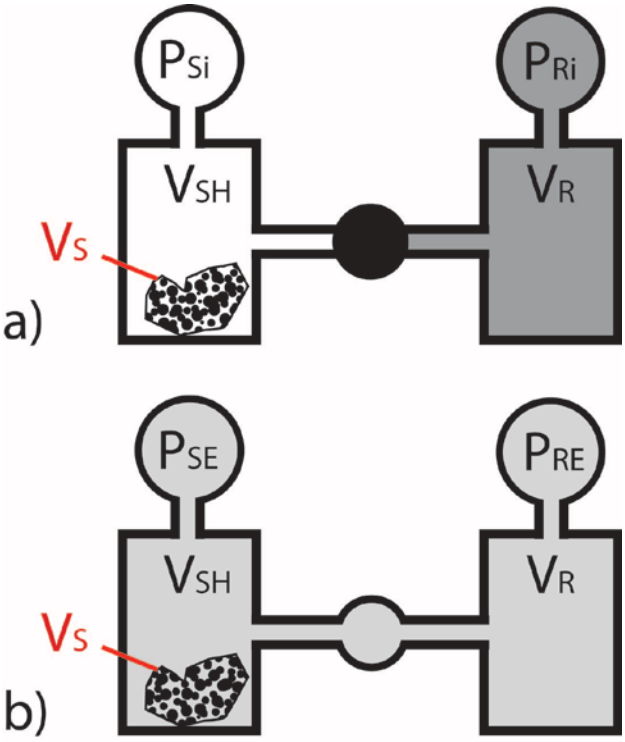

Figure 61. Schematic operation of a gas pycnometer.

In this simplistic example it is assumed that the system is maintained at a constant temperature *T* and there is no net loss or gain of gas (the number of gas molecules *n* is constant throughout the experiment). Under these conditions, the gas displacement volume of the sample is determined as follows. In the first step (or initial state) the sample holder has been evacuated or filled to a measurable low pressure and the calibrated reservoir is charged with gas at a higher pressure. In this initial state (Figure 61a) the gas balance equation is:

Equation 25 $$P_{Si}(V_{SH} - V_S) + P_{Ri}V_R = nRT,$$

where P_{Si} is the initial measured pressure in the sample holder, V_{SH} is the pre-calibrated volume of the sample holder, V_S is the gas displacement volume of the sample, P_{Ri} is the initial measured pressure in the reservoir, V_R is the pre-calibrated volume of the reservoir (or dosing volume), *n* is the total moles of the gas present, *R* is the gas constant, and *T* is the temperature of the gas (which is assumed to be the same everywhere). The equation assumes that the gas (helium) is, for all practical purposes, an ideal gas at the measured pressure and temperature, that the valve has no change in volume on going from the closed to the open state and that the sample has no appreciable gas adsorption.

When the valve is opened and the gas has had enough time to come into thermal equilibrium with its surroundings, the equilibrium pressure condition becomes:

Equation 26 $$P_{SE}(V_{SH} - V_S) + P_{RE}V_R = nRT,$$

where the total moles of gas is preserved. Equating the *nRT* terms, the two equations combine to give:

Equation 27 $$P_{SE}(V_{SH} - V_S) + P_{RE}V_R = P_{Si}(V_{SH} - V_S) + P_{Ri}V_R$$

Solving for the gas displacement volume of the sample (V_S) gives:

Equation 28 $$V_S = ((P_{SE} - P_{Si})V_{SH} + (P_{RE} - P_{Ri})V_R) / (P_{SE} - P_{Si})$$

One possibility for pycnometry measurements on hydrogen storage materials is that if the instrument being used to measure hydrogen uptake properties is a volumetric instrument, it may be capable of making sample volume measurements as well, using an inert gas. In this case, the volume of the empty sample holder V_{SH} must be accurately measured to be able to apply Equation 28. This can be done with any gas. Because the free gas volume of the sample holder with sample is needed for volumetric hydrogen sorption measurements, most instruments are already set up for making these volume measurements. It is simply a matter of measuring the empty sample holder volume first and then performing a pycnometry measurement on the sample of interest using the same sample holder. The volume measurement of the empty sample holder is given by:

Equation 29 $$V_{SH} = V_R(P_{Ri} - P_{RE})/(P_{SE} - P_{Si})$$

Gas pycnometers exist in a variety of configurations. This includes simple manual systems to highly sophisticated automated systems. They may have only one pressure transducer, or two or more, as well as multiple calibrated reference volumes. Sophisticated apparatus and software will have some or all of the following features:

- made of components compatable with the gases and samples to be used
- have active system temperature control
- make corrections for temperature variations
- reduce temperature gradients in the gas
- do not use valves or other components that will impact temperature stability

- take valve volume changes into account
- allow for proper degassing (bake-out) of samples
- have reference volumes appropriately matched to sample quantities
- are set up for use with different gases
- take account for the potential non-ideal behavior of the test gas
- have high-resolution pressure transducers with temperature compensation and automatic zeroing features
- allow for airless sample transfer and testing
- are designed for ease of handling powder samples

All of these features contribute in varying degrees to improved accuracy in the measurement of a sample's gas displacement volume. Note that the last point is critical for very fine powder samples that may be difficult to transfer (due to issues such as static electricity). To arrive at an accurate density measurement, both the volume and mass must be measured on the same sample without the loss, contamination, or physical changes to the sample. This can be very challenging with fluffy low density powders, especially those that are air reactive, contain impurities, or will adsorb significant amounts of water, oxygen, etc. For such materials, the instrument and procedures used should be able to address these issues. It is advisable to make trial runs with a control sample and worst case scenarios (such as very small sample quantities, lost material, air exposed samples) to have a measure of the degree to which these issues contribute to error in the density measurements.

Some other important considerations that can impact the accuracy and precision of the gas pycnometry measurements are: 1) the test gas should be of high purity to avoid contaminating the sample and affecting both mass and volume measurements, 2) the sample must be free of any volatile substances that can contribute partial pressures causing error, and 3) temperature gradients, instabilities, or errors in temperature measurement should be reduced to a minimum. Samples, particularly high surface area materials, should be outgassed by heating under vacuum at an appropriate temperature for time long enough to ensure that most, if not all, impurities have been removed.

Typically helium is used for pycnometry because it is non-reactive and a small enough molecule to be able to access small pores in the material. Other gases may be used specifically because of the way the gas adsorbs to the surface or because of the difference in the size of the gas molecule. Doing measurements with different gases having different size molecules may provide information about the different pore sizes of a material.[129]

Another consideration for some materials is that helium may adsorb to the surface in significant enough quantities as to cause errors in the skeletal volume measurement. While this is typically assumed to not be the case at near ambient conditions, it should not be overlooked, and becomes worse at low temperatures and high pressures. Sircar[130,131,132] and others[26,133,134] have addressed this issue extensively. More information on the subject of important considerations in the measurement of gas displacement volume can be found in Sections 5.3 and 5.11 of the document "Recommended Best Practices for the Characterization of Storage Properties of Hydrogen Storage Materials".[24]

2.1.3 Bulk density measurement

The bulk density of a powder is determined by measuring the volume of a known weight of powder sample, that may have been passed through a sieve, into a graduated cylinder (Method I)[135], or by measuring the mass of a known volume of powder that has been passed through a volumeter into a cup (Method II) or a measuring vessel (Method III). These methods are described well in the United States Pharmacopeial Convention 616.[136] Method I is commonly used and consists of passing a quantity of material sufficient to complete the test through a sieve, to break up agglomerates into a dry graduated 250 mL cylinder. This must be done gently to avoid changing the nature of the material and without compacting. The sample is then carefully leveled without compacting the powder. The apparent volume is measured to the nearest graduated unit. The bulk density is calculated by dividing the mass of the powder in the graduated cylinder by the measured bulk volume.

2.1.4 Tap density measurement

The tap density is the bulk density that has been increased after mechanically tapping a container holding a powder sample. Tap density is measured by mechanically tapping a graduated cylinder or vessel containing the sample and measuring the volume after each series of taps until there is no further change in volume. The mechanical tapping is achieved by raising the cylinder or vessel and allowing it to drop under its own weight a specified distance. Devices that rotate the cylinder or vessel during tapping may be preferred to minimize any possible separation of the mass during tapping down. Three different methods for performing Tap Density measurements are presented in the United States Pharmacopeial Convention 616.[136] The ASTM standard test method for the determination of Tap Density of metallic powders and compounds is ASTM B527-06.[137] A schematic diagram representing a typical Tap Density measurement instrument is shown below.

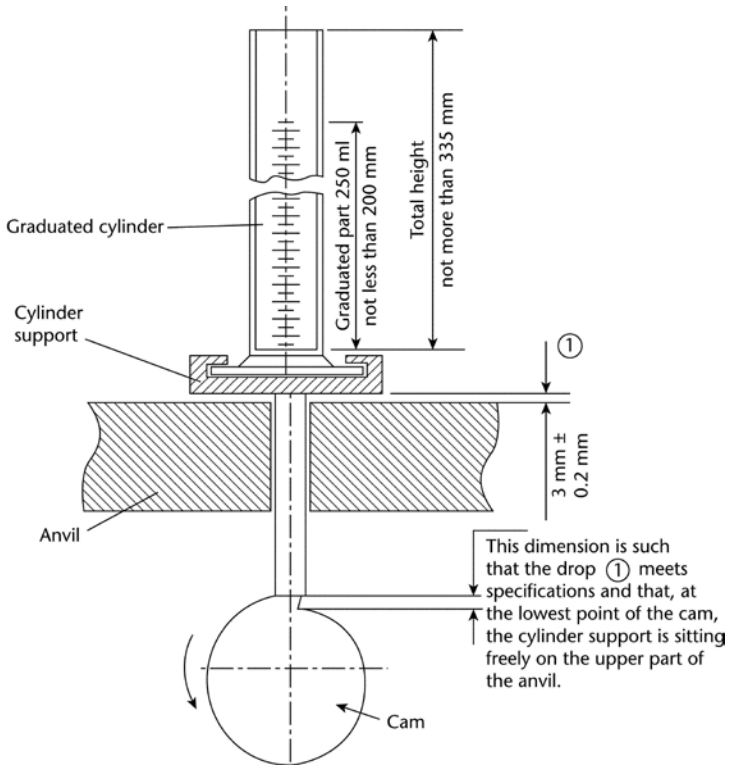

Figure 62. Schematic diagram of a Tap Density measurement instrument.[136]

2.2 Particle Size Measurements

Particle sizing methods can be separated into three basic classes:

- Ensemble Methods: all particles in a sample are measured at the same time. Size distribution data is "extracted" from a combined signal for all particles.
- Counting Methods: individual particles are measured and counts of similar size particles are places into "size bins" to construct a distribution.
- Separation Methods: an outside force/process is used to separate particles according to size. The quantities of the separated different sizes are determined.

A variety of instruments can be used for the analysis of dry powders and powders dispersed in suspension. A good review of the methods and protocols for particle size measurements of powders can be found in the NIST best practices guide on the subject, as well as the ASTM "Standard Guide for Powder Particle Size Analysis".[138] Whenever possible, it is desirable to analyze powders dispersed in a state similar to that in which they will be used. For this reason, and because powder materials for hydrogen storage are often reactive with liquids, it is

generally recommended to use dry measurement techniques. In the choice of methods, one should consider that some techniques allow measurements on materials having a very broad size range while others enable analysis over a fairly narrow size distribution.

2.2.1 Considerations in Particle Size Analysis

Particle size analysis can be very challenging due to a number of factors including spacial distribution, particle shape, porosity, etc. No less challenging is the practice of assigning a single number (diameter) to a particle that is 3-dimensional and very unlikely to be a perfect sphere.

Particle Diameter:

The term "particle diameter" should be used with caution to represent a quantitative measure of particle size. While diameter is an exact descriptor for the size of a sphere, real powders are generally composed of irregular shapes that can vary significantly from that of a sphere.

The determination of a particle size should be conducted using a technique that gives results relevant to the property of the powder that is critical for the material's application. For example, powders used in chemical reactions should be characterized by their surface area. Because diameter represents a three-dimensional property of a particle its use is most valid for applications that are influenced by some volume-based properties (density, surface area, etc.).

The following are some commonly used Volume-based diameters:[139,140]

Drag diameter (d_d): Diameter of a sphere that has the same resistance to motion in the same fluid (having same viscosity), moving at the same velocity as the particle

Free-falling diameter (d_f): Diameter of a sphere having the same density and the same free-falling speed as the particle in the same fluid

Surface diameter (d_s): Diameter of a sphere having the same surface area as the particle

Surface volume diameter (d_{sv}): Diameter of a sphere having the same surface to volume ratio as the particle

Stokes' diameter (d_{St}): Diameter of a free falling sphere (i.e., particle having attained the Stokes velocity) in the laminar flow region

Sieve diameter (d_A): Diameter of a sphere equivalent to the size of the minimum square aperture through which the particle will pass

Volume diameter (d_v): Diameter of a sphere having the same volume as the particle

Equivalent circle diameters are often used when powders are being examined using methods that provide only the projected profile of particles, such as for optical or electron microscopy-based techniques. Again these expressions are valid for spherical particles, however, the irregular shaped particles can produce inaccurate resluts if adequate precautions are not taken. In particular, the orientation of the irregular particle at rest and the resulting projected image can significantly influence the calculated diameter. The following are some commonly used Circular Diameter definitions:[139,140]

Projected area diameter (d_a): Diameter of a circle having the same area as the projected area of the particle at rest in a stable position

Projected area diameter (d_p): Diameter of a circle having the same area as the projected area of the particle at rest in a random orientation

Perimeter diameter (d_c): Diameter of a circle having the same perimeter as the projected area of the particle, irrespective of the particle orientation

Equivalent sphere:

If one is able to determine some other unique one-number parameter such as mass or volume of a particle, this number can be converted into an equivalent spherical particle with the same mass or volume, etc. This equivalent sphere then provides a unique one-dimensional number (diameter) to represent the size of the particle. Of course, this has its issues, because particles of very different shapes can have the same equivalent volume, and the experimental method used to measure size may be more or less affected by shape. For example, for particles with a large aspect ratio, the equivalent sphere diameter will be quite different if measured by sieve analysis, sedimentation rate, laser diffraction, or microscopy. With microscopy for instance, the results will vary considerably depending on whether one chooses to measure maximum length, minimum length, area, or some other metric for the “size” of the particle. The table below shows how cylindrical particles of the same diameter can have very different equivalent-volume spherical diameters by a factor of about 6 and extremely different aspect ratios by a factor of 200. Because different methods will be affected in different ways by the aspect ratio, the results could be significanly different. For instance, taking a sample consisting of the same number of each length of particles in the table, the results of a counting technique based on minimum diameter microscopy would count all of the particles as being the same size. Whereas, a seiving or sedimentation rate technique would likely find very different sizes depending strongly on the aspect ratio.

Size of cylinder		*Aspect Ratio*	*Equivalent Spherical Diameter*
Height	***Diameter***		
2	**20**	**0.1:1**	**10.6**
10	**20**	**0.5:1**	**18.2**
20	**20**	**1:1**	**22.9**
100	**20**	**5:1**	**39.1**
400	**20**	**20:1**	**62.1**

So, while it is convenient to describe particles by a spherical equivalent, the actual shape of particles can have a strong impact on the materials mechanical properties. One common method to express the average shape of particles is Wadell's sphericity (Ψ):

Equation 30 $$\Psi = \frac{\boldsymbol{Surface\ Area\ of\ the\ Equivalent\ Spherical\ Volume}}{\boldsymbol{Surface\ Area\ of\ the\ Particl}} = \frac{\pi^{\frac{1}{3}}(6V_P)^{\frac{2}{3}}}{A_P}$$

Where V_P is volume of the particle and A_P is the surface area of the particle. The sphericity of a sphere is 1 and, by the isoperimetric inequality, any particle which is not a sphere will have sphericity less than 1. The following are Wadell's sphericity (Ψ) for common particle shapes:

Shape	*Wadell's sphericity (Ψ)*
Sphere	**1.00**
Rounded particle	**0.82**
Cubic	**0.81**
Angular	**0.66**
Flaky	**0.54**
Platelet	**0.22**

Particle Size Distribution:

Once an equivalent particle size distribution of a sample has been measured, one typically presents some statistical description of the size distribution. Once again, it is important to present as many details of the measurement process and resulting distribution as possible, because simple numbers such as the mean or median values can be misleading.

Mean diameter, median diameter and modal diameter are often used to describe a distribution of particle sizes in a powder sample:

Mean Diameter: The mean diameter of a powder can be expressed according to the measured characteristics. For example, by the number, length, surface volume and weight of the particles.

The arithmetic mean is calculated by dividing the sum of the diameters of all the individual particles in the distribution, by the total number of particles in the distribution. The geometric mean is calculated by calculating the n^{th} root of the products of the diameters of the n particles constituting the system under study.

Median Diameter: The median diameter is the diameter at which half of all the particles have a larger diameter and the remaining half have smaller diameters. Thus, the median diameter is the 50% size of a cumulative distribution curve of the particle sizes.

Modal Diameter: The modal diameter is the most frequently occurring diameter of the particles in the sample being measured. It is represented by the peak of the differential size distribution curve.

For a Normal (or Gaussian) distribution, the mean, median, and modal diameters are all equivalent (see Figure 63).

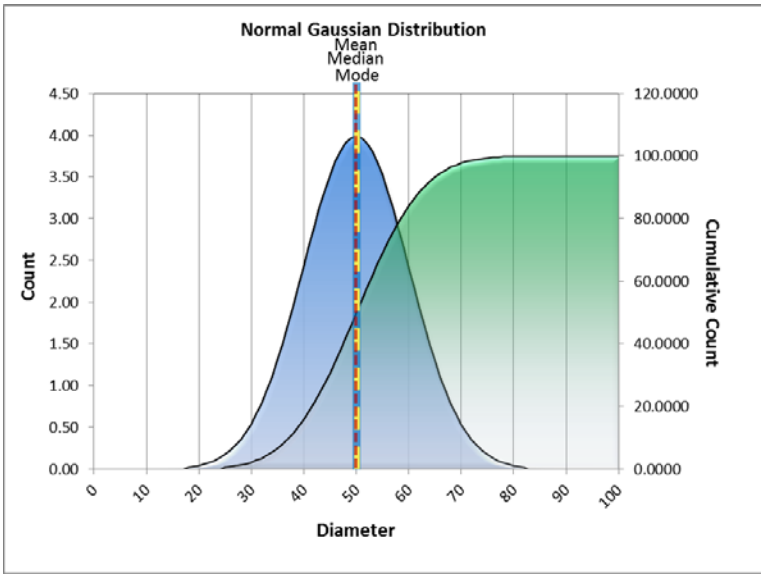

Figure 63. Example of a distribution of particle diameters with a perfect Normal or Gaussian) distribution, blue = count, green = cumulative.

However, it is not uncommon for real powder samples to have particle size distributions which are somewhat, or even significantly different that a Gaussian. In the example of Figure 64, two different distributions are shown which have the same median values, but a significantly different shape and, thus, very different modes and means.

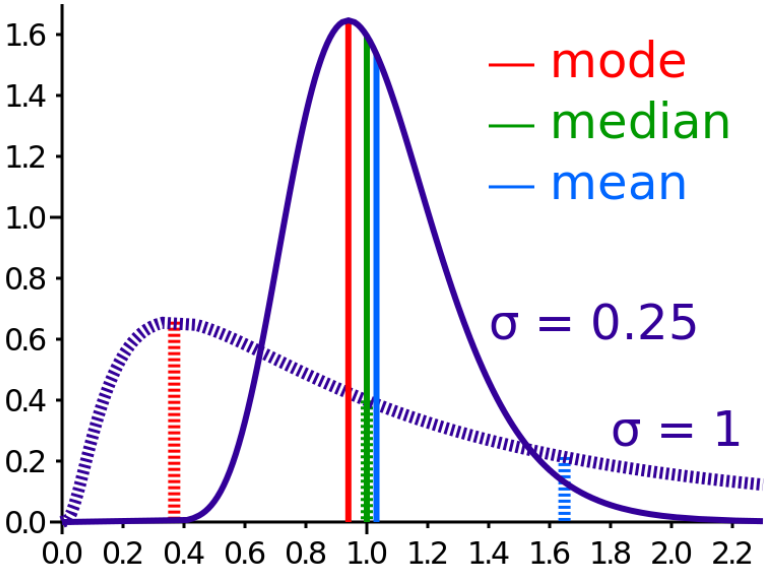

Figure 64. Comparison of mean, median and mode of two log-normal distributions with different skewness.[141]

Figure 65 presents an extreme, but not necessarily uncommon case of a bimodal distribution in which the sample contains few or no particles with a diameter represented by the mean and median and the modal diameter is poorly representative of the bulk of the particles.

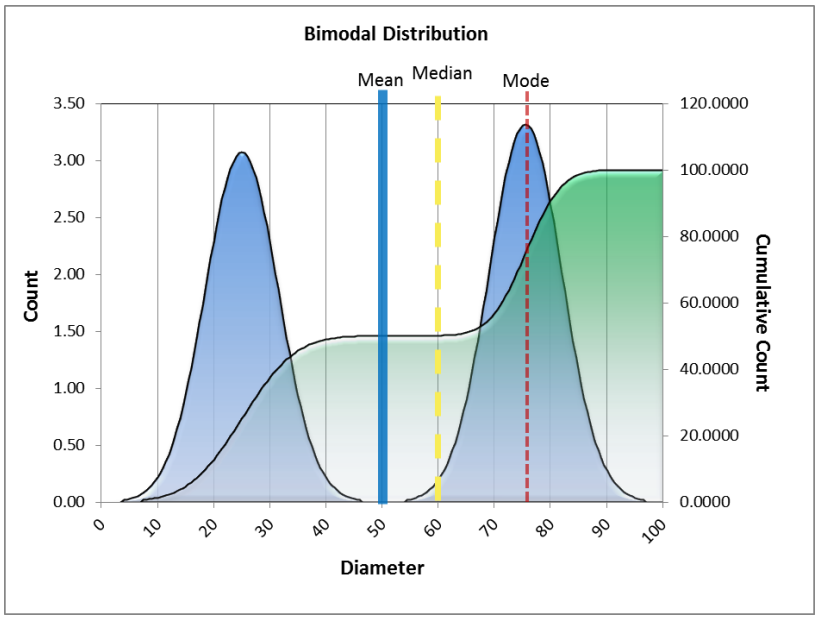

Figure 65. Example of a bi-modal distribution of particle diameters (2 Gaussians), blue = count, green = cumulative.

As these examples point out, using a single number to try to describe the particle size properties of a material can be very misleading. It is highly recommended that the particle size distribution measurements be shown along with as many details as possible about how the sample was collected and prepared, the measurements were made, and the results were analyzed.

Equally important as obtaining accurate particle size information is how that information is reported. There are common standards that are often used in reporting particle size data. The ASTM E1617-97 (2007), Standard Practice for Reporting Particle Size Characterization Data covers the means for reporting particle size measurement data. The ISO standard, ISO 9276-1 through 6, describes the Representation of Results of Particle Size Analysis.

The following is an extended list of ASTM Standards for Particle Size measurements and reporting.

ASTM Standards for Particle Size Measurement of Powders	
B330-12	Standard Test Method for Fisher Number of Metal Powders and Related Compounds
B761-06(2011)	Standard Test Method for Particle Size Distribution of Metal Powders and Related Compounds by X-Ray Monitoring of Gravity Sedimentation
B822-10	Standard Test Method for Particle Size Distribution of Metal Powders and Related Compounds by Light Scattering
C110-11	Standard Test Methods for Physical Testing of Quicklime, Hydrated Lime and Limestone
C690-09	Standard Test Method for Particle Size Distribution of Alumina or Quartz Powders by Electrical Sensing Zone Technique
C958-92(2007)	Standard Test Method for Particle Size of Alumina or Quartz by X-Ray Monitoring of Gravity Sedimentation
C1070-01(2007)	Standard Test Method for Determining Particle Size Distribution of Alumina or Quartz by Laser Light Scattering
D4438-85(2007)	Standard Test Method for Particle Size Distribution of Catalytic Material by Electronic Counting
D4464-10	Standard Test Method for Particle Size of Catalytic Materials by Laser Light Scattering
D5861-07	Standard Guide for Significance of Particle Size Measurements of Coating Powders
E2490-09	Standard Guide for Measurement of Particle Size Distribution of Nanomaterials in Suspension by Photon Correlation Spectroscopy (PCS)
F577-03(2009)	Standard Test Method for Particle Size Measurement of Dry Toners
F2149-01(2007)	Standard Test Method for Automated Analysis of Cells – the Electrical

	Sensing Zone Method of Enumerating and Sizing Single Cell Suspensions
ISO 22412:2008	Particle size analysis -- Dynamic light scattering (DLS)
ISO 13320:2009	Particle size analysis -- Laser diffraction methods
ISO 13317-1:2001	Determination of particle size distribution by gravitational liquid sedimentation methods -- Part 1: General principles and guidelines
ISO 20998-1:2006	Measurement and characterization of particles by acoustic methods -- Part 1: Concepts and procedures in ultrasonic attenuation spectroscopy
ISO 13322-1:2004	Particle size analysis -- Image analysis methods -- Part 1: Static image analysis methods
ISO 13317-1:2001	Determination of particle size distribution by gravitational liquid sedimentation methods -- Part 1: General principles and guidelines
ISO 9276-1:1998	Representation of results of particle size analysis -- Part 1: Graphical representation
ISO 9276-5:2005	Representation of results of particle size analysis -- Part 5: Methods of calculation relating to particle size analyses using logarithmic normal probability distribution
ISO 9276-1:1998	Representation of results of particle size analysis -- Part 1: Graphical representation
ISO 9276-2:1998	Representation of Results of Particle Size Analysis -- Part 2: Calculation of average particle sizes/diameters and moments from particle size distributions
ISO 9276-3:1998	Representation of Results of Particle Size Analysis -- Part 3: Calculation of means and moments of particle size distributions
ISO 9276-4:1998	Representation of Results of Particle Size Analysis -- Part 4: Characterization of a classification process
ISO 9276-5:1998	Representation of Results of Particle Size Analysis -- Part 5: Validation of calculations relating to particle size analyses using the logarithmic normal probability distribution
ASTM E1617-97	Standard Practice for Reporting Particle Size Characterization Data

Table 6. Chart of ASTM and ISO Standards for Particle Size Measurements and Reporting of powders.

2.2.2 Methods for Measuring Particle Size

Table 7 illustrates some of techniques for particle size analysis, the physical principle on which the technique is based, and the general sample concentration and size range over which these techniques are applicable.

Some important considerations before selecting an instrument for particle size and size distribution analysis include, but are not limited to: (1) the amount of sample available, (2) the desired number of points on the size distribution (for data interpretation and/or resolution), and (3) number and frequency of analyses required (ie. laboratory versus on-line methods).

Method	Physical principle	medium	Sample (g)	Size (μm)	Time*	Measured Equivalent Spherical Diameter	Volume Fraction range (%)
Microscopy: Optical	Particle counting	Liquid/gas	<1	400-0.5	S-L	Projected Area	NA
Microscopy: Electron		Vacuum	<0.1	400-0.001	S-L	Feret	
Sieving: air	sieving	air	50	8000-37	M	Sieve	NA
Sieving: liquid	sieving	liquid	5-20	5000-5	L		NA
Sedimentation: Gravity	sedimentation	liquid	<5	100-0.5	M-L	Mass	
Sedimentation: Centrifuge (Optical)	sedimentation	liquid	0.01-2	300-0.02	M	Projected Areas	
Sedimentation: centrifuge (X-Ray)	sedimentation			0.01-100			Instrumental Dependent
Sedimentation: Analytical Ultra C.	sedimentation		<0.1	0.001…	M-L	Hydrodynamic	
Light Scattering: Diffraction		Liquid/gas	<0.1-2	3000-0.05	S	Volume	
Light Scattering: Dynamic (Quasi-Elastic)		liquid	<0.1	0.5 (1)-0.002 or 0.003-6 according to NIST	S	Hydrodynamic	<0.005
Light Scattering: Tracking		liquid	<0.1	>20nm			
Elect. Sensing Zone (Optical)		liquid	<1	(1200) 250-0.4	S-M	Volume	
Elect. Sensing Zone (Particle Counting, Coulter Counter)	Particle counting			0.4-1200			>0.1
Gas Adsorption	Surface area	Gas/vacuum	<5	5-0.005	L	Surface-Volume	NA

dBET	analysis						
Acoustic Attenuation Spectroscopy (Ultrasonic)	ultrasonic			0.05-10			>1
Electroacoustic Spectroscopy	ultrasonics			0.1-10			>1
Laser Light Diffraction	Electromagnetic wave interaction and scattering			0.04-1000			0.01-5
Colloid Vibration Current	ultrasonic			<10			>1
Electronic Sonic Amplitude	ultrasonics			<10			>1
Micro-electrophoresis	Electromagnetic wave interaction and scattering			5-100,000			NA

*Analysis times; S-short, less than 20 min., M=moderate (20-60min), L=long, more than 60 minutes

Table 7. Chart of Particle Size Measurement Methods and Sample Properties.[142]

2.2.3 Selecting a particle size technique

General particle size distribution is sufficient information for the majority of particle characterization applications. But some techniques are higher resolution than others. Laser diffraction and dynamic light scattering are powerful techniques that are “resolution limited” compared to high resolution techniques which are based on particle counting (such as electro zone counting or image analysis). For this reason, if the goal of the measurement is finding small populations of particles larger or smaller than the main distribution, then an investigation of the sensitivity to second distributions should be part of the selection process.

Another important consideration may be a broad analysis of the shape of particles in a material. Particle shape influences bulk properties of powders including flow and compaction behavior, which may be important in powder-filled hydrogen storage beds, or compacts of storage materials. In the case of off-board storage materials that will be loaded, removed, or utilized in a fluid suspension, particle shape can have a significant influence on the viscosity of the suspensions. Microscopy and image analysis are the only techniques that provide an accurate ability to collect and evaluate particle shape information. Manual microscopy provides basic qualitative size and shape information, but automated image analysis generates quantitative data that is statistically significant. For this reason, both dynamic and static image analysis are growing techniques replacing manual microscopy.

Hydrogen storage materials that cannot be suspended in a liquid will limit the use of certain Laser Diffraction methods and preclude Dynamic Light Scattering, Electroresistance, Acoustic Spectroscopy, and Sedimentation techniques. Hydrogen storage materials that are air sensitive may further exclude the use of Laser Diffraction and Air Elutriation methods.

Sieve analysis

Sieve analysis is often employed because of its simplicity, low cost, and ease of interpretation. Methods may be simple shaking of the sample in sieves until the amount retained becomes more or less constant. Alternatively, the sample may be washed through with a non-reacting liquid (usually water) or blown through with an air current.

Advantages: This technique is well-adapted for bulk materials.

Disadvantages: Many applications are concerned with particles too small for sieving to be practical. A very fine sieve, such as 37 μm, is exceedingly fragile, and it is very difficult to get material to pass through. Another disadvantage is that the amount of energy used to sieve the sample is generally arbitrarily determined. Over-energetic sieving can cause attrition of the particles and thus changes the results. On the other hand, insufficient energy fails to break down loose agglomerates. Although manual sieving procedures may not be practical for many applications, automated sieving technologies using image fragmentation analysis software are available. These technologies can sieve material by capturing and analyzing a photo of material.

Air Elutriation analysis

Powders may be separated by means of an elutriator, which consists of a vertical tube up which fluid is passed at a controlled velocity. Sample particles are introduced into the vertical tube, often through a side tube. Smaller particles are carried up with the fluid stream while the larger particles settle against the fluid current. By starting with low flow rates, small less dense particles will attain terminal velocity and flow out with the fluid. These particles are collected in an overflow device and separated from the rest of the material. The fluid flow rates are then increased to separate larger size particles. This process is then carried out in a sequence of separation for analysis. Such systems can be further refined by having the overflow from the first tube pass vertically upwards through a second tube of greater cross-section, and then on to any number of such tubes arranged in series to separate particles in a sequence of batches.

Advantages: Samples are analyzed using centrifugal classification and the technique is non-destructive. Each cut-point can be recovered for future size-respective chemical analyses. This technique determines particle size as a function of settling velocity in an air stream (as opposed to water, or some other liquid).

Disadvantages: A bulk sample (about ten grams) must be obtained. It is a fairly time-consuming analytical technique. The actual test method has been withdrawn by ASME due to obsolescence and therefore calibration materials are therefore no longer available.

Photoanalysis

Photoanalysis procedures consist of taking a photo of a sample of the materials to be measured and using software to analyze the photo.

Advantages: Compared to sieve analyses, which can be time-consuming and inaccurate, photoanalysis methods can provide rapid and accurate measurements. Image analysis provides far more data values and options than any of other technique. Measuring each particle allows unmatched flexibility for calculating and reporting particle size results. Image analysis instruments may report distributions based on particle length as opposed to spherical equivalency, and they may build volume distributions based on shapes other than spheres. Another advantage is that the material can be analyzed without being directly handled or suspended in a solution.

Disadvantages: Images may have to be acquired using Scanning Electron Microscopy (SEM) for samples with particles smaller than about 1 micron. Such equipment must be able to do air-less sample transfers for materials that are air sensitive. For accurate measurements, methods must be employed to separate clusters of particles.

Microscopic counting methods

An extension of photoanalysis is that particle size distributions (PSDs) can be measured microscopically by sizing against a calibrated scale and counting. For a statistically valid analysis, millions of particles must be measured. For this to be done manually is impractical. However, automated analysis of systems and software are commercially available.

Advantages: Microscopic evaluation often gives a great deal of information that other methods are unable to give.

Disadvantages: It may be difficult to distinguish between particles that are overlapping which may be counted as bigger particles. This can lead to significant errors in reported size distribution.

Optical counter

In a light counting apparatus, particles are fed through a counting chamber, where a focused laser beam is partially blocked as the particle passes. A detector reads the reduction in light intensity that is related to the optical cross-section of the particle. This data can be converted to a size distribution.

Advantages: The method is quick and easily calibrated using standards.

Disadvantages: The dynamic size range is limited and may require several runs to cover a wide range of particle sizes. Similar to resistance methods, the sample must be suspended in a conductive fluid, which may be incompatible with hydrogen storage materials.

Electroresistance counting methods

A Coulter counter is an example of this method. It is an apparatus for sizing particles suspended in electrolytes. It is typically used in bio-medical research. Poorly conductive particles alter the effective cross-section of the conductive micro-channel or orifice. If these particles are less conductive than the surrounding liquid medium, the electrical resistance across the channel increases, causing the electric current passing across the channel to briefly decrease. The number of particles for a given volume of fluid can be counted by monitoring the pulses in electric current. Because the size of the change in the electric current is related to the size of the particle, the method enables a particle size distribution to be measured.

Advantages: Very small sample aliquots can be examined.

Disadvantages: The sample must be dispersed in a liquid medium which may not be feasible for some hydrogen storage materials. The results are only related to the projected cross-sectional area that a particle displaces as it passes through an orifice. This is a physical diameter, not really related to mathematical descriptions of particles. Also, conductive particles are a common concern for the application of this method. This is rarely an issue because the conductivity difference between most conductive materials and ions in liquid is so great that most conductive materials act as insulators in a Coulter counter. However, it is a consideration to be addressed before making measurements on metal or carbon powders.

Sedimentation techniques

Sedimentation techniques involve the measurement of the terminal velocity acquired by particles suspended in a viscous liquid. Sedimentation time is longest for the finest particles, so this technique is useful for sizes below 10 µm, but sub-micron particles cannot be reliably measured due to the effects of Brownian motion. A typical apparatus disperses the sample in liquid and then measures the density of the suspension in a vertical column at timed intervals. Other techniques determine the optical density of successive layers using visible light or X-rays.

Advantages: This technique determines particle size as a function of settling velocity which is important for suspensions, but which is not necessarily directly related to particle size. Thus, it may not be appropriate for applications employing dry powders.

Disadvantages: Sample must be dispersed in a liquid medium, which may not be appropriate for hydrogen storage materials. For those that can be studied in a liquid medium, it is possible that some particles may (partially or fully) dissolve in the medium altering the size distribution, requiring careful selection of the dispersion media. Density is highly dependent upon fluid temperature remaining constant. X-rays will not count carbon (organic) particles. Many instruments can require relatively large samples (e.g. two to five grams).

Laser diffraction methods

Advances in the development of sophisticated data processing and automation have made laser diffraction the dominant particle size distribution technique. The most basic laser diffraction system can measure solid particles in suspensions and emulsions. With the addition of a dry powder feeder the instrument can then also measure dry powders in air. The method measures the "halo" of diffracted light produced when a laser beam passes through a dispersion of particles in air or in a liquid. The angle of diffraction increases as particle size decreases. The method is particularly good for measuring sizes between 0.1 and 3,000 μm. This is a low concentration technique, so dilution is often required. The complex refractive index of the sample and diluent must be known for optimum accuracy.

Advantages: Speed, ease of use, and flexibility. Use with liquid or air suspensions. This technique can be performed on very small samples. A particular advantage is that the technique can generate a continuous measurement for analyzing process streams.

Disadvantages: Converting a volume result from laser diffraction to a number basis can lead to errors depending on the shape factors of the particles.

Dynamic Light Scattering

Dynamic Light Scattering (DLS), also known as quasi-elastic light scattering (QELS), uses the Brownian motion of sub-micron particles in a suspension. A laser beam is scattered by particles in which the motion causes rapid fluctuations in scattering intensity around a mean value. The method can measure suspensions and emulsions of particles from 1 nm to 1 μm. Both the lower and upper limits are sample dependent. The lower limit is influenced by concentration and how strongly the particles scatter light. A low concentration sample of weakly scattering particles near 1 nm can be difficult to reproduce. The upper size limit is determined mainly by the density of the particles. Particles settled on the bottom of the sample cuvette cannot be inspected by the laser light source. Particles with a high density will settle more quickly than low density particles. The upper limit of DLS may be 8 μm for emulsion samples where the two phases have similar density. The upper limit of particles with a density of 1.7 g cm^{-3} may be around 1 μm.

Advantages: The method can measure very small particle sizes and only a small amount of sample is needed. DLS does not require any knowledge of the sample's refractive index unless one wants to convert from intensity to volume distribution or concentration. What is required is viscosity, especially for higher concentration samples. Detailed DLS investigations could involve a study of dilution to determine the nature of the particle-particle interactions and presence of multiple scattering. Sophisticated DLS systems can also measure other sample characteristics including zeta potential, molecular weight, and second virial coefficient. Generating this additional information may require a greater skill set of the operator.

Disadvantages: DLS has relatively low resolution and is most appropriate for applications involving particles in suspensions.

Acoustic spectroscopy or ultrasound attenuation

This method employs ultrasound for collecting information on the particles dispersed in fluid. The particles will absorb and scatter ultrasound similarly to light. In the case of ultrasound, transmitted energy versus frequency is measured. The ultrasound attenuation frequency spectrum is used to determine the particle size distribution.

Advantages: The method can be applied to any fluid system with no dilution or other sample preparation. Calculation of particle size distribution is based on theoretical models that are well verified for up to 50% by volume of dispersed particles. The method allows particle size determination down to 10 nm.

Disadvantages: As with many other methods, liquid dispersion of the particles is required.

2.2.4 Particle Size Measurements of Hydrogen Storage Materials

Particle size is one physical property that can have a strong impact on the performance of hydrogen storage materials. Thus, accurate particle size analysis has an important role in the developing advanced materials. However, materials for hydrogen storage cover a very wide range with very vastly different physical properties. Examples are: liquids (Liquid Organic Hydrogen Carriers), highly structured bulk materials (MOFs), and nanomaterials (CNTs) among others. Therefore, the methods used to do particle size analysis will be highly material dependent and may be very different from one type of material to another.

For example, for nanomaterials with highly structured shapes such as SWNTs or nanoclusters, the best option may be to measure the dimensions of a finite set of particles using microscopic techniques to arrive at a particle size distribution of a particular sample. This was done for ropes or ribbons of single-walled carbon nanotube (SWNT) bundles by Cheng et al. using HRTEM observations on the as-synthesized samples.[143] The figure below shows typical images of isolated SWNTs.

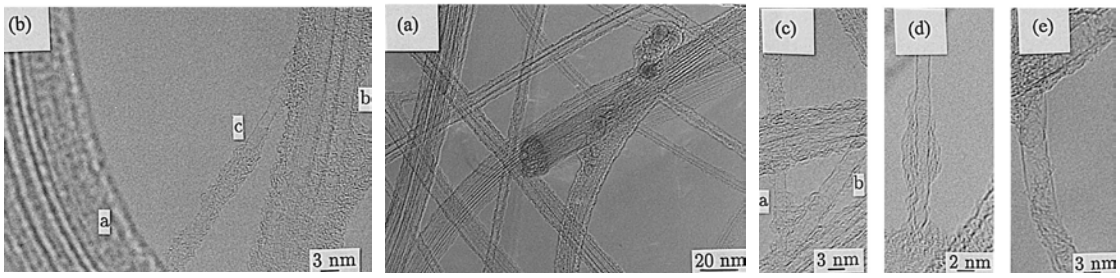

Figure 66. HRTEM images of the as-synthesized SWNTs by the catalytic decomposition of hydrocarbons. (a) Bundles of aligned SWNTs. (b) Two bundles of aligned SWNTs and an isolated SWNT. (c) Two isolated SWNTs. (d) An isolated SWNT with a wavy morphology. (e) An isolated SWNT having the largest observed diameter of 4.3 nm.[143]

Figure 66 (a) shows a well-aligned SWNT bundle with a diameter of 30 nm, four parallel SWNTs aligned one-by-one, and an isolated SWNT with a diameter of 1.7 nm, as denoted by a, b and c, respectively. Most of the isolated SWNTs that were observed in that study have diameters ranging from 1.2 to 2.0 nm, as shown in portion c of Figure 66 (a), portion "a" of Figure 66 (c) and Figure 66 (d). A few very large SWNTs were also observed, such as those shown in portion "b" of Figure 66 (c) (3.2 nm) and in Figure 66 (e) (4.3 nm), where the nominal projected diameters were given in parentheses.

In this example study, the diameters of 74 isolated SWNTs were measured, with an accuracy of about ± 0.1 to 0.15 nm based on HRTEM images similar to those shown in Figure 66. From these measurements a diameter distribution of the SWNTs in the sample was deduced, and are shown in the figure below. It can be seen that more than 75% of the SWNTs have diameters ranging from 1.2 to 2 nm, with a Gaussian mean diameter of 1.69 ± 0.34 nm. The conclusion in that particular study was that the SWNTs synthesized by the group's hydrocarbon catalytic decomposition method have larger diameters than those grown both by the laser vaporization method, whose diameters have a mean value of 1.38 nm[144] or a Gaussian mean value of 1.39 ± 0.1 nm, as fitted by the authors to the STM measurements by Wildöer et al.[145] and by the electric-arc method with diameters of about 1.4 nm.[146]

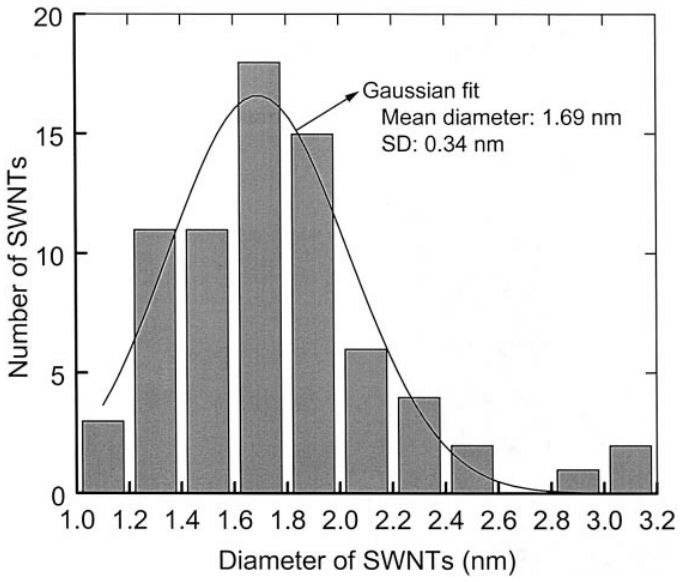

Figure 67. Diameter distribution of the SWNTs obtained by the catalytic decomposition of hydrocarbons using data obtained from HRTEM images. The Gaussian fit to these data gives a mean diameter of 1.69 ± 0.34 nm for the SWNTs.[143]

In another example, as a part of their model validation effort, Smith et al. had particle size distribution measurements performed on the high pressure metal hydride alloy $Ti_{1.1}CrMn$ using laser diffraction.[65] To prepare the materials in a fully activated (and decrepitated) state, the alloy was cycled with hydrogen, hydriding and dehydriding the alloy as described in reference 39. Some of the laser diffraction particle size distribution measurements were performed with the sample in an air environment. Because $Ti_{1.1}CrMn$ is moderately pyrophoric the sample required controlled oxidation to passivate the exterior surfaces of metal hydride particles prior to those measurements.

The laser diffraction method employed requires the sample powder to be dispersed in a fluid media (air or water) to achieve accurate measurements of particle size distribution. Both wet and dry methods were utilized and are outlined in IS013320-1.[147] The wet method was employed primarily to assess particle size in the absence of agglomeration. In this case the powder particles were dispersed in water with and without ultrasonic excitation. The particle size distributions of the sonicated samples were measured as a function of sonicating time to determine when agglomerates were completely fragmented. The result was that three minutes of ultra-sonication were required in order to achieve adequate dispersion of the passivated particles.[65] Laser diffraction measurements were performed on the sonicated and un-sonicated samples dispersed in water. The dry laser diffraction PSD measurements were performed by dispersing and accelerating the powder sample in air by a pressure differential induced across a Venturi tube in which shear stresses act to reduce agglomeration. The resulting particle size distributions of the material under differing measurement and preparation conditions are displayed in Figure 68.

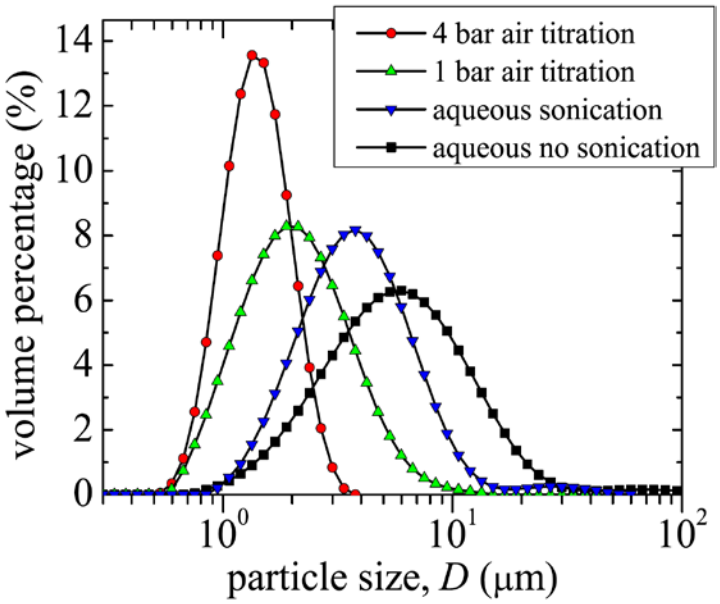

Figure 68. Particle size distributions of passivated $Ti_{1.1}CrMn$ by laser diffraction.[74] Air titration (dry) and aqueous (wet) methods were used to disperse particles.[65]

The wet measurements showed a reduction in measured particle size upon sonication. However, agglomerates still appeared to be present, as reflected by a small secondary peak near 20 μm.[65] The dry method resulted in much smaller median particle diameters of 1.4 and 2.0 μm for 4 and 1 bar applied pressure, respectively. The difference between the measurements at different flow rates indicated that particles had undergone attrition (and thus, particle size reduction).[74] Sparks were observed during acceleration of particles at 4 bar indicating fresh pyrophoric surfaces and supporting the idea of attrition of the samples at higher flow rates. The authors concluded that these results support the notion that metal hydride particles possess an abundance of internal cracks. This is the case even after the particle size reduction due to hydrogen cycling decrepitation has stabilized. Important lessons from this example at a fundamental understanding level and a practical measurement level is that 1) microstructure within particles must be accounted for in the modeling of hydrogen diffusion kinetics and heat flow in metal hydride powders and, 2) particle size distribution measurement results can vary significantly depending on how the measurements are performed and how the samples are prepared.

2.3 Surface Area Measurements

2.3.1 The Langmuir Surface Area Measurement Method

Whenever a gas is in contact with a solid there will be an equilibrium established between the molecules in the gas phase and the corresponding adsorbed species (molecules or atoms) which are bound to the surface of the solid. The Langmuir equation (also known as the Langmuir isotherm, Langmuir adsorption equation or Hill-Langmuir equation) describes the dependence of the surface coverage of an adsorbed gas on the pressure of the gas above the surface at a fixed temperature. The equation was developed by Irving Langmuir in 1916.

The Langmuir equation is:

Equation 31

$$\theta = \frac{\alpha \cdot P}{1 + \alpha \cdot P},$$

where θ is the fractional coverage of the surface, P is the gas pressure or concentration, and α is Langmuir adsorption constant which increases with an increase in the binding energy of adsorption and with a decrease in temperature. The Langmuir model makes the following assumptions:

1. the surface containing the adsorbing sites is a perfectly flat homogeneous plane with no corrugations,
2. the adsorbing gas adsorbs into an immobile site,
3. all sites are equivalent,
4. each site can hold at most one molecule of A (mono-layer coverage only), and
5. there are no interactions between adsorbate molecules on adjacent sites.

Examples of Langmuir curves are shown in the figure below.

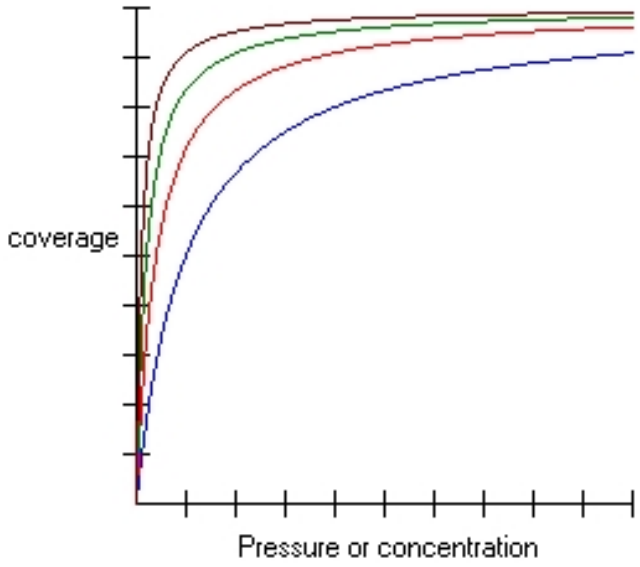

Figure 69. Langmuir isotherm. The value of the Langmuir constant increases from blue, red, green and brown.[148]

There are many other types of isotherm (Temkin, Freundlich …) which differ in the assumptions made in deriving the expression for the surface coverage. The Langmuir isotherm is simple, and as such may not describe the adsorption interaction sufficiently to derive accurate surface area measurements. The example in the figure below compares a Langmuir isotherm with that of a BET isotherm.

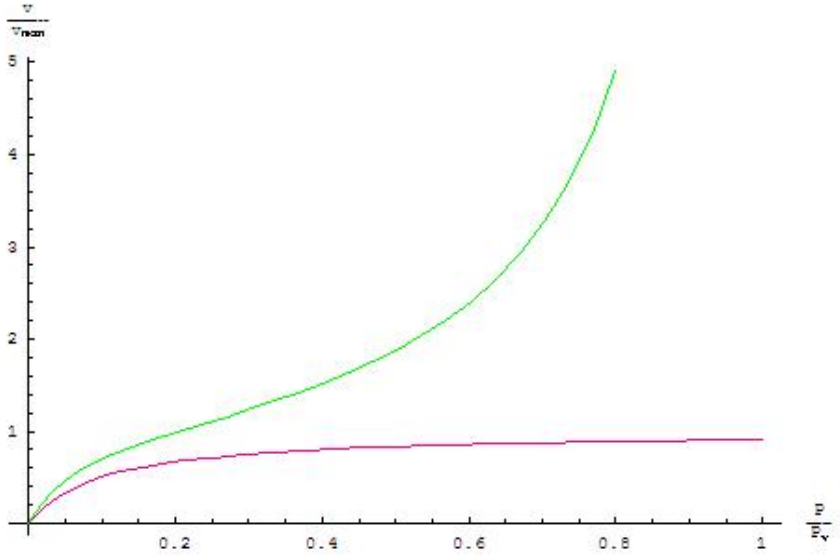

Figure 70. Langmuir isotherm (red) and BET isotherm (green).[149]

2.3.2 The BET Method

BET analysis (named for the authors of the method Stephen Brunauer, Paul Hugh Emmett, and Edward Teller) is an analytical technique for measuring the specific surface area of a material. The theory behind the method was published by the three authors in 1938.[150]

BET theory is an extension of the Langmuir theory, which relates the coverage of monolayer of molecules on a solid surface to gas pressure or concentration of a medium above the solid surface at a fixed temperature.

BET theory extends this model to multilayer adsorption with the following assumptions:

1. gas molecules physically adsorb on a solid in layers infinitely,
2. there is no interaction between each adsorption layer, and
3. the Langmuir theory can be applied to each layer.

The model leads to the following BET equation:

Equation 32

$$\frac{1}{v\left[(p_0/p)-1\right]} = \frac{c-1}{v_m c}\left(\frac{p}{p_0}\right) + \frac{1}{v_m c} \ ,$$

where p is the equilibrium pressure, p_o the saturation pressure of the adsorbate at a given temperature, v is the adsorbed gas quantity or concentration, v_m is the monolayer adsorbed gas quantity, and c is the BET constant given by:

Equation 33

$$c = \exp\left(\frac{E_1 - E_L}{RT}\right) \ ,$$

where E_1 is the heat of adsorption for the first layer, and E_L is the heat of adsorption for subsequent layers and is equal to the heat of liquefaction.

Plotting experimentally measured values of $1/v[(p_0/p)-1]$ (y-axis) versus $\phi = p/p_0$ (x-axis) produces an adsorption isotherm. This plot is called a BET plot (Figure 71).

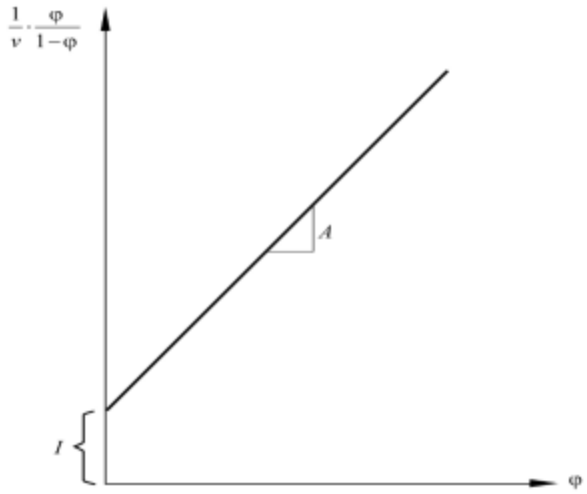

Figure 71. BET plot.[151]

According to Equation 32, the plot should be linear. However, in practice the linear relationship of this equation is maintained only in the range of $0.05 < p/p_0 < 0.35$. The slope *A* and the y-intercept I of the data line are used to calculate the monolayer adsorbed gas quantity v_m and the BET constant *c* according to:

Equation 34

$$v_m = \frac{1}{A+I}$$

Equation 35

$$c = 1 + \frac{A}{I}$$

The BET method is commonly used for determining surface areas of solids by measuring the adsorption of a gas. A total surface area S_{total} and a specific surface area S_{BET} are determined from:

Equation 36

$$S_{\text{total}} = \frac{(v_{\text{m}} N s)}{V}$$

Equation 37

$$S_{BET} = \frac{S_{total}}{a}$$

where v_m is in units of volume N is Avogadro's number, s is the adsorption cross section of the adsorbing species, V is molar volume of adsorbate gas, and a is the mass of adsorbent.

While the BET equation is applicable to nonporous solids and materials consisting of pores of large diameter it is not necessarily applicable to microporous adsorbents. The type of porosity (macro-, meso- or micropores) is key to the applicability of the BET equation. It is difficult to separate mono/multilayer adsorption from micropore filling. The size and shape of adsorptive molecules may also have a strong impact on the results of BET analysis. At one extreme very narrow cylindrical micropores leads BET analysis to produce surface areas significantly smaller than the total geometric area because of the assumption that molecules are adsorbing on a flat surface, which is small compared to the circumference of a cylinder. At the other extreme, BET analysis of materials with super-micropores (> 0.7 nm) leads to an overestimation of the surface area by including molecules in the center of the pores that do not touch the surface.

The linearity of a BET measurement can also affect the accuracy of the analysis. The range over which the analysis is performed should be reported along with results. Rouquerol et al. suggested a formal procedure for identifying the acceptable linear range over which BET analysis can safely be applied.[152] The metrics are that the BET constant *c must* be positive and the BET equation should be limited to a pressure range where $v(p_o - p)$ or $v(1 - p/p_o)$ increases continuously with p/p_o.

An example pointing out this issue was presented in a publication by Quantachrome and is shown below in Figure 72. This is BET data for an argon adsorption isotherm at 87.3 K on a faujasite zeolite (surface area: ca 1200-2300 m^2/g). [153,154] Based on Rouquerol's criterion, all of the data points above a relative pressure of 0.053 should be eliminated from the BET calculation.

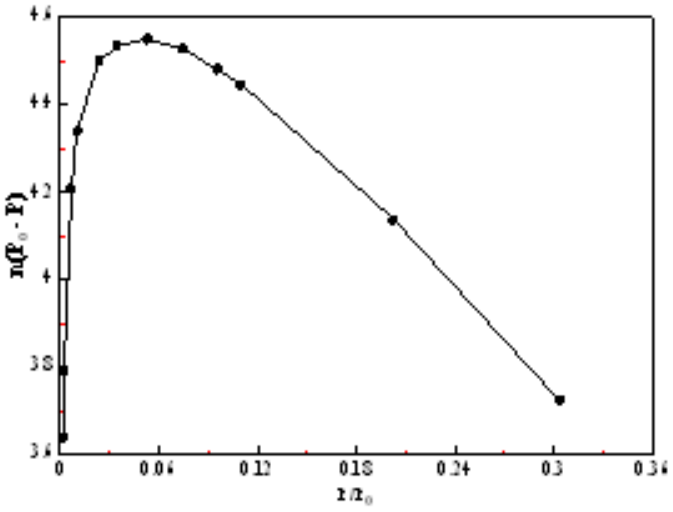

Figure 72. Plot of the term $n(P_o - P)$ vs. P/P_o.[153]

The resulting plot is shown in Figure 73 where the BET equation was applied for relative pressures from 0.01 to 0.053 producing a linear plot with a positive BET constant *c*.

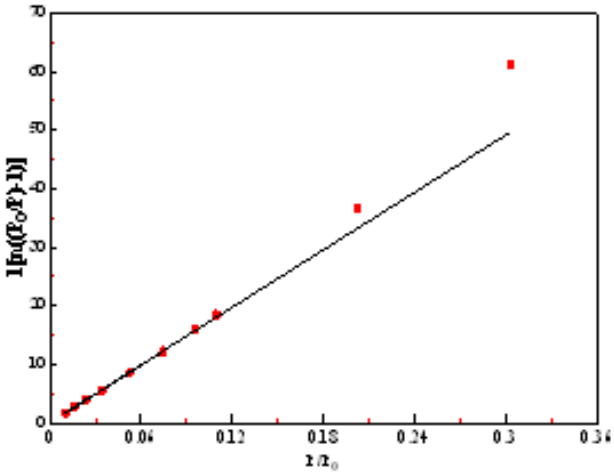

Figure 73. BET plot for argon on a faujasite zeolite at 87 K.[153]

An example is shown below of the measured surface areas of many low temperature adsorption materials considered for hydrogen storage and the related hydrogen storage capacity.

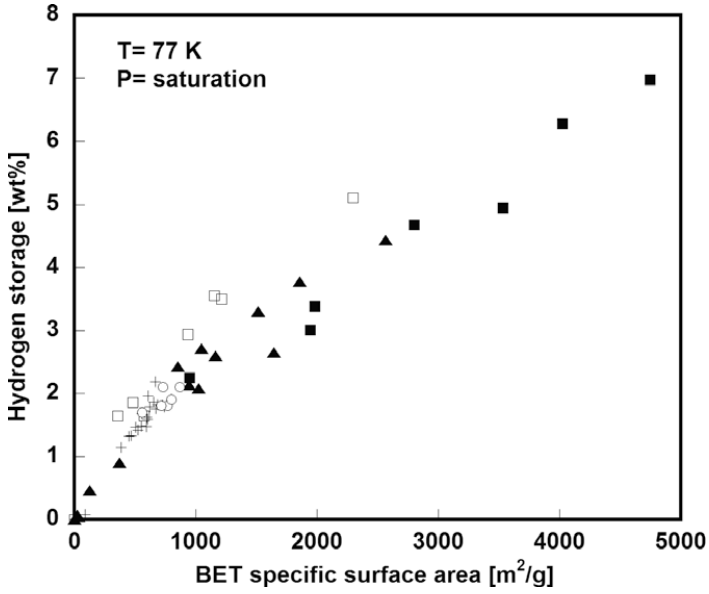

Figure 74. Maximum hydrogen storage capacity versus BET SSA of different porous materials: MOFs (open squares), filled squares, carbon materials (triangles), zeolites (crosses), Prussian blue analogues (circles).[155]

2.4 Measurements of Mechanical Durability of Hydrogen Storage Materials

2.4.1 Lattice Volume Expansion Measurements

AB_5-type intermetallic hydrides based on $LaNi_5$ have found wide applications as active electrode materials in rechargeable batteries. In the case of pure $LaNi_5$, the storage capacity declines dramatically during repeated charge-discharge cycles. This decline is believed to be due to decrepitation of the alloy during the hydriding-dehydriding process, which causes isolation and enhanced corrosion of the resulting fine alloy particles.[156Error! Bookmark not defined.] Decrepitation or pulverization is a result of the large volume expansion, which occurs upon hydride formation. AB_5-type hydrides typically exhibit a discrete solid-solution (α-phase) to metal-hydride (β-phase) phase transition which is accompanied by volume expansion of up to 25 vol. %. Notten and coworkers proposed that internal stresses created at the phase boundary are relieved through crack formation, which ultimately leads to pulverization of the material.[157] They suggested that a reduction of the discreet lattice expansion upon hydriding will lead to enhanced cycle life properties.[158]

Many investigations have shown that the cycling stability of $LaNi_5$ can be improved by partial substitution of nickel with cobalt, aluminum, silicon, manganese or a combination of these elements.[159,160,161,162,163] Among all the substitutions cobalt appears in many cases to significantly aid in maintaining cycle life. Unfortunately, the influence of cobalt on the cycling stability was not well understood, but it is generally believed that cobalt is important for reducing pulverization during hydriding.

For most AB_5-type hydrides, the α-to-β phase transition is observed as a single plateau in the gas-phase pressure-concentration isotherm (PCT) curves, as well as in potential versus concentration electrochemical measurements. However, the alloy $LaNi_4Co$ exhibits two plateaus during both hydrogen absorption and desorption. The presence of a double plateau in both absorption and desorption and throughout the cycle life of $LaNi_4Co$ indicates the formation of a stable intermediate phase of stoichiometry $LaNi_4CoH_{\approx 4}$ referred to as the γ-phase.

One example of lattice volume expansion measurement to gain insight into the fundamental mechanisms of improved electrochemical cycle-life performance of metal hydrides is the study that was conducted by Chartouni and Gross on Co substituted $LaNi_5$.[164] In that work, phase and crystal structure changes during the electrochemical hydriding and dehydriding of $LaNi_4Co$ were investigated using *in situ* X-ray diffraction.

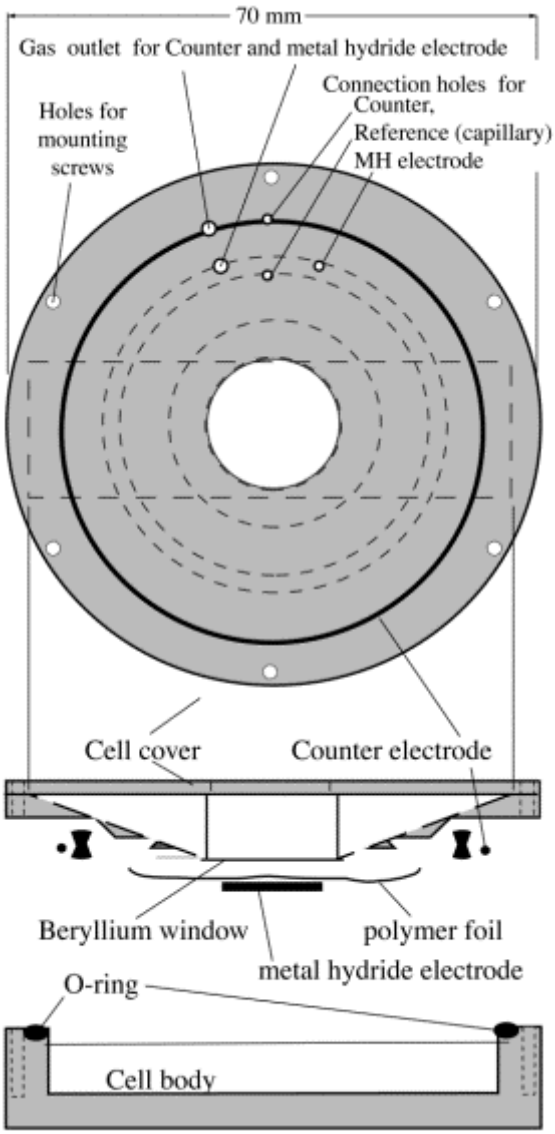

Figure 75. Electrochemical cell for *in situ* XRD. The MH-electrode is slightly pressed against the Be-window in order to maintain the electrode at the same position upon cycling. The Polymer foil, separating the Be-window from the MH-electrode is clamped to the cell cover using an O-ring. Counter and MH-electrodes are wired out through the corresponding holes in the cell cover.[164]

In situ time resolved X-ray diffraction during gas-phase hydrogen absorption and desorption was developed by Gross et al. to investigate the hydrogen storage properties of doped $NaAlH_4$.[165] In this example, a similar concept was applied to develop a special electrochemical cell to do *in situ* X-ray diffraction during electrochemical charge/discharge cycles (Figure 75).

This new setup provided a real time probe to observe phase transition, crystal structure changes, and activation effects *in situ*. Using this method, it was found that the double plateau behavior, seen in the gas-phase PCT measurements of $LaNi_4Co$, is also present in the electrochemical potential-composition isotherms. In addition, crystal lattice information derived from these measurements helped to explain the long cycle life of cobalt containing AB_5-type battery alloys. The formation of an intermediate γ-phase hydride between the hydrogen solid-solution α-phase and the fully hydrided β-phase was clearly observed during absorption and desorption. The volume expansion in the formation of the γ and β hydride phases is highly anisotropic. Lattice expansion in the α-phase to γ-phase transformation occurs mainly in the basal plane, whereas the transition from the γ-phase to the β-phase causes a lattice expansion in the c-axis direction. It is believed that the two-step phase transition in this Co-substituted alloy generates less internal stress than the single-step volume expansion of the archetype $LaNi_5$ compound. This reduces the stress-induced decrepitation that occurs during electrochemical cycling. Consequently, the metal hydride electrode maintains larger particle sizes and, thus, smaller surface areas subject to corrosion by the electrolyte, which is the principle cause of capacity loss.

PCT (Pressure/Potential-Concentration-Temperature) Measurements

Measurements of the chemical equilibrium potential versus the hydrogen content of a $LaNi_4Co$ electrode were first measured for both charging and discharging (Figure 76). The plot in the inset shows gas-phase hydrogen absorption and desorption PCT measurements of the same alloy.

The appearance of a double plateau can be readily observed in both types of measurements. This double plateau behavior was first observed by Van Mal et al. in their studies on the effects of varying the cobalt content in substituted $LaNi_{5-x}Co_x$.[166] Since this behavior is reproduced in both the electrochemical and the gas phase measurements, it is clearly a property of the material.

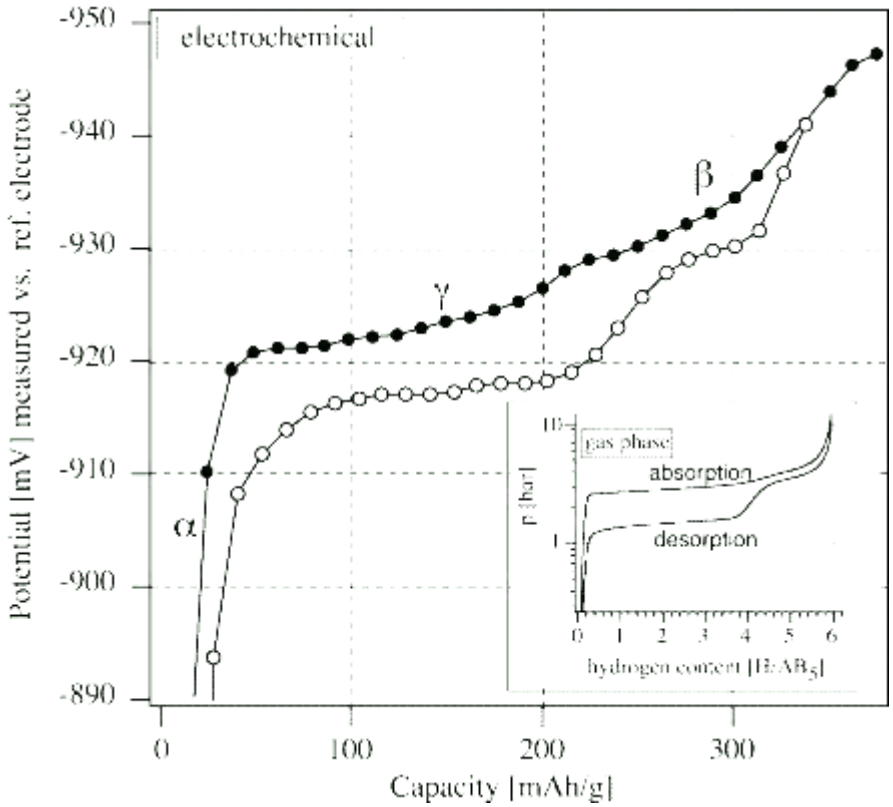

Figure 76. Electrochemical potential measurements of $LaNi_4Co$ at room temperature for the 20th cycle (charge ● and discharge ○). The active electrode potential was measured vs. a Hg/HgO/6M KOH reference electrode in the same electrolyte. Each point was measured at zero current after a rest time of 5 minutes.[164] (Inset for comparison: gas phase hydrogen charging PCT of the $LaNi_4Co$ measured at 40 °C [161])

In Situ XRD/Electrochemical Cycling Measurements

During the *in situ* XRD/electrochemical cycling experiment, a series of 244 consecutive 2θ scans were measured during the first five charge-discharge cycles of a $LaNi_4Co$ electrode to provide a real-time view of the phase and crystal structure changes that take place during cycling (Figure 77). The corresponding contour plot is shown in Figure 78. Large angle scans (34° to 85°) were made at specific hydrogen concentrations to obtain a larger number of reflections for more accurate lattice parameter and structural calculations.

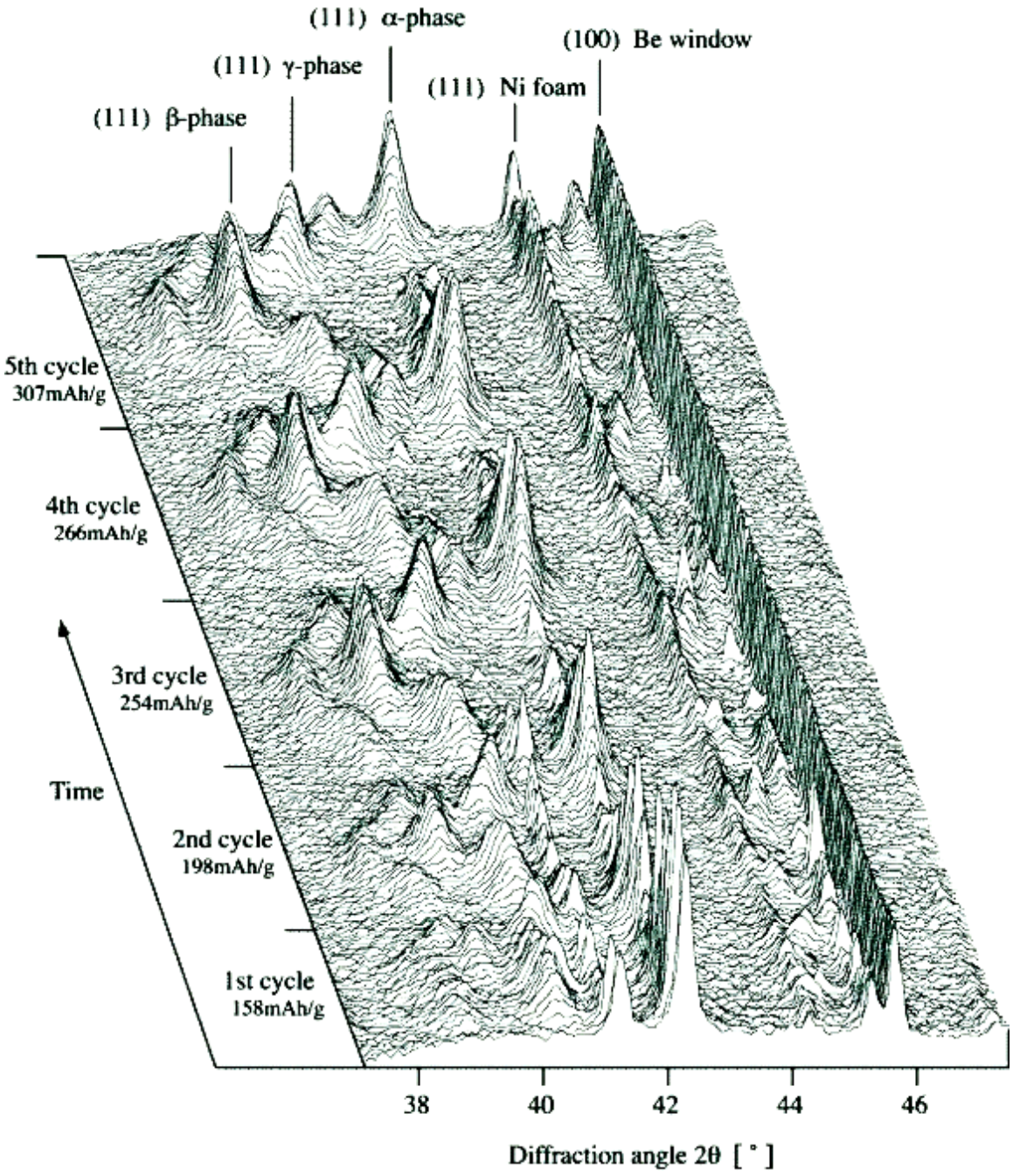

Figure 77. A compiled series of X-ray diffraction measurements during electrochemical cycling, showing phase changes and the structural behavior of the active material. The values in $mAhg^{-1}$ signify the discharge capacities for the corresponding cycles.[164]

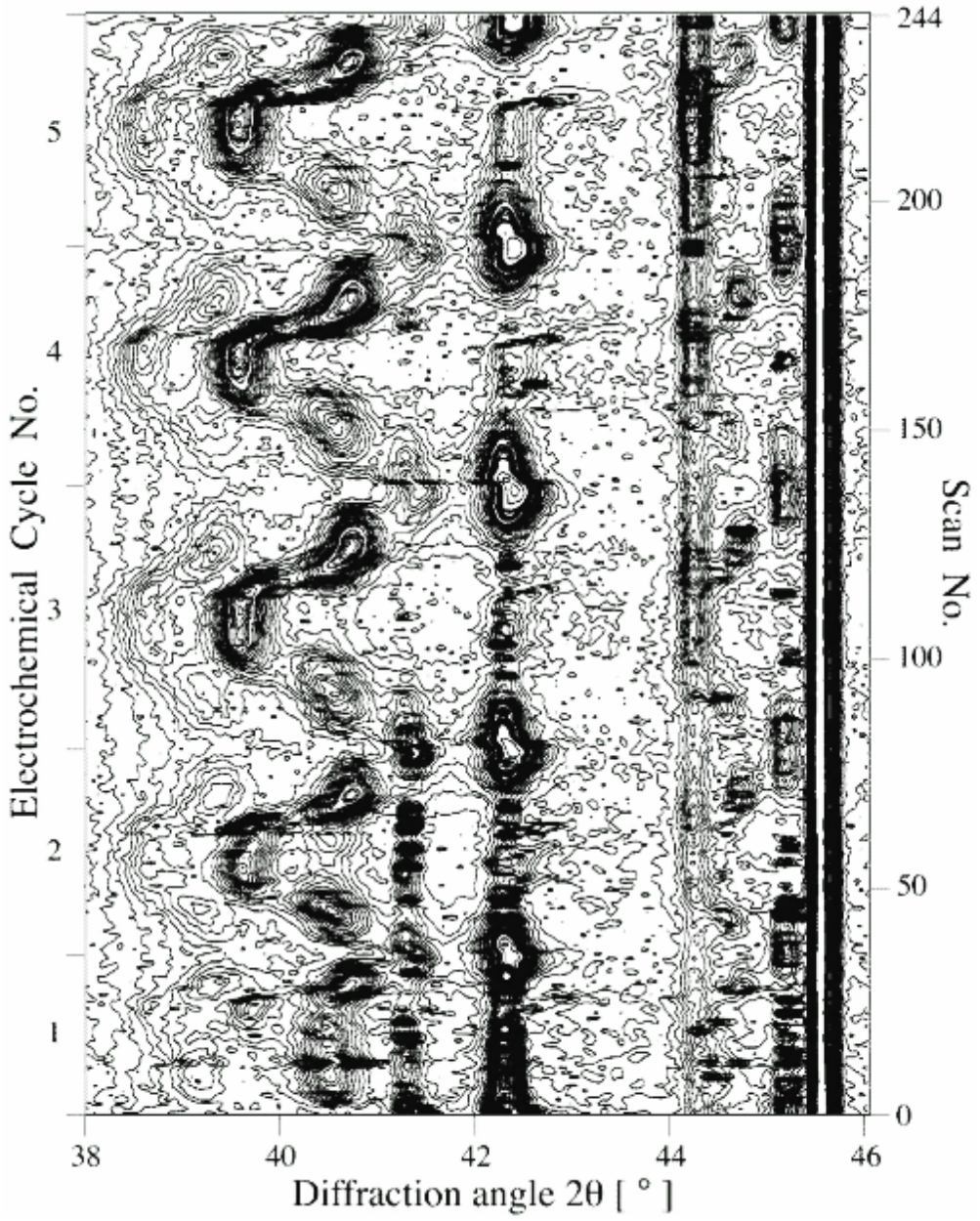

Figure 78. A contour plot of the X-ray diffraction intensities vs. time for the compiled series of X-ray diffraction measurements shown in Figure 77.[164]

The phase transitions during charging and the reverse transitions during discharge can be clearly discerned from the formation and disappearance of the characteristic diffraction peaks of each phase. These XRD measurements confirmed the chemical potential and PCT results by directly demonstrating the transition of the α-phase hydrogen solid solution to the γ-phase hydride followed by the formation of the β-phase hydride. All three phases maintained hexagonal crystal symmetry, but the decreasing peak positions show that there are lattice expansions on going

from the α-phase to the γ-phase and then to the β-phase. The difference in the lattice expansions of each transition is associated with different hydrogen occupancies of interstitial sites in the alloy.[167] The different site occupancies of the two hydride phases is responsible for the observed difference in the equilibrium potentials (plateau pressures) of the α to γ and the γ to β phase transition.

Activation Effects

In contrast to more conventional measurements, one of the powerful and unique aspects of this time resolved *in situ* XRD technique is that it enables the direct observation of the activation processes. In the first cycle, some percentage of the peaks of the α-phase are present over the entire charge-discharge procedure. Furthermore, the γ-phase peaks show low intensities and also do not completely disappear with the transition to the β-phase. Finally, the β-phase shows only very weak peak intensities. This indicates that some portion of the particles of the electrode material were not hydrided in the first cycle. It also demonstrates that the γ to β phase transition was far less complete than the α to γ phase transition. During the first cycle, many particles are still relatively large and therefore have low surface to volume ratios. In the electrochemical charging process, the transport of hydrogen into the bulk is rate limiting by surface mechanisms. The limited surface areas of the larger particles reduce the total amount of hydrogen that can diffuse into the bulk of the particle to form a hydride. Under the given charging conditions (50 mA g^{-1}) large particles will only become partially hydrided in the first few cycles. In addition to this, the alloy material is initially covered with a surface oxide layer. This layer causes poor electrical contact with the current collector. Electrically isolated particles will not charge at all and those with poor contact will only be partially hydrided.

With each charge-discharge cycle the lattice expansion and contraction causes the alloy to decrepitate to smaller particles, which reduces diffusion distances and creates new oxide-free active and conductive surfaces. Moreover, cycling reduces surface oxides to the metallic state, greatly enhancing the electrical contact between active material and the current collector. When the activation process is complete, the entire electrode will hydride and dehydride. In this study, the lack of any residual unhydrided material demonstrates that the activation process was completed by the fifth cycle.

Lattice Volume Expansion Measurements

The lattice parameters of each of the three phases were determined at each scan taken during the fifth cycle. These are presented in Figure 79, which illustrates that the lattice expansion is highly anisotropic for both phase transitions.

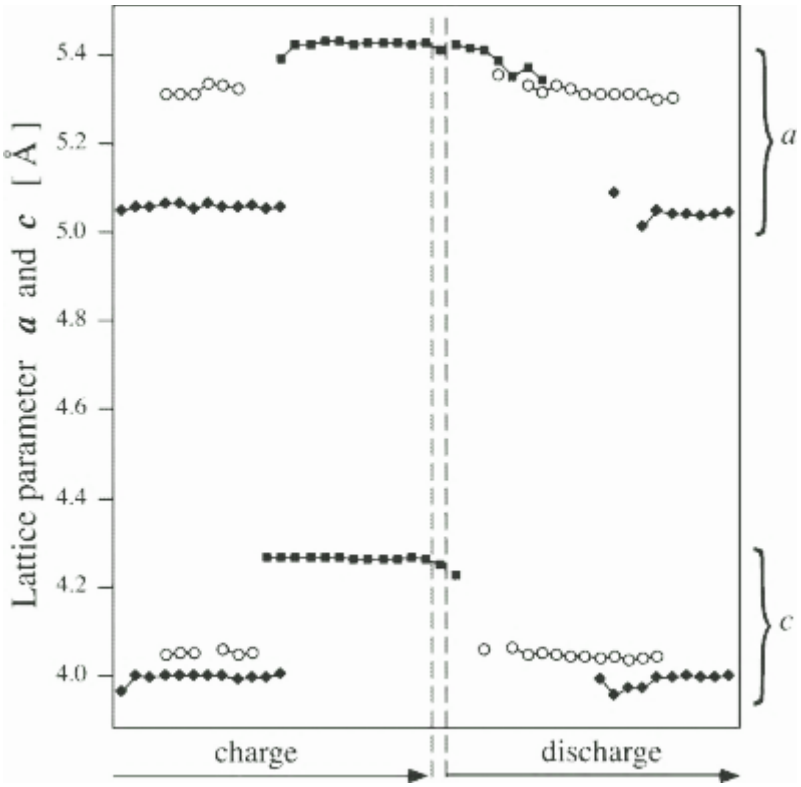

Figure 79. Calculated lattice parameters a and c during charge and discharge (◆ α-phase, ○ γ-phase, and □ β-phase). The error in calculating the lattice parameters using only three peaks is significant (on the order of ±0.02 Å). The values after charging (between the dashed lines) were taken at zero current after a rest period of 30 min.[164]

The lattice expansion in going from the α-phase to the γ-phase is principally in the basal plane (a/b axis), whereas for the γ to β transition only the c lattice parameter increases. The discrete lattice volume expansion in going from the α-phase to the γ-phase is $\Delta V_{\alpha\text{-}\gamma}/V_{\alpha}$ = 12.2 ± 0.1% and the discrete lattice volume expansion in the γ to β transition is $\Delta V_{\gamma\text{-}\beta}/V_{\beta}$ = 9.5 ± 0.1%. The total volume expansion is $\Delta V_{\alpha\text{-}\beta}/V_{\alpha}$ = 22.8 ± 0.1%.

Improved Cycle Life Performance

The authors of the study concluded that the existence of two separate hydride phases and the stepwise increase in lattice volume in $LaNi_4Co$ contributes greatly to the extended cycle life capacity of this alloy. This concept is presented schematically in Figure 80, which includes the measured volume changes on hydriding $LaNi_5$ and $LaNi_4Co$.

Unlike the hydriding of $LaNi_5$, volume changes in $LaNi_4Co$ occur in two steps; the α to γ phase transition and the γ to β phase transition. The different lattice dimensions of the coexisting phases create large mechanical stresses at the phase transition boundary. Since both the PCT and XRD measurements show a relatively large volume fraction of the γ-phase, it was concluded

that the two types of phase boundaries are separated by enough distance that they create stress locally and independently. The separate phase transitions have much smaller lattice expansion than that found for the single phase transition of $LaNi_5$. This results in a lower localized stress, which reduces decrepitation and therefore lowers the rate of corrosion of the active material.

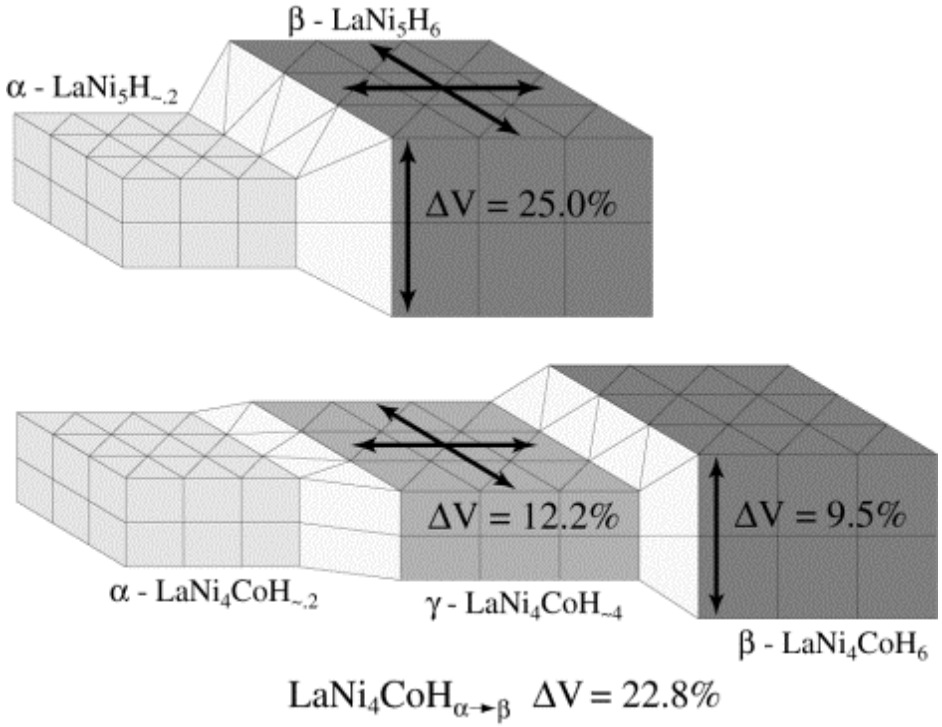

Figure 80. Schematic representation of the two-step lattice expansion associated with the α-to-γ and the γ-to-β phase transitions.[164]

By using *in situ* XRD/electrochemical measurements, a dynamic insight into phase transitions and lattice expansions can be achieved with a view to improving the mechanical stability and thus performance of commercial hydrides.

2.4.2 Strength of Materials Measurements

One mechanical property of hydrogen storage materials that may in some cases be important to the function and durability of the hydrogen storage system is the material's strength. That is, it may be desirable that the bulk material maintains its form during use. There are several reasons why this may be important, for instance, to maintain good thermal contact and heat transfer through all stages of the hydrogen storage life-cycle. For example, if a compressed powder compact is to maintain good heat transfer through its bulk and to some heat transfer device, then the compact should be structurally sound enough to maintain its form and not break apart

with use. Another possible reason would be if the storage material (e.g. a physisorption material) plays some critical role in the structural integrity of the system. For example, the material is needed to provide strength in maintaining the structure of a conforming tank. Thus, strength of materials measurements may be an important part of the design and development of certain hydrogen storage systems.

An important consideration in this respect is that while the materials strength properties of physisorption materials may (but not necessarily) be stable during hydrogen uptake and release, this is unlikely to be the case for hydrides. This is because hydride-based systems store hydrogen through chemical means that will undoubtedly modify the mechanical strength properties of the material during the process of releasing (or absorbing) hydrogen. For these materials the mechanical strength properties will need to be tested during hydrogen release (off-board regenerable hydrides) or at a regular interval during cycling (on-board reversible hydrides).

While the materials strength requirements will be very different from material to material and system to system, a starting point with respect to the best practices in the measurement of the materials strength properties is to look at what is being done in other fields of materials development. Because many of the materials that have been investigated for hydrogen storage are ultimately in powder form, it is worth looking at what is being done in the fields of Powder Metallurgy and Ceramics. In particular, the investigations of mechanical properties of powder compacts. A host of references exist for these well-developed fields of materials science.[168,169,170,171,172,173]

The following ASTM and ISO standard test methods may be applicable to strength of materials measurements of hydrogen storage materials.

- ASTM B312-96(2002) Standard Test Method for Green Strength for Compacted Metal Powder Specimens
- ASTM B331-95(2002) Standard Test Method for Compressibility of Metal Powders in Uniaxial Compaction
- ISO 3995:1985 Metallic powders – Determination of green strength by transverse rupture of rectangular compacts

The compaction properties of powders are characterized by their compressibility and compactability. While compressibility is the ability of the powder to deform and consequently be reduced in volume under pressure, compactability is the ability to form mechanically strong compacts. Compaction of powder consists of the simultaneous processes of compression and consolidation of a two-phase (particulate solid-gas) system due to an applied force.

Compression of Powders

With the application of external mechanical forces, there is usually a reduction in volume due to closer packing of the powder particles. This is often the main mechanism of initial volume reduction. As the load increases, rearrangement of particles becomes more difficult and further compression leads to some type of particle deformation. When the compression forces are released, if the deformation is reversible then the deformation is said to be elastic. In some compressed powder materials an elastic limit may be reached such that removal of the applied force above this level does not immediately reverse the deformation. In this case, the bulk volume reduction comes from plastic deformation and/or viscous flow of particles into the remaining void spaces. This mechanism dominates in materials in which the shear strength is less than the tensile or breaking strength. In materials for which the shear strength is greater than the tensile strength, particles may be preferentially fractured into smaller fragments fill into void spaces.

Four stages may occur during compression:

1. Initial repacking of particles.
2. Elastic deformation of the particles until the elastic limit (yield point) is reached.
3. Plastic deformation and/or brittle fracture then predominates until the voids are essentially eliminated.
4. Compression of the solid crystal lattice then occurs.

Consolidation of Powders

Consolidation is the increase in the mechanical strength of a material due to particle/particle interactions. The compression of powders in a die can be divided up into several stages. One example description of these stages is listed below.[174] These are:

1. Consolidation time: time to reach maximum force.
2. Dwell time: time at maximum force.
3. Contact time: time for compression and decompression excluding ejection time.
4. Ejection time: time during which ejection occurs.
5. Residence time: time during which the formed compact is within the die.

A host of strength of materials testing can be performed on powder compacts, from observations of samples at regular intervals during cycling to yield pressure testing and three-point cross-bending measurements. In general, the goal is to produce powder compacts of hydrogen storage materials that have densities that have been increased by compression to a maximum value that has little to no impact on the material's hydrogen storage capacity and

hydrogen permeability. At the same time, one would like to maximize the formation strength or stability of the material without detriment to hydrogen storage properties. Typically the formation strength increases with increased density caused by compression.

Examples

The following are some examples of the observations or measurement of changes in the mechanical strength properties that have been made of some hydrogen storage materials.

With a theoretical storage capacity of 7.6 wt. %, MgH_2 has been one of the most studied materials for hydrogen storage. Unfortunately, its high thermodynamic stability and slow hydrogen uptake and release kinetics have prevented widespread use in storage applications.[175,176] Much work and progress has been made in improving kinetics by reducing particle size and the addition of catalysts.[177,178,179,180,181] The addition of Nb_2O_5 catalyst has been particularly successful.[182,183,184] In a recent study on the scaled-up testing of a MgH_2 based powder storage bed, a degradation in hydrogen storage capacity and kinetics with cycling was observed.[185] This degradation led to a loss of half the capacity and a significant reduction in kinetics after only 20 cycles (Figure 81).

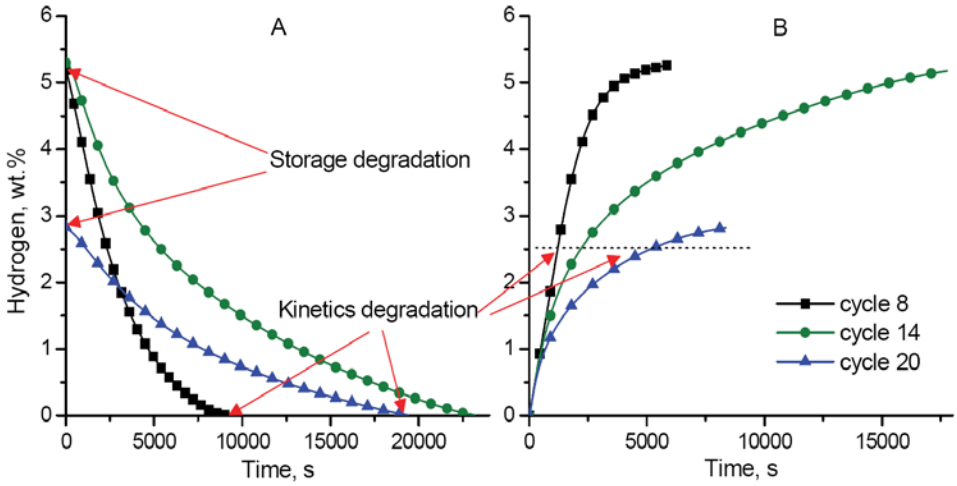

Figure 81. ***Performance degradation of scaled-up device in desorption (A) and absorption (B) modes.***[185] **These observations motivated the study of MgH_2 based powders moderately pressed in the form of pellets with the addition of some binding agent in order to retain stable mechanical consistency and structure with persistent free paths for hydrogen diffusion. The use of pellets instead of powder should improve the hydrogen transport inside the storage vessel avoiding pressure gradients and further compaction of the material. Moreover, in principle, each pellet should behave as an independent system reducing scaling up effects on the a/d kinetics.**[186]

On opening the Mg-H bed it was found that the Mg powder had been compacted *in situ* (Figure 82). It was concluded that local overheating and the resulting compaction lead to the degradation in hydrogen storage properties observed.

Figure 82. Mg/MgH_2 powder compaction during cycling experienced in the reactor studied in reference 185.[186]

With the realization that the performance degradation may have been due to changes in the mechanical properties of the materials on cycling, a follow-up study was performed on the hydrogen storage properties and the mechanical stability of compressed pellets of catalyzed MgH_2.[186,187] Improvement of thermal conductivity had been reported for MgH_2 mixed with expanded natural graphite and compacted into disks.[188] In the investigation by Khandelwal, Agresti and coworkers aluminum powder was added to the catalyzed MgH_2 to enhance the thermal conductivity and mechanical stability of the compressed pellets. That investigation provides one good example of the modification and testing of the mechanical properties of hydrogen storage materials.

In the referenced study, MgH_2 powders mixed with Nb_2O_5 (5 wt. %), and graphite (1 wt. %) were ball-milled for 20 hours. The catalyzed MgH_2 powder materials were prepared with the addition of 0, 5, and 20 wt. % Al powder by ball-milling for 5 min. The powders were pressed into pellets (0.3 g, 0.7 cm diameter and 0.7 cm height) following an approach developed earlier.[189] In addition some Al containing powder samples were annealed under vacuum at 450 °C in a Sieverts apparatus for 10 min prior to hydrogen testing. Hydrogen desorption was measured at 320 °C and an H_2 pressure of 1.2 atm. Absorptions were performed at 320 °C and 15 atm. Desorption cycles are shown for the 4 samples in Figure 83.

The cat-MgH_2 pellet sample with 0% Al (Figure 83a) maintained its 5.6 wt. % with 20 cycles but lost some kinetic performance. The pellet gradually lost its mechanical consistency during the 20 cycles, returning completely to a powder. Mg undergoes a volume expansion of 32% on forming MgH_2; this induced stress during absorption is the likely cause of the pulverization of the pellet.

The cat-MgH_2-Al20 pellet sample with 20% Al (Figure 83b) and an initial capacity of 4.3 wt. % dropped to 3.6 wt. % after 50 cycles. This decrease was explained by the formation of Mg-Al phases during cycling. [190] The pellet started to mechanically degrade before 20 cycles and was completely pulverized by 50 cycles.

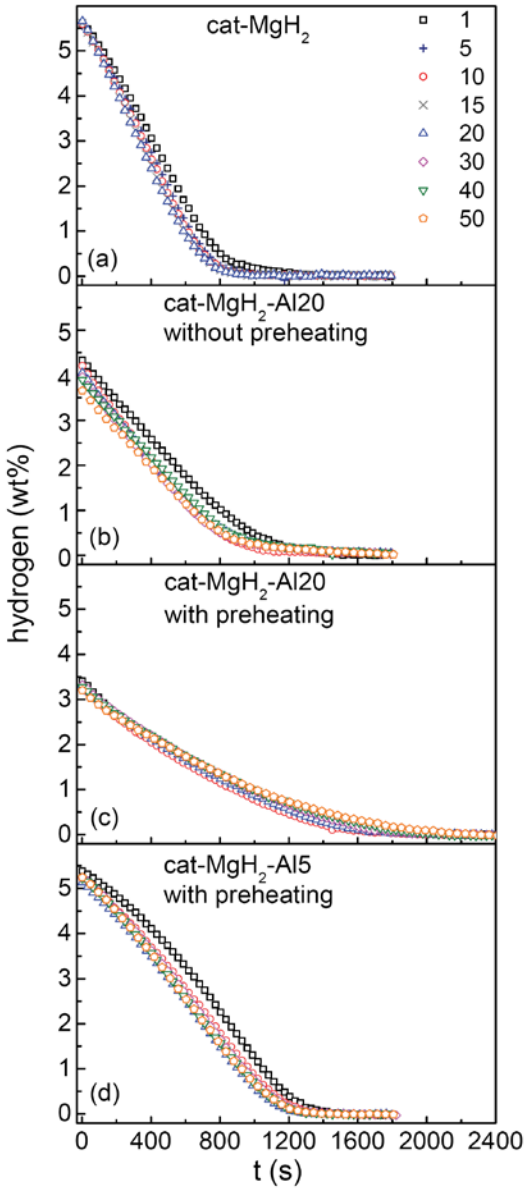

Figure 83. Desorption cycles performed at 320 °C and 1.2 atm H_2 of pellets cat-MgH_2 (a), catMgH_2-Al20 without preheating (b), cat-MgH_2-Al20 with preheating (c) and cat-MgH_2-Al5 with preheating (d).[186]

A similar pellet was annealed under vacuum before hydrogen testing (Figure 83c). The initial hydrogen capacity was lower (3.3 wt. %) but was essentially stable for 50 cycles. The mechanical degradation was started before 50 cycles but was not as severe as the un-annealed sample.

The annealed cat-MgH_2-Al5 pellet with 5% Al (Figure 83d) had a higher capacity of 5.3 wt. % with much faster kinetics and reduced capacity and mechanical degradation. The pellet remained mechanically intact after 50 cycles.

In this example study, the pellets were visually inspected before, during and after cycling (pictures are shown in Figure 84). From the images, it can be seen that the pellets without aluminum have expanded in size with cycling, while the 5 wt. % Al containing pellets did not.

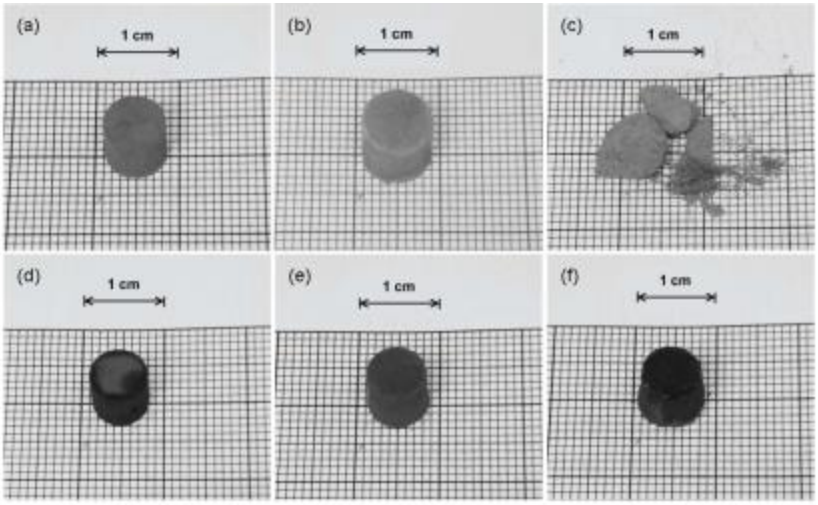

Figure 84. Pictures of the pellets after different cycles. (a), (b) and (c) were the pellets cat-MgH_2 after 10, 20 and 50 hydrogen a/d cycles, respectively, while (d), (e) and (f) were the pellets catMgH_2-Al5 preheated at 450 °C after 10, 20 and 50 hydrogen a/d cycles, respectively.[186]

XRD measurements and analysis were performed as a part of this work by Agresti et al. They found Mg, significant quantities of the intermetallic eutectic phase $Al_{12}Mg_{17}$, and residual amounts of MgH_2, MgO, and Al in the cycled and desorbed cat-MgH2-Al20. The same sample after hydrogenation contained $Al_{12}Mg_{17}$ and Al_3Mg_2 in addition to MgH_2. This agreed with the study of the hydrogenation of ball milled Mg-Al powders by Crivello et al.[191,192] which was shown to follow two completely reversible steps:

Equation 38 $$\mathbf{Al_{12}Mg_{17} + 9H_2 \Leftrightarrow 9MgH_2 + 4Al_3Mg_2}$$

Equation 39 $$\mathbf{4Al_3Mg_2 + 8H_2 \Leftrightarrow 8MgH_2 + 12Al}$$

The XRD pattern of the cat-MgH_2-Al5 dehydrogenated pellet after heat treatment and 50 cycles showed no evidence of Mg-Al intermetallic phases. According to the Mg-Al phase diagram, the smaller amount of Al was sufficient to form a solid solution of Al in Mg but not a eutectic phase. The authors found from the XRD analysis that lattice parameters of Mg were smaller than those of pure Mg, supporting the presence of a Mg(Al) solid solution.[193]

In the same study PCT measurements were made on the annealed cat-MgH_2-Al5 pellet (Figure 85). There was only a single plateau and the values of the enthalpy (ΔH = -73 kJ mol^{-1} H_2) and the entropy (ΔS = -135 J K^{-1} mol^{-1} H_2) from the van't Hoff plot (inset of Figure 85), were in good agreement with those of pure MgH_2, further indicating the lack of a Eutectic Mg-Al phase.[194]

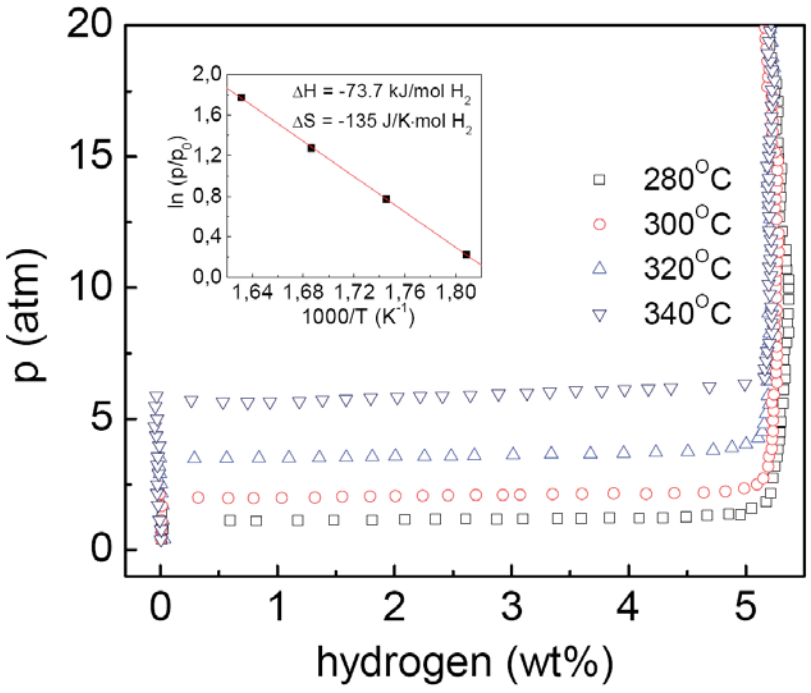

Figure 85. Lattice pressure-composition-isotherms at different temperatures for the cat-MgH_2Al_5 pellet preheated at 450 °C. The inset shows the corresponding van't Hoff plot.[186]

It was concluded that the better mechanical stability of the 5% versus 20% Al content samples was due to the presence of Al only in solid solution versus in the $Al_{12}Mg_{17}$ intermetallic phase. The eutectic $Al_{12}Mg_{17}$ phase, being fragile, can cause an embrittlement of the whole material. The ductility of the material can be improved by reducing the amount of this phase,[195] even in view of its localization along grain boundaries of the hosting Mg alloy.[196]

Mechanical testing was performed in the referenced study on hydrogenated pellets with and without 5 wt. % Al before and after 50 cycles (Figure 86). The results supported the prior observations. The better performance of the 5 wt. % Al containing pellets was attributed to the presence of an Al matrix surrounding the MgH_2 particles.

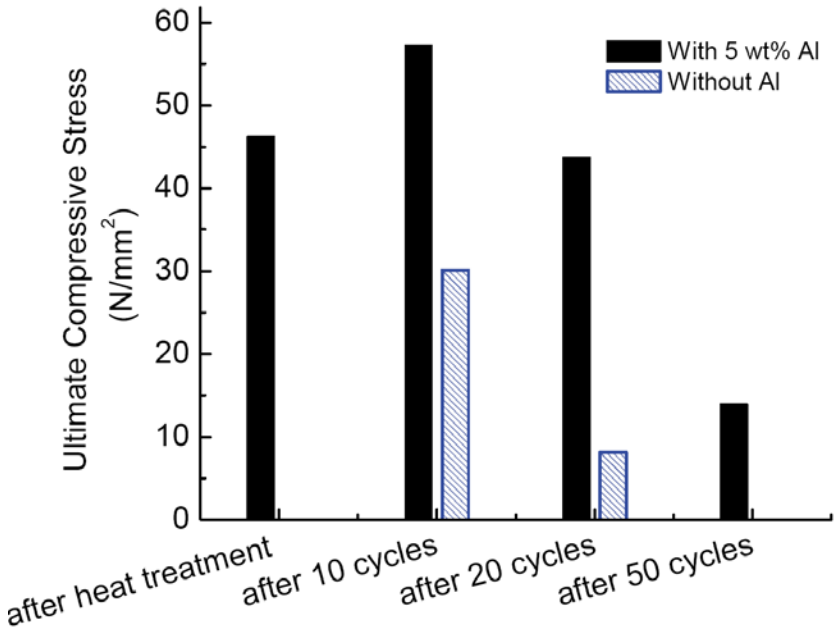

Figure 86. Results of the compression tests to estimate the mechanical strength of the pellets without and with 5 wt. % Al.[186]

This conclusion was supported by SEM analysis, which showed the formation of a connected aluminum matrix. The imaging results demonstrated that cycling increased the homogeneity of the aluminum matrix/MgH_2 phase composite.

In this example the authors concluded that the mechanical strength of pellets made by mixing catalyzed MgH_2 with aluminum powder as a binding agent and pressing into pellets improves the hydrogen storage performance and mechanical stability with hydrogen cycling.[186,187] It was found that a preheating treatment of the pellet to the temperature sufficient to form intermetallic phases and/or solid Mg-Al solutions (450 °C) increases the resulting performance of the material. Better mechanical stability was observed for pellets with 5 wt. % Al versus those with 20 wt. % Al. The enhanced stability of the pellets was attributed to the presence of the Al in solid solution with Mg. This example demonstrates that the strength of materials can impact the mechanical and hydrogen storage properties of materials and provides an example of how these

properties can be well investigated using a combination of standard material science techniques.

2.4.3 Cycling and Mechanical Durability

The ability to test and quantify hydrogen storage performance and mechanical durability with cycling of hydrogen storage materials is critical for systems development. A good example of this type of measurements comes from a recent study of the cycle durability of sodium alanates. Johnson et al. reported on the cycle testing of a reduced-scale sodium alanate sample in preparation of the production of a scale-up demonstration system.[197] For this work a sample holder was designed to hold about 20 grams of material. It incorporated three thermocouple wells; one embedded in the sample and two monitoring the wall temperature as shown in Figure 87.

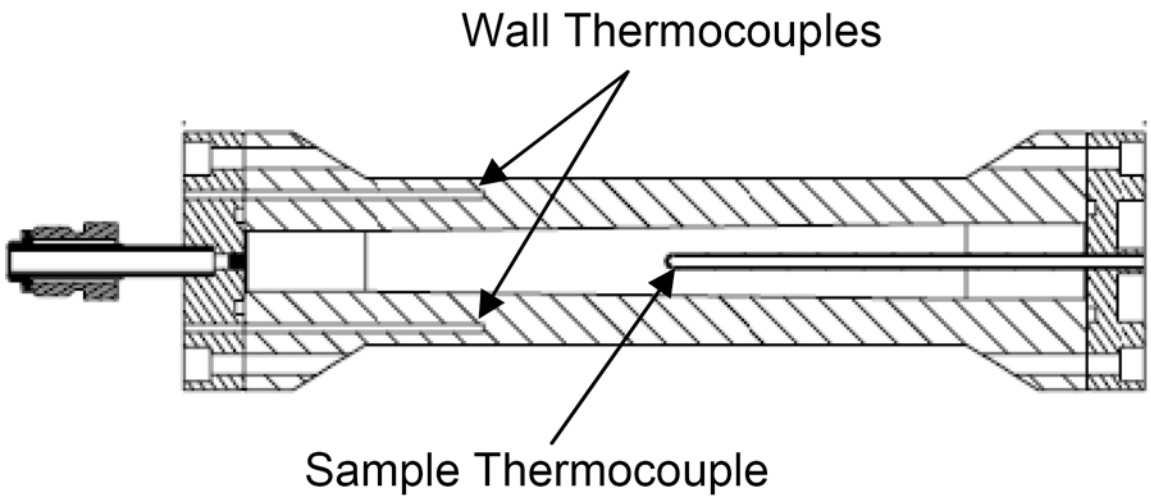

Figure 87. Sample holder for a 100-cycle durability test of sodium alanate.[197]

The sample holder attached to the hydriding system is shown in Figure 88. A Sieverts-type apparatus was used for semi-automated cycling of sample. The following hydrogen sorption procedure was carried out for all 100 cycles of the test. The sample was preheated to 140 °C, then exposed to hydrogen at 1800 psi for 30 minutes while the temperature was ramped to 155 °C to improve the absorption kinetics of the tetrahydride phase. For the desorption part of each cycle, the pressure was lowered and the sample temperature was increased from 155 °C to 200 °C and then held for 1 hour. The temperature ramping rate was designed so that the tetrahydride phase would fully decompose by the time the temperature reached 175 °C, then

the hexahydride phase began to decompose at around 190 °C. The 1 hour duration was sufficient to completely desorb the sample.

Figure 88. Sample holder attached to the hydriding system.[197]

The hydrogen capacity data from several absorptions between 5 and 96 cycles is presented in Figure 89. A reduction in the hydriding kinetics is clearly observed for both hydride phases as well as a drop in the capacity at 30 minutes of absorption.

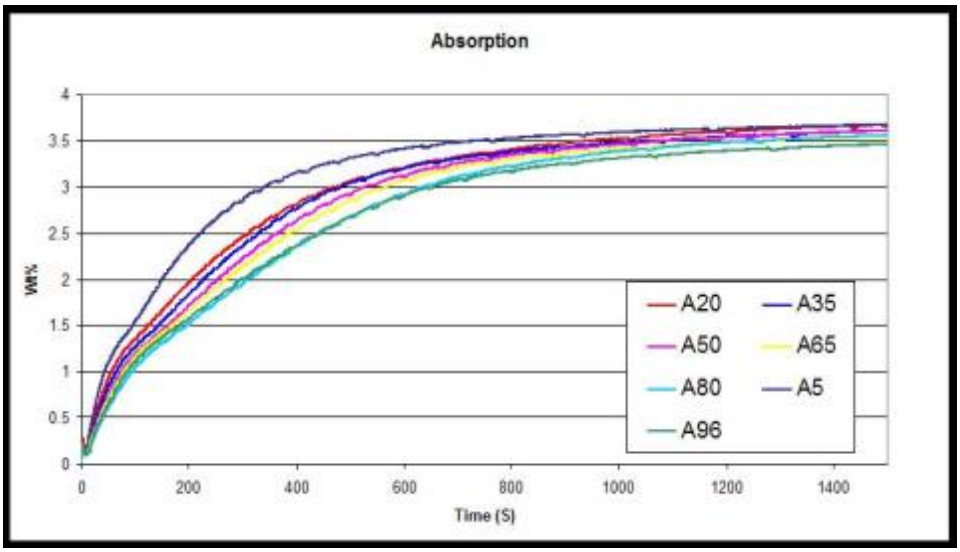

Figure 89. Absorption data from the 100 cycle tests.[197]

The capacity reduction was shown as a function of cycle in Figure 90. Note that the hydrogen capacity is an "effective capacity" because the fixed duration of the measurement means that the final capacity is also a function of kinetics.

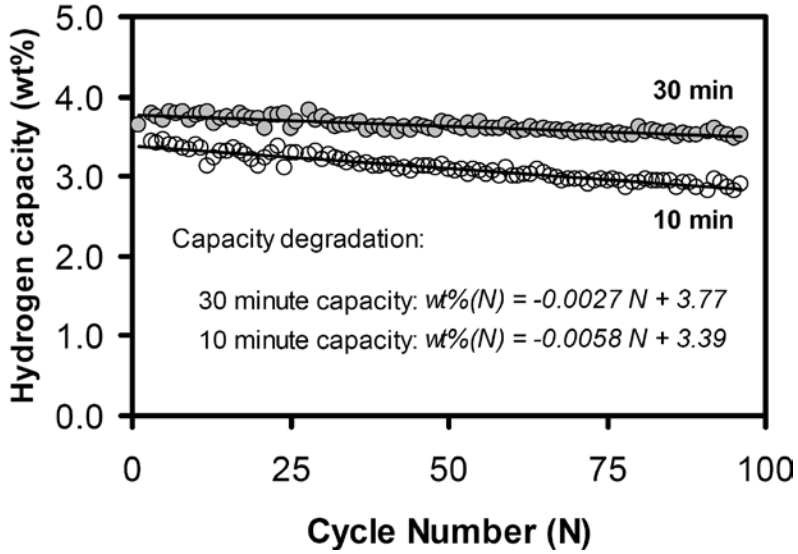

Figure 90. Small sample capacity degradation as a function of cycle number for ten minute and thirty minute refueling times.[197]

One way to get a feeling for the impact of a change in kinetics on the final capacity values is to plot the effective capacity at two different times (in this case after ten and thirty minutes, shown in Figure 90). The ten minute capacity decreased at a greater rate (0.006 wt. % per cycle)

than the thirty minute capacity (0.003 wt. % per cycle). Another possibility to have a feeling for the relative impact of the effects of intrinsic capacity loss versus kinetics effects would be to fit each sorption curve (typically with a double exponential) and extrapolate the capacity of each cycle to infinite time.

The authors of the study concluded that several causes for the observed kinetics (~capacity) degradation were possible including:

1. Sample contamination with organic material entrained in the hydrogen stream
2. Oxidation of the alanate from O_2 and/or H_2O entrained in the hydrogen stream
3. Morphological changes in the material that reduces the reactive surface area of the solid reacting species
4. A decrease in catalytic activity due to changes in the titanium catalyst

To better understand potential causes of the observed degradation in performance, the total hydrogen capacities of each phase of the material were measured.[197] These tests indicated that both alanate phases of the material after 100 cycles showed nearly a 10% reduction in full capacity relative to that measured for the un-cycled material. Therefore, the reduced effective capacity was not just due to declining kinetics and was not phase dependent.

With this knowledge the authors then perused investigations of possible contamination of the materials. The hydrogen gas used for cycling the alanate had undetectable levels of hydrocarbons, 5.6 ppm of water, and 1.3 ppm levels of oxygen. In their assessment these levels of water and oxygen were insufficient to cause the observed degradation.[197]

Next, the materials were examined for morphological changes using SEM/EDX on the fresh and cycled materials.[197] SEM imaging indicated the presence of two distinct types of particles. A spherical phase was more prevalent in the fresh materials while a fine cluster was more common in the cycled materials. EDX measurements showed that the spherical phase tended to be predominately aluminum with very little detectable titanium, while the fine clusters tended to be titanium rich sodium particles.

To test whether these morphological effects was the source of degradation, the cycled material was ball milled again and then measured for hydrogen uptake. The results are shown in Figure 91. After re-milling, the hexahydride capacity was fully restored. The tetrahydride kinetics were restored and the capacity recovered to within 0.17 wt. % of the fresh material. This indicated that much of the degradation in this sample was due to morphology changes, not contamination.[197]

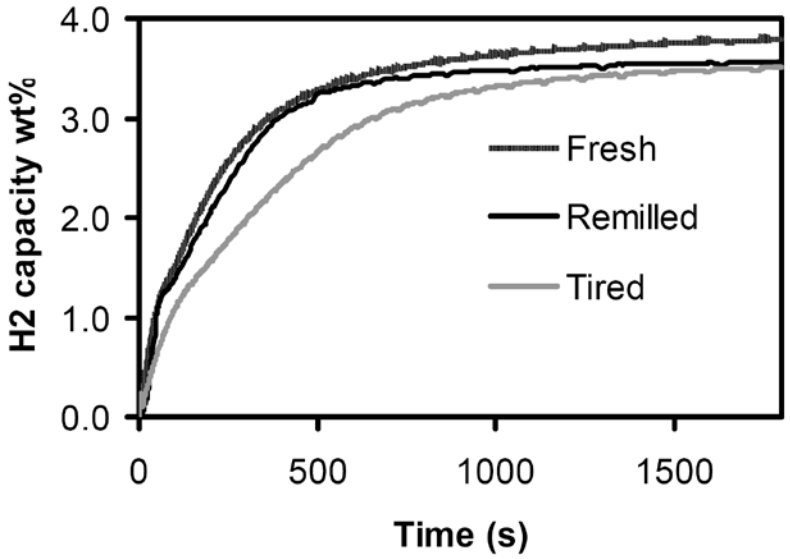

Figure 91. Relative kinetic and capacity comparison for fresh, aged, and re-milled samples undergoing 30 minute absorptions at 122 bar and 150 °C.[197]

In a follow-on study, a scaled-up demonstration hydrogen storage system was developed by Sandia.[197] The system consisted of four identical storage modules and was tested for similar performance degradation issues. Each module contained twelve tubes filled with sodium alanate arranged in a staggered 4 by 3 array all enclosed within a heat exchanger shell. One of these modules is shown in Figure 92.

Figure 92. Demonstration System hydrogen storage module.[197]

Details of the results of testing can be found in a report prepared by Sandia.[197] To summarize, the kinetics of both phases diminished and final capacity decreased with cycling similarly to the small sample degradation presented above. The authors concluded that while the results of initial cycle testing were not directly comparable to the small sample results due to the differences in the cycle procedure, they did indicate a similar degradation rate in the vehicle-scale system. Additional degradation was observed with further cycling. Due to the continued drop in hydrogen capacity, the scope of the work was modified.

In this additional part of the study the capacity loss was investigated by disassembling one of the modules to remove and section individual tubes.[197] A novel procedure, developed earlier in the program, was performed in order to deactivate any potentially unstable oxides that might have formed from air or moisture contamination.[198] The procedure involved exposing the module to a 25 psi overpressure of CO_2 for a period of about one hour. Any sodium alanates that had been oxidized would react with CO_2 to form more stable carbonates.

The CO_2 exothermically reacts with alanate-oxides. Monitoring of changes in the bed temperature upon introduction of CO_2 was performed using a handheld thermocouple and an infrared camera. The temperatures at the end of the bed's alanate containment tube rose to nearly 70 °C. This was close to the equilibrium temperature for the carbonate reaction at the applied pressure. IR imaging (shown below in Figure 93) indicated that the reaction was restricted to the first several inches of the tubes. These novel measurements proved very useful and demonstrated through the reaction with CO_2 that at least some fraction of the sodium alanate materials were oxidized.

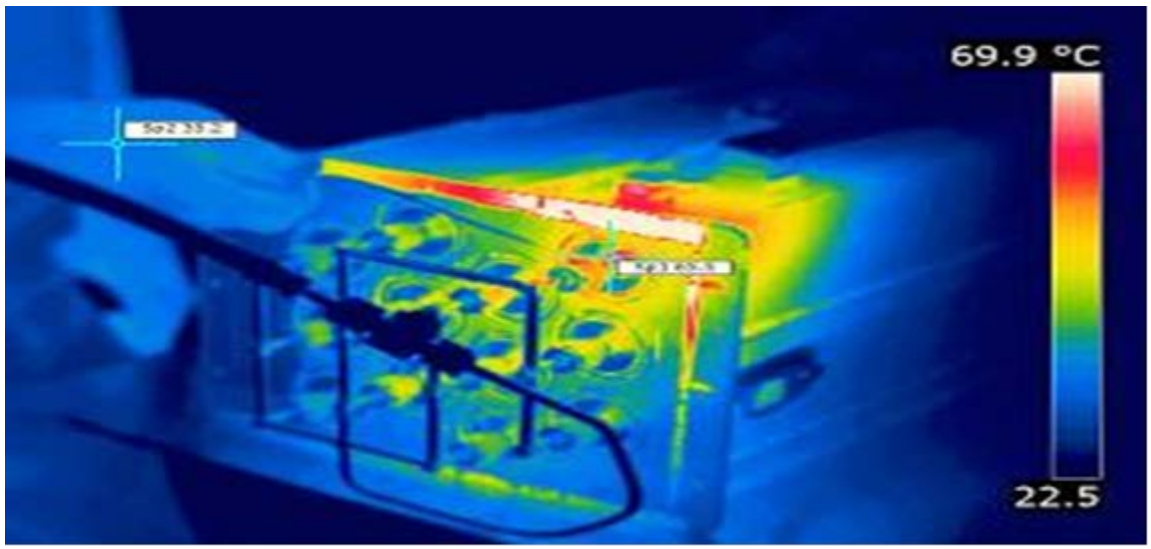

Figure 93. Infrared image of Module 3 while exposed to 25 psi CO_2. The exotherm suggests carbonate formation from oxidized alanates.[197]

Following the CO_2 treatment, the module was disassembled and two tubes were sectioned in an inert gas glove box. The tubes were subjected to a final CO_2 treatment prior to sectioning and IR measurement showed that the middle section of the tube still contained unconverted oxides. However, the oxidation appeared to have not reached the far end of the tube. By sectioning it was observed that sodium alanate had sintered into a solid cylinder over most of the length and shrunk away from the inner wall of the tubes and, thus, could be removed easily.

Through visual observations of the material, there was not a strong indication of oxidation from the physical appearance of the sodium alanate. The material appeared much the same as it had when it was initially loaded, except for the sintering.

In order to quantify the degree of oxidation, measurements were performed using a Simultaneous Thermogravimetric Modulated Beam Mass Spectrometer (STMBMS) instrument. The measurements involve heating a sample contained in a Knudsen cell under vacuum to produce a molecular beam that is characterized with a quadrupole mass spectrometer. Measured signals provide information on the quantity and the evolution rate of volatiles including CO_2. An experiment was run in which 3.0 mg of $NaHCO_3$ was mixed with 65 mg of a sample taken from the inlet region. The mass spectrometer CO_2 signal from the experiment with the added sodium bicarbonate was over 100 times larger than the CO_2 signals from the inlet sample by itself. In the sample from the inlet by itself the CO_2 evolves between 70 and 150 °C. In the experiment with the added $NaHCO_3$, the CO_2 and H_2O evolve between 100 and 175 °C. This suggests that the CO_2 that evolves from the sample inlet does not evolve from pure $NaHCO_3$ in the sample.

The results allowed a quantitative predication of the amount of alanate oxides that would have to have been present in the bed. The observed capacity degradation in the bed was nearly 10% of the starting hydrogen capacity. Assuming that each mole of sodium bicarbonate originated from one mole of sodium oxide, one would expect to see that nearly 10 mol % of the sodium was oxidized and subsequently converted into sodium bicarbonate upon CO_2 treatment, but this was not observed. It was concluded that the contamination process was much more complex potentially including oxidation of the aluminum, and titanium present in the materials.

The CO_2 treatment used in this example has proven to be a very important tool in the investigation of materials degradation. In this case it explained some, but not all of the observed capacity loss. Further investigation is warranted to determine the source of capacity loss whether it is from contamination, segregation, mechanical separation, etc. This study introduced new and valuable tools in the study of the engineering properties in the development of hydrogen storage materials.

2.5 Induced Mechanical Force Measurements

It is known that pressure due to volume expansion of some storage materials during hydrogen absorption can cause serious detriment or failure to storage vessels (see section 1.5). This effect presents itself with classic metal hydrides, which experience significant expansion of the crystal lattice during hydrogen absorption. For the containment vessel to be impacted by this lattice expansion, the metal hydride powders must be compacted in a way that the crystal expansion forces cannot be accommodated in any other way except by strain imposed on the vessel. This can occur through a process of particle size reduction and packing due to decrepitation and powder densification (possibly by vibration). Decrepitation is the systematic physical pulverization of larger particles into smaller ones due to high strain induced by hydrogen cycling (see
section 1.4). Following decrepitation, the particles tend to settle and realign under the influence of gravity and/or vibration causing densification of the powder (see section 1.10). With further hydrogen cycling, the high density powder sections of the bed expand. Because of settling, there is little or no void space in the vessel around the powder and so the expansion is directed outward, exerting large forces on the wall of the containment vessel. In extreme cases, structural failures of the containment vessel can occur, causing a release of hydrogen gas and exposure of the reactive storage materials to the surrounding environment. For this reason, a hydride containment vessel would have to withstand not only the hydrogen gas pressure but also the mechanical pressure exerted by bulk material expansion. This may add unreasonable weight and cost to the storage vessel. A better option is to include in the engineering design of the containment system a means to prevent the powders from compacting and/or mitigate the transfer of the hydride expansion forces to the vessel.

Prior to pursuing any system design based on potential material volume expansion forces, an in-depth analysis of hydrogen storage materials mechanical behavior should be completed. A recent study by Charlas et al. provides a good example of an in depth study of the mechanical characteristics and effects on the storage bed of metal hydride absorption/desorption cycles.[199] Storage materials will not all behave the same in this respect. Complex hydrides have generated a lot of interest for the reversible chemical storage of hydrogen. The very promising Ti-doped alanates are a good example. It is known that, like conventional metal hydrides, sodium alanates expand and contract during the sorption of hydrogen. From a simple calculation of the single crystal density of stoichiometric sodium alanates, the solid material volume decreases by 33% during dehydrogenation or increases by 49% on hydrogen uptake.

Equation 40	**MIXTURE A (Stoichiometric Ti-doped $NaAlH_4$)[200]**	
2.17 g cm^{-3}	2.02 g cm^{-3}	1.46 g cm^{-3}
100 NaH + 100 Al +4Ti + 12 NaCl ⇔	**$33Na_3AlH_6$ + 66Al +4Ti + 12 NaCl** ⇔	**$100NaAlH_4$ + 4Ti + 12 NaCl**

This is more than twice the (fully dense) material volume expansion than is found in the $LaNi_{4.78}Sn_{0.22}$ alloy that caused the vessel expansion shown below.[51,201]

Figure 94. Hydride hydrogen storage vessel deformation caused by material expansion on hydride formation.[51]

However, it is important to understand that many complex hydrides take-up and release hydrogen through decomposition/formation reactions rather than the dissolution of atomic hydrogen and formation of hydride through M-H bonding of hydrogen in interstitial sites of an intermetallic compound. This is particularly true of the Ti-doped sodium alanates reactions described in Equation 40. The hydrides $NaAlH_4$, Na_3AlH_6, and NaH are not equivalent in their Al/Na ratios (1, 1/3, and 0 respectively). This means that long range transport of some form of Na or Al must occur to form the hydrides. This means that particles of the constituent compounds $NaAlH_4$, Na_3AlH_6, NaH and Al are either formed or consumed in the reversible reactions of Equation 40.[202] Ultimately, the material volume changes that occur on going from Na+Al to the hydride $NaAlH_4$, are simply the difference in densities in the (growth of) product particles and the (consumption of) reactant particles. It can be imagined that (through whatever means) the mobility of metal atoms allows the growth of particles into unconstrained directions (e.g. voids in the powders). Even with highly compressed powders, this mobility should allow the relaxation of local strain that may present itself differently on a bulk scale than what is observed for interstitial metal hydrides. In the case of interstitial metal hydrides, lattice expansion takes place in single crystal domains causing crack formation and particle-to-particle forces. Crystal structures remain relatively intact and so expansion occurs in the crystal domain that does not necessarily accommodate stress in the same manner as hydride formation through decomposition/formation reactions. Ultimately, bulk forces may be significantly different for some complex hydrides compared to interstitial metal hydrides.

An additional consideration is whether confining a hydrogen storage material in a compressed state will have any effect on the storage properties of the material itself. This was the driver behind the investigations by Dedrick et al. on experimental measurements of expansion forces in Ti-doped sodium alanates.[200,203] In two sets of investigations the pressure exerted by the bulk

expansion of a sodium aluminum hydride bed was measured as a function of hydrogen content. An initial system was designed to measure pressure exerted on a metal diaphragm during hydriding of a stoichiometric (Equation 40) Ti-doped sodium alanate sample.[203] The test apparatus is shown in Figure 95.

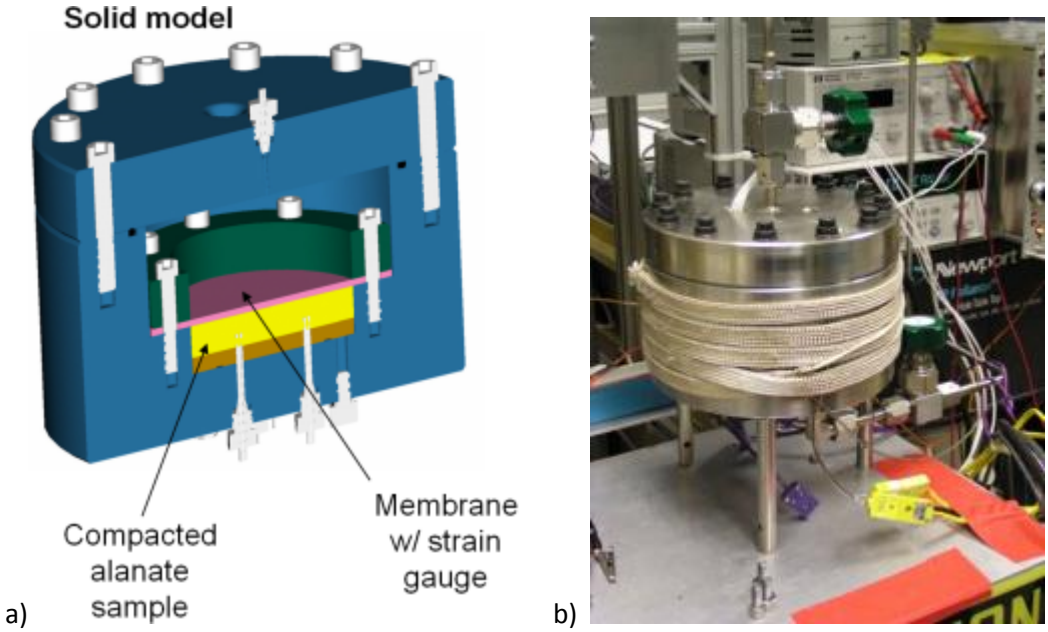

Figure 95. a) Solid mechanics model of expansion pressure testing system, and b) mechanical properties test cell.[203]

In this setup desorbed alanate material was compressed into the bottom of the cell at different compaction loadings. A membrane was fixed at the top surface of the alanate. Hydrogen gas could pass on either side of the cell membrane such that the force on the membrane was only that of the expansion of the alanate, which was hydrided *in situ*. A strain gauge was attached to the top of the plate to measure deformation in the plate with hydride expansion.

The equation for the maximum stress at the center of a circular plate with a clamped outer edge and a uniform expansion pressure is:

Equation 41

$$\sigma = \frac{3 \cdot \left(q \cdot a^2 \cdot (1 - v)\right)}{8 \cdot t^2}$$

and the strain is given by:

$$\varepsilon = \frac{\sigma \cdot (1 - v^2)}{(1 - v) \cdot E}$$

Equation 42

where σ = stress, ε = strain, q = pressure, v = Poisons ratio, a = radius of the plate, t = thickness of the plate, and E = Young's modulus.

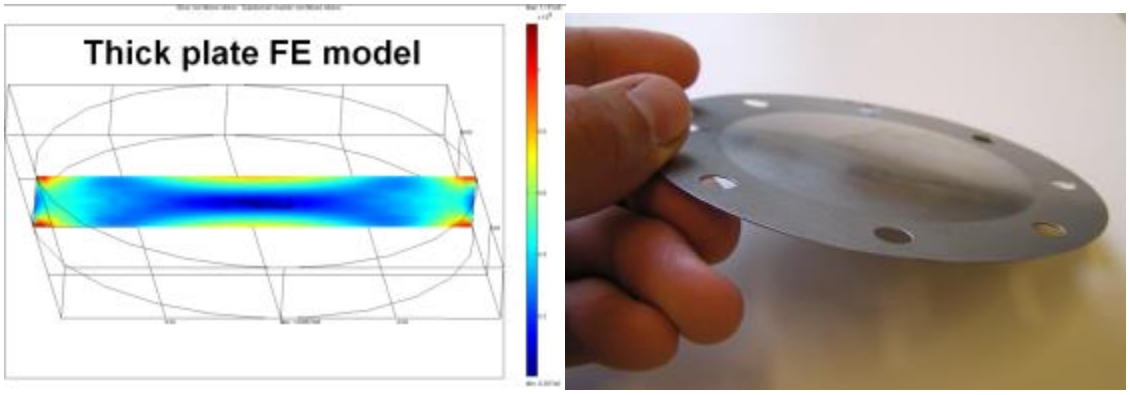

Figure 96. Finite element modeling of deflection forces in the strain measurement plate and an image of the plate after deformation.[203]

Plate wall stain was measure on desorbed alanate samples, which were compressed to measured densities of 0.7, 0.9, and 1.0 g cm^{-3}. At these densities the maximum expansion pressure from alanate expansion was determined from the strain measurements to be about 7 bar, thus contributing very little to the overall wall pressure. No measurable effects on capacity or sorption rates were observed. The authors concluded that when constrained, the alanate material appears to self-compact during absorption with very little additional force on the vessel wall.

The materials were then tested at a maximum compaction density of 1.2 g cm^{-3}, approaching the crystal density of the unhydrided material.

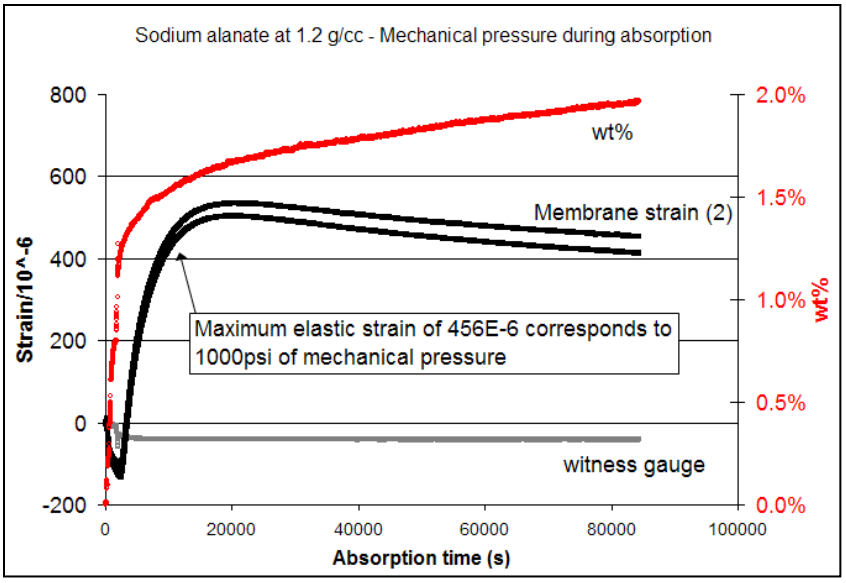

Figure 97. Strain gauge and capacity measurements for alanate compressed to 1.2 g cm^{-3} or 90% of single crystal density of $NaAlH_4$.[203]

At this density the measurement (Figure 97) indicated mechanical pressure exerted on a wall of ~70 bar in addition to gas pressure. The measurements also demonstrated high gas flow restriction along with unfavorable absorption characteristics (max capacity 2.3 wt. %). Thus, while the measurements at lower packing density were found to exert negligible pressure up to capacities of 3.3 wt. %, these results were disconcerting and pointed out the need for a more detailed and precise study.[200] It was concluded that the current measurement apparatus lacked direct calibration and temperature compensation which adversely affected the measurement accuracy.

The strain measurement of a hydride-containing vessel wall can be difficult for two reasons: 1) the temperature excursions intrinsic to the uptake and release of hydrogen can cause significant strain measurement errors, and 2) the strain induced by the gas pressure can complicate the measurement of mechanical expansion-induced strain. In practice, these difficulties can be overcome with advanced instrumentation design, which includes temperature compensation and gas pressure induced signal calibration. One example of another method for measuring stress and strain in a hydride-containing vessel wall was described by Nasako et al.[204]

For the above reasons a second study was completed by Dedrick et al. utilizing a new apparatus.[200] To more closely simulate full-scale bed designs a new cell was constructed with the sample in cylindrical geometry and measuring the radial expansion force. Temperature compensation was added to the pressure sensing circuit, and direct calibration capabilities were incorporated in the measurement procedures. The measurement apparatus consisted of two parts: 1) a hydrogen pressure vessel to allow *in situ* cycling of the hydrogen storage material and

2) an expansion force sensing vessel. The expansion force sensing vessel was designed to measure the material bulk expansion without the influence of the gas pressure by maintaining equal gas pressure on each side of the sensing element. A rendering of the experimental system is shown in Figure 98.

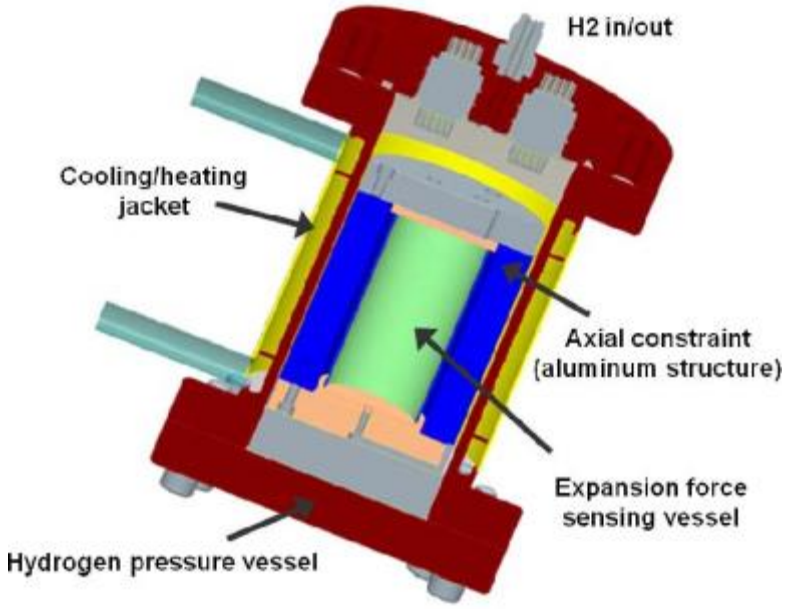

Figure 98. Experimental hardware developed for the expansion force measurements included an external hydrogen pressure vessel and an internal force-sensing vessel.[203]

The expansion force-sensing vessel was an open-ended 304 series stainless steel cylinder of 0.030 inch wall thickness. Two transducer-quality strain gauges were affixed to the surface of the cylinder. Axial expansion of the material is limited by an aluminum structure (Figure 98). The sensing vessel is capped on each end by a PTFE spacer that functions to provide a physical and thermal barrier between the hydrogen storage material and the surrounding components. Tolerances were designed into the structure to accommodate thermal expansion of all materials and to maintain the sensing vessel in a normally unconstrained state.

The two bi-axial strain gauges were mounted on the expansion force-sensing vessel using a special high temperature adhesive (M-Bond 610) (Figure 99a). Each bi-axial gauge consisted of two sensors oriented perpendicular to each other. The bi-axial gauges were positioned such that one sensor was in the radial direction to measure the expansion forces. The perpendicular sensor was therefore in the axial unconstrained direction, and used to provide temperature compensation. The two sensors of the bi-axial gauge experienced the same temperature changes and thus the same thermal resistance changes. The two sensors of each gauge were

wired in a Wheatstone bridge configuration (Figure 100). If each sensor of a gauge, including the leads, has the same resistance then the bridge is balanced and, regardless of temperature, the two outputs cancel. Figure 99b shows the electrical resistance diagram of the sensors in a bi-axial gauge. The values R_1, R_2 and R are resistance values of the short lead wires connected to the solder pad. Given that the resistance of the sensors is the same, then R should be equal to the sum of R_1 and R_2.

a)  b) 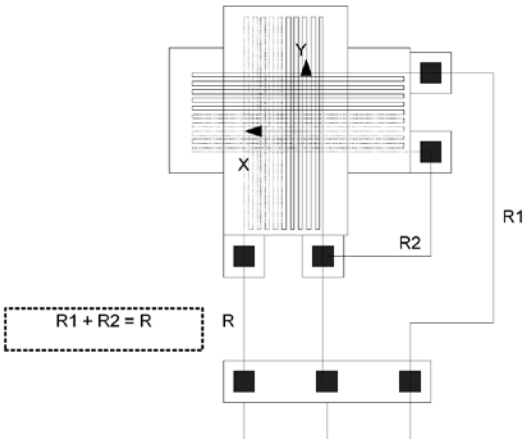

Figure 99. a) Bi-axial strain gauge attachment to expansion force-sensing vessel, and b) and bi-axial sensor setup.[200]

Temperature compensation is essential if one is to accurately measure strain since it can be on the order of 0.5 ppm K^{-1} (ppm; thermal coefficient of electrical circuit parts). For this particular test case, the temperature increase was 200 K potentially producing temperature related errors as high as a 100 ppm. This thermal error can be substantial on test specimens with low average strain measurements and may be lost in the noise if special attention is not given to the setup.

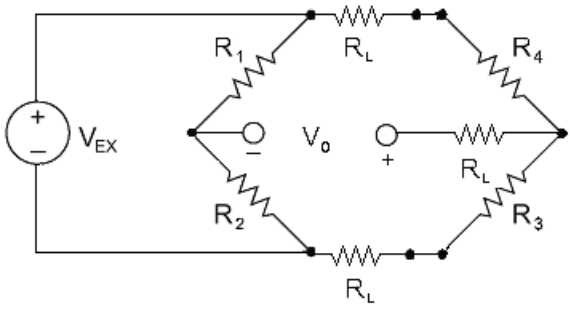

Figure 100. Wheatstone Bridge Circuit.[200]Error! Bookmark not defined.

Figure 100 shows the Wheatstone bridge circuit used in this reported measurement, where V_{EX} = excitation voltage, V_0 = Bridge output voltage, R_1 and R_2 = bridge completion resistances, R_3 and R_4 = strain gauges, and R_L = lead wire resistance. If the lead resistance is the same in each arm, R_L is a constant and the bridge circuit voltage reduces to:

Equation 43

$$V_O = \left[\frac{R_3}{R_3 + R_4} - \frac{R_2}{R_1 + R_2}\right] \bullet V_{EX}$$

Note that all lead resistance must be the same or the bridge will not balance and will lead to erroneous strain measurements. In the temperature compensated setup, R_3 was the active gauge and R_4 was the temperature compensation gauge. Temperature change causes the resistance in R_3 and R_4 to change equally, removing most of the temperature effects from the measurements. It was also important that the lead wires were routed close to each other so that they were all at the same temperature to reduce any other temperature related errors in the measurements. When a strain is applied to R_3 a voltage which is proportional only to the strain was measured. Thus, the measured output of the bridge is generated solely by the strain from the test cell. For this reason it is also important that no strain exist in the axial direction.

The procedures described by Dedrick et al. included rigorous and direct calibration methodologies to ensure the highest level of accuracy.[200] A direct gas pressure calibration method was designed to characterize each of the sensing vessels. The method was performed externally from the hydrogen pressure vessel, using aluminum caps with O-ring seals. Helium was introduced into the expansion force sensing cell and a correlation of pressure and strain was generated. This calibration was completed at various temperatures to capture the effect of variations in the strength and modulus of elasticity of the stainless steel of the cell.

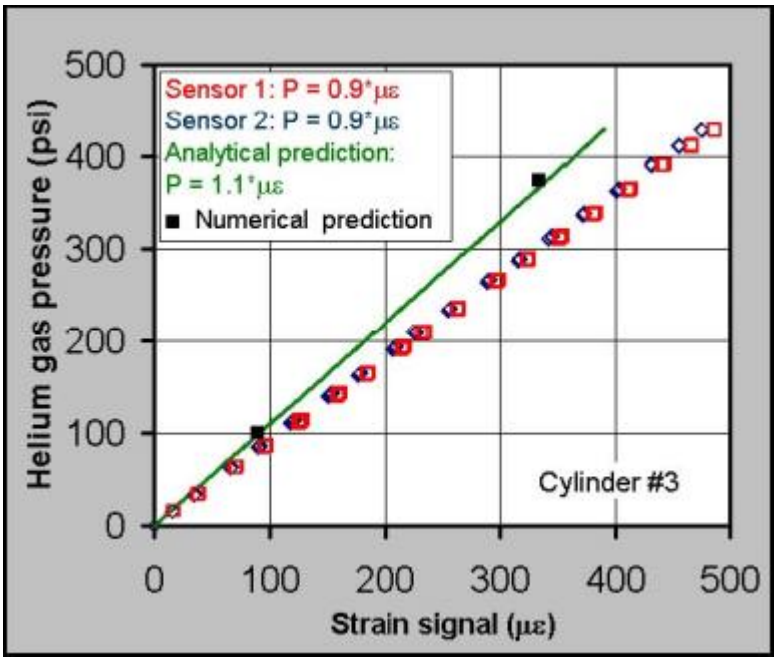

Figure 101. Example of direct calibration of expansion force sensing vessel. The pressure response is highly linear.[200]

The three calibrated sensing vessels each had a pressure response of 0.9 psi/με. Analytic and numerical calculations predict a pressure response of 1.1 psi/με. This difference between prediction and actual measurements (Figure 101) was suspected to be caused by physical properties estimation error of the cylinder, gauge misalignment, and/or strain-sensing error caused by the bonding process.[200] Direct calibration was used to reduce the impact of such effects. However, the differences point out the importance of direct calibration.

In addition to temperature compensation by the Wheatstone bridge, any residual temperature response was also incorporated into the external direct calibration. Eleven total temperature response tests were performed on cylinder #3. The magnitude of the response was approximately 0.6 ± 0.125 με/K (0.5 psi/K). This temperature response was removed from the strain signal by measurement of the cell temperature during experiments. The existence of the residual temperature response was assumed to likely be due to elemental differences in wires or contact resistances. The following is an assessment by Dedrick et al. of the errors involved in their measurements.[200]

Sources of measurement error include:

- Amplifier balance/calibration: Balance and calibration process was accurate to within 1 με.

- Temperature response: Temperature variation was kept below 40 K during testing – this would result in a signal error of 5 με at 0.125 με/K temperature response error.
- Amplifier drift: Maximum drift rate observed was 0.2 με/hr. Measurements were completed within 24 hours providing a maximum drift of 4.8 με.
- Calibration gas pressure measurement (especially below 100 psi): This error was negligible due to the calibration record of the pressure transducer and the linear response of the sensing vessel.
- Lead resistance changes: These variations were not accounted for due to minimal environmental changes and small temperature response of the lead wire material (Cu).

They found that direct calibration eliminates the following sources of error:

- Sensor placement/misalignment with the axial and radial direction.
- Inaccurate material properties estimation.
- Inaccurate vessel dimensions (thickness and diameter).
- Uncompensated lead resistance.

Additional errors were present due to gas flow resistance and/or thermal expansion. This caused a transient pressure signal that was not specifically correlated to the hydrogen uptake/release of the hydride material. The result of the study's error analysis was that the measurements were accurate to within < 11 με (12 psi).

In the second investigation, the authors used a slightly modified sample composition. They found in prior work that compositions that contain excess aluminum were more appropriate for full-scale systems.[205] Hydrogen capacities exceeding 3.8 wt. % were routinely achieved and higher packing densities were attainable due to the increase in aluminum content. Due to the significant differences in performance between Mixture A and Mixture B, additional wall pressure measurements were undertaken using the excess aluminum composition. The following non-stoichiometric mixture was for the expansion measurements. It contains a single crystal density decreased by 29% during desorption (with a 40% expansion in absorption):

Equation 44 MIXTURE B (Non-stoichiometric Ti-doped $NaAlH_4$)[200] Error! Bookmark not defined.

2.23 g cm^{-3}	2.09 g cm^{-3}	1.59 g cm^{-3}

$100\ NaH + 127\ Al + 4Ti + 12\ NaCl \Leftrightarrow 33Na_3AlH_6 + 93Al + 4Ti + 12\ NaCl \Leftrightarrow 100NaAlH_4 + 27Al + 4Ti + 12\ NaCl$

Measurements of the above Mixture B were completed at 1.0, 1.1, and 1.16 g cm^{-3} compression densities. The results from each density were found to be similar. The following is a summary of the measurements (all for the 1.16 g cm^{-3} density sample).

The first two absorption tests on all samples produced a complex pressure signal that was not well understood and difficult to correlate to any specific physical process (see cycles 1 and 2 in Figure 102). The authors speculate that strain is introduced to the pressure sensor during loading of the alanate precursors. This strain is then relieved during the first few sorption cycles and does not reappear. Regardless of the cause, what is observed as a pressure excursion was on the order of 100 psi – a small quantity compared to the gas pressures present. After the first two cycles, the pressure change on subsequent absorptions was small and of the same order as the system error (12 psi).

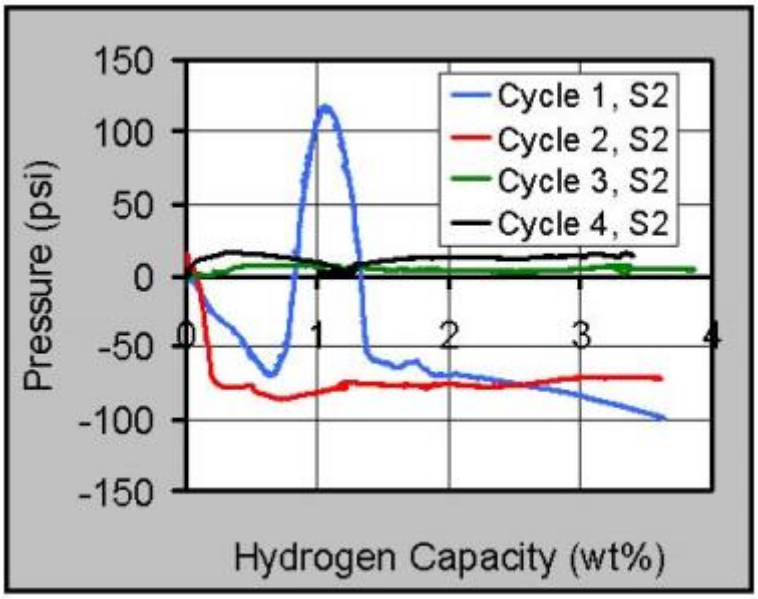

Figure 102. Pressure measured during absorption cycles 1 - 4 demonstrates that the sample initially relaxes, then exerts minimal pressure during absorption.[200]

No pressure changes were observed during the decomposition of the sodium aluminum tetrahydride ($NaAlH_4$) phase. However, the authors did find that as the system is heated to decompose the sodium aluminum hexahydride phase (Na_3AlH_6), a steady increase of pressure up to ~ 250 psi was observed, and decreased as the reaction neared completion (Figure 103).

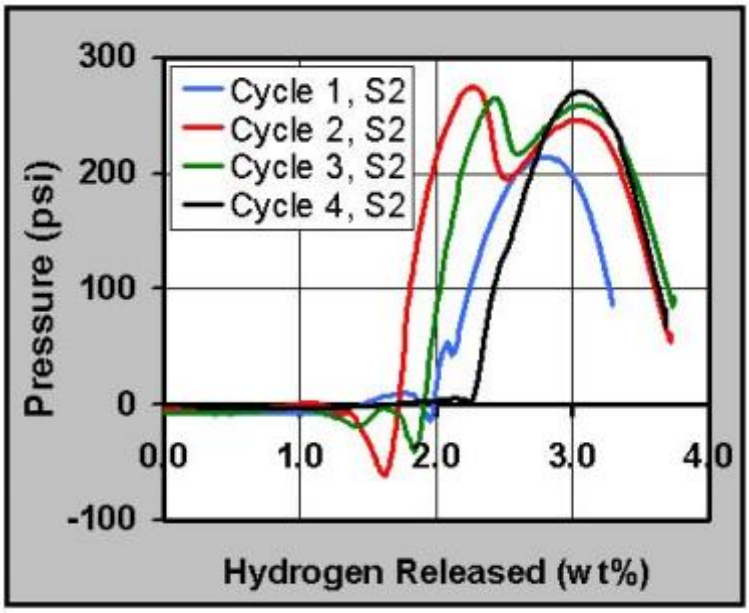

Figure 103. Decomposition of the tetrahydride phase exerts minimal pressure. Up to 250 psi of pressure is exerted, possibly due to thermal expansion.[200]

That measurement was followed by reheating the desorbed material bed but no pressure change was observed. Both temperature ramping pressure measurements are shown in (Figure 104). The authors of the study concluded that the pressure measured during desorption was due to the thermal expansion of the sodium aluminum hexahydride phase.[200]

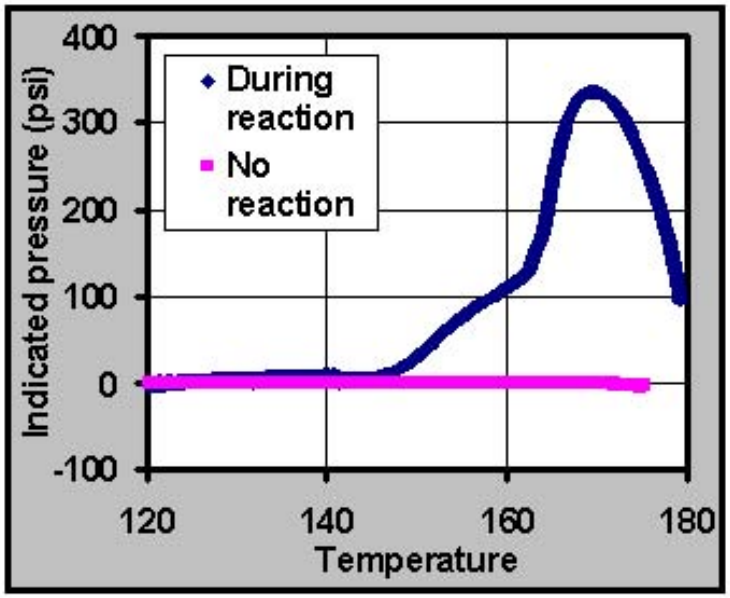

Figure 104. Pressure due to hydride heating is only observed during decomposition of the hexahydride phase. Heating of the decomposed bed does not result in a pressure signal.[200]

The presence of two different gauges in the test cell gave the experimenters the ability to check the spatial similarity of the bed's behavior. Figure 105 presents a typical pressure profile for each gauge during decomposition. The pressure sensor in the center of the bed recorded up to 300 psi higher pressure than the sensor near the edge. Pressure differences were observed between the two sensors especially during the first 1 wt. % of decomposition. These were attributed to gas pressure gradients within the sample.[200]

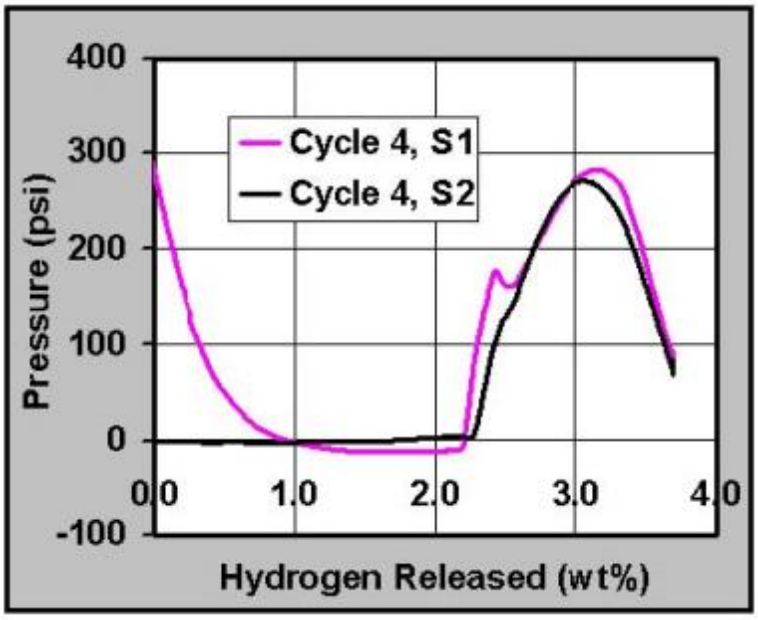

Figure 105. Gas pressure gradients are present within the bed during the first 10 minutes (1 wt. %) of desorption. "S1" represents the gauge near the mid-point of the bed (high pressure) while "S2" is placed near the edge (low pressure).[200]

In general, there was a poor correlation between exerted pressure and hydrogen capacity of the sodium alanates at all measured densities.[200] It was concluded that mechanical pressure due to the hydrogenation of sodium alanates is not significant enough to influence full-scale system design. However, it was noted that gas pressure gradients within the material may limit reaction rates, especially for high aspect ratio beds. It was recommended that strain be monitored in the development of large-scale systems during operation to verify that trends do not change over many cycles. Other compositions, chemistries, and geometries may exhibit different behavior and should be analyzed individually as necessary.

This series of investigations pointed out many of the important issues that must be considered when making these complex materials expansion measurements with a high degree of accuracy. These measurements will play an increasingly important role in the development and engineering design of materials-based hydrogen storage systems.

There is a possibility that these measurements and the measurements of cycling studies of alanates by Lozano et al. (section 1.15 Apparent Density Changes with Cycling) point to real physical property changes that are occurring in these compacted materials in the first few cycles.[85] In the Lozano et al. measurements of hydrogen absorption on 4 and 8 mm compacts the apparent densities of the alanates change in the first 3 cycles (Figure shown again below for clarity).

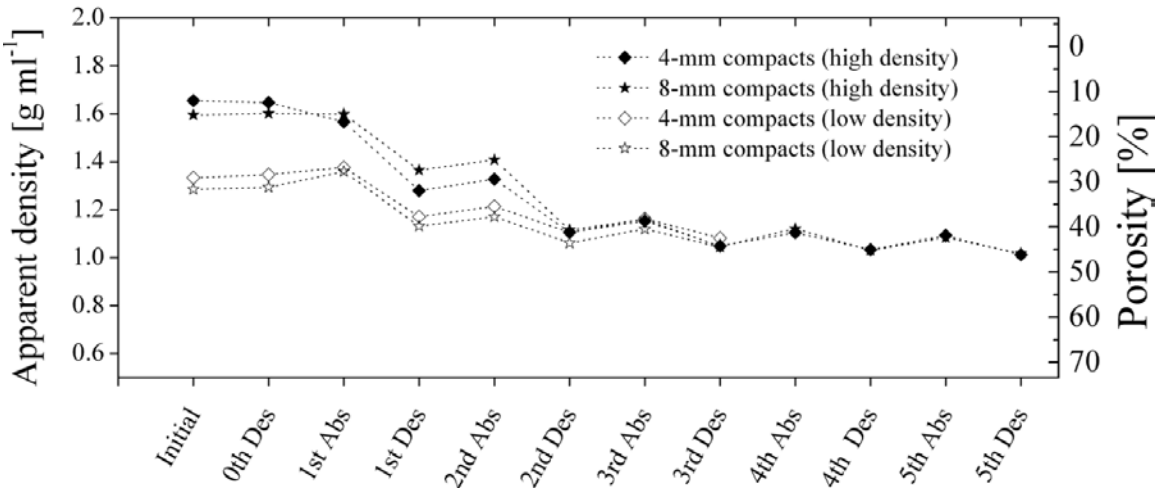

Figure 106. Apparent densities of compacts after hydrogen absorption and desorption cycles for compacts of initial low (1.3 g cm^{-3}) and high (1.6 g cm^{-3}) density.[85]

They found that the apparent density of the compacts decreases for both low and high density compacts, and that the apparent density of both low and high density compacts approach the same value of about 1.1 g cm^{-3} after the third cycle. The decrease in density was significantly greater for the high starting density compacts and most of the change occurred in the first two cycles. Also an interesting observation was that the compacts expanded more during hydrogen desorption than absorption (shown more clearly in Figure 50). This would appear to be the same behavior observed in Dedrick et al.'s work above that observed pressures on the cell wall during the first two to three cycles were more dramatic in desorption than absorption.[200]

One possible explanation put forth by Dedrick et al. is that the wall pressures they measured came from the hydrogen gas being released in the cell being blocked by poor permeation and, thus, causing a buildup of gas pressure. This may be possible. One way to do this is to overlay

the van't Hoff pressures of the decomposition of $NaAlH_4$ and Na_3AlH_6 against temperatures on their TPD data of Figure 104. This is shown in the figure below.

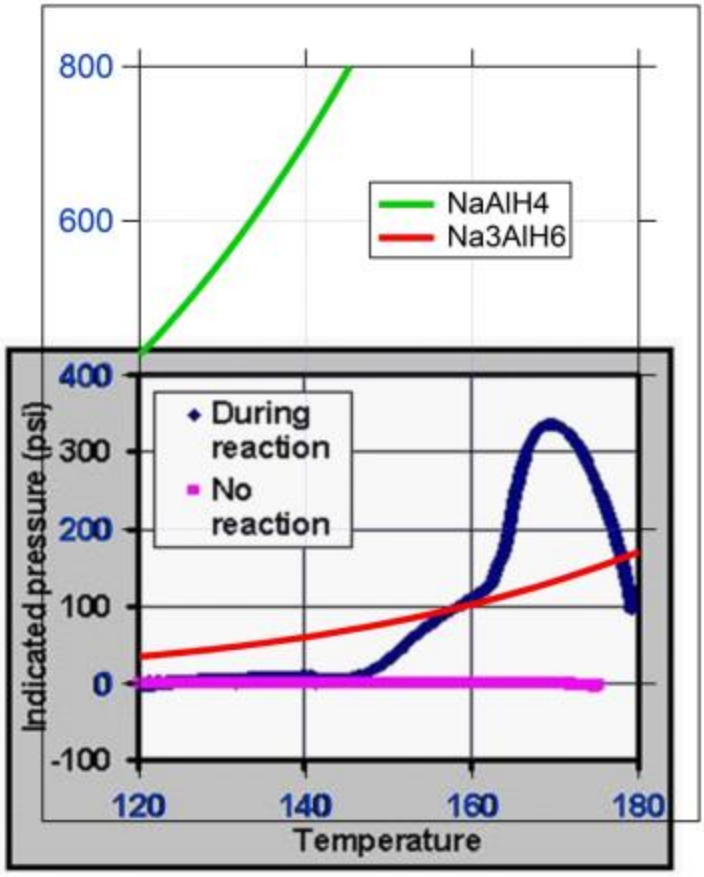

Figure 107. Van't Hoff equilibrium pressures of $NaAlH_4$ and Na_3AlH_6[206] overlaid on cell pressure measurements observed during decomposition of the hexahydride phase.[200]

It can be seen that the measured pressure rise is below the Na_3AlH_6 decomposition pressure just up to what appears to be a secondary increase in pressure. It may not be by accident that the inflection point occurs almost exactly at the van't Hoff pressure. If that were the case, then poor local hydrogen permeability would allow the pressure to build up locally to the equilibrium decomposition pressure. The decomposition reaction would then be thermodynamically slowed to a rate that is less than or matches the temperature ramping rate. There is not enough data in this one comparison to conclusively support this mechanism, but it is certainly worth further consideration. The second pressure peak cannot be easily explained in the absence of $NaAlH_4$ and may, in fact, be due to other physical phenomena.

The next question regards the disappearance of these pressure peaks after 2 to 3 cycles. This may be explained with the aid of the observations of Lozano et al.[85] Not only did their compacts

expand in the first 2 to 3 cycles, but inspection of the compacts showed that after cycling the surface was no longer smooth or shiny and fissures appeared on the surface of the initially high density compacts. Clearly morphological changes are occurring to the compacted powders in the first cycles, most likely to accommodate expansion forces, buildup of gas pressure, and interfacing of the reactive component phases. Such long-range compositional and morphological reorganization is credible given that the hydrogen uptake and release in these alanate materials occurs through multicomponent formation and decomposition reactions. It appears that the materials reach an organizational equilibrium after the first few cycles that relax the initially induced mechanical forces and potentially compositional imbalances.

These observations bring up interesting questions about not only the mechanisms involved, but also whether the materials could be improved by secondary compaction or the effects of additives. Certainly further investigations and improved accuracy in this area is warranted.

2.6 Mass Transport Measurements

Typically mass transport (hydrogen permeation and uptake) studies are made by performing hydrogen kinetics measurements at a system level. (See Section 2: Kinetics Measurements of the document "Recommended Best Practices for the Characterization of Storage Properties of Hydrogen Storage Materials"[24]) However, these techniques do not give details of how hydrogen gas flows through and is absorbed/adsorbed in the material in a storage bed. For this, a technique that allows time resolved special resolution of hydrogen concentration is required.

Hydrogen-sensitive, *in situ* neutron imaging has the capability of mapping hydrogen concentration profiles in real-time in three dimensions during absorption/desorption cycling of hydrogen storage systems.[207,208,209,210,211] A recent study by Jacobson et al. showed that neutron imaging can be a powerful and invaluable analytical tool to aid in the engineering design of hydrogen storage tanks for vehicular and stationary applications.[207] In this work, a series of neutron radiography and tomography measurements were used to study the transient and steady-state distributions, respectively, of hydrogen within a $LaNi_{4.78}Sn_{0.22}$-based hydrogen storage bed during and after various absorption and desorption steps.

The development of materials-based hydrogen storage vessels for hydrogen-powered passenger vehicles places severe mass and volume constraints on storage systems that must not only reliably and safely contain these materials but also permit potentially significant heat transfers during both hydrogen absorption and desorption.[40] Most designs for hydride-based hydrogen storage beds incorporate various features such as highly conductive porous metallic foams, fins, or films to enhance heat transfer within the powder and to the exterior, as well as to allow sufficient hydrogen gas permeation.[40,212,213,214,215,216] The design of modern storage beds have been aided by numerical modeling. [19,40Error! Bookmark not defined.,217,218] However, there is a need to

reveal the complexities of the gas-powder interactions that take place in real-life systems. Detailed assessments of temperature gradients and variations in hydrogen content within the beds would be extremely valuable for refining these calculations.

Neutron transmission imaging methods allow investigations capable of penetrating the metal components and provide quantitative hydrogen concentration profiles.[219] Two-dimensional (2-D; radiography) and three-dimensional (3-D; tomography) neutron imaging techniques allow nondestructive *in situ* visualization and quantification of hydrogen transport and concentration gradients at various stages of absorption and desorption throughout the cycling of a hydrogen storage system.[220,221] The intent of the work by Jacobson et al. was to assess real-time 2-D/3-D imaging of hydrides contained in hydrogen storage beds that contain internal components for enhancement of heat and mass transfer.[207]

The Jet Propulsion Laboratory (JPL) has developed, fabricated, and delivered two hydrogen sorption cryocoolers that provide cooling at 19 K to instruments for the Planck flight mission which was launched in May 2009.[222,223] Each Planck Sorption Cryocooler (PSC) contains six hydride compressor elements that operate in serial heating and cooling cycles to provide a closed-loop refrigerant circulation.[222] A flight version of the PSC compressor element is shown in Figure 108a. The compressor element hydride bed vessel consisted of 316L stainless steel circular tubing with a porous stainless steel tube located along the center of the bed to promote axial distribution of gas during absorption and desorption. Bed heating was provided by a single heater assembly spaced along the inner wall in grooves of the open-pore 11% dense Al foam. The heater-foam components are shown in the photograph of Figure 108b. The hydrogen storage material was 616 g of high-purity $LaNi_{4.78}Sn_{0.22}$ powder, which filled the aluminum foam. The completed hydride bed (Figure 108c) would be installed in the compressor element (CE, Figure 108a) for the flight application. The space between the inner hydride bed and the outer Al housing of the CE formed a gas gap heat switch (GGHS).[212,224] The novel GGHS reduced the input power required during heating of the CE sorbent bed by nearly 80%.[224]

The *in situ* neutron imaging experiments were performed on a hydride bed identical to the one shown in Figure 108c. The engineering details of these cryocooler hydride beds are similar to those, which must be dealt with in future hydrogen sources for hydrogen powered cars.

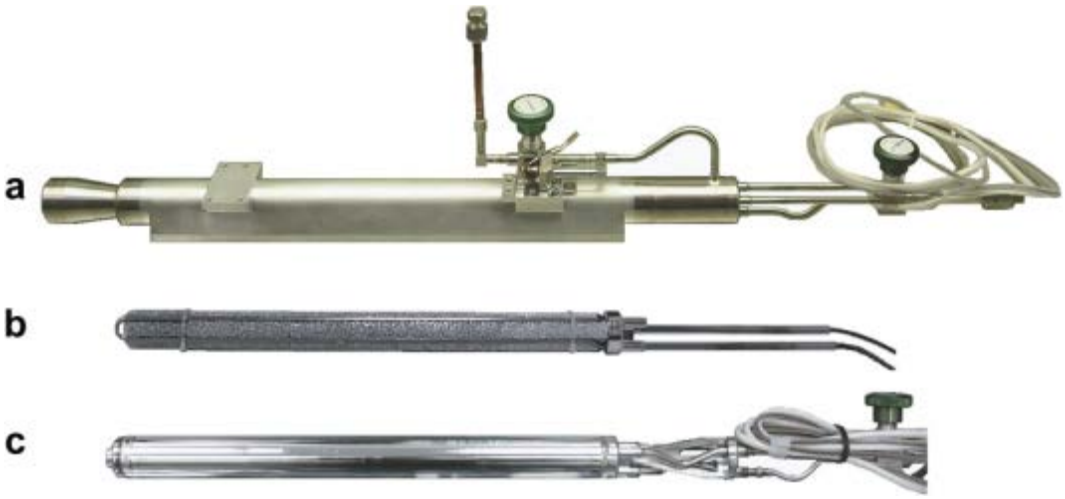

Figure 108. Images of (a) the Planck Sorption Cryocooler (PSC) Compressor Element (CE) containing an inner hydride sorbent bed and the gas gap heat switch assembly, (b) the porous Al foam and heater assembly of the inner hydride bed prior to assembly, and (c) the complete CE hydride sorbent bed after filling with $LaNi_{4.78}Sn_{0.22}$ alloy, which was the status of the bed used during the neutron-imaging experiments.[207]

An optimized bed configuration and GGSH is shown schematically in Figure 109.[225]

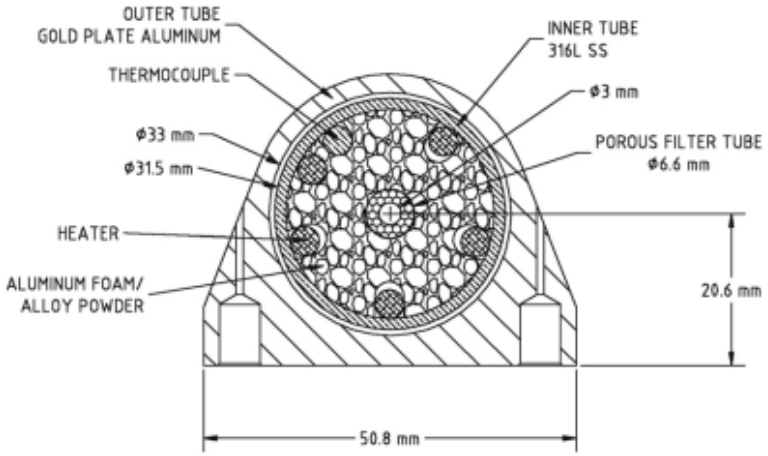

Figure 109. Cross sectional view of a prototype Planck Sorption Cryocooler (PSC) compressor element (CE) showing the gas gap spacing of 0.75 mm between the inner bed that contains the sorbent alloy and the outer housing. Powder of the hydrogen sorbent alloy $LaNi_{4.78}Sn_{0.22}$ fills the voids in the aluminum foam pieces (from Reference 225). There was no gold plating on the CE used during the neutron imaging experiments.[207]

Motivated by advances in digital imaging and the interest to study hydrogen fuel-cells[226], new neutron radiography facilities were built in 2003 at the NIST Center for Neutron Research (NCNR)[227] and upgraded in 2006[228] to provide high-resolution digital radiography capabilities. The radiography and tomography experiments performed by Jacobson et al. were done at the NIST Neutron Imaging Facility (NNIF), the layout of which is shown schematically in Figure 110.

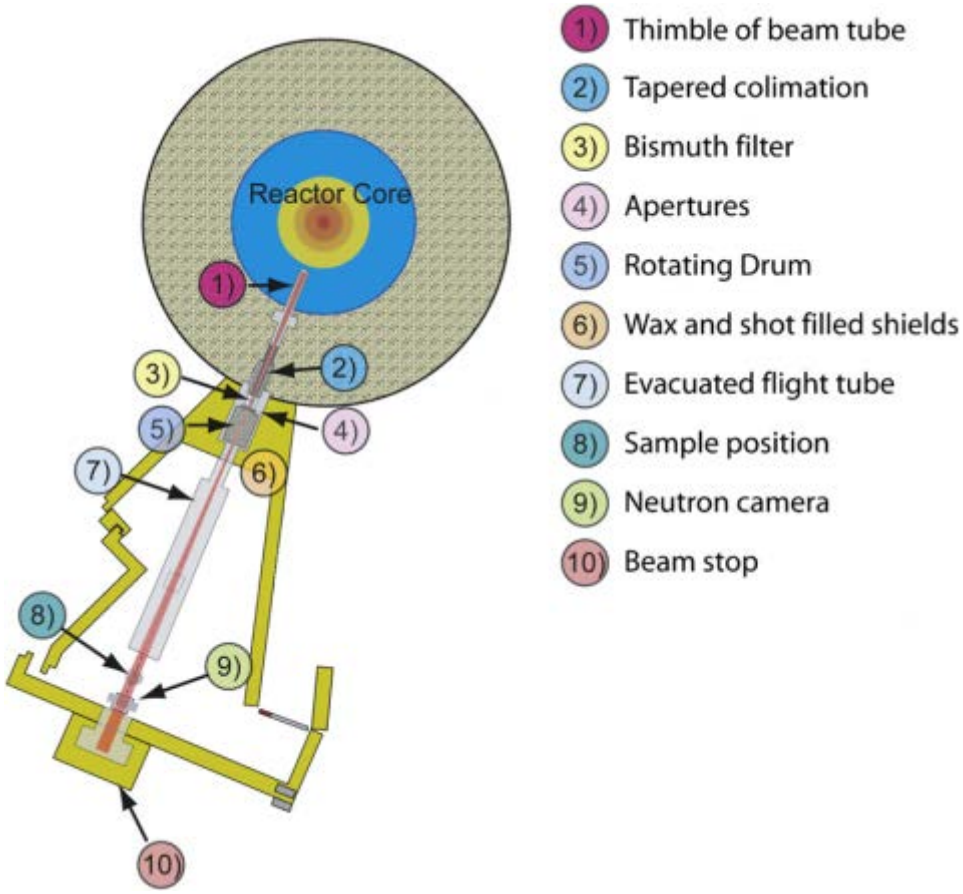

Figure 110. Schematic of the BT2 NIST Neutron Imaging Facility used for *in situ* radiography and tomography measurements. The hydride bed was mounted at (8) to a rotation stage with its axis in the horizontal, transverse direction so as to reduce the possibility that the powder would settle from its initial distribution.[207]

The essential components of a radiography beam line are illustrated in Figure 111. The primary parameters to optimize in neutron radiography are the detector-to-sample distance *z* and the *L*/*d* ratio, where *L* is the distance between the detector and an aperture of diameter *d*. Samples are placed between the detector and aperture, and the resulting geometric spatial blur λ_g is defined as:

Equation 45

$$\lambda_g = \frac{zd}{L-z} \approx \frac{zd}{L}$$

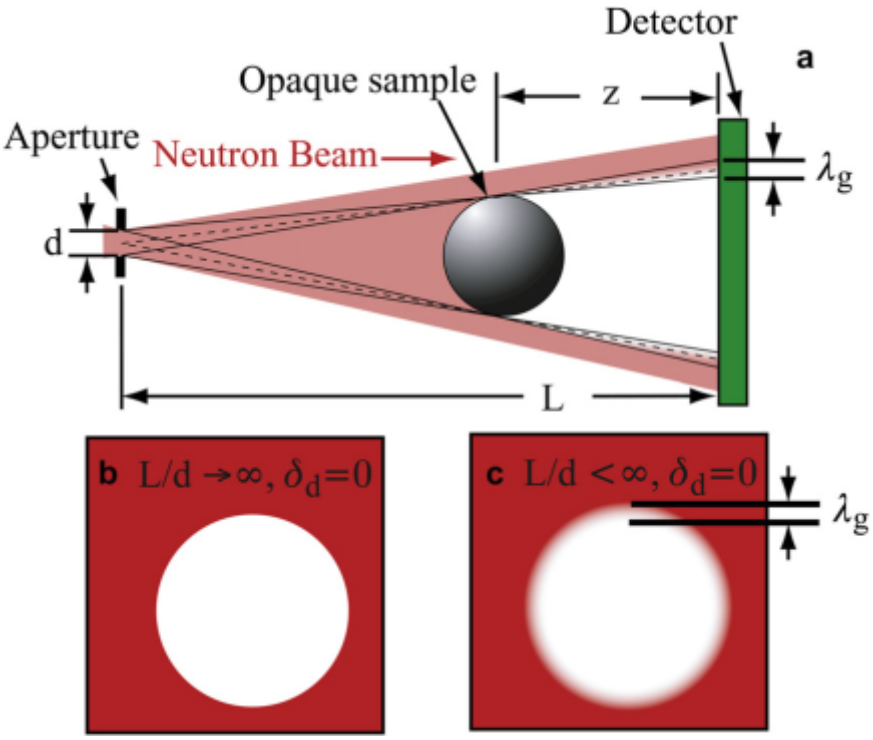

Figure 111. Schematic representation of a typical neutron imaging configuration: a) schematic of the essential components of a neutron imaging facility; b) a sharp image of an object; c) blurring due to finite geometric unsharpness.[207]

To minimize λ_g it is necessary to minimize *z* and *d* and maximize *L*. One factor in determining the largest object that can be radiographed in one image is the diameter of the neutron beam, which is linearly proportional to *L*. At the largest distance of *L* inside the NNIF (6.3 m), the resulting beam size is 26 cm in diameter. For dynamic measurements, the choice of high spatial resolution (high *L*/*d* value) results in a corresponding decrease (as the inverse square) in neutron intensity and, therefore, worse temporal resolution. The tradeoff between spatial resolution and temporal resolution results in nothing above *L*/*d* = 6000 being of practical use.[229] In the present example, Jacobson et al. used the optimal beam conditions of *L*/*d* = 450, 250 spatial resolution, and 20 cm x 25 cm field of view to achieve rapid data acquisition and resolving of the primary components, as opposed to individual grains of metal hydride powder.[207]

A neutron radiograph is the 2-D imaging of neutron intensity measured by a neutron detector plate. The intensity of the beam transmitted through the sample is a function of the atom

density, total neutron cross-section, and material thickness, among other things. In principle, individual isotopes can be distinguished, as the neutron cross-section can vary not only from atom to atom, but between isotopes as well. Separating individual components in neutron radiography can be challenging, but is made much easier in devices that have two different states, such as empty and filled hydrogen storage beds. In such cases, the empty bed can be removed from the images of the filled bed by dividing the filled bed radiograph by the empty bed radiograph.

Energy-dependent values of total neutron cross-section for certain materials are tabulated in tables such as ENDF.[230] Values in this study were estimated based on the measured energy distribution of the beam and the tabulated total neutron scattering cross section for hydrogen or deuterium. The assumption was that the chemical binding of hydrogen to $LaNi_{4.78}Sn_{0.22}$ does not significantly modify the effective hydrogen or deuterium total neutron scattering cross-section. For certain hydrogenous compounds such as water, this is a poor estimate. To be able to precisely measure the actual special hydrogen or deuterium content would require an attenuation calibration measurement. For this study, estimating the cross section was adequate to demonstrate the range of questions that can be addressed using neutron radiography and tomography.

Neutron tomography is a form of computed tomography that creates a three-dimensional image of an object by combining multiple planar images with a known separation by the detection of the absorbance of neutrons. The spatial resolution of the tomographic image is determined by the detector, the beam, and the angular step size used to rotate the object to obtain the projections. To achieve the same reconstructed spatial resolution or voxel dimension as the detector for all points in the reconstruction of the object, the angular step size must be chosen to be $60 < 2/r$, where A is the detector pixel pitch and r is the distance between the center of rotation and the furthest spatial feature to be resolved (more details on this can be found in ref 207). In the experiments of Jacobson et al., A = 127 μm and r = 16.5 mm so the length of the arc $\delta\theta < 7.7$ mrad (0.44°) where δ is the angular step size and θ is the outer radial distance to the axis of rotation r.[207] This means that to capture the full 3-D data set, at least 400 projections had to be obtained. Because the amount of time for such measurements can be substantial it was determined that the tomography measurements had to be done only for the case of when the density of the sample was at steady-state (static measurement rather than time resolved measurements during absorption or desorption). Tomographic measurements under non-equilibrium conditions can result in reconstruction artifacts in the filtered back-projection algorithm.

Dynamic time resolved measurements were probed using radiography. Radiography was used to capture transient behavior during gaseous deuterium absorption by the bed, and tomography was used to capture the full 3-D density distribution once equilibrium was reached after absorption/desorption steps.[207] Radiography and tomography measurements were first performed on the empty bed in order to remove its contributions to the transmission

measurements of the loaded bed. Using deuterium extends the maximum measurable bed thickness. This and the fact that the neutron transmission through the $LaNi_{4.78}Sn_{0.22}$ powder was reduced to 10% only halfway through the unhydrided bed made it necessary to use D_2 for the fully hydriding (deuteriding) measurements.

An important consideration in this initial state subtraction was that the metal hydride powders in the bed had to remain stationary. This was aided by the fact that the powder expanded with absorption and locked itself into place inside the Al foam. The bed was also mounted horizontally to avoid resettling of the powder as the bed was moved.

A detailed description of the data analysis can be found in reference 207, however, one important consideration to simplify the analysis was to ensure that the object axis was aligned with the axis of rotation and also aligned with an axis defined by the data set coordinate system. In practice, there is always a slight misalignment of the axes that can be corrected during data analysis. Some results of the neutron imaging and analysis are presented in Figure 112. These images illustrate representative sagittal slices associated with the storage bed (deuterium absorption), which were produced via tomographic reconstructions under steady-state conditions.

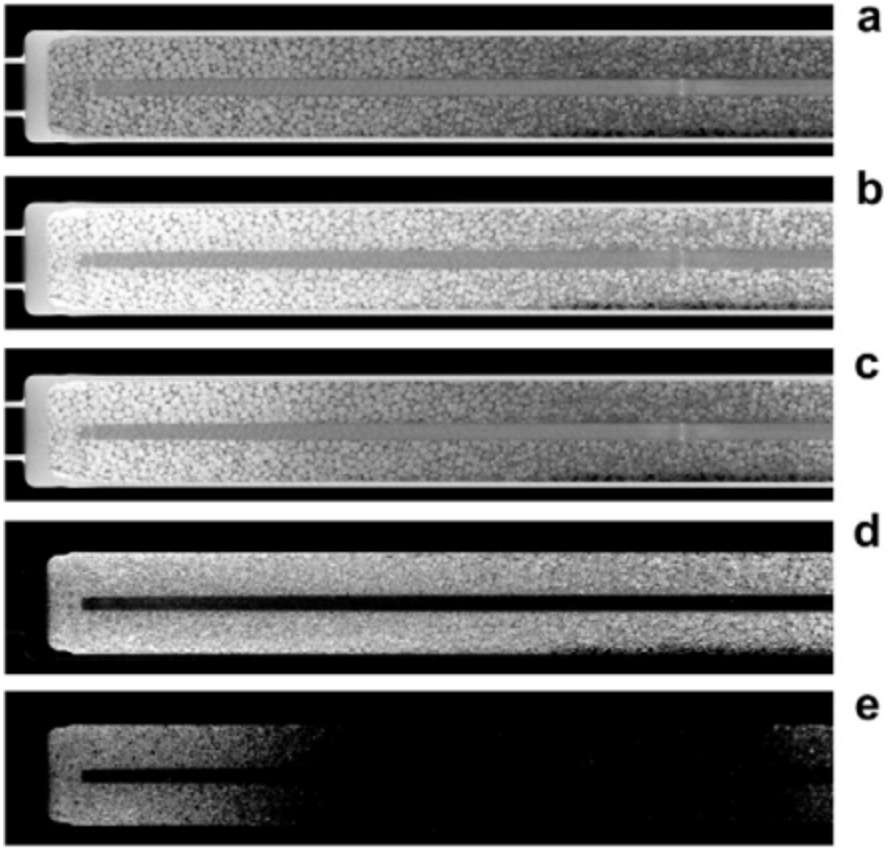

Figure 112. Sagittal slices through the tomographic reconstructions. (a) The total attenuation coefficients of (a) the empty bed, (b) the bed filled with 94.5 L of D_2, and (c) the bed after desorbing 60 L of D_2; subtracting the empty bed attenuation coefficient yields the D content of the bed, (d) after the absorption of 100 L and (e) after desorption of 60 L of D_2.[207]

The images of Figure 112 are for (a) the empty bed, (b) the fully hydrided bed, and (c) the bed after desorbing 60 L of D_2. Black and white corresponds to attenuation coefficients of 0 cm^{-1} and 1.0 cm^{-1}, respectively. Subtracting the empty bed attenuation coefficient yields the D content of the bed, which is shown in Figure 112d and (e) for the fully hydrided bed and after desorption of 60 L of D_2, respectively.

These neutron imaging experiments enabled the following observations that would be difficult to obtain otherwise: First, the large, open-pore structure of the aluminum foam is clearly visible. From Figure 112a it can be seen that the metal/hydride powder in the bed is non-uniformly distributed, with a decrease in density towards the center of the bed (at ~ 180 mm). Despite the non-uniform powder distribution, the D content of the filled bed appears rather uniform in Figure 112d. Figure 112e demonstrates that deuterium is released preferentially from the center region of the bed. It was proposed that this is likely due to the thermal control of the bed during

desorption. The heater does not reach the end of the bed, and this cooler region will be slower to desorb deuterium than the rest of the bed.[207]

In Figure 113 the mass of deuterium is plotted at various points along the length of the bed versus time during a series of multi-step absorption and desorption processes. After 10,000 seconds the final stage of absorption had been reached and the D content can be seen to decrease with distance from the end of the bed (Figure 113a). This is consistent with the observation from the neutron imaging above of a decrease in the powder density towards the center region of the bed. The desorption rate (given by the deuterium concentration change in time) was also more uniform near the center of the bed (~ 180 mm) where the temperature was slightly more uniform.

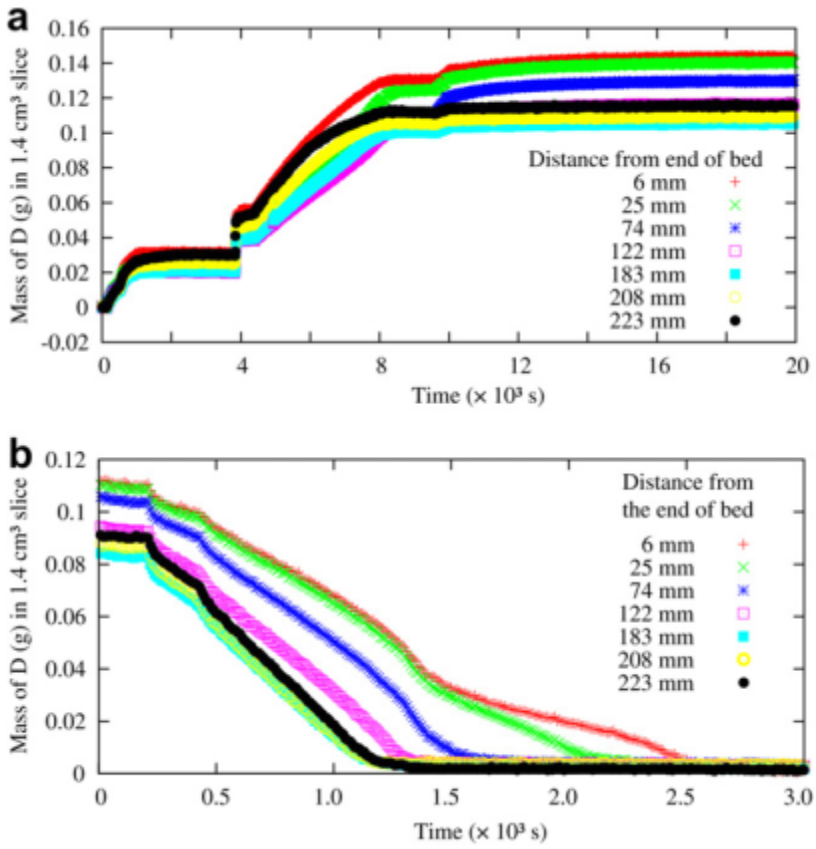

Figure 113. The D content at several points along the length of the bed during multi-step (a) absorption and (b) desorption processes with distances measured from the beginning of the powder-filled region.[207]

The same data is plotted in Figure 114 as spatial concentrations of deuterium at various times. The lower metal powder density at the center of the bed results in reduced absorbed D in this

region. Figure 114c shows the D released along the bed length indicating essentially full release from the center region (distances > 120 mm) has occurred within 1250 s, while the amount of desorption decreases towards the end cap where the temperatures are lower because of the positioning of the heating element. The neutron imaging demonstrated that the combination of gradients in powder density and local bed temperature resulted in a variation of D release along the length of the bed.

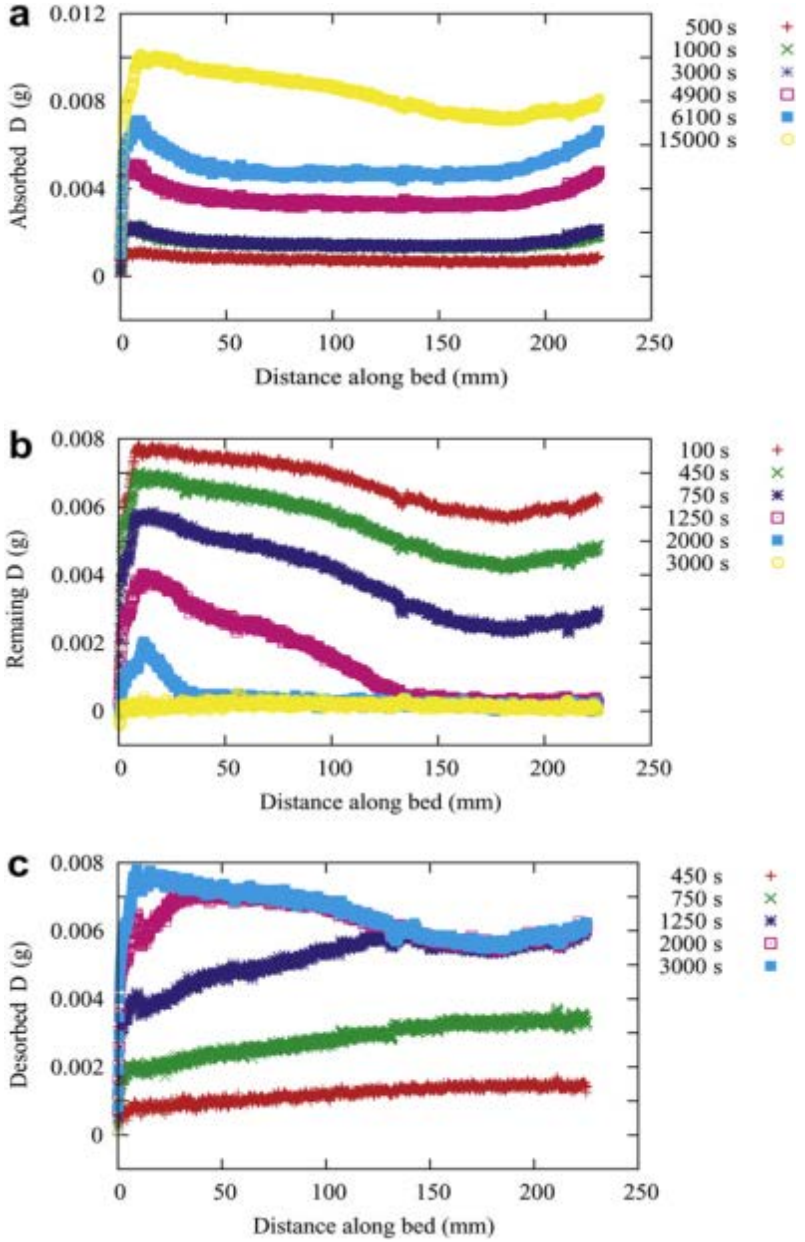

Figure 114. The mass of deuterium along the metal bed length at selected times during the same (a) absorption and (b) desorption processes as in Figure 113. (c) Total mass of D evolved from each point in the bed during the desorption process.[207]

Tomographic cross-sections of the radial hydrogen distribution at three different points along the length of the bed following absorption of 12 L H_2 are shown in Figure 115. The two long oval-shaped dark spots in Figure 115a are the bends in the internal heaters at the end of the bed. Other images show the central gas delivery tube and five heater lines, run axially. In addition to the observed axial differences in hydrogen concentration (also observed in the deuterium measurements above), the imaging showed that hydrogen is absorbed preferentially at the outer radius for this particular set of experimental conditions. This was believed to be the consequence of radial temperature gradients during the absorption process.[207]

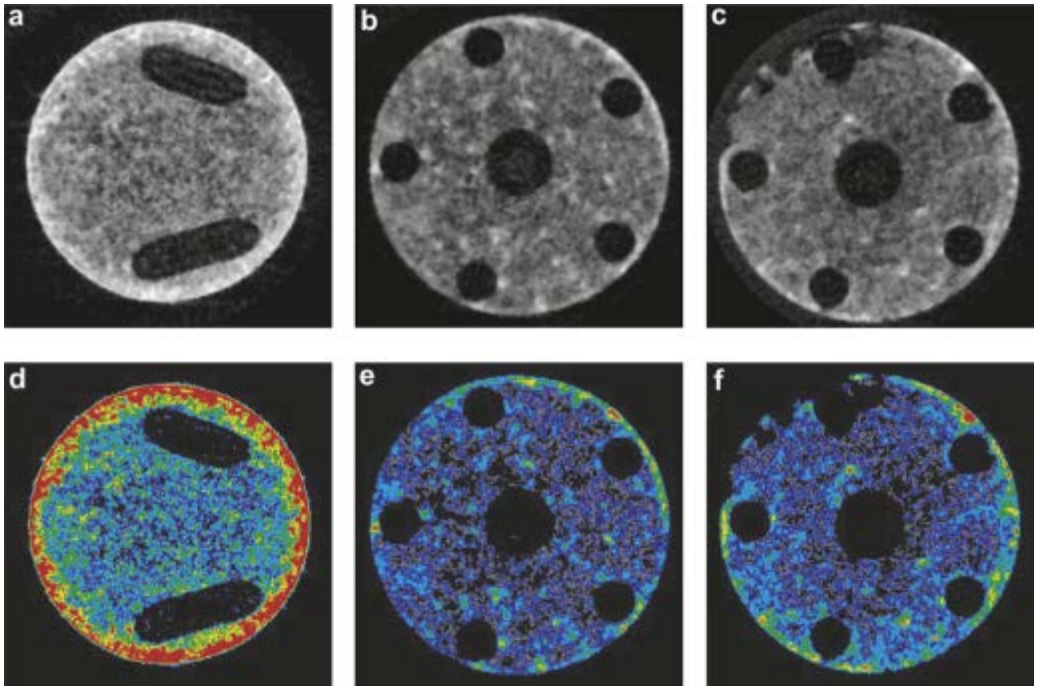

Figure 115. Radial H distribution after absorption of 12 L of H_2 at three different points along the bed: (a) near the end of the bed at the bends in the internal heaters, (b) near the center of the imaged area, and (c) at the opposite end of the imaged area. (d—f) are colorized images at the same locations; red indicates high H concentration, black no H concentration (For interpretation of the references to color in this figure legend, the reader is referred to the web version of this article).[207]

This example shows that hydrogen-sensitive, *in situ* neutron imaging is a powerful technique that can be used to investigate real-time hydrogen concentration profiles in three dimensions during absorption/desorption cycling of prototype hydrogen storage systems. These methods allow a non-destructive analytical tool for understanding mechanical properties of hydrogen

storage systems that should prove very useful in the modeling and engineering design of future material-based hydrogen storage tanks for vehicular and stationary applications.

3 Options for Improving Mechanical Properties

3.1 Increased Mechanical Durability of Hydrogen Storage Materials

Decrepitation due to hydride formation can have significant implications for real-world applications including hydrogen storage. A closely related application with similar issues to gaseous hydrogen storage in metal hydrides has been the development of stable metal hydrides for battery applications. The degradation of metal hydride battery electrodes has been associated with oxide formation on the metal alloy surface, and thus degradation (capacity loss with cycling) is directly related to the surface area of the metal hydride. Because the surface area depends on material's particle size, which is a function of the hydrogen cycling decrepitation behavior of the alloy, it has been found that alloys that were more resistant to decrepitation showed significantly better cycle-life behavior.

The ability of $LaNi_5$ (the parent AB_5 compound) to absorb and desorb large amounts of hydrogen was discovered by Van Vucht et al. in the late 1960s.[231] However, it took almost two decades before AB_5 type materials were commercialized in NiMH batteries chiefly due to the poor electrochemical cyclability of $LaNi_5$ in alkaline media. Improvements were achieved by partly replacing La atoms by other lanthanides, and Ni atoms by different transition metals in the AB_5 crystal structure. Willems and Van Beek succeeded in stabilizing $LaNi_5$, and accomplished a breakthrough with these multicomponent compounds in the development of NiMH batteries.[156,232] Further work on substitution within the AB_5 stoichiometry proved to offer a wide variety of prospects for optimizing metal hydride batteries which contributed to a robust commercial sector for many years.[233,234,235]

The following example study by Notten et al. demonstrates how modifying lattice expansion was correlated to stabilizing the degradation of metal hydride electrode materials.[236] X-ray diffraction of the as-prepared alloy materials was used to determine lattice parameters. In this work, single-phase, non-stoichiometric $La(Ni/Cu)_X$ compounds were prepared by annealing the materials at appropriate temperatures. The non-stoichiometric composition was varied in the range
$5.0 \leq x \leq 6.0$, and the chemical composition was changed by varying the Ni/Cu ratio. The crystallographic and electrochemical characteristics of these single-phase compounds were found to be strongly dependent on both the non-stoichiometric and chemical material composition.

It is typical of the non-stoichiometric compounds that they are characterized by an anisotropic crystal lattice deformation, implying that the *a*-axis decreases, while the *c*-axis simultaneously increases, with an increasing degree of non-stoichiometry. However, the introduction of larger Cu atoms into a structure with constant non-stoichiometric composition results in an isotropic

lattice expansion. On the basis of these and other crystallographic data, it was argued that an excess amount of B-type atoms is incorporated into the AB_5 crystal lattice by substituting a portion of the La atoms with crystallographically oriented dumb-bell pairs of B-type atoms. It was proposed that the dumb-bells themselves consist of Ni atoms only, while the Cu atoms preferentially occupy the spacious areas neighboring the dumb-bells.[236]

The study examined two sets of composition changes in the alloy $La(Ni/Cu)_X$:

1. ***1.*** one series in which the non-stoichiometric composition x was varied in the range $5.0 < x < 6.0$, while the Cu content of these materials remained constant;

2. ***2.*** another series using the non-stoichiometric composition optimized in (***1***), in which the Ni/Cu ratio was varied over a broad range.

In previous work the authors showed have shown that non-stoichiometric AB_x ($x > 5$) compounds can be made by partially replacing the lanthanide atoms at the A positions in the AB_5 crystal structure with dumb-bell pairs of B-type atoms.[237,238] This special substitution mechanism is schematically represented in Figure 116. It should be noted that, for the sake of clarity, the sizes of the atoms within the AB_x hexagonal unit cell are not drawn to scale.

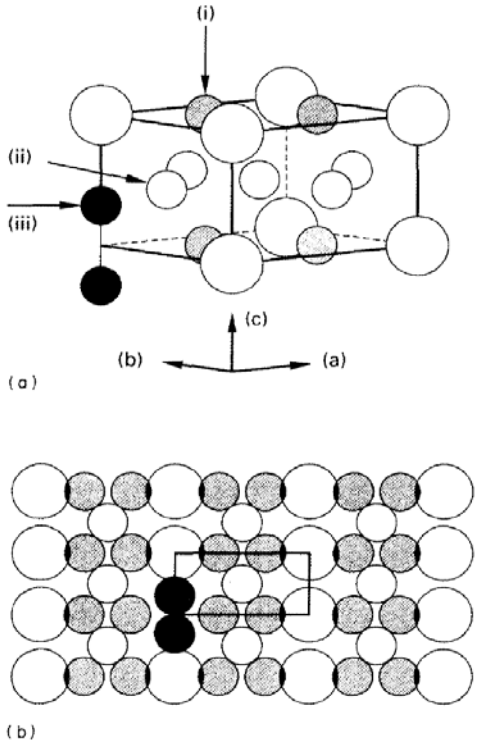

Figure 116. (a) Schematic three-dimensional representation of a nonstoichiometric AB_X compound. The large atoms positioned at the corners of the hexagonal crystallographic unit cell represent La. The smaller atoms represent the B-type atoms. Three different

B-type positions are indicated. By replacing a La atom by a dumb-bell pair of B-type atoms, an excess of B-type elements can be incorporated into the structure, making the materials non-stoichiometric. (b) Planar view of the [110] plane, in which the atomic dimensions are drawn to scale. Note the overlapping atoms.[194]

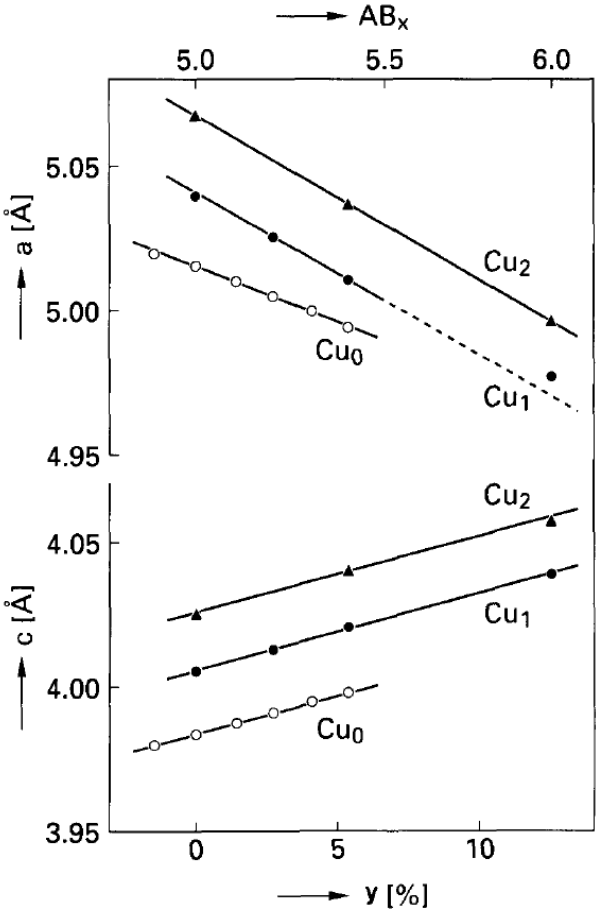

Figure 117. Lattice constants a and c as a function of the degree of non-stoichiometry for the single-phase starting materials with constant Cu content ($LaNi_{X-1}Cu$), indicated by Cu1. For comparative reasons, the results obtained for the ternary $LaNi_{X-2}Cu_2$ system (curves Cu2) and the binary $LaNi_X$ systems (curves Cu0) are also included.[236]

The lattice constants from X-ray diffraction using the hexagonal hP6-$CaCu_5$ crystal structure of the AB_x compounds prepared with a constant Cu content are represented as a function of the fraction of La replacements by the curve Cu in Figure 117. Some results obtained in earlier work with the ternary $LaNi_{X-2}Cu_2$ system[238] and the binary $LaNi_X$ system[237,239] are also included, and are represented by the curves Cu_2 and Cu_0 respectively. Straight lines are obtained in almost all cases. As can be deduced from Figure 117, it is typical for all non-stoichiometric compounds within a homologous series that the *a*-axis decreases, whereas the *c*-axis increases with increasing degree of non-stoichiometry.

The introduction of Cu into the crystal structure induced both the *a*- and *c*-axes to increase, as a comparison of the curves Cu_1 and Cu_2 with curve Cu_0. The displacements of the *c*-axis curves were all parallel and equidistant within the accuracy of the measurements. However, the *a*-axis was found to be dependent on the chemical composition of the homologous series: the slope of the Cu-free binary materials curve changed substantially compared with those found with the Cu-containing series (curves Cu_1 and Cu_2).

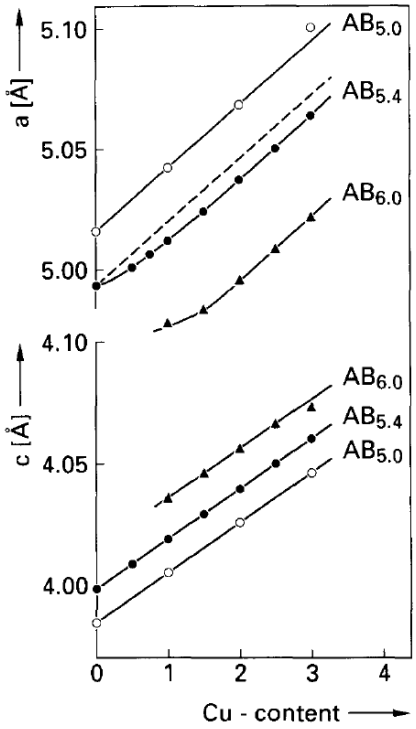

Figure 118. Lattice constants a and c as a function of the Cu content of single-phase compounds with different stoichiometric compositions. The broken line corresponds to the dependence expected on the assumption that Cu is randomly introduced at the atomic positions (i) and (ii) of the $AB_{5.4}$ compounds only.[236]

Figure 118 shows the dependence that was found for the lattice constants as a function of the Cu content for materials with different stoichiometries. The lattice expansion for the $AB_{5.0}$ stoichiometry (open symbols) is clearly isotropic. The *c*-axis curves of the $AB_{5.4}$ (full circles) and $AB_{6.0}$ compounds (triangles) are both displaced parallel over the entire Cu concentration range with respect to the $AB_{5.0}$ curve (open circles). This indicated that the substitution of Ni by Cu occurs in a similar way as in the stoichiometric $AB_{5.0}$ compounds, suggesting that the dumb-bells (atomic position (iii) in Figure 116) were composed of Ni atoms only. More information on the crystal structure analysis can be found in the original publication by Notten et al.[236]

The most striking aspect of the electrochemical cycling results was that the cycling stability was strongly affected by the degree of non-stoichiometry and chemical composition. Electrochemically stable compounds are only obtained when the materials used have a minimum degree of non-stoichiometry combined with a certain amount of Cu. $LaNi_{4.4}Cu$ can be regarded as optimum in terms of both storage capacity and long-term cycling stability. Microscopic investigations of the cycled electrodes clearly showed that the improved cycling stability of non-stoichiometric compounds was related to reduced or even absent decrepitation of the hydride-forming powder particles (Figure 119).

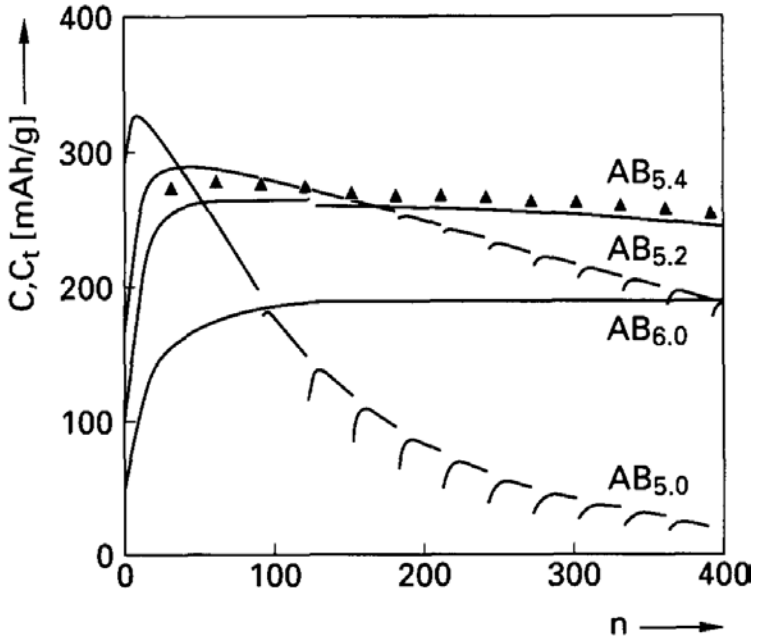

Figure 119. Storage capacity *C*, resulting from discharging (350 mAg^{-1}), as a function of the number *n* of electrochemical charge-discharge cycles for various single-phase, non-stoichiometric AB_X compounds with constant Cu content ($LaNi_{X-1}Cu$). The total storage capacities *Ct*, as obtained from deep discharging (35 mAg^{-1}), are indicated by triangles for the $AB_{5.4}$ compound only.[236]

In contrast to the stoichiometric compound, which was found to lose its storage capacity *C*(n) very rapidly upon electrochemical cycling (n), the cycling stability was considerably improved for higher values of x. The Cu-containing alloys became more stable with an increasing degree of non-stoichiometry. The $AB_{5.4}$ compound was regarded as a very good compromise with respect to its high storage capacity and long cycle life. Inspection of the stability factors obtained for the Cu-containing $AB_{5.4}$ alloy and those obtained for the corresponding binary $AB_{5.4}$ alloy revealed that the cycling stability of the binary alloy was much poorer.

3.2 Reduction of Compositional Degradation

One of the potential mechanisms for capacity loss with cycling that occurs with some hydrogen storage materials is the loss of reactive components that participate in the storage. For example, the loss of nitrogen through the evolution of ammonia in amide storage materials has been shown to contribute to capacity loss.[240,241] In addition, the release of ammonia into the hydrogen supply is detrimental to polymer electrolyte membrane fuel cells. The introduction of additives to the amides has been shown to not only improve the cycling capacity but also reduce the production of ammonia. One example is the work by Ma et al. which investigated the benefits of introducing $LiNH_2$ and Li_3N additives to Li-Mg-N-H.[110]

Several recent efforts have explored the use of additive compounds to improve the reversible dehydrogenation performance of amide hydrogen storage materials.[242,243,244,245,246] For example, the addition of $LiBH_4$ was shown not only to enhance low temperature kinetics but to also suppress ammonia release. This was primarily attributed to the formation of solid solution $Li_4BN_3H_{10}$ and the product seeding of $Li_2Mg(NH)_2$.[244,245] The kinetic barriers in the Li-Mg-N-H system have been ascribed to the interface reaction of reactants and mass transport through the product layer.[247] $Li_2Mg(NH)_2$ seeding has been reported to be effective in lowering the kinetic barrier associated with the product nucleation.[244,246]

In the work of Ma et al., systematic X-ray diffraction analysis indicated that Li_3N additive transforms into $LiNH_2$ and LiH phases, and that the $LiNH_2$ "seeding" could be responsible for the observed enhancement in capacity. Some of the results of that study are presented in Figure 120 which shows that by increasing Li_3N additive, the desorption capacity increases, reaching a maximum value (4.7 wt. % H_2) at 10 mol % Li_3N addition. However, the addition of Li_3N above this amount reduces the total capacity. The 10 mol % Li_3N was shown to increase capacity approximately 20% more than the additive-free sample. This is approaching the theoretical capacity of 4.9 wt. % hydrogen (taking into account impurities and Li_3N additive).

In addition, Ma et al. also found that Li_3N additives help to suppress ammonia release. As shown in Figure 121 the ammonia release from the samples with $LiNH_2$ and Li_3N additive was measured using MS. Less ammonia was observed for the sample with Li_3N additive. Prior studies attributed this improved hydrogen purity to the presence of excess LiH which served as an effective ammonia trapping agent.[248,249] In this case, excess LiH appears due to the decomposition of the additive Li_3N.

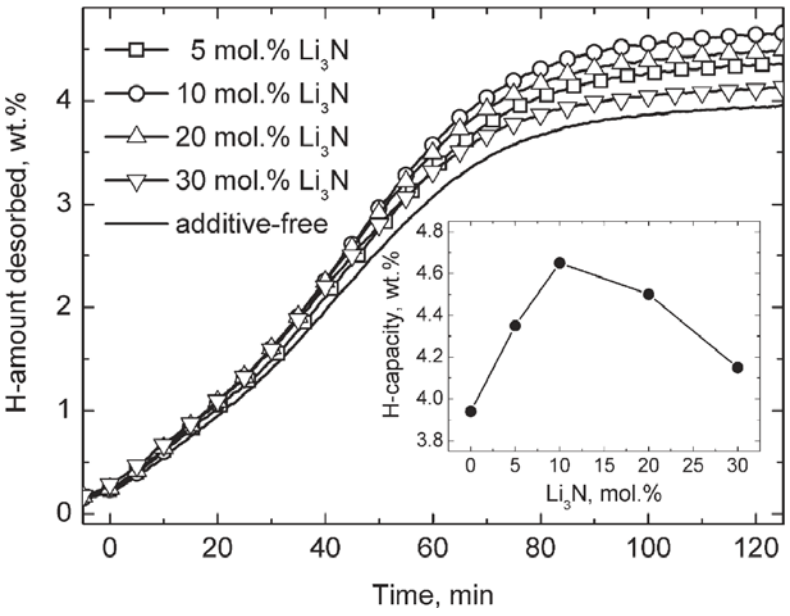

Figure 120. Effect of Li_3N additive on the hydrogen desorption performance of the Li-Mg-N-H sample at 0.1 MPa and 200 °C in the 2nd cycle. The inset highlights the evolution of hydrogen capacity as a function of the Li_3N addition, with the deviation of ± 0.05 wt. % in capacity values.[110]

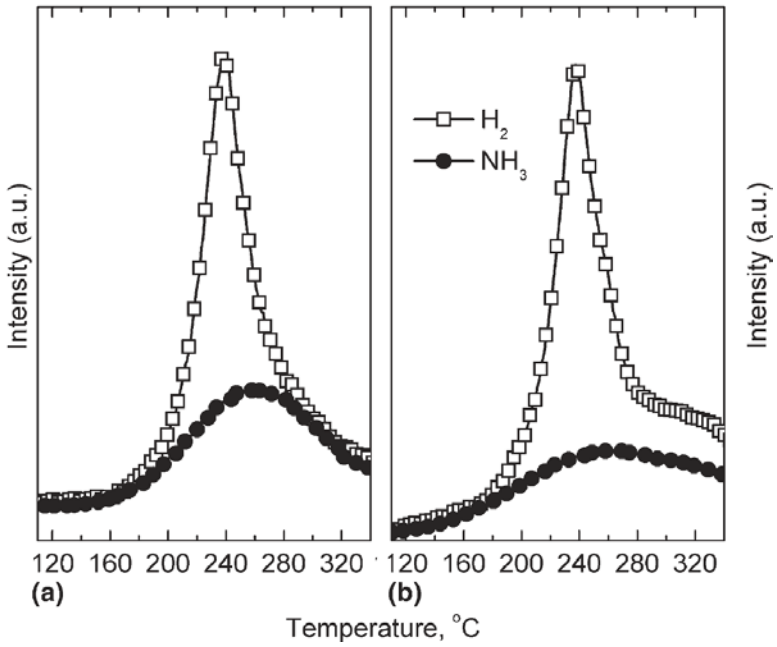

Figure 121. Mass spectroscopy results of the gas released from the Li-Mg-N-H samples containing different additives: (a) 10 mol % $LiNH_2$ and (b) 10 mol % Li_3N. Hydrogen (m/e = 2, open square) and ammonia (m/e = 17, closed circle) were monitored using MS. Ammonia signals were multiplied by 20 for clarity.[110]

This example demonstrating the identification of effective additives to improve the properties of the Li-Mg-N-H system also showed the value of mass spectrometry as an analytic technique to aid in the improvement of hydrogen storage materials.

3.3 Powder Densification

Many hydrogen storage materials exist as powders having low bulk densities. To improve system volumetric capacity, gravimetric capacity (since containment system weight increases with volume) and heat transfer, these powders should be compressed into the smallest functioning area possible. Thus, the study of powder densification plays an important role in the system design. There is extensive literature on the packing of granular materials; however, little exists on the controlled densification of nanometer scale powdered materials.

One significant engineering challenge for hydrogen storage systems based on powdered hydride materials was to develop methods of tightly packing the low density hydride powder inside a finned heat exchanger contained within a composite vessel.[250] In a project at UTRC, a powder loading method was developed to achieve both practical pressure vessel/heat exchanger assembly and high powder packing densities. A novel powder densification apparatus was designed and fabricated for the project that produced vibrations in two orthogonal directions in combination with other densification enhancements. Three different vessel configurations were used in the development of powder densification methods (Figure 122).

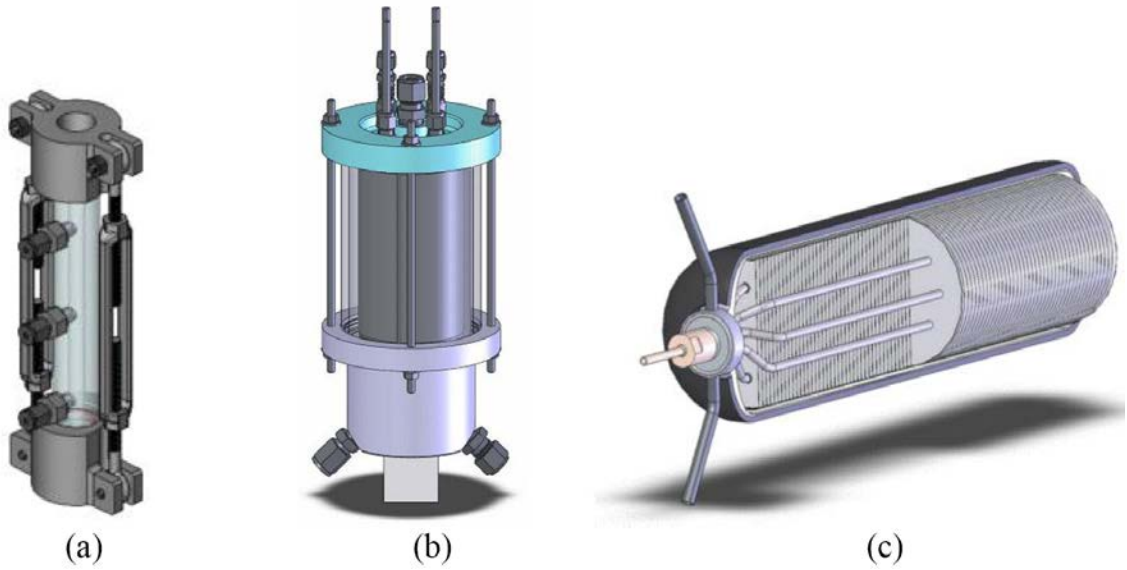

Figure 122. Three configurations used to develop powder densification methods. (a) Column of powder; (b) Finned heat exchanger which can be disassembled; (c) Prototype 2 carbon fiber composite vessel with heat exchanger.[250]

Vessel (a) was constructed from a clear acrylic tube, allowing for visual inspection of the densification process. Tests with this vessel examined the more fundamental characteristics of powder densification for different: 1) vibration frequencies and amplitudes; 2) vibration directions – parallel and perpendicular to the densification axis; and 3) densification enhancement details, in order to provide information on the optimal and near optimal densification conditions to be applied in the other two vessel configurations. Test vessel (b) was used to develop a loading process for filling the space between a stack of horizontal fins. The final configuration (c) represented an actual prototype system with densification optimized in (a) and loading optimized in (b).

Figure 123. Apparatus with independently controlled, dual axis shakers set up with powder vessel to examine fundamental powder densification characteristics.[250]

In this study a unique apparatus was developed which used two electromagnetic shakers to vibrate the test configurations in independent orthogonal directions. For vessel (a), these directions were parallel and perpendicular to the densification axis. For vessels (b) and (c), these directions were perpendicular to and in the plane of the fins, but generally not parallel to the radial densification direction. The shaker apparatus with vessel (a) is shown in Figure 123.

Two accelerometers were attached to the test vessel to measure the intensity of vibration. The signal generators used to drive each shaker could sweep the vibrational frequency as shown in Figure 124.

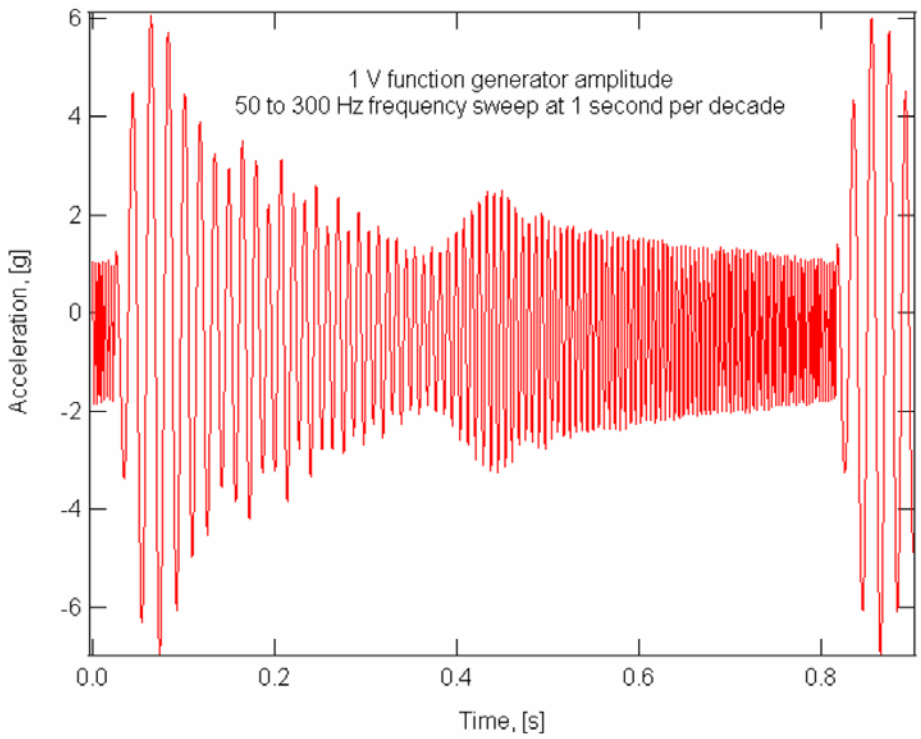

Figure 124. Frequency sweeping from 50 to 300 Hz to promote activation past particle rearrangements obstacles (amplitude variation is due to shaker characteristics and a minor structural resonance at 0.45 s).[250]

Inert materials were measured first to test the system, then measurements were performed on attrition milled $NaAlH_4$ (with 3%$TiCl_3$ * 1/3 $AlCl_3$ additives).[250] Densification was found to occur under vibration alone, but higher densities could be achieved using enhanced settling methods. These results are shown in Figure 125. Final densification measurements on $NaAlH_4$ with 3% $TiCl_3$ * 1/3 $AlCl_3$ additives of 0.62 g cm^{-3} was significantly lower than that obtained with the 6% TiF_3 additive (0.75 g cm^{-3}). This result motivated further studies on the different behavior of dehydrided versus hydrided states on powder densification. It was theorized that densification should increase after dehydriding the material; however, the measurements on hydrided and dehydrided materials gave the opposite result.[250]

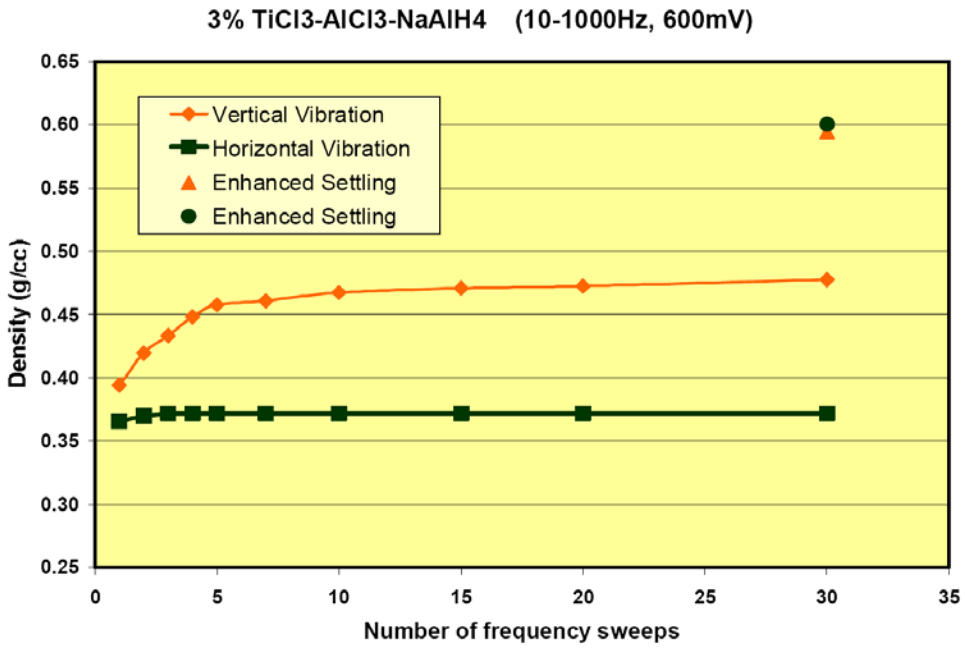

Figure 125. Effect of horizontal and vertical frequency sweeping on densification or attrition milled $NaAlH_4$ (with 3% $TiCl_3$ * 1/3 $AlCl_3$ additives) material followed by enhanced settling methods.[250]

It was also apparent that the batch size of the attrition milled material had an effect on densification with the larger batch size having the lower density. Solid lubricants to facilitate particle rearrangement were explored. Graphite powder was added in 0.5 wt. % and 5 wt. % concentrations and attrition milled together with $NaAlH_4$. Densification tests showed that SPEX milling of the control sample for 10 minutes resulted in a 33% increase in powder densification from 0.629 to 0.835 g cm^{-3} demonstrating that milling procedures are important to achieve not only rapid kinetics, but also high powder densification. The addition of graphite on densification was not as significant. High-resolution SEM images (Figure 126) did not show a significant visual difference in particle size or morphology between the attrition milled and SPEX milled powders.

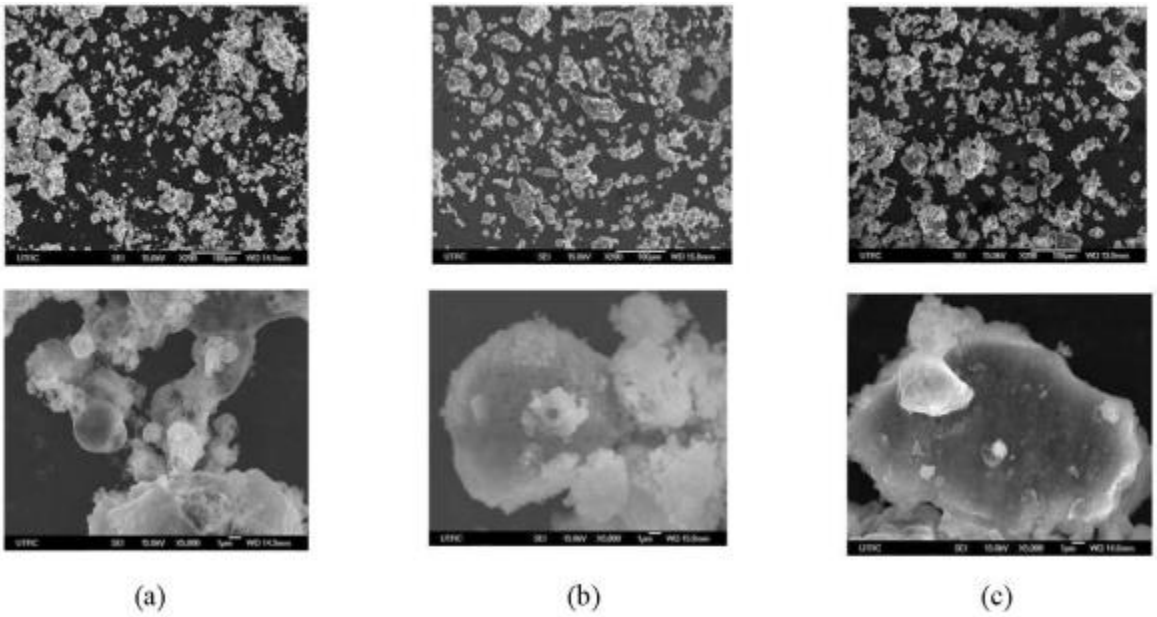

Figure 126. High resolution SEM micrographs of 3% $TiCl_3$ * 1/3 $AlCl_3$ $NaAlH_4$ powder which underwent three different milling procedures. Densities achieved were (a) 0.64, (b) 0.85 and (c) 0.72 g cm^{-3}.[250]

The UTRC project then investigated powder densification of a 100 g batch attrition milled material using the finned tube heat exchanger test configuration shown in Figure 122(b). Initial tests were not successful in meeting target densities, resulting in 0.57 g cm^{-3} and severe warping of the 0.004" thick aluminum fins. To remedy this, the fins were modified by creating shallow corrugations to increase their structural integrity as shown in Figure 127(a). A maximum density of 0.66 g cm^{-3} was achieved in the finned structure shown in Figure 127(b) which compared well with measurements using the column configuration of density for the 100 g batch attrition milled material of 0.629 g cm^{-3}.

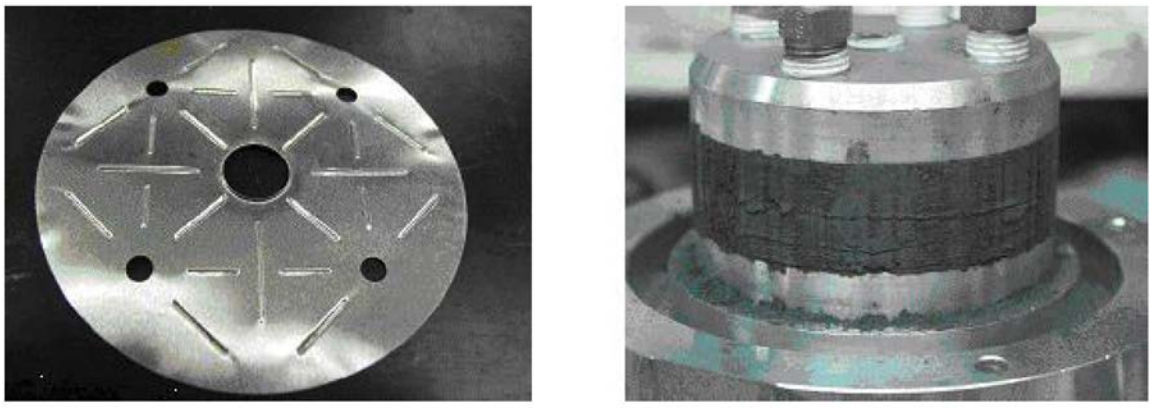

(a) (b)

Figure 127. (a) Stiffened fin used to achieve an average density of 0.66 g cm^{-3} in stack (b).[250]

In addition to the studies performed on sodium alanates, UTRC applied powder densification techniques to other novel materials.[250] The results of those measurements are presented in Figure 128 in terms of the material volumetric density, calculated from the measured powder densities for three preparation conditions and the theoretical H_2 capacity. Note that while $LiMg(AlH_4)_3$ has good gravimetric potential, its volumetric performance in the as-synthesized state is low. The authors of this work suggested that milling and other processing could improve densification of these powders as was demonstrated by their work on $NaAlH_4$.

Compound	Theoretical Rev. H_2 wt fraction	Initial Density kg H_2/liter	Vibratory Settling kg H_2/liter	Enhanced Settling kg H_2/liter
$LiMg(AlH_4)_3$*	0.089	0.010	0.014	0.019
M-B-N-H System A *	0.088	0.033	0.041	0.042
M-B-N-H System B *	0.082	0.035	0.044	0.044
$NaAlH_4$- best result **	0.056	0.026	0.041	0.042

Figure 128. Volumetric density of three novel storage materials in comparison with $NaAlH_4$ (theoretical capacities).[250]

3.4 Application of Vibrational Powder Loading and Densification

In a continuation of the small scale testing discussed above, UTRC applied powder densification techniques to the scaled-up system to test and validate the process at an applications level.[250] A second prototype system was constructed with advances that included:

1. Lighter weight end closure for the composite vessel
2. Improved heat exchanger performance with the use of fins rather than foam
3. Compact oil manifolds
4. Greater powder densification

In order to achieve this, the advanced powder loading approach discussed above was implemented. Using this loading method required biaxial shaking of the entire system. This system was assembled and filled by vibrational shakers in a nitrogen glove box. A sketch of the Prototype 2 design is shown in Figure 129.

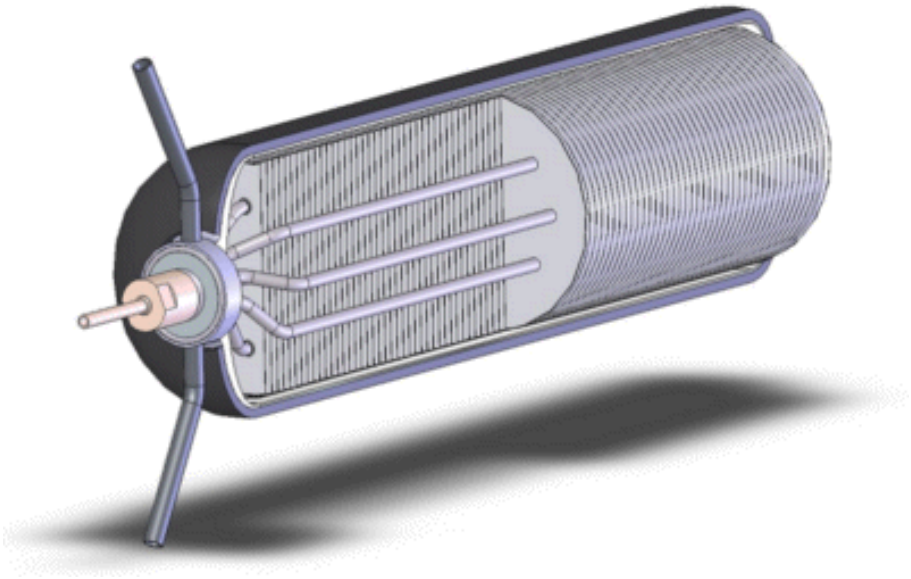

Figure 129. Sketch of the second prototype design.[250]

The system was fabricated in the following major steps:

1. Form the heat exchanger fins and tubing
2. Assemble the heat exchanger
3. Fabricate the vessel lining in two pieces
4. Weld the tubing to the integrated manifold section of the liner
5. Insert the heat exchanger into the second liner section and weld the two liner pieces
6. Wind the assembled liner with carbon fiber composite and proof test with dry gas
7. Install the vessel onto the shaker rig within the assembly glove box
8. Load the catalyzed $NaAlH_4$ (3525 g)
9. Install the combined porous metal filter/cap

To determine specific positions of the eight heat exchanger tubes both steady state and transient thermochemical FEA simulations were conducted. FEA analysis was also used to optimize other system components such as the heat exchanger fin design. To minimize weight, thin 0.004" aluminum heat exchanger fins were used. However, reinforcing features were needed to strengthen them. Using FEA analysis, the pattern shown in Figure 130 and Figure 131 were selected.

Figure 130. (a) Fin stack showing reinforcing features; (b) example displacement contour plot from FEA to select best reinforcement design.[250]

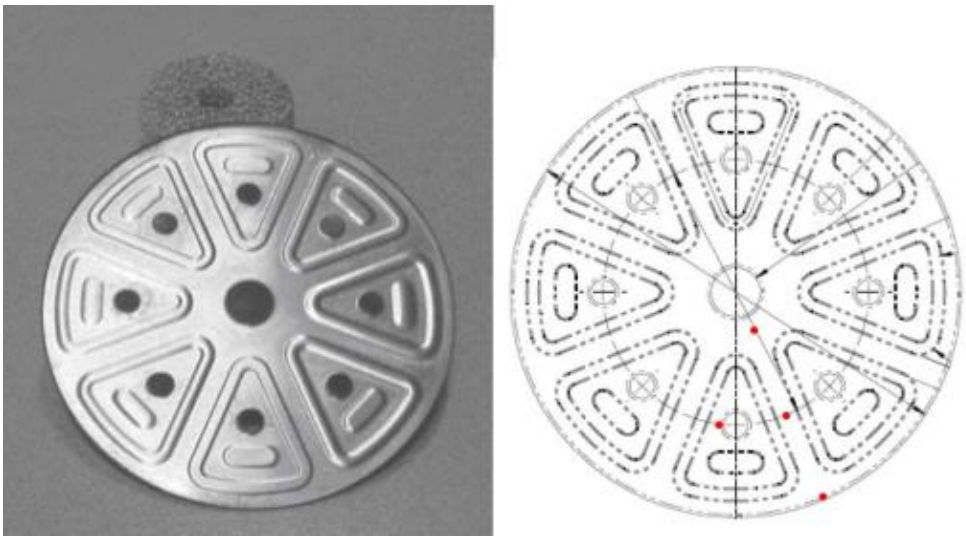

Figure 131. Heat exchanger fin geometry; (a) fabricated fin with reinforcement features; (b) red circles indicate the cross section locations of the four thermocouples.[250]

A set of 80 fins were installed with a spacing of 0.1875" between fins on the contoured heat exchanger tubing as shown in Figure 132.

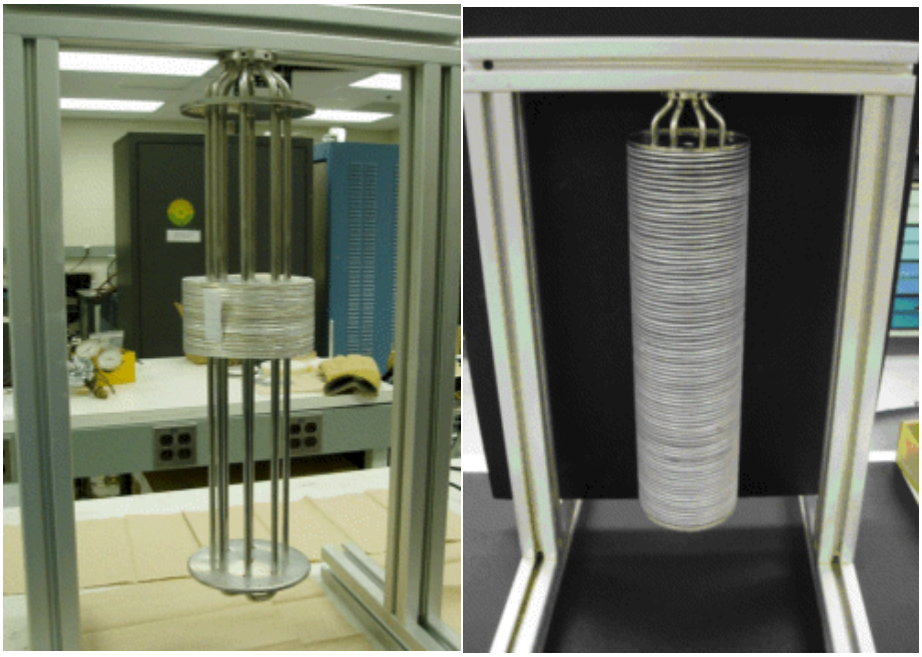

Figure 132. (a) Prototype 2 heat exchanger assembly with consolidated fin stack; (b) assembly with distributed fins.[250]

Aluminum foam was used to provide conduction enhancement in the two domed end sections of the system. The components including the main liner section were welded together and the tank was then wound with carbon fiber and high temperature epoxy. Upon completion, the empty system was pressure tested to 2250 psi. A support structure to hold the vessel and shakers was designed as shown in Figure 133.

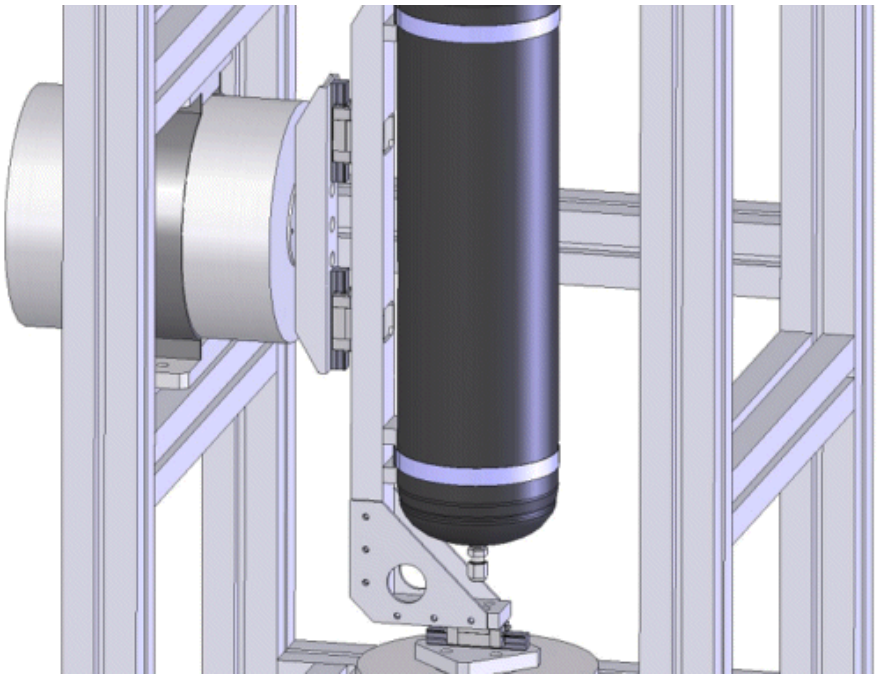

Figure 133. Solid model of shaker assembly with linear roller bearings and vessel support for independent biaxial vibration.[250]

The $NaAlH_4$ powder was loaded at a rate of between 100 and 200 g/hr using vibrational settling and compaction in the nitrogen glove box. A porous stainless steel filter was inserted into the center to provide hydrogen gas flow to and from the alanate materials. The weight of hydride loaded into the system was determined to be 3525 g.

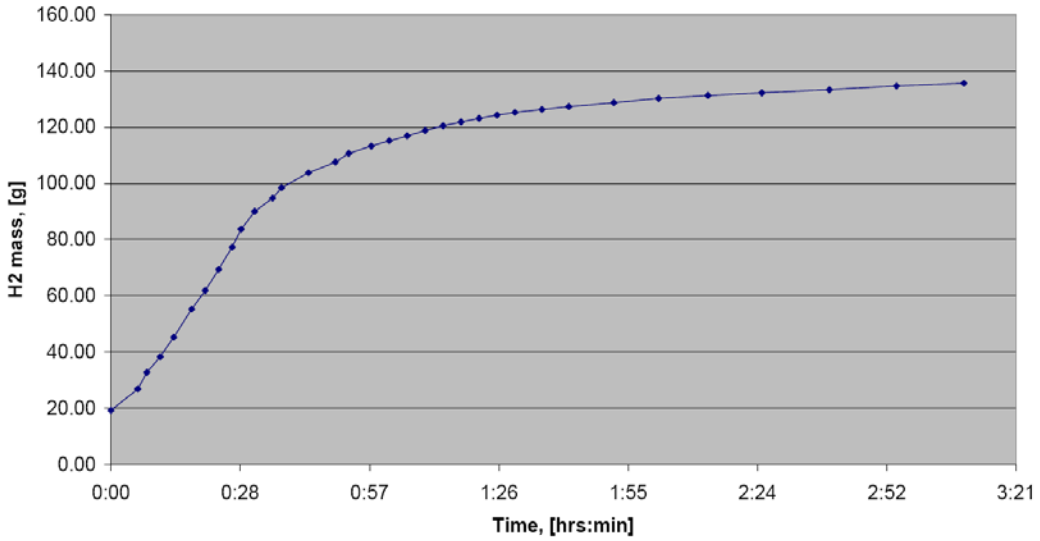

Figure 134. Absorption data for the first experiment performed at pressures starting at 1500 psi and dropping due to absorption in between each data point dosing.[250]

The system was then tested using a Sieverts apparatus. A preliminary desorption test was performed at 150 °C with final desorption pressures of nominally 15 psi. An absorption test was then conducted with peak hydrogen pressures of 1500 psi. Hydrogen was supplied to the system in doses after which the pressure would drop as hydrogen was absorbed. The measured mass of hydrogen supplied to the system versus time is plotted in Figure 134. After 3 hours, 136 g of hydrogen had been stored within the system (13 g of that being compressed H_2 gas). After an initial warm up period, the system was pressurized in doses with nominally 100 bar hydrogen. Temperature data from the thermocouples within and on the outside of the system are shown in Figure 135 as a function of time for the same uptake measurement. The waviness occurs due to the hydrogen dosing and pressure fluctuations. The exothermic hydrogen absorption reaction produces an increase in hydride/fin temperature above the circulated oil temperature for about 45 minutes, after which the interior temperatures are seen to lag during fluctuations of the oil temperature due to thermal inertia (heat capacity).

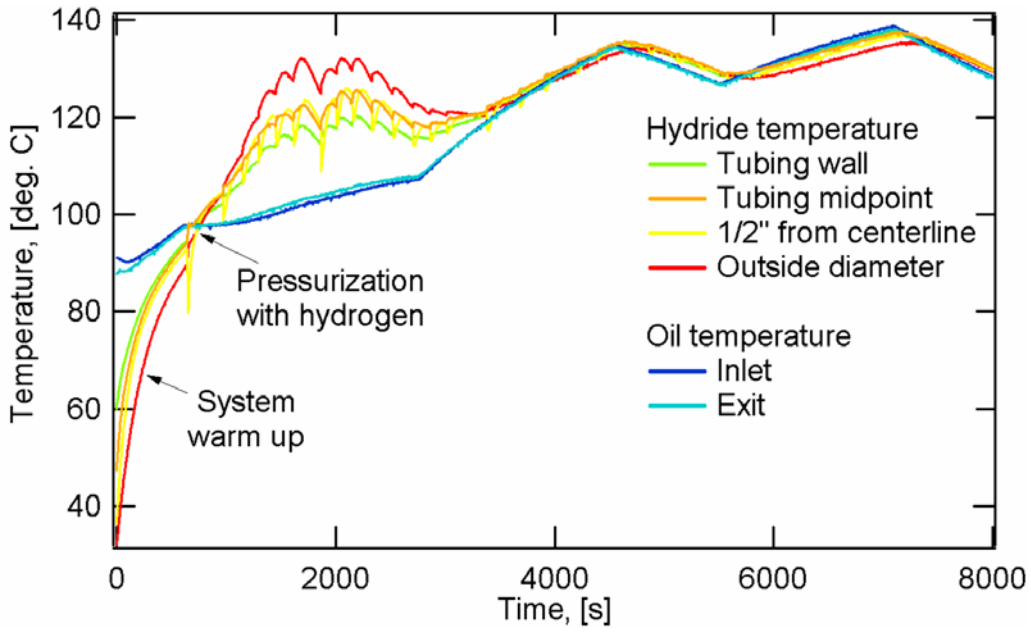

Figure 135. Temperatures for the four internal thermocouples and heat transfer oil during a Prototype 2 absorption test.[250]

A full analysis (including simulations) of the measurements provided information on the system performance relative to DOE hydrogen storage targets. From the results, UTRC proposed that potential improved performance could be achieved through the following optimizations:[250]

1. An average loaded hydride density of 0.85 g cm^{-3}. This density was obtained consistently in powder column densification tests on $NaAlH_4$. Results from a number of experiments have demonstrated that a finned tube heat exchanger can be loaded to essentially the same density as measured in powder column tests, i.e. 0.85 g cm^{-3}.

2. Making minor improvements to the system design, the loaded hydride mass would be 0.85 g cm^{-3} * 4900 cm^3 = 4165 g for this prototype. Scaling the vessel to nominally full size which would be approximately 10 times larger than the current prototype (1.36 kg per vessel – four vessels integrated into an automobile), there will be a reduction in specific mass (mass per unit volume) which will be most significant for two components:

3. The liner is needed for its gas impermeability, chemical inertness and as a form for filament winding. The 10X vessel can retain the 0.020" liner thickness which would result in the liner mass scaling as (Volume)^(2/3) or by a factor of 10^(2/3) = 4.64. With the prototype pressure vessel, the liner is over 70% of the mass, weighing 1375 g compared with 515 g for the composite overwrap,

4. The conventional hydrogen valve which is quite heavy, was not optimized for weight and could accommodate the 10X flow rates. As a first approximation use the same mass valve could be used for the 10X system,

5. The above two adjustments result in a gravimetric efficiency of 0.63 (kg hydride / kg system),

6. To meet a 2.3 wt. % system performance, the total effective wt. % of the material would need to be 2.3% / 0.63 = 3.65%, and

7. At 0.85 g cm^{-3}, 140 °C and 100 bar, the compressed gas storage is effectively 0.25% (kg H_2 gas / kg hydride),

8. Accounting for the compressed gas, the capacity of the material then would need to be 3.65% – 0.25% = 3.40%.

This study provides one example of the development of hydrogen storage systems based on materials engineering design supported by detailed measurements of various mechanical properties of advanced hydrogen storage materials.

Summary

It is our intent that this overview of measurements of the engineering properties of hydrogen storage materials will aid research and development of advanced systems for hydrogen storage. In particular we hope to have clarified some of the recommended practices and caveats in performing high-quality experiments to measure many of the important mechanical properties of hydrogen storage materials.

Acknowledgements

We gratefully acknowledge assistance and financial support from the U.S. Department of Energy Office of Energy Efficiency and Renewable Energy Hydrogen Storage Program. This work supported the President's Hydrogen Fuel and Advanced Energy Initiatives. The authors also acknowledge technical advice and contributions from many experts in the field including Dr. Philip Parilla and Dr. Thomas Gennett of the National Renewable Energy Laboratory in Golden CO, Dr. Carole Read of the U.S. Department of Energy, Dr. Gary Sandrock, Dr. George Thomas, and Dr. Robert Bowman Jr. consultants to the U.S. Department of Energy, Professor Gavin Walker of the University of Nottingham, United Kingdom, dr. Thomas Autrey of Pacific Northwest National Laboratory, Dr. Michael Miller of Southwest Research Institute in San Antonio TX, Dr. Anne Dailly, Dr. Frederick Pinkerton, Dr. Scott Jorgensen of General Motors GM R&D Center, Dr. Ole Martin Løvvik of the Institute for Energy Technology in Kjeller, Norway, Dr. Eric Poirier of General Motors/Optimal CAE Inc., Professor Channing Ahn of the California Institute of Technology in Pasadena CA, Dr. Kevin Ott, Dr. Anthony Burrell, and Dr. Troy Semelsberger of Los Alamos National Laboratory, Professor Richard Chahine and Dr. Renju Zacharia of the Université du Québec à Trois-Rivières, Canada, Andrea Sudik, Ford Motor Company, USA, Professor Klaus Yvon of the University of Geneva, Switzerland, Professor Sam Mao of the University of California Berkeley in Berkeley CA, and Dr. Nobuhiro Kuriyama and Dr. Tetsu Kiyobayashi of the National Institute of Advanced Industrial Science and Technology in Osaka, Japan, Dr. Robert Bowman Jr., Consultant to U.S. Department of Energy, Dr. Ewa Rönnebro, Pacific Northwest National Laboratories, Dr. Bart van Hassel, United Technologies Research Center, Dr. Lars Röntzsch, Fraunhofer Institute for Manufacturing Technology and Advanced Materials, Dresden, Germany, Dr. Michel Latroche, Institut de Chimie et des Matériaux de Paris Est CNRS, France, Dr. Patricia De Rango, Institut Néel CNRS, Grenoble, France, Dr. Mike Veenstra and Dr. Jun Yang of Ford Motor Co., USA, Dr. David Grant, of the University of Nottingham, United Kingdom, Daniel Dedrick, Sandia National Laboratories, Livermore, CA.

Disclaimer

"This report was prepared as an account of work sponsored by an agency of the United States Government. Neither the United States Government nor any agency thereof, nor any of their employees, nor the authors of this work, nor their respective employers nor the institutions they represent make any warranty, express or implied, or assumes any legal liability or responsibility for the accuracy, completeness, or usefulness of any information, apparatus, product, or process disclosed, or represents that its use would not infringe privately owned rights. Reference herein to any specific commercial product, process, or service by trade name, trademark, manufacturer, or otherwise does not necessarily constitute or imply its endorsement, recommendation, or favoring by the authors, the United States Government or any agency thereof."

References

1 Walker, G.S. (editor), “Solid-state hydrogen storage: materials and chemistry”, Woodhead Publishing Ltd, Cambridge, UK, (**2008**).

2 Barnes, R.G. (editor), “Hydrogen Storage Materials.” Trans Tech Publications, (**1988**).

3 Schlapbach, L., and Züttel, A., “Hydrogen-storage materials for mobile applications.” *Nature*, 414 (**2001**) p.353-358.

4 Broom D.P., “Hydrogen Sorption Measurements on Potential Storage Materials”, JRC Scientific and Technical Reports (**2008**), JRC 43223, EUR 23242 EN, ISBN 978-92-79-08345-7 ISSN 1018-5593 DOI: 10.2790/86100

5 Wiberg, E., and Amberger, E., “Hydrides of the Elements of Main Groups”, Z-ZV, Elsevier, Amsterdam, (**1971**), 2, D.A. Armitage.

6 Muller, W.M., Blackledge, J.P., Libowitz, G.G. editors, “Metal Hydrides”, Academic Press, New York, (**1968**).

7 Dedieu, A., “Transition Metal Hydrides”, Wiley-VCH (**1991**).

8 Sandrock, G., “A panoramic overview of hydrogen storage alloys from a gas reaction point of view.*” J. Alloys and Compounds*, 293-295 (**1999**): p. 877-888.

9 Sandrock, G., “State-of-the-art Review of Hydrogen Storage in Reversible Metal Hydrides for Military Fuel Cell Applications.” Department of the Navy, Office of Naval Research, NTIS Report # AD-A328073/2INZ, (**1997**).

10 Stephens, F.H., Vincent Pons, V., and Baker, R.T., “Ammonia–borane: the hydrogen source par excellence?“, *Dalton Trans*., (**2007**), 2613–2626 DOI: 10.1039/b703053c

11 Zidan, R., “Aluminum Hydride” in “Handbook of hydrogen storage: New Materials for Future Energy Storage”, eds. Hirscher, M., Hirose, K., Weinheim : Wiley-VCH, (**2009**) p. 249

12 Thomas, K.M., “Hydrogen adsorption and storage on porous materials.” *Catalysis Today*, 120 (**2007**): p. 389–398.

13 van den Berg, A.W.C., Arean, C.O., “Materials for hydrogen storage: current research trends and perspectives.” *Chemical Communications*, (**2008**): p. 668–681.

14 Schmitz, B., Muller, U., Trukhan, N., Schubert, M., Ferey, G. Hirscher, M., “Heat of Adsorption for Hydrogen in Microporous High-Surface-Area Materials.” *Chem Phys Chem*, 9 (**2008**): p. 2181–2184.

15 Perry, R.H. and Green, D.W., “Perry's Chemical Engineers”, Handbook, McGraw-Hill, (**1984**), ISBN 0-07-049479-7.

16 Roy, B.N., “Fundamentals of Classical and Statistical Thermodynamics”, John Wiley & Sons, (**2002**) ISBN 0-470-84313-6.

17 Reif, F., "Chapter 5 – Simple applications of macroscopic thermodynamics", Fundamentals of Statistical and Mechanical Physics, McGraw-Hill (**1965**), ISBN 0070518009.

18 Wiswall, R., "Hydrogen Storage in Metals" Chapter 5 in the book "Hydrogen in Metals II Application-Oriented Properties", G. Alefeld and J. Völkl eds. Topics in Applied Physics, V29 (**1978**) Springer-Verlag Berlin Heidelberg New York, p. 201-242.

19 Dantzer, P., "Metal-Hydride Technology: A Critical Review" Chapter 7 in the book "Hydrogen in Metals III: Properties and Applications" W. Wipf ed. Topics in Applied Physics, V73 (**1997**) Springer-Verlag Berlin Heidelberg, p. 278-340.

20 Sandrock, G., Suda, S., and Schlapbach, L., "Applications" Chapter5 in the book "Hydrogen in Intermetallic Compounds II: Surface and Dynamic Properties, Applications" L. Schlapbach ed., Topics in Applied Physics, V67 (**1992**) Springer-Verlag Berlin Heidelberg New York, p. 197-258.

21 "Engineered Hydrogen Storage Systems" D. Dedrick, Chapter 9, T. Johnson and P. Bénard, Ch. 10, and B. Bowman, D. Anton, and N. Stetson, Ch. 11 in the book "Hydrogen Storage Technology", (**2013**) CRC Press, Taylor & Francis Group, Boca Raton, London, New York p. 331-404.

22 Wanibe, Y. and Itoh, T., "New Quantative Approach to Powder Technology", Wiley, New York, (**1999**).

23 McGlinchey, D., "Bulk Solids Handling", Wiley, New York, (**2008**).

24 Gross, K.J., Carrington, R.K., Barcelo, S., Karkamkar, A. Purewal, J., Ma, S., Zhou, H.-C., Dantzer, P., Ott, K., Burrell, T., Semeslberger, T., Pivak, Y., Dam, B., and Chandra, D., "Recommended Best Practices for the Characterization of Storage Properties of Hydrogen Storage Materials", DOE publication.

25 Lowell, S., Shields, J.E., Thomas, M.A., Thommes, M., "Characterization of Porous Solids and Powders: Surface Area, Pore Size, and Density", Klewer Academic: Dordrecht, The Netherlands, (**2004**).

26 Malbrunot, P., Vidal, D., Vermesse, J., "Adsorbent Helium Density Measurement and Its Effect on Adsorption Isotherms at High Pressure", *Langmuir*, 13 (**1997**) p. 539-544.

27 Webb, P.A., "Volume and Density Determinations for Particle Technologists", Application Note, Micromeritics Instrument Corp., February (2001)

28 US DOE EERE Hydrogen Program, "Technical System Targets: Onboard Hydrogen Storage for Light-Duty Fuel Cell Vehicles" https://www1.eere.energy.gov/hydrogenandfuelcells/storage/pdfs/targets_onboard_hydro_storage.pdf

29 US DOE EERE Hydrogen Program, "Targets for Onboard Hydrogen Storage Systems for Light-Duty Vehicles" Sept. **(2009)**, http://www1.eere.energy.gov/hydrogenandfuelcells/storage/pdfs/targets_onboard_hydro_storage_explanation.pdf

30 Yang, J., Sudik, A., Wolverton, C., and Siegel, D.J., "High capacity hydrogen storage materials: attributes for automotive applications and techniques for materials discovery", Chem. Soc. Rev. **(2010)**, 39, p. 656–675.

31 Gross, K.J., Chartouni, D., Fauth, F., "A new hexagonal Laves phase deuteride

$CeMn_{1.5}Al_{0.5}D_x$ (0<x<4)" *J. Alloys and Compounds*, 306 (**2000**), p. 203-218.

32 Fukai Y., The metal-hydrogen system basic bulk properties, Springer, second ed. (**2005)**.

33 Checchetto, R., Carotenuto, G., Bazzanella, N., Miotello, A., "Synthesis and characterization of polymer embedded $LaNi_5$ composite material for hydrogen storage*", J. Phys D App Phys* 40 (**2007**), p.4043-4048.

34 Schlapbach, L., ed., "Hydrogen in Intermetallic Compounds II: Surface and Dynamic Properties, Applications", Topics in Applied Physics, (**1992**) Springer: Berlin.

35 Sakai, T., Miyamura, H., Kuriyama, N., Ishikawa, H., Uehara, I., "Hydrogen storage alloys for nickel metal hydride battery", *Z Phys Chem* 183 (**1994**), p.333-346.

36 Kojima, Y., Kawai, Y., Towata, S., Matsunaga, T., Shinozawa, T., and Kimbara, M., "Development of metal hydride with high dissociation pressure", *J. Alloys and Compounds*, 419 (**2006**), p.256-261.

37 Hahne, E., and Kallweit, J., "Thermal conductivity of metal hydride materials for storage of hydrogen: Experimental investigation", *Int. J. Hydrogen Energy*, 23 (**1998**), p.107-114.

38 Rudman, P.S., "Hydrogen-diffusion-rate-limited hydriding and dehydriding kinetics", *J Appl Phys*, 50 (**1979**), p.7195-7199.

39 Flueckiger, S., Voskuilen, T., Pourpoint, T., Fisher, T.S., and Zheng, Y., "In situ characterization of metal hydride thermal transport properties", *Int. J. Hydrogen Energy*, 35 (**2010**), p.614 - 621.

40 Zhang, J., Fisher, T.S., Ramachandran, P.V., Gore, J.P., and Mudawar, I., "A review of heat transfer issues in hydrogen storage technologies", *J Heat Transfer*, 127 (**2005**), p.1391-1399.

41 Kim, K.J., Montoya, B., Razani, A., and Lee, K.H., "Metal hydride compacts of improved thermal conductivity", Int. J. Hydrogen Energy, 26 (**2001**), p.609-613.

42 Klein, H.P., and Groll, M., "Heat transfer characteristics of expanded graphite matrices in metal hydride beds", *Int. J. Hydrogen Energy*, 29 (**2004**), p.1503-1511.

43 Sanchez, A.R., Klein, H.P., and Groll, M., "Expanded graphite as heat transfer matrix in metal hydride beds", *Int. J. Hydrogen Energy*, 28 (**2003**), p.515 -- 527.

44 Ron, M., Bershadsky, E., and Josephy, Y., "The thermal-conductivity of porous metal matrix hydride compacts", *J Less Comm Met*, 172 (**1991**), p.1138-1146.

45 Josephy, Y., Eisenberg, Y., Perez, S., Bendavid, A., and Ron, M., "Hydrogen and thermal yields of porous metal matrix hydride compacts of $MmNi_{4.15}Fe_{0.85}H_x$", *J Less Comm Met*, 104 (**1984**), p.297-305.

46 Bershadsky, E., Josephy, Y., and Ron, M., "Permeability and thermal conductivity of porous metallic matrix hydride compacts", *J Less Comm Met*, 153 (**1989**), p.65-78.

47 Cantrell, J.S. and Bowman, Jr., R.C., "Phase composition and the effect of thermal cycling for VH_x, $V_{0.995}C_{0.005}H_x$, and $V_{0.975}Zr_{0.020}C_{0.005}H_x$*" J. Alloys and Compounds,* 293-295 (**1999**) p. 156-160.

48 Bowman, Jr., R.C., Lynch, F.E., Marmaro, R.W., Luo, C.H., Fultz, B., Cantrell, J.S., and Chandra, "Effects of thermal cycling on the physical properties of VH_x", *Z. Physk. Chem*., 181 (**1993**) p. 269-273.

49 Marmaro, R.W., Lynch, F.E., and Chandra, D., "Investigation of Long Term Stability in Metal Hydrides", NAS9-18175 report by HCI, 12410 North Dumont Way, Littletown, CO 80125 November, (**1991**).

50 Arun, C. and Ramaprabhu, S., "Hydrogen absorption studies in $Zr_{0.2}Tb_{0.8}Co_3$ and decrepitation and cyclic stabilities in $Zr_{0.2}Tb_{0.8}Co_3$ and ZrMnFe*", J. Alloys and Compounds,* 259 (**1997**) p. 254-259.

51 Bowman, R.C., Reiter, J.W., Mosher, D.A., Thomas, G., Hardy, B.G., and Anton, D.A., "Survey of Solid State Hydride Tanks for Hydrogen Storage and Energy Conversion Applications" Presentation at Summer School Lectures MH2008.

52 Horiba Scientific, "A Guidebook to Particle Size Analysis", (**2012**) HORIBA Instruments, Inc.

53 Allen, T., "Particle Size Measurement", 4th ed., Chapman and Hall, London (**1990**).

54 Svarovsky, L., "Characterization of Powders, in Principles of Powder Technology", M.J. Rhodes, ed., John Wiley &Sons, Chichester (**1990**) p. 35.

55 Jillavenkatesa, A., Dapkunas, S.J., Lum, L-S.H., "Particle Size Characterization", NIST Recommended Practice Guide, Special Publication 960-1, January (**2001**).

56 ASTM E799 – 03 (**2009**) "Standard Practice for Determining Data Criteria and Processing for Liquid Drop Size Analysis". ASTM International, West Conshohocken, PA, **(2009)** DOI: 10.1520/E0799-03R09, www.astm.org.

57 ISO 13320: (**2009**) "Particle size analysis -- Laser diffraction methods".

58 Hampel, C.A., and Hawley, G.G., "Glossary of Chemical Terms", 2nd ed., New York (**1982**), Van Nostrand Reinhold Company.

59 Gregg, S.J., and Sing, K.S.W., "Adsorption, Surface Area and Porosity", London (**1982**), Academic Press, Inc.

60 Do, D.D., "Adsorption Analysis: Equilibria and Kinetics", Singapore (**1998**), Imperial College Press.

61 Murata, K., Kaneko, K,. Kokai, F., Takahashi, K., Yudasaka, M., and Iijima, S., "Pore structure of single-wall carbon nanohorn aggregates", *Chem. Phys. Lett.*, 331, **(2000)** p. 14.

62 Robens, E., Keller, J.U., Massen, C.H., and Staudt, R., "Sources of Error in Sorption and Density Measurements", *J. of Thermal Analysis and Calorimetry*, 55 (**1999**) p. 383-387.

63 Sircar, S., "Excess Properties and Thermodynamics of Multicomponent Gas Adsorption," J. Chem. Soc. Faraday Trans. I, 81, 1527– 1540 (1985). Sircar, S., "Measurement of Gibbsian Surface Excess," AIChE J., 47(5), 1169–1176 (2001). Sircar, S., "Role of Helium Void Measurement in Estimation of Gibbsian Surface Excess," in Proc. of FOA 7, K. Kaneko, H. Kanoh, and Y. Hanzawa (Eds.), pp. 656–663, IK International, Chiba-City, Japan 2001b.

64 Gumma, S., and Talu, O. "Gibbs Dividing Surface and Helium Adsorption", *Adsorption*, 9(1), **(2003)**, p. 17-28.

65 Smith, K.C. and Fisher, T.S., "Models for metal hydride particle shape, packing, and heat transfer*", Int. J. Hydrogen Energy*, 37 (**2012**), p.13417–13428.

66 Smith, K.C., Alam, M., and Fisher, T.S., "Athermal jamming of soft frictionless Platonic

solids", *Phys Rev E*, 82, (**2010**), p.051304.

67 Smith, K.C., Fisher, T.S., and Alam, M., "Isostaticity of constraints in amorphous jammed systems of soft frictionless Platonic solids", *Phys Rev E* , 84 (**2011**), p.030301.

68 Smith, K.C., Mukherjee, P.P., and Fisher, T.S., "Columnar order in jammed LiFePO4 cathodes: Ion transport catastrophe and its mitigation", *Chem Phys*, 14 (**2012**), p.7040-7050.

69 Asakuma, Y., Miyauchi, S., Yamamoto, T., Aoki, H., and Miura, T., "Homogenization method for effective thermal conductivity of metal hydride bed", *Int. J. Hydrogen Energy*, 29 (**2004**), p.209 – 216.

70 Ueoka, K., Miyauchi, S., Asakuma, Y., Hirosawa, T., Morozumi, Y., Aoki, H., et al., "An application of a homogenization method to the estimation of effective thermal conductivity of a hydrogen storage alloy bed considering variation of contact conditions between alloy particles*", Int. J. Hydrogen Energy*, 32 (**2007**), p.4225 - 4232.

71 Tsotsas, E., and Martin, H., "Thermal conductivity of packed beds: A review", *Chem Eng Process*, 22 (**1987**), p.19-37.

72 Solomon, H., "Geometric probability", SIAM, (**1978**).

73 Smith, K.C., "Isotropic random fracture model for metal hydride powder", (**2011**), doi:10.4231/D31V5BC8W. https://nanohub.org/resources/12012/download/rndmfrc_manual.pdf

74 Mujat, C., "Measurements of particle size and size distributions of titanium chromium manganese by dry and wet laser diffraction", (**2009**), communicated to KC Smith.

75 "HWT" is an AB2 alloy: $Ti_{0.98}Zr_{0.02}V_{0.43}Fe_{0.06}Cr_{0.05}Mn_{1.52}$ per, Wanner, M., Hoffmann, G., Groll, M., "Thermodynamic and Structural Changes of an AB_2-Laves-Phase Alloy ($Ti_{0.98}Zr_{0.02}V_{0.43}Fe_{0.06}Cr_{0.05}Mn_{1.52}$) During Extended Thermal Cycling" Hydrogen Power: Theoretical and Engineering Solutions (**1998**), p. 257-262.

76 Donev, A., Cisse, I., Sachs, D., Variano, E. A., Stillinger, F. H., Connelly, R., Torquato, S., Chaikin, P. M. "Improving the Density of Jammed Disordered Packings Using Ellipsoids". *Science* 303, 5660, **(2004)**, p. 990–993.

77 Song, C., Wang, P., Makse, H.A., "A phase diagram for jammed matter". *Nature* 453, 7195 **(2008)**, p. 629–632.

78 Jaoshvili, A., Esakia, A., Porrati, M., and Chaikin, P.M., "Experiments on the random packing of tetrahedral dice", *Phys Rev Lett*, 104 (**2010**), p.185501.

79 Pasini, J.M., Corgnale, C., van Hassel, B.A., Motyka, T., Kumar, S., Simmons, K.L., "Metal hydride material requirements for automotive hydrogen storage systems", *Int. J. Hydrogen Energy,* 38 (**2013**), p. 9755-9765.

80 van Hassel, B., Pasini, J.M., Gorbounov, M., Holowczak, J., Fedchenia, I., Khalil, J., Sun, F., Tang, X., Brown, R., Pryor, L., and Laube, B. United Technologies Research Center (UTRC) DOE Hydrogen and Fuel Cells Program FY (**2011**) Annual Progress Report

81 Hardy, B.J., and Anton, D.L., "Hierarchical methodology for modeling hydrogen storage systems. Part I: Scoping models", *Int. J. Hydrogen Energy,* 34 (**2009**), p. 2269-2277.

82 Hardy, B.J., and Anton, D.L., "Hierarchical methodology for modeling hydrogen storage systems. Part II: Detailed models*", Int. J. Hydrogen Energy,* 34 (**2009**), p. 2992-3004.

83 van Hassel, B.A., Mosher, D., Pasini, J.M., Gorbounov, M., Holowczak, J., Tang, X., Brown, R., Laube, B., and Pryor, L., "Engineering Improvement of $NaAlH_4$ System", AIChE Topical Conference: Hydrogen Production and Storage: Hydrogen Storage System Engineering and Applications, (**2010**), Salt Lake City, UT, USA, *Int. J. Hydrogen Energy* 37 (2012) p. 2756-2766

84 Lozano, G.A., Na Ranong, C., Bellosta von Colbe, J.M., Bormann, R., Hapke, J., Fieg, G., Klassen, T., Dornheim, M., "Optimization of hydrogen storage tubular tanks based on light weight hydrides", *Int. J. Hydrogen Energy*, 37, (**2012**), p.825–2834

85 Lozano, G.A., "Development of Hydrogen Storage Systems using Sodium Alanate", Dissertation, Technische Universität Hamburg-Harburg, Hamburg (**2010**).

86 Dedrick D.E., Kanouff M.P., Replogle B.C., Gross K.J., "Thermal properties characterization of sodium alanates*", J. Alloys and Compounds,* 389 (**2005**) p. 299-305.

87 Meyer D., "Effekt der Kompaktierung auf das Wasserstoffspeicherverhalten von Natriumalanat" Bachelorarbeit, Helmut-Schmidt-Universität / Universität der Bundeswehr Hamburg, Hamburg **2009**.

88 Zhang, N. and Rosato, A.D., "Experiments and Simulations on Vibration Induced Densification of Bulk Solids", *KONA* 24 (**2006**) p.93-103

89 Cumberland, D. J., and Crawford, R.J., "The Packing of Particles", Vol. 6 (Elsevier, **1987**).

90 An, X.Z., Yang, R.Y., Dong, K.J., Zou, R.P., and Yu, A.B., "Micromechanical simulation an analysis of one dimensional vibratory sphere packing", *Phys Review Letters*, 95, (**2005**), p.205502.

91 Nowak, E.R., Povinelli, M., Jaeger, H.M., Nagel, S.R., Knight, J.B., and Ben-Naim, E., "Powders & Grains 97", edited by R. Behringer and J.T. Jenkins (Balkema, Durham, NC, **1997**), p. 377 - 380.

92 Walton, O.R., "Numerical simulation of inclined chute flows of monodisperse, inelastic, frictional spheres", Mechanics of Materials, 16 (**1993**), p.239-247. Walton, O.R., "Particulate Two-Phase Flow", edited by M.C. Roco (Butterworths, Boston, **1992**), p. 884-911. Walton, O.R., and Braun, R.L., "Stress calculations for assemblies of inelastic spheres in uniform shear", *Acta Mechanica*, 63, (**1986**), p.73-86.

93 O'Hern, C.S., Silbert, L.E., Liu, A.J., and Nagel, S.R., "Jamming at zero temperature and zero applied stress: The epitome of disorder", *Phys Rev E*, 68 (**2003**), p.011306.

94 Yonezawa, F., and Cohen, M.H., "Granular effective medium approximation", *J Appl Phys*, 54 (**1983**), p.2895.

95 Sen, P.N., Scala, C., and Cohen, M.H., "A self-similar model for sedimentary-rocks with application to the dielectric-constant of fused glass-beads", *Geophysics*, 46 (**1981**), p.781-795.

96 Incropera, F.P., DeWitt, D.P., Bergman, T.L., and Lavine, A.S., "Fundamentals of Heat and Mass Transfer", Wiley, (**2007**).

97 Yang, R.Y., Zou, R.P., Yu, A.B., "Computer simulation of the packing of fine particles", *Phys*

Rev E, 62 (**2000**) p. 3900–3908.

98 Valverde, J.M., Quintanilla, M.A.S., Castellanos, A., "Jamming threshold of dry fine powders", *Phys Rev Lett*. 92 (**2004**) p. 258303.

99 Castellanos, A., Valverde, J.M., Quintanilla, M.A.S., "Physics of compaction of fine cohesive particles", *Phys Rev Lett*. 94 (**2005**) p. 075501.

100 Dedrick, D.E., Kanouff, M., Keller, J., Voskuilen Detlef Stolten, T., and Grube, T., (Eds.) "Optimization of Hydrogen Uptake and Release in Automotive-scale Metal Hydride Systems": 18th World Hydrogen Energy Conference 2010 - WHEC 2010 Parallel Sessions Book 4: Storage Systems / Policy Perspectives, Initiatives and Co- operations Proceedings of the WHEC, May 16.-21. 2010, Essen Schriften des Forschungszentrums Jülich / Energy & Environment, Vol. 78-4 Institute of Energy Research - Fuel Cells (IEF-3) Forschungszentrum Jülich GmbH, Zentralbibliothek, Verlag, (**2010**) ISBN: 978-3-89336-654-5

101 van Hassel, B.A., Mosher, D., Pasini, J.M., Gorbounov, M., Holowczak, J., Tang, X., Brown, R., Laube, B., Pryor, L., "Engineering improvement of $NaAlH_4$ system", Int. J. Hydrogen Energy, 37, 3 (**2012**), p. 2756-2766.

102 Information Report on the Development of a Hydrogen Quality Guideline for Fuel Cell Vehicles, SAE International Surface Vehicle Information Report, J2719 APR2008, Revised **2008**-04

103 Bowman, R.C., and Fultz, B. "Metallic Hydrides I: Hydrogen Storage and Other Gas- Phase Applications", MRS BULLETIN/SEPTEMBER (**2002**), p. 688-693.

104 Suda. S., and Sandrock, G*.,* "Three Decades of Intermetallic Hydrides - What happened to the Applications?", *Z. Phys. Chem*. 183 (**1994**) p. 149.

105 Sandrock, G*.J., Alloys Comps*., "A panoramic overview of hydrogen storage alloys from a gas reaction point of view" J. Alloys Compounds 293–295 (**1999**) p. 877, IEA/DOE/SNL Hydride Databases, http://hydpark.ca.sandia.gov/ (accessed July 2002).

106 Bowman, R.C., Jr., Luo, C.H., Ahn, C.C., Witham, C.K., and Fultz, B., "The effect of tin on the degradation of $LaNi_{5-y}Sn_y$ metal hydride during thermal cycling", *J. Alloys and Compounds,* 217 (**1995**) p. 185–192.

107 Friedlmeier, G., Manthey, A., Wanner, M., and Groll, M., "Cyclic stability of various application-relevant metal hydrides", *J. Alloys and Compounds,* 231 (**1995**) p. 880.

108 Wanner, M., Hoffmann, G., and Groll, M., "Hydrogen Power: Theoretical and Engineering Solutions", edited by T.O. Saetre (Kluwer Academic Publishers/Academic Press, Dordrecht, (**1998**) p. 257.

109 Lee, H.-H., and Lee, J.-Y., "The intrinsic degradation behaviour of the Laves phase alloy $Zr_{0.9}Ti_{0.1}Cr_{0.9}Fe_{1.1}$ upon temperature-induced hydrogen absorption-desorption cycling", *J. Alloys and Compounds,* 202 (**1993**) p. 23.

110 Ma, L.-P., Fang, Z.-Z., Dai, H.-B., Kang, X.-D., Liang, Y., Wang, P.-J., Wang, P., and Cheng, H.-M., "Effect of Li_3N additive on the hydrogen storage properties of Li-Mg-N-H system"., *J. Mater. Res*., 24, (**2009**), p. 1936-1942.

111 Purewal, J., Liu, D., Sudik, A., Veenstra, M., Yang, J., Maurer, S., Müller, U., and Siegel, D.J.,

"Improved Hydrogen Storage and Thermal Conductivity in High-Density MOF 5 Composites", *J. Phys. Chem. C*, 116, (**2012**) p. 20199−20212.

112 Müller, U., Schubert, M., Teich, F., Puetter, H., Schierle-Arndt, K., Pastre, J., "*Metal–organic frameworks—prospective industrial applications*", *J. Mater. Chem*. 16, (**2006**), p. 626−636.

113 Czaja, A.U., Trukhan, N., Müller, U., "Industrial applications of metal–organic frameworks", *Chem. Soc. Rev*. 38, (**2009**), p. 1284−1293.

114 Jorgensen, S.W., "Hydrogen storage tanks for vehicles: Recent progress and current status", *Curr. Opin. Solid State Mater. Sci*. 15, (**2011**), p. 39−43.

115 Purewal, J.J., Liu, D., Yang, J., Sudik, A., Siegel, D., Maurer, S., Mueller, U., "Increased volumetric hydrogen uptake of MOF-5 by powder densification", *Int. J. Hydrogen Energy,* 37, (**2012**), p. 2723−2727.

116 Hu, Y.H., Zhang, L., "Amorphization of metal-organic framework MOF-5 at unusually low applied pressure", *Phys. Rev. B* 81, (**2010**), p. 174103.

117 Zacharia, R., Cossement, D., Lafi, L., Chahine, R., "Volumetric hydrogen sorption capacity of monoliths prepared by mechanical densification of MOF-177", *J. Mater. Chem*. 20, (**2010**), p. 2145−2151.

118 Dailly, A., Poirier, E., "Evaluation of an industrial pilot scale densified MOF-177 adsorbent as an on-board hydrogen storage medium", *Energy Environ. Sci*. 4, (**2011**), p. 3527−3534.

119 Jordá-Beneyto, M., Lozano-Castelló, D., "Advanced activated carbon monoliths and activated carbons for hydrogen storage", Suárez-García, F., Cazorla-Amorós, D., Linares-Solano, A., *Microporous Mesoporous Mater*. 112, (**2008**), p. 235−242.

120 McGeary, R.K., *J. Am. Ceram. Soc*. 44, (**1961**), p. 513−522.

121 Liu, D., Purewal, J.J., Yang, J., Sudik, A., Maurer, S., Mueller, U., Ni, J., Siegel, D., *Int. J. Hydrogen Energy,* 37, (**2012**), p. 6109−6117.

122 Halsey, G., Taylor, H.S., "The Adsorption of Hydrogen on Tungsten Powders", *J. Chem. Phys*. 15, (**1947**), p. 624−630.

123 Temkin, M., Pyzhev, V., "Kinetics of ammonia synthesis on promoted iron catalysts.", *Acta Physicochimica*, *URSS* 12, (**1940)**, p. 327−356.

124 Sips, R., "On the Structure of a Catalyst Surface", *J. Chem. Phys*. 16, (**1948**), p. 490−495.

125 Honig, J.M., Reyerson, L.H., "Adsorption of Nitrogen, Oxygen and Argon on Rutile at Low Temperatures; Applicability of the Concept of Surface Heterogeneity", *J. Phys. Chem*. 56, (**1952**), p. 140−144.

126 Bhatia, S.K., Myers, A.L. "Optimum Conditions for Adsorptive Storage", *Langmuir* 22, (**2006**), p. 1688−1700.

127 Fuller, E.L., Poulis, J.A., Czanderna, A.W., Robens, E., "Volumetric and gravimetric methods of determining monolayer capacities", *Thermochim. Acta* 29, 2, (**1979**) p. 315-318.

128 Tamari, S., "Optimum design of the constant-volume gas pycnometer for determining the volume of solid particles", *Meas. Sci. Technol*. 15 (**2004**) p. 549–558.

129 Huang, H., Wang, K., Bodily, D.M., Hucka, V.J., "Density measurements of Argonne Premium coal samples", *Energy & Fuels*, 9 (**1995**) p.20-24

130 Sircar, S., "Gibbsian Surface Excess for Gas Adsorption — Revisited", *Industrial & Engineering Chemistry Researc*h, 38 (**1999**) p. 3670-3682.

131 Sircar, S., "Measurement of Gibbsian Surface Excess", *AIChE Journal*, 47 (**2001**) p. 1169-1176.

132 Sircar, S., *Int. Adsorption Society*, (**2002**) p. 377.

133 Haas, M.K, Zielinski, J.M., Dantsin, C.G., Coe, Pez, G.P., Cooper, A.C., "Focus Section: Tailoring single walled carbon nanotubes for hydrogen storage", *J. Materials Research*, 20 (**2005**) p. 3214-3223.

134 Lachawiec, A.J., Jr., DiRaimondo, T.T., Yang, R.T., "A Robust Volumetric Apparatus and Method for Measuring High-Pressure Hydrogen Storage Properties of Nanostructured Materials", *Review of Scientific Instruments*, 79 (**2008**) p. 063906-12.

135 ASTM D7481 – 09, "Standard Test Methods for Determining Loose and Tapped Bulk Densities of Powders using a Graduated Cylinder", ASTM International, West Conshohocken, PA, **(2003)** DOI: 10.1520/D7481-09, www.astm.org.

136 USP616, "Bulk Density and Tapped Density of Powders", **(2012)** The United States Pharmacopeial Convention Stage 6 Harmonization.

137 ASTM B527 – 06, "Standard Test Method for Determination of Tap Density of Metallic Powders and Compounds" ASTM International, West Conshohocken, PA, (2006) DOI: 10.1520/B0527-06, www.astm.org.

138 ASTM E2651 – 13, "Standard Guide for Powder Particle Size Analysis" ASTM International, West Conshohocken, PA, (2013) DOI: 10.1520/E2651, www.astm.org.

139 T. Allen, "Particle Size Measurement", 4th ed., Chapman and Hall, London (1990).

140 L. Svarovsky, "Characterization of Powders", in Principles of Powder Technology, M.J. Rhodes, ed., John Wiley &Sons, Chichester (1990) p. 35.

141 Wikipedia, "Log-normal distribution", Derivative by Mikael Häggström from the original, File:Lognormal distribution PDF.png by User: Par, http://en.wikipedia.org/wiki/Log-normal_distribution; http://creativecommons.org/licenses/by-sa/3.0 .

142 Compilation from: Jillavenkatesa, A., Dapkunas, S.J., Lum, L-S.H., "Particle Size Characterization", NIST Recommended Practice Guide, Special Publication 960-1, January (**2001**), and Bowen, P., "Particle Size Measurement - A comparison of methods in the nanometre (to millimetre) range in liquids", presentation Co-Nanomet (**2010**).

143 Cheng, H.M., Li, F., Sun, X., Brown, S.D.M., Pimenta, M.A., Marucci, A., Dresselhaus, G., Dresselhaus, M.S., "Bulk morphology and diameter distribution of single-walled carbon nanotubes synthesized by catalytic decomposition of hydrocarbons", *Chem. Physics Letters*, 289 (**1998**) p. 602–610

144 Thess, A., Lee, R., Nikolaev, P., Dai, H.J., Petit, P., Robert, J., Xu, C.H., Lee, Y.H., Kim, S.G., Rinzler, A.G., Colbert, D.T., Scuseria, G.E., Tomanek, D., Fischer, J.E., Smalley, R.E., *Science* 273 (**1996**) p.483.

145 Wildöer, J.W.G., Venema, L.C., Rinzler, A.G., Smalley, R.E., Dekker, C., "Electronic structure of atomically resolved carbon nanotubes", *Nature* 391 (**1998**), p. 59.

146 Journet, C., Maser, W.K., Bernier, P., Loiseau, A., Lamy de la Chapelle, M., Lefrant, S.,

Deniard, P., Lee, R., Fischer, J.E. "Large-scale production of single-walled carbon nanotubes by the electric-arc technique" ,*Nature* 388 (**1997**), p.756.

147 ISO 13320-1: (**1999**), Particle size analysis -- Laser diffraction methods -- Part 1: General principles.

148 Wikipedia article, "Langmuir equation", http://en.wikipedia.org/wiki/Langmuir_isotherm, Figure: "Langmuir isotherm", http://creativecommons.org/licenses/by-sa/3.0.

149 Wikipedia article, "Adsorption", http://en.wikipedia.org/wiki/Adsorption, Figure: "Langmuir isotherm (red) and BET isotherm (green)", http://creativecommons.org/licenses/by-sa/3.0.

150 Brunauer, S., Emmett, P.H., and Teller, E., "Adsorption of Gases in Multimolecular Layers", *J. Am. Chem. Soc*., 60 (**1938**), p.309. doi:10.1021/ja01269a023

151 Wikipedia article, "BET Theory", http://en.wikipedia.org/wiki/BET_theory, Figure: "BET Plot", http://creativecommons.org/licenses/by-sa/3.0.

152 Rouquerol, J., Llewellyn, P., and Rouquerol, F., "Is the BET equation applicable to microporous adsorbents?" In: Characterization of Porous Solids VII. P. Lewellyn, F. Rodriguez-Reinoso, J. Rouquerol, N. Seaton (Eds): Studies in Surface Science and Catalysis, 160 (**2007**) p. 49-56.

153 http://helios.princeton.edu/zeomics/cgi-bin/view_structure.pl?src=iza&id=FAU&token=7ffba5f41d52f297da8ab530245a0419

154 http://www.quantachrome.com/newsletter/Dec_08newsletter.html

155 Hirscher, M., & Panella, B. "Hydrogen storage in metal-organic frameworks", *Scripta Materialia*, 56, (**2007**) p. 809-812.

156 Willems, J.J.G., *Philips J. Res. Suppl*., 39 (1) (**1984**) p. 10.

157 Notten, P.H.L., Daams, J.L.C., De Veirman, A.M., and Stahls, A.A. ., "In situ X-ray diffraction: a useful tool to investigate hydride formation reactions", *J. Alloys and Compounds,* 209 (**1994**) p. 85-91.

158 Notten, P.H.L., Daams, J.L.C., and Einerhand, R.E.F., "On the nature of the electrochemical cycling stability of non-stoichiometric LaNi5-based hydride-forming compounds Part II. In situ x-ray diffractometry",*J. Alloys and Compounds,* 210 (**1994**) p.233-241.

159 Meli, F., Züttel, A., and Schlapbach, L. ., "Surface and bulk properties of $LaNi_{5-x}Si_x$ alloys from the viewpoint of battery applications", *J. Alloys and Compounds,* 190, (**1992**) p.17-24

160 Meli, F., Ph.D. Diss. Nr. 1023, University of Fribourg, Switzerland (**1993**).

161 Chartouni, D., Meli, F., Züttel, A., Gross, K., and Schlapbach, L., "The influence of cobalt on the electrochemical cycling stability of $LaNi_5$-based hydride forming alloys", *J. Alloys and Compounds*, 241, (**1996**) p.160-166.

162 Sakai, T., Muta, K., Miyamura, H., Kuriyama, N., and Ishikawa H., in "Hydrogen Storage Materials, Batteries and Electrochemistry", D.A. Corrigan and S. Srinivasan, (Editors), The Electrochemical Society Proceedings Series, Pennington, NJ (**1992**).

163 Sakai, T., Matsuoka, M., and Iwakura C., in "Handbook on the Physics and Chemistry of Rare Earths", K.A. Gschneidner, Jr., and L. Eyring, Editors, *Elsevier Science*, 21, (**1995**) p.

133-178.

164 Chartouni, D, and Gross, K., "Phase Transitions in LaNi4Co during Electrochemical Cycling An In Situ X-Ray Diffraction Study", *J. Electrochem. Soc*. 148 (**2001**) p. 241-248.

165 Gross, K.J., Guthrie, S., Takara, S., and Thomas, G., "In-situ X-ray diffraction study of the decomposition of $NaAlH_4$",*J. Alloys and Compounds,* 297 (**2000**) p.270-281

166 Van Mal, H.H., Buschow, K.H.J., and Kuijpers, F.A., "Hydrogen absorption and magnetic properties of $LaCo_{5x}Ni_{5-5x}$ compounds",*J. Less-Common Met*. 32 (**1973**) p.289-296.

167 Flanagan, T.B., and Oates, W.A., "Hydrogen in Intermetallic Compounds I, Topics in Applied Physics", Springer-Verlag, Berlin, New York, 63, 81 (**1988**).

168 Beer & Johnston (2006). Mechanics of Materials (5th ed.). McGraw Hill.

169 Thummler, F., and Oberacker, R., "An Introduction to Powder Metallurgy" The institute of Materials, London **(1993)**.

170 Ceramics Science and Technology: Volume3: Synthesis and Processing, First Edition. Edited by Ralf Riedel and I-Wei Chen 2012 Wiley-VCH Verlag GmbH & Co. KGaA. Published 2012 by Wiley-VCH Verlag GmbH & Co. KGaA.

171 Kendall, K., "The Strength of green bodies", *Special ceramics*, Edited by S. P. Howlett and D. Taylor Shellon: Stoke-an-Trent: The Institute of Ceramics **(1985)** p. 255-255.

172 Abdel-Ghani, M. et al. "Mechanical properties of cohesive particulate solids", Powder Technol. 65, **(1991)**, p. 113-123.

173 Bortzmeyer, D. et al. "Fracture mechanics of green products", *J. Eur. Ceram. Soc.* 11. **(1993)** p.9-16.

174 Jones, T.M., "The physicotechnical properties of starting materials used in tablet formulation", *Int. J. Pharm. Prod. Manuf.*, 2 **(1981)**, p. 17-24.

175 Dornheim, M., Doppiu, S., Barkhordarian, G., Boesenberg, U., Klassen, T., Gutfleisch, O., Bormann, R., "Hydrogen storage in magnesium-based hydrides and hydride composites." *Scripta Mater*. 56 (**2007**) p.841.

176 Mushnikov, N.V., Ermakov, A.E., Uimin, M.A., Gaviko, V.S., Terent'ev, P.B., Skripov, A.V., Tankeev, A.P., Solonin, A.V., Buzlukov, A.L., "Kinetics of Interaction of Mg-based mechanically activated alloys with hydrogen", *Phys. Met. Metallogr*. 102 (**2006**) p. 421.

177 Gupta, R., Agresti, F., Lo Russo, S., Maddalena, A., Palade, P., Principi, G., "Structure and hydrogen storage properties of MgH_2 catalysed with La_2O_3*", J. Alloys and Compounds,* 450 (**2008**) p. 310.

178 Oelerich, W., Klassen, T., Bormann, R., "Metal oxides as catalysts for improved hydrogen sorption in nanocrystalline Mg-based materials", *J. Alloys and Compounds,* 315 (**2001**) p. 237.

179 Polanski, M., Bystrzycki, J., Plocinski, T., "The effect of milling conditions on microstructure and hydrogen absorption/desorption properties of magnesium hydride (MgH_2) without and with Cr_2O_3 nanoparticles*", Int. J. Hydrogen Energy*, 33 (**2008**) p.1859.

180 Schulz, R., Huot, J., Liang, G., Boily, S., Lalande, G., Denis, M.C., Dodelet, J.P., "Recent developments in the applications of nanocrystalline materials to hydrogen technologies",

Mater. Sci. Eng. A 267 (**1999**) p. 240.

181 Zaluska, A., Zaluski, L., Ström-Olsen, J.O., "Nanocrystalline magnesium for hydrogen storage", *J. Alloys and Compounds,* 288 (**1999**) p.217.

182 Barkhordarian, G., Klassen, T., Bormann, R., "Fast hydrogen sorption kinetics of nanocrystalline Mg using Nb_2O_5 as catalyst", *Scripta Mater*. 49 (**2003**) p.213.

183 De Piccoli, C., Dal Toé, S., Lo Russo, S., Maddalena, A., Palade, P., Saber, A., Sartori, S., Principi, G., "Hydrogen storage in magnesium hydride doped with niobium pentaoxide and graphite", *Chem. Eng. Trans*. 4 (**2004**) p. 343.

184 Friedrichs, O., Aguey-Zinsou, F., Ares Fernández, J.R., Sánchez-López, J.C., Justo, A., Klassen, T., Bormann, R., Fernández, A., "MgH_2 with Nb_2O_5 as additive, for hydrogen storage: Chemical, structural and kinetic behavior with heating", *Acta Mater*. 54 (**2006**) p. 105.

185 Verga, M., Armanasco, F., Guardamagna, C., Valli, C., Bianchin, A., Agresti, F., Lo Russo, S., Maddalena, A., Principi, G., "Scaling up effects of Mg hydride in a temperature and pressure-controlled hydrogen storage device", *Int. J. Hydrogen Energy,* 34 (**2009**) p. 4602.

186 Khandelwal, A., Agresti, F., Capurso, G., Lo Russo, S., Maddalena, A., Gialanella, S., Principi, G., "Pellets of MgH_2-based composites as practical material for solid state hydrogen storage", *Int. J. Hydrogen Energy,* 35 (**2010**) p.3565–3571

187 Agresti, F., "Hydrogen Storage in Metal and Complex Hydrides: From Possible Niche Applications towards Promising High Performance Systems", Doctoral Thesis, Università degli Studi di Padova, Dipartimento di Ingegneria Meccanica – Settore Materiali.

188 Chaise, A., De Rango, P., Marty, P., Fruchart, D., Miraglia, S., Olivès, R., Garrier, S., "Enhancement of hydrogen sorption in magnesium hydride using expanded natural graphite*", Int. J. Hydrogen Energy,* 34 (**2009**) p. 8589.

189 Glage, A., Ceccato, R., Lonardelli, I., Girardi, F., Agresti, F., Principi, G., Molinari, A., Gialanella, S., "A powder metallurgy approach for the production of a MgH_2-Al composite material", *J. Alloys and Compounds*, 478 (**2009**) p.273.

190 ASM Handbook, vol. 3, Alloy Phase Diagrams, ASM International (**1992**) p.305-306.

191 Crivello, J.C., Nobuki, T., Kato, S., Abe, M., Kuji, T., "Hydrogen absorption properties of the γ-$Mg_{17}Al_{12}$ phase and its Al-richer domain", *J. Alloys and Compounds,* 446 (**2007**) p. 157.

192 Crivello, J.C., Nobuki, T., Kuji T., "Improvement of Mg-Al alloys for hydrogen storage applications", *Int. J. Hydrogen Energy*, 34 (**2009**) p.1937.

193 Raynor, G.V., "The Physical Metallurgy of Magnesium and Its Alloys", New York: Pergamon Press, **1959** p. 73.

194 Sandia National Laboratories– Hydride Information Centre, available at: http://hydpark.ca.sandia.gov/

195 Kleiner, S., Beffort, O., Wahlen, A., Uggowitzer, P.J., "Microstructure and mechanical properties of squeeze cast and semi-solid cast Mg-Al alloys*", J. Light Metals* 2 (**2002**) p.277.

196 Kostka, A., Coelho, R.S., Dos Santos, J., Pyzalla, A.R., "Microstructure of friction stir

welding of aluminium alloy to magnesium alloy", *Scripta Mater*, 60 (**2009**) p.953.

197 Johnson, T.A., Dedrick, D.E., and Behrens, R., "Durability Study of a Vehicle-scale Hydrogen Storage System", SAND2010-7802 Unlimited Release Printed November (**2010**).

198 Dedrick, D.E. et al. "The reactivity of sodium alanates with O_2, H_2O, and CO_2", SAND2007-4960, Sandia National Laboratories, **2007**

199 Charlas, B., Gilli, O., Doremus, P., Imbault, P., "Experimental investigation of the swelling/shrinkage of a hydride bed in a cell during hydrogen absorption/desorption cycles", *Int. J. Hydrogen Energy,* 37 (**2012**) p. 16031-116041.

200 Dedrick, D.E., Perras, Y.E., Zimmerman, M.D., "Wall pressure exerted by hydrogenation of sodium aluminum hydride" SANDIA REPORT, SAND2009-3812, Printed June **2009**.

201 Bowman, R.C. Jr., Nakamara, Y., Etsuo, A., "In situ x-ray and neutron powder diffraction study of $LaNi_{5-x}Sn_x$-H systems", Fall Meeting of the Materials Research Society, Symposium: Materials for Hydrogen Storage, December 1-2, **2004**.

202 Note: Gross, K., Author's experience in measurements on Ti-doped sodium alanates. Excessive milling of Al+NaH+$TiCl_3$ powders in Ar atmosphere caused the formation of large Al particles (1mm flakes) in the starting materials. These flakes disappeared with visual inspection (assumed consumed) after the first few hydrogen absorption/desorption cycles.

203 Dedrick, D., "Engineering properties of complex hydrides for system optimization" ASM Materials Solutions Conference Columbus, Ohio, **2004**.

204 Nasako, K., Ito, Y., Hiro, N., Osumi, M., "Stress on a reaction vessel by the swelling of a hydrogen absorbing alloy" *J. Alloys and Compounds,* 264 (**1998**) p. 271–276.

205 Johnson, T.A., (Livermore, CA) , Dedrick, D.E., Stephens, R.D., Chan, J.P., "Sodium Alanate Hydrogen Storage Material", US Patent Pending 20070178042

206 Gross, K. values derived from van't Hoff diagram (Figure 6) in: Qiu, C., Opalka, S.M., Olson, G.B. and Anton, D.L., "Thermodynamic modeling of the sodium alanates and the Na-Al-H system", *Int. J. Mat. Res*. 97 (**2006**) p. 11.

207 Jacobson, D.L., Hussey, D.S., Baltic, E., Udovic, T.J., Rush, J.J., Bowman, R.C. Jr., "Neutron imaging studies of metal-hydride storage beds", *Int. J. Hydrogen Energy,* 35 (**2010**) p. 12837-12845.

208 Payzant, E.A., Bowman, R.C. Jr., Johnson, T.A., Jorgensen, S.W., "In-situ chemistry mapping of hydrogen storage materials by neutron diffraction", *Materials Science and Technology (MS&T)* (**2013**).

209 Gondek, Ł., Selvaraj, N.B., Czub, J., Figiel, H., Chapelle, D., Kardjilov, N., Hilger, A., Manke, I., "Imaging of an operating $LaNi_{4.8}Al_{0.2}$–based hydrogen storage container", *Int. J. Hydrogen Energ*y, 36, 16, (**2011**) p. 9751-9757.

210 Bellosta von Colbe, J.M., Metz, O., Lozano, G.A., Klaus Pranzas, P., Schmitz, H.W., Beckmann, F., Schreyer, A., Klassen, T., Dornheim, M., "Behavior of scaled-up sodium alanate hydrogen storage tanks during sorption", *Int. J. Hydrogen Energy,* 37, 3, (**2012**) P.2807-2811.

211 Pranzas, P. K., Bösenberg, U., Karimi, F., Münning, M., Metz, O., Minella, C. B., Schmitz, H.-

W., Beckmann, F., Vainio, U., Zajac, D., Welter, E., Jensen, T. R., Cerenius, Y., Bormann, R., Klassen, T., Dornheim, M. and Schreyer, A., "Characterization of Hydrogen Storage Materials and Systems with Photons and Neutrons" *Adv. Eng. Mater.*, 13 (**2011**) p. 730–736.

212 Wilson, P.R., Bowman, R.C., Jr., Mora, J.L., Reiter, J.W., "Operation of a PEM fuel cell with $LaNi_{4.8}Sn_{0.2}$ hydride beds", *J. Alloys and Compounds,* 446-447 (**2007**) p. 676-80.

213 Groll, M., "Reaction beds for dry sorption machines", *Heat Recovery System & CHP* 13 (**1993**) p.341-6.

214 Nasako, K., Yonesaki, T., Satoh, K., Imoto, T., Fujitani, S., Hiro, N., et al., "The development of refrigeration systems using hydrogen-absorbing alloys", 183 (**1994**) p. 235-43.

215 Willers, E., Wanner, M., Groll, M., "A multi-hydride thermal wave device for simultaneous heating and cooling", *J. Alloys and Compounds,* 293-295 (**1999**), p. 915-8.

216 Levesque, J., Ciureanu, M., Roberge, R., Motyka, T., "Hydrogen storage for fuel cell systems with stationary applications- I. Transient measurement technique for packed bed evaluation*", Int. J. Hydrogen Energy,* 25 (**2000**) p. 1095-105.

217 Bhandari, P., Prina, M., Ahart, M., Bowman, R.C., Wade, L.A., "Sizing and dynamic performance prediction tools for 20 K hydrogen sorption cryocoolers", In: Ross Jr RG, editor, New York: Kluwer Academic/Plenum, **2001**, p. 531-40. Cryocoolers 11.

218 Prina, M., Bhandari, P., Bowman, R.C., Wade, L.A., Pearson, D.P., Morgante, G., et al. "Performance prediction of the planck sorption cooler and initial validation", In: Breon, S., Adams, M., DiPirro, M., Glaister, D., Hull, J.R., Kittel, P., Pecharsky V., editors, Advances in cryogenic engineering, *Am Inst Phys*, vol. 47, **2002**, p. 1201-8, New York, NY.

219 Udovic, T.J., Arif, M., Majkrzak, C.F., Jacobson, D.L., Yildirim, .T, Neumann, D.A., Rush, J.J., Pivovar, A.M., "Neutron metrology for the hydrogen economy", In: Chandra D, Bautista RG, Schlapbach L, editors, Advanced Materials for Energy Conversion II, (**2004**) p. 101-10, The Minerals, Metals & Materials Society.

220 Sakaguchi, H, Kohzai, A., Hatakeyama, K., Fujine, S., Yoneda, K., Kanda, K., Esaka, T., "Visualization of hydrogen in hydrogen storage alloys using neutron radiography". *Int. J. Hydrogen Energy,* 25 (**2000)** p. 1205-8.

221 Sakaguchi, H., Satake, Y., Hatakeyama, K., Fujine, S., Yoneda, K., Matsubayashi, M., Esaka, T., "Analysis of hydrogen distribution in hydrogen storage alloy using neutron radiography*", J. Alloys and Compounds,* 354 (**2003**) p. 208-15.

222 Bhandari, .P, Prina, M., Bowman, Jr R.C., Paine, C., Pearson, D., Nash, A., "Sorption coolers using a continuous cycle to produce 20 K for the Planck flight mission", *Cryogenics* 44 (**2004**) p. 395-401.

223 Pearson, D., Bowman, R., Prina, M., Wilson, P., "The Planck sorption cooler: using metal hydrides to produce 20 K*", J. Alloys and Compounds,* 446-447 (**2007**) p. 718-22.

224 Reiter, J.W., Karlmann, P.B., Bowman, Jr R.C., Prina, M., "Performance and degradation of gas-gap heat switches in hydride compressor beds". *J. Alloys and Compounds,* 446-447 (**2007**) p. 713-7.

225 Bowman, R.C., Jr., "Development of metal hydride beds for sorption cryocoolers in space

applications", *J. Alloys and Compounds,* 356-357 (2003) p. 789-93.

226 Trabold, T.A., Owejan, J.P., Gagliardo, J.J., Jacobson, D.L., Hussey, D.S., Arif, M." Use of neutron imaging for PEMFC performance analysis and design", In: Vielstich, W, Gasteiger, HA, Yokokawa, H, editors, Handbook of fuel cells: advances in electrocatalysis, materials, diagnostics and durability, Chichester, UK: John Wiley & Sons Ltd., (**2009)**, Vol. 5 & 6, p. 658-672.

227 Hussey, D.S., Jacobson, D.L., Arif, M., Huffman, P.R., Williams, R.E., Cook, J.C., "New neutron imaging facility at the NIST", *Nucl Instr and Meth* 542 (**2005**) p. 9-15.

228 Jacobson, D.L., Hussey, D.S., Baltic, E., LaRock, J., Arif, M., Gagliardo, J., et al., "Neutron radiography and tomography facilities at NIST to analyze in-situ PEM fuel cell performance", In: M. Arif, R.G. Downing, editors, Neutron radiography, proceedings of the 8th world conference on neutron radiography, Lancaster, PA: DES Tech Publications, **2008**, p. 50-7.

229 Hussey, D.S., Jacobson, D.L., Arif, M., Coakley, K.J., Vecchia, D.F., "In situ fuel cell water metrology at the NIST neutron imaging facility", *ASME J Fuel Cell Sci and Technol*, 7(2) (**2010)**, p. 021024.

230 Chadwick, M.B., Oblozinsky, P., Herman, M., et al., ENDF/B-VII.O: "Next generation evaluated nuclear data library for nuclear science and technology", *Nucl Data Sheets*, 107 (**2006**) p. 2931-3060.

231 van Vucht, J.H.N., Kuijpers, F.A., and Bruning, H.C.A.M., "Reversible Room Temperature Absorption of Large Quantities of Hydrogen by Intermetallic Compounds," *Philips Res. Rep*., 25 (**1970**) 133.

232 van Beck, J.R.G.C.M., Willems, J.J.G. and Donkersloot, H.C., in L.J., Pearce (ed.), Proc. 14th Int. Power Sources Syrup., Brighton, Power Sources, 10 (**1985**) p. 317.

233 Notten, P.H.L. & Einerhand, R.E.F., "Electrocatalytic hydride-forming compounds for rechargeable batteries". *Advanced Materials*, 3(7-8), (**1991**) p. 343-350.

234 Sakai, T., Takagi, A., Hazama, T., Miyamura, H., Kuriyama, N., Ishikawa H. and Iwakura, C., Proc. 3 Int. Conf. on Batteries for Utility Energy Storage, Kobe **1991**, p. 499.

235 Iwakura, C. and Matsuoka, M., *Prog. Batt. Mater*., 10 (**1991**) p. 81.

236 Notten, P.H.L., Einerhand, R.E.F. and Daams, J.L.C., "On the nature of the electrochemical cycling stability of nonstoichiometric $LaNi_5$-based hydride-forming compounds Part I, Crystallography and electrochemistry", *J. Alloys and Compounds,*, 210 (**1994**) p. 221-232

237 Notten, P.H.L., Einerhand, R.E.F. & Daams, J.L.C., "Non-stoichiometric hydride-forming compounds: an excellent combination of long-term cycling stability and high electrocatalytic activity"*, Z Physikalische Chemie*, 183, (**1994**) p. 267-279.

238 Coene, W., Notten, P.H., Hakkens, L F., Einerhand, R.E.F., and Daams, J.L.C., *Philos. Mag.*, 4, 65 (**1992**) p. 1485.

239 Notten, P.H.L., Daams, J.L.C., and Einerhand, R.E.F., "Melt-spinning of $AB_{5.5}$-type hydride-forming compounds and the influence of annealing on electrochemical and

crystallographic properties", B*erichte der Bunsen-Gesellschaft fuer Physikalische Chemie*, 96, (**1992**) p.656-667

240 Orimo, Nakamori, Y., Eliseo, J.R., Zuettel, A., and Jensen, C.M., "Complex hydrides for hydrogen storage", *Chem. Rev.* 107, (**2007**) p. 4111.

241 Luo, W.F. "($LiNH_2$-MgH_2): A viable hydrogen storage system*", J. Alloys and Compounds,* 381, (**2004**) p.284.

242 Luo, S., Flanagan, T.B., and Luo, W., "The effect of exposure of the H-storage system ($LiNH_2$+MgH_2) to water-saturated air", J. Alloys and Compounds, 440, (**2007**) p.L13-17.

243 Liu, Y., Hu, J., Xiong, Z., and Wu, G., "Improvement of the hydrogen-storage performances of Li-Mg-N-H system", *J. Mater. Res*., 22, (**2007**) p.1339.

244 Yang, J., Sudik, A., Siegel, D.J., Halliday, D., Drews, A., Carter, R.O., Wolverton, C., Lewis, G.J., Sachtler, J.W.A., Low, J.J., Faheem, S.A., Lesch, D.A., and Ozolins, V., "A self-catalyzing hydrogen-storage material", *Angew. Chem. Int. Ed*., 47, (**2008**) p. 882.

245 Hu, J., Liu, Y., Wu, G., Xiong, Z., Chua, Y.S., and Chen, P., "Improvement of hydrogen storage properties of the Li-Mg-N-H system by addition of $LiBH_4$", *Chem. Mater*. 20, (**2008**) p.4398.

246 Sudik, A., Yang, J., Halliday, D., and Wolverton, C., "Kinetic improvement in the $Mg(NH_2)_2$-LiH storage system by product seeding*", J. Phys. Chem. C* 111, (**2007**) p.6568.

247 Chen, P., Xiong, Z.T., Yang, L., Wu, G., and Luo, W., "Mechanistic investigations on the heterogeneous solid-state reaction of magnesium amides and lithium hydrides", *J. Phys. Chem. B* 110, (**2006**) p.14221.

248 Hu, Y., and Ruckenstein, E., "Ultrafast reaction between LiH and NH_3 during H_2 storage in Li_3N", *J. Phys. Chem. A* 107 (**2003**) p.9737.

249 Ichikawa, T., Hanada, N., Isobe, S., Leng, H., and Fujii, H., "Mechanism of novel reaction from $LiNH_2$ and LiH to Li_2NH and H_2 as a promising hydrogen storage system*", J. Phys. Chem. B* 108, (**2004**) p. 7887.

250 Mosher, D.A., Tang, X., Brown, R.J., Arsenault, S., Saitta, S., Laube, B.L., and Dold, R.H., "High Density Hydrogen Storage System Demonstration Using $NaAlH_4$ Based Complex Compound Hydrides", Final Report United Technologies Research Center prepared for Department of Energy Office of Energy Efficiency and Renewable Energy Hydrogen Program, Hydrogen Storage Under Contract DE-FC36-02AL67610.